RNP

Stará Lesná - 2012

RELATIVISTIC NUCLEAR PHYSICS: from HUNDREDS of MeV to TeV

РЕЛЯТИВИСТСКАЯ ЯДЕРНАЯ ФИЗИКА: от СОТЕН МэВ до ТэВ

Объединенный институт ядерных исследований

RELATIVISTIC NUCLEAR PHYSICS: from HUNDREDS of MeV to TeV

Proceedings of the 11th International Workshop

*Slovak Republic, Stara Lesna,
June 17–23, 2012*

РЕЛЯТИВИСТСКАЯ ЯДЕРНАЯ ФИЗИКА: от СОТЕН МэВ до ТэВ

Труды 11-го международного совещания

*Словакия, Стара Лесна,
17–23 июня 2012 г.*

Дубна 2013

УДК 539.17(042)
ББК 22.383.5я431
R41

The contributions are reproduced directly from the originals presented by the Organizing Committee.

Relativistic Nuclear Physics: from Hundreds of MeV to TeV: Proceedings
R41 of the 11th International Workshop (Stara Lesna, Slovakia, June 17–23, 2012). — Dubna: JINR, 2013. — 161 p., photo.

ISBN 978-5-9530-0354-4

From 17 to 23 June 2012 in Stara Lesna (Slovak Republic) there was held the traditional International Workshop «Relativistic Nuclear Physics: from Hundreds of MeV to TeV».

The Workshop was organized by the Joint Institute for Nuclear Research, the Institute of Physics of the Slovak Academy of Sciences, and the University of name Safarik (Kosice, Slovak Republic). At the Workshop there were presented new physical results obtained at the JINR Nuclotron, at the Large Hadron Collider at CERN, and in a number of other physical centres. There were discussed prospects of a new accelerator centre NICA at JINR and the research programme on it.

Релятивистская ядерная физика: от сотен МэВ до ТэВ: Труды 11-го Международного совещания (Стара Лесна, Словакия, 17–23 июня 2012 г.). — Дубна: ОИЯИ, 2013. — 161 с., фото.

ISBN 978-5-9530-0354-4

С 17 по 23 июня 2012 г. в Стара Лесне (Словацкая Республика) было проведено традиционное международное рабочее совещание «Релятивистская ядерная физика: от сотен МэВ до ТэВ».

Совещание было организовано Объединенным институтом ядерных исследований, Институтом физики Словацкой академии наук и Университетом им. П. Й. Шафарика (Кошице, Словацкая Республика). На совещании были представлены новые физические результаты, полученные на нуклотроне ОИЯИ, на большом адронном коллайдере в ЦЕРН и в ряде других физических центров. Были обсуждены перспективы создания нового ускорительного центра НИКА в ОИЯИ и программа исследований на нем.

УДК 539.17 (042)
ББК 22.383.5я431

ISBN 978-5-9530-0354-4

RNP

Stará Lesná - 2012

Hotel ACADEMIA
Stará Lesná
June 17 - 23, 2012
Slovak Republic

INTERNATIONAL WORKSHOP

"RELATIVISTIC NUCLEAR PHYSICS: FROM HUNDREDS MeV to TeV"

Organizers: *Joint Institute for Nuclear Research, Dubna, Russia*
Institute of Physics, Slovak Academy of Sciences, Bratislava, Slovakia
P.J.Šafárik University, Košice, Slovakia

The workshop continues the series of topical meetings started already in 1996. It will cover all aspects of the relativistic nuclear physics.

Main topics:

- **Recent Relativistic Nuclear Physics Experiments and Current Theoretical Developments**
- **Progress in Understanding of Exotic Phenomena (phase transitions, mixed-phase, etc.)**
- **The JINR Research Programme at the NUCLOTRON Beams, NICA/MPD**
- **Applied Research and Experimentation Using Relativistic Ion Beams**
- **LHC Physics**
- **Physics Programme at FAIR Facility**

For more information, please contact:

Yu. S. Anisimov: E-mail: anisimov@lhe.jinr.ru
Tel.: +7 (09621) 65113,
Fax: +7 (09621) 65180

Stefan Gmuca: E-mail: gmuca@savba.sk
Tel.: +421 (2) 5941 0532,
Fax.: +421 (2) 5477 6085

International Advisory Committee:

Ts. Baatar, IP MAS, Ulan-Bator
V.V. Burov, JINR, Dubna
S. Dubnicka (co-chairman), IP SAS, Bratislava
M. Gazdzicki, Frankfurt, Germany
T. Hallman, BNL, Upton
V.D. Kekelidze, JINR, Dubna
E. Kistenev, BNL, Upton
J. Kliman, IP SAS, Bratislava
A. D. Kovalenko, JINR, Dubna
A. Kugler, NPI, Prague – Rez
A. I. Malakhov (co-chairman), JINR, Dubna
G. Martinska, Safarik University, Kosice
Y. Miake, KEK, Tsukuba
Ch. Perdrisat, College. of Wiliam & Mary, Newport News
P. Senger, GSI, Darmstadt
A. N. Sissakian, JINR, Dubna
I. Stamenov, INRNE BAN, Sofia
Yu. V. Zanevski, JINR, Dubna
M. Zamany, Aristotle University, Thessaloniki

Local Organizing Committee:

Yu. S. Anisimov (co-chairman), JINR, Dubna
S. Gmuca (co-chairman), IP SAS, Bratislava
N.M. Dokalenko, JINR, Dubna
S. Hlavac, IP SAS, Bratislava
V.P. Ladygin, JINR, Dubna
V. Matousek, IP SAS, Bratislava
I. I. Migulina, JINR, Dubna
K. Petrik, IP SAS, Bratislava
E. B. Plekhanov,JINR, Dubna
A. S. Sorin, JINR, Dubna
S. Vokal, Safarik University, Kosice
M. Veselsky, IP SAS, Bratislava
P.I. Zarubin, JINR, Dubna

Contents

A. Malakhov
The Main Physical Result at the Dubna Synchrophasotron 6

C. Adamuščín, E. Bartoš, S. Dubnička, A. Z. Dubničková
Proton Charge rms Radius from All Reliable Nucleon EM FF's Data Respecting SU(3) Symmetry 16

M. Veselsky, Y. G. Ma
Symmetry Energy and Nucleon - Nucleon Cross Sections 29

A. Yu. Isupov, V. P. Ladygin, S. G. Reznikov
Proposal of the DAQ System for the BM@N Project 43

S. Vokál, J. Vrláková
Relativistic Particles Produced in ^{197}Au Induced Nuclear Collisions at 11.6 A GeV/c 62

S. V. Afanasiev *et al.*
Search for η-Mesic Nuclei at the Nuclotron 82

M. Janek *et al.*
Short Range Correlations in Experiments with Deuterons at Intermediate Energies 89

S. M. Piyadin *et al.*
New Data of the $dp \to ppn$ Reaction at 500 MeV Energy of Deuteron at ITS at Nuclotron 101

A. A. Terekhin *et al.*
Experiments to Study the Dense Baryonic Matter at Nuclotron 106

P. Filip
Ground-State Properties of Nuclei and Initial State in Relativistic Heavy Ion Collisions 111

J. Łukasik *et al.*
Kratta, a Triple Telescope Array for the ASY-EOS Experiment 119

G. L. Melkumov
Onset of Deconfinement and Search for Critical Point by NA49 and NA61 at CERN SPS 131

A. S. Sorin *et al.*
NICA Complex at JINR 147

A. Butenko *et al.*
VB LHEP Acceleration Complex Development 154

THE MAIN PHYSICAL RESULTS AT THE DUBNA SYNCHROPHASOTRON

A.I.Malakhov
Join Institute for Nuclear Research, Dubna, Russia
malakhov@lhe.jinr.ru

Abstract

The report summarizes the main results obtained at the Synchrophasotron in connection with its 55th anniversary. A considerable part of the results has not been included in the report due to their large number. The reader can get acquainted with them on the cited literature.

1. Introduction.

The Laboratory of High Energy was founded by its first director V.I.Veksler in 1953. At first it was named as the Electrophysical Laboratory of the Academy of Sciences of the USSR (EFLAN), but in 1956 it got the name of the Laboratory of High Energy (LHE) and since 2008 its name has been the Laboratory of High Energy Physics (LHEP).

For many years Synchrophasotron, the main basic facility of the LHE, was the largest accelerator in the world for 10 GeV proton energy [1].

One of the most important achievements of the previous century was a discovery of the phase stability principle for the charged particles in 1944 by V.I.Veksler [2-4], and later – by E.M.Mak-Millan [5]. The discovery of this principle allowed physicists in the USSR to develop and build the electron and proton accelerators with the energy of several hundred MeV.

In 1948 scientists of FIAN began to develop theories for the Synchrophasotron designing. Such a theory was presented in 1951 by M.S.Rabinovich, A.M.Baldin, A.A.Kolomensky, V.V.Mikhailov, V.A.Petukhov and L.L.Sobsovich [6-8].

During a short period of time a big amount of work was fulfilled in many organizations and in April 17, 1957 the Synchrophasotron was commissioned at LHE, it was constructed under the leadership of academicians V.I.Veksler and A.L.Mints [9, 10].

In 1959 for the realization of the Synchrophasotron project the Lenin Prize was awarded to its builders: V.I.Veksler, F.A.Vodopianov, D.V.Efremov, L.P.Zinoviev, A.A.Kolomensky, E.G.Komar, A.L.Mints, N.A.Monoszon, V.A.Petukhov, M.S.Rabinovich, S.M.Rubchinsky, A.M.Stolov.

The Synchrophasotron was used for intensive physical researches under the leadership of the first LHE director V.I.Veksler, and then-by its second LHE director I.V.Chuvilo. From 1968 till 1997 academician A.M.Baldin was the third LHE director who supported further development of the accelerator complex and carrying out physical experiments on it. During 1997- 2002 the Synchrophasotron was successfully used for physical and applied researches under the leadership of the fourth LHE director A.I.Malakhov.

When the Synchrophasotron reached the record on the energy of particles, it was necessary to find a new place in the physical research. The decision to develop the accelerator complex for accelerating relativistic nuclei with the energy up to 5 GeV per nucleon was made, first of all, for the new scientific direction - the relativistic nuclear physics. [11].

Obtaining of the polarised deuterons with the energy of 4.5 GeV per nucleon was the next step to develop the LHE accelerator complex. The polarised deuteron beams (and secondary neutron beams) opened new opportunities to study spin effects in interactions of particles and nuclei.

However, the performed physical studies required to improve the beam parameters and obtain heavier accelerated ions. These qualities could not be provided by the old Synchrophasotron any longer.

In this connection by the initiative of A.M.Baldin the proposal to construct a modern accelerator of relativistic nuclei Nuclotron on the basis of the superconducting magnetic systems has been made. Now practically all researches on the LHE accelerator complex have passed to the new accelerator Nuclotron.

In 1992 the LHE was named after academicians V.I.Veksler and A.M.Baldin (VBLHE) for the big scientific merits and contribution to the development of the Laboratory and JINR.

In a short review it is impossible to cover all the results obtained at the Synchrophasotron for 55 years, therefore here we have presented only the brightest ones, to our opinion, received for this period of time.

2. The main results on the Synchrophasotron

2.1. Discovery of antisigma-minus-hyperon

One of the first brightest results received in the first years of the Synchrophasotron operation was the discovery of a new antiparticle - antisigma-minus-hyperon (the diploma №59, 1968, a priority from November, 1963). This work was fulfilled by an international group of scientists [12]. Among them were V.I.Veksler, M.I.Solovev, N.M.Viryasov, E.N.Kladnitskaya, A.A.Kuznetsov, A.V.Nikitin, I.Vrana , A.Mikhul, Kim Khi In, Nguen Dyn Ti, Van Ganchan, Van Tsutszen, Din Datsao.

The experiment was carried out on the beam of negative π-mesons with the momentum of 8.3 GeV/c on the propane bubble chamber. Fig. 1 shows the authors of the discovery, a photo of the event of the antisigma-minus-hyperon decay and its scheme registered in the propane bubble chamber in one of 40 000 photos.

Fig.1. The authors of the discovery of the antisigma-minus-hyperon, photo of its decay, and the scheme of the decay of antisigma-minus-hyperon (right), registered in the bubble chamber.

The most probable reaction in a primary star is the following process:

$$\pi^- + C \rightarrow anti\text{-}\Sigma^- + K^0 + anti\text{-}K^0 + K^- + p + \pi^+ + \pi^- + a\ return\ nucleus.$$

The value of the life time for antisigma-minus-hyperon was obtained equal to $(1.18\pm0.07)\cdot10^{-10}$ seconds.

2.2. Discovery of the $\varphi \rightarrow e^+ e^-$ decay

The discovery of the φ meson decay on the electron-positron pair by means of the Cherenkov mass spectrometer became the next important result at the Synchrophasotron [13]. Authors of this discovery (the diploma №94, 1971, a priority from February, 1967) are A.M.Baldin, I.V.Chuvilo, M.N.Khachaturyan, J.Gladky, A.T.Matyushin, V.S.Pantuev, M.A.Azimov, M.S.Khvastunov, R.G.Astvatsaturov, L.I.Zhuravleva, V.I.Ivanov, V.T.Matyushin, L.N.Shtarkov, A.S.Belousov.

In 1964 a new detector - the Cherenkov mass spectrometer was proposed and developed at LHE. This detector allowed physicists to measure the effective mass for a wide class of decays e^+e^-, $\gamma\gamma$, $\pi^0\gamma$, $\pi^0\pi^0$, $\pi^0e^+e^-$ ... and identify the nature of secondary particles (electrons, γ-quanta)

For the process of the type $X \rightarrow e^+e^-$, $\gamma\gamma$ the expression for the effective mass of a decay particle has the following view:

$$M^2 = 2E_1E_2(1\text{-}\cos\Theta), \qquad (1)$$

where E_1 and E_2 are the electron or γquanta energy, Θ is a scattering angle between them.

The measurements of these parameters were carried out in the Cherenkov mass spectrometer as well as measurements of the angles of the electrons by means of the spark chambers. The Cherenkov spectrometers of the full energy absorption were used to measure the energy of electrons.

Investigations of the process $\pi^- p \rightarrow e^+e^- n$ whose effective cross-section has an order of 10^{-33} cm^2, set high requirements to equipment parameters. One of the basic characteristics is the accuracy of the measurement of the effective mass. Developed at LHE the Cherenkov gamma spectrometers allowed one to measure the electron energy within ±5 % (in the energy range from 1 to 4 GeV) and the scattering angle with the accuracy of ± 1.7 mrad. It made possible to have the measurement accuracy of the φ-meson effective mass $\Delta M_\phi = \pm$ 36 MeV. The setup scheme is presented in Fig. 2.

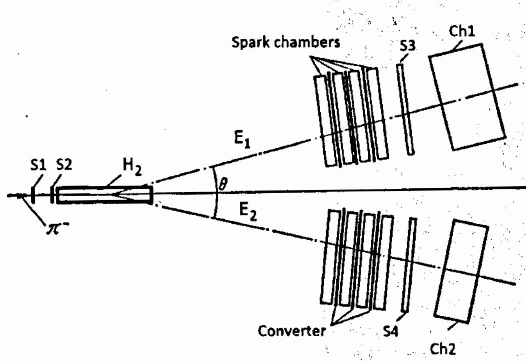

Fig.2. Scheme of the Cherenkov mass-spectrometer.
S1-S4 – the scintillation counters; Ch1; Ch2 –the Cherenkov gamma-spectrometers full absorption; H_2 – liquid hydrogen target.

Two series of measurements were performed and the data are shown in Tab. 1. The number of ρ and ϕ mesons was obtained by means of the kinematic formula (1) connecting the mass of the resonance, energy and the opening angle of the electron and positron.
The results of these analyses are presented in Fig. 3a (for the first series of measurements) and in Fig. 3b (for the second series of measurements). The curves Δ_1 and Δ_2 in these pictures designate borders of admissible values of function $E_1/E_2 = f(\Theta)$ for the $\rho^0 \to e^+e^-$ decays and are calculated with errors of the measured values (the angles and energies) and ρ^0 meson width.
In the sum on the two series of measurements there are thirty seven events grouped within kinematic corridors Δ_1 and Δ_2 which satisfy the kinematics of the $\rho^0 \to e^+e^-$ decay and the five events - kinematics of $\phi \to e^+e^-$ decay. The events closer to the left Δ_1 are the background, they are formed as a result of conversion of γquanta (basically from $\eta^0 \to \gamma\gamma$).

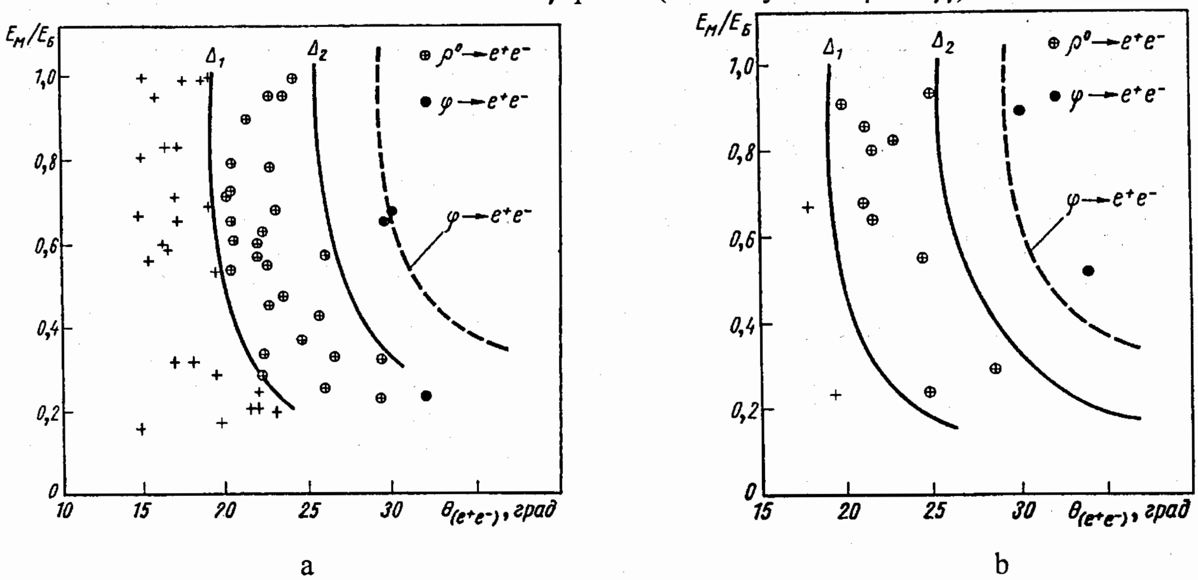

Fig.3. Analysis of the e^+e^- pairs on the kinematics of production and the decay of the vector particles *(V)* in the reaction of $\pi^- p \to V^0 \to e^+e^-$ decays of: (a) for the first series of measurements; b) for the second series of measurements. Curves Δ_1 and Δ_2 denote the domain of the allowed values of the function $E_M/E_Б = f(\Theta)$ for the decays of $\rho^0 \to e^+e^-$ taking into account error angles and energies and Γ_ρ. $E_M/E_Б \leq 1$ and Θ, accordingly, the ratio of the less energy decay particles to the larger one and the opening angle of the electrons in the laboratory system. The dotted curve was calculated by the formula (1) for $\phi \to e^+e^-$. The domain of the allowed values of the function $E_M/E_Б = f(\Theta)$ for ϕ mesons is not specified.

Since the number of the identified $\phi \to e^+e^-$ decays were five events, it was important to consider the imitation of these events by background processes. The obtained estimations have shown that the probability of the imitation of the five decays by the fluctuations of the average level of the background is less than 0.1 %.

In the experiment the values of the relative probabilities (B), the coupling constants ($f^2/4\pi$) and the partial widths (Γ) of $\rho^0 \to e^+e^-$ и $\phi \to e^+e^-$ decays have been defined. These results are presented in Tabs. 2 and 3.

Table 1.

Parameter	The first series	The second series
The length of the liquid hydrogen target, cm	50	25
The number of the registered π^- mesons, 10^9	3.36	3.53
Number of the identified $\rho^0 \to e^+e^-$ decays	27	10
Number of the identified $\phi \to e^+e^-$ decays	3	2
The efficiency of the registration of $\rho^0 \to e^+e^-$ decays, %	9.0	9.5
The efficiency of the registration of $\phi \to e^+e^-$ decays, %	2.6	4.1
Corner between axes of detectors, degrees	26	29
Interval of the transferred 4-momenta, $(Gev/c)^2$	from 0 up to 0.3	
Interval of the angles of the vector meson in the mass central system, degrees	from 0 up to 8	
Interval of the angles of the vector meson in the laboratory system, degrees	from 0 up to 30	
Vector meson energy in the mass central system, GeV	from 3.83 up to 4.0	
The effective mass resolution, MeV	$\Delta M_\rho = \pm 27$ $\Delta M_\phi = \pm 36$	

Table 2

Parameter	$\rho^0 \to e^+e^-$, 37 events		
	The first series	The second series	Average
$B(\rho^0 \to e^+e^-)\cdot 10^5$	5.9±1.5	4.5±1.3	5.1±1.0
$\Gamma(\rho^0 \to e^+e^-)$, keV	7.1±1.8	5.5±1.7	6.2±1.2
$f_\rho^2/4\pi$	2.16±0.56	3.16±0.96	2.4±0.48

Table 3

Parameter	$\phi \to e^+e^-$, 5 events
$B(\phi \to e^+e^-)\cdot 10^5$	66^{+44}_{-28}
$\Gamma(\phi \to e^+e^-)$, KeV	$2.5^{+1.7}_{-1.1}$
$f_\phi^2/4$	$7.2^{+4.8}_{-3.2}$

2.3. Observation of the effect of the total disintegration of nuclei

The effect of the total disintegration of nuclei of silver and bromine under the influence of the protons and light nuclei in the energy region from several GeV to several hundred GeV, was one of interesting effects found by the photo emulsion LHE group headed by K.D.Tolstov in 1970-80 [14].

The events, in which the nuclei of the target fragmented in the separate nucleons without formation of the residual nuclei of the considerable mass, were observed.

In Table 4 the data on the probabilities of the observation of events with the total disintegration of nuclei Ag, Br and Pb under the influence of the protons and some other nuclei, are presented. The data show the increasing probability of the observation of events of the full decay of nuclei with increase of masses of the interacting nuclei.

Table 4.

Projectile nucleus	Momentum, GeV per nucleon	Target	Probability of the full disintegration of nuclei, %
P	10-400	Ag, Br	$3 \pm 0,3$
P	70	Pb	$6 \pm 1,5$
^{4}He	4.5	Pb	10 ± 2
^{4}He	4.5	Ag, Br	7 ± 1
^{12}C	4.5	Ag, Br	18 ± 2
^{22}Ne	4.5	Ag, Br	20 ± 2
^{28}Si	4.5	Ag, Br	26 ± 4

The big surprise was the fact that the probability of the total disintegration of nuclei Ag and Br under the influence of the protons is constant (3 %) in the energy region from 10 to 400 GeV while the number of the $\pi^{\pm}$ mesons grows from 4 to 32.

Later the phenomenon of the total disintegration of nuclei was studied in detail in [15] on the data obtained with the LHE propane bubble chamber.

The study of this phenomenon is important both from the point of view of the construction of the theory of a nucleus, and from the point of view of the practical application. In particular, the phenomenon of the total disintegration of nuclei can be used in nuclear power and when transmutation of a radioactive waste as a source of a large number of nucleons.

2.4. The phenomenon of potential scattering of the high energy protons

The phenomenon of potential scattering of the high energy protons was registered as the discovery in 1981 (the diploma № 246). Authors of this discovery were L.F.Kirillova, V.A.Nikitin, A.A.Nomofilov, V.A.Sviridov, L.N.Strunov, M.G.Shafranova.

Before this work performed by the authors of this discovery, it had been supposed that scattering of the strongly interaction elementary particles at high energy (over 1 GeV) could be described in analogy to optics within the limits of the dispersion model in which potential scattering disappears with energy increasing.

Similar representations were based, on the one hand, on the well-known fact of intensive increase of meson production processes in this energy region, i.e. the contribution of inelastic processes, on the other hand, on the criterion of simplicity of the nature accepted among physicists at that time. It turned out that this model of the dispersion of particles at high energy was very much simplified.

The experiment performed at the Synchrophasotron to study elastic scattering of the protons with the energy above 1 GeV showed the existence of the considerable potential scattering corresponding to the forces of repulsing between two protons. Differently, it was shown that the nuclear amplitude of the scattering was complex, and its real part was considerable and made approximately 30 % of the imaginary.

To carry out the experiments became possible because of applying a new experimental method. This method consisted in realisation of a special mode repeated ($\sim 10^4$ times) passages of the internal beam of the Synchrophasotron through a thin ($\sim 30\ \mu g/cm^2$) film containing a hydrogen target under condition of registration of slow particles by means of nuclear emulsions.

Thus, all the above provided the unusually high efficiency of the target, high statistical accuracy, and methodical reliability of the experiment [16-18].

For the first time a pronounced interference effect of the Coulomb and nuclear scattering were observed. So, a new physical phenomenon was discovered - the existence of the potential scattering of protons at high energy, which drastically changed the existing ideas about the nature of the particle interaction at high energies. The results of the experiments were used to check the feasibility of the causality principle in the micro world. It turned out that this principle is not violated up to the distances of $\sim 10^{-14}$ cm.

2.5. Nuclear cumulative effect

Beams of high energy particles for a long period of time were obtained by the proton and electron accelerators, i.e. the acceleration of particles with a single electric charge.

The acceleration of particles with a charge more than units in principle gives an opportunity to obtain the energy of accelerated particles (in case of identical parameters of the accelerator) larger than the energy of the protons, by a number of times equal to the multiplicity of the charge. So, for example, on the Dubna Synchrophasotron, accelarating of protons with the energy of 10 GeV, can be obtained by helium nuclei with the energy of 20 GeV, and the neon nuclei (charge 10 e) -with the energy of 100 GeV.

A natural question arises: is the mentioned above a result of a collision with the target nuclei, for example, neons with the energy of 100 GeV, bundles of secondary particles generated at the accelerator in Serpukhov, accelerating the protons up to 70 GeV energy? An affirmative response to this question would mean that by means of acceleration of heavy nuclei with a higher charge, beams of particles of high enough energy can be obtained. Usually the question about the possibility of transmission of high-energy compound nucleus of a single proton, was answered in the negative. Were the following statements correct: nucleus is enough "friable" and there is a low probability of the concentration group energy of nucleons in a single nucleon? In [19] A.M.Baldin was the first who considered this problem and made some predictions on the basis of analysis of experimental data and gave a positive answer to this question. More detailed checking of the drawn conclusion required to perform experimental tests.

The formation of secondary particles in the interaction of relativistic nuclei with the participation of the group of nucleons received the title of the nuclear cumulative effect.

The term "cumulative" comes from the Latin cumulatio - "cluster" or cumulo -" accumulate" and literally means increasing or enhancing of any effect due to addition or accumulation of several similar effects.

In 1970 the Synchrophasotron of the Laboratory of High Energy of the Joint Institute for Nuclear Research in Dubna accelerated the simplest nuclei - deuterons, consisting of 2-x nucleons, up to 9 GeV. Usually for measuring the energy of nuclei it is necessary to use the energy value assigned to one nucleon. In these energy units the deuteron beam at 9 GeV corresponds to the amount of 4.5 GeV per nucleon, or, as it is often written, 4.5 AGeV (A is the atomic number of the nucleus).

The presence of the deuteron beam in Dubna allowed one to carry out the first experiments with relativistic nuclei.

The nuclear cumulative effect was first observed by the following group of authors: A.M.Baldin, S.B.Gerasimov, N.Giordenesku, V.N.Zubarev, L.K.Ivanova, A.D.Kirillov, V.A.Kuznetsov, N.S.Moroz, V.B.Radomanov, V.N.Ramzhin, V.S.Stavinsky, M.I.Yatsuta [20].
In this experiment the primary beam of accelerated deuterons interected with the copper targets $T_{1\div5}$ (Fig.4). Produced in the direction of the incident deuteron the pions were analysed by the momentum of the accelerator magnetic field and captured in the magnetic channels K_1 and K_2. The magnets H_1, H_2 , H_3, together with the magnetic field of the accelerator determined the energy of the secondary particles. Since the geometry of the magnetic channels is fixed, different energies of secondary particles can be obtained, either by changing the target in the chamber of the accelerator ($T_{1\div5}$), or changing the magnetic field of the accelerator, i.e. changing the energy of the accelerated deuterons.

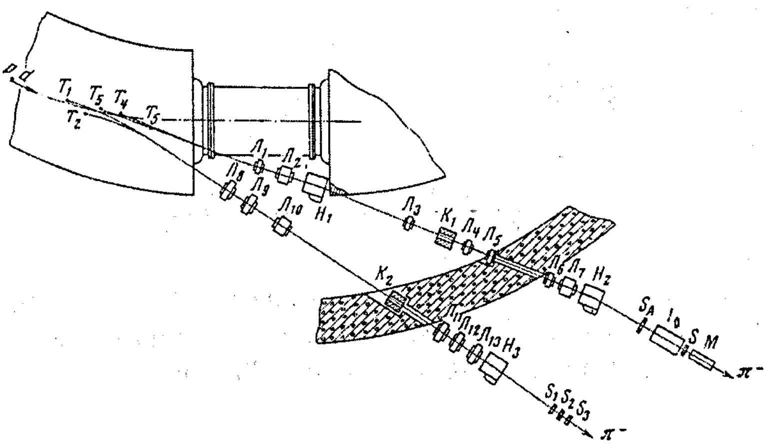

Fig.4. Scheme of the experiment on the observation of the nuclear cumulative effect.

The experiment measured the ratio of the double differential cross-sections for the production of the pion by deuterons and protons on the copper target:

$$\alpha(x_d)= d^2\sigma(d+Cu \rightarrow \pi^- + ...)/d^2\sigma(p+Cu \rightarrow \pi^- + ...),$$

where $x_d = p_\pi/p_\pi^{max}$ (p_π is π-meson momentum, p_π^{max} is the maximum value of the π-meson momentum).
Figure 5 shows the results of measurements. It is seen that the value of relative output pion $\alpha(x_d)$ within the limits of errors of measurements does not depend on argument x_d. The average value of $<\alpha>$ is equal to the following:

$$<\alpha> = 0.06\pm0.007.$$

To evaluate the contribution of the Fermi motion of nucleons in the cross-section of the pion production, the relevant theoretical calculations of $\alpha(x)$were completed.

For numerical calculations, two variants of wave functions of the deuteron were used: with a repulsive core and the wave function without a core. Figure 5 shows the results of calculations. The solid curve corresponds to the wave function without the core, and the dotted one - with the core. The figure shows that the calculated α in the absolute value is by about two orders of magnitude smaller than the experimental values, and, in addition, the estimated curve depending on $\alpha(x_d)$ decreases significantly with the growth of x_d, while the experimental value practically does not depend on the argument x_d.

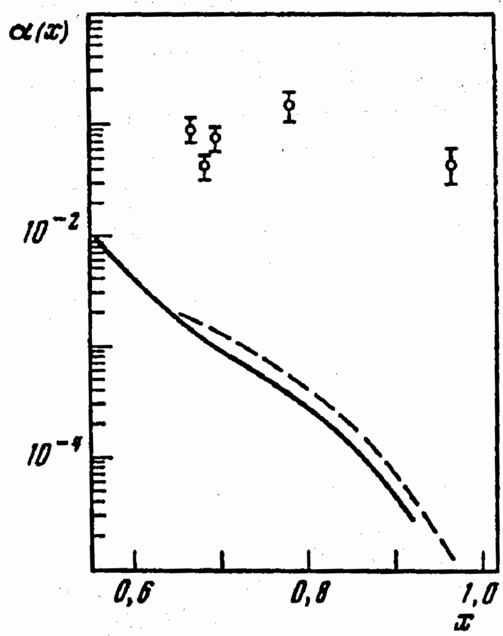

Fig.5. Comparison of the experimental values of α with the calculation. Points - experimental data. The dashed line - the wave function of the deuteron with the core (deuteron momentum 10 GeV/c), the solid line - without the core.

The analysis of the above experimental data on the pion production by the relativistic deuterons enabled the authors of the work to make the following conclusions:

- the nuclear cumulative effect was discovered and the cross section of the cumulative pion production was measured in deuteron-nucleus interactions at high energies;
- the ratio of the outputs of the reactions $d + Cu \rightarrow \pi^- + ...$ and $p + Cu \rightarrow \pi^- + ...$, at such energies of mesons cannot be explained by the Fermi motion of nucleons in the deuteron.

After the first experimental observation of the nuclear cumulative effect its systematic study began in many physical centers of the world.

3. Conclusion

At the Synchrophasotron many interesting experiments were completed:

- investigations on the record energy (4.5 GeV per nucleon) of the polarized deuteron beam [21, 23];
- study of the nuclear multifragmentation and observation of the phase transition of the type of gas-liquid on the PHASA setup [24, 25];
- the study of the nuclear cumulative effect at the DISK [26] and SPHERE [27-29] setups;
- the observation of the deviation of the charged beam by a bent crystal [30];
- investigation of the hypernuclei [31];
- the study of the cluster structure of light nuclei in the framework of the project BECQUEREL [32];

- applied research [33].

However, in the framework of one report it is not possible to cover the whole spectrum of investigations and therefore, we refer the reader to the corresponding publications [21-36].

Thus, the Synchrophasotron performed a large number of physical experiments which are of great scientific importance.

References

1. И.Н.Семенюшкин. ЭЧАЯ, том 27, вып.3, 1996, 571-592.
2. В.И. Векслер. ДАН, т.43, 1944, 346.
3. В.И. Векслер. ДАН, т.44, 1944, 393.
4. V.I.Veksler. Journ. of Phys. USSR, vol.9, 1945, 153.
5. E.M. McMillan. Phys. Rev. Lett., vol.68, 1945,1434.
6. М.С. Рабинович. Труды ФИАН, т.Х, 1958, 23.
7. А.А. Коломенский, Л.Л. Сабсович. ЖТФ, т.26, 1956, 578.
8. В.И. Векслер и др. АЭ, т.4, 1956, 22.
9. V.I. Veksler. In: Proc. Intern. Conf. On Peaceful Uses of Atomic Energy, Geneva, 2, vol.30, 1958, 3.
10. А.М. Балдин. В кн.: Очерки по истории развития физики в СССР. Киев, Наукова думка, 1982, 152.
11. А.М. Балдин и др. ОИЯИ, Р9-5442, Дубна, 1970.
12. Ван Ган-чан и др. ЖЭТФ, т.38, 1960, 1356.
13. М.Н. Хачатурян. ЭЧАЯ, том 2, вып.3, 1972, 584-634.
14. K.D. Tolstov. Nucl. Tracks Radiat. Meas., Vol.19, No. 1-4, 1991, 657-664.
15. А.И Бондаренко и др. ЯФ, , том.62, №9, 1999, 1612-1624.
16. Л.Ф. Кириллова и др. ЖЭТФ, т.45, 1963, 1261.
17. Н. Далхажав и др. ЯФ, т.8, вып. 2, 1968, 342.
18. В.Д. Бартенев и др. ЯФ, т.15, вып. 6, 1972, 1174.
19. А.М. Балдин. Краткие сообщения по физике. ФИАН, №1, 1971, 35
20. А.М. Балдин и др. ЯФ, т.18., вып.1, 1973, 79.
21. Л.С. Ажгирей и др. ЯФ, т.74, №10, 2011, 1420-1437.
22. F. Lehar. Phys.Part.Nucl. 36 , 2005, 501-528.
23. L.N. Strunov et al. Czechoslovak Journal of Physics, No.56, 2006, 343-357.
24. V.A. Karnaukhov et al. Journal of Physics G, v.39, No.12, 2012, 1-8.
25. V.A. Karnaukhov et al. Physics of Atomic Nuclei, v.69, 2006, 1142-1148.
26. G.S. Averichev et al. JINR - 1(69)-95, Dubna, 2005, 37-46.
27. Yu.S.Anisimov et al. JINR Rapid Comm., 5(73)-95, 1996, pp.31-40.
28. S.V.Afanasev et al. JINR Rapid Comm., 5(51)-91, 1992, pp. 5-1.
29. S.V.Afanasev et al. JINR Rapid Comm., 7(46)-90 , 1990, pp. 6-18.
30. А.С. Водопьянов и др. Письма в ЖЭТФ, т.30. вып.7, 1979, 474-478.
31. А. В. Аверьянов. ЯФ, т.71, №12, 2008, 2137-2145.
32. N.P. Andreeva et al. Eur.Phys.J. A27S1, 2006, 295-300.
33. M.I. Krivopustov et al. JINR Preprint, E1-2007-7, Dubna , 2007.
34. A.M. Baldin, A.I. Malakhov and A.N. Sissakian. Physics of Particles and Nuclei, v.32, Suppl.1, 2001, S4-S30.
35. A.I.Malakhov et al. Physics of Particles and Nuclei, vol. 38, No. 4, 2007, 407-446.
36. A.I.Malakhov. Fizika B, v.17, 2, 2008, 279-292 .

PROTON CHARGE *rms* RADIUS FROM ALL RELIABLE NUCLEON EM FF's DATA RESPECTING $SU(3)$ SYMMETRY

C.Adamuščín[a], E.Bartoš[a], S.Dubnička[a] and A.Z.Dubničková[b1]

a) Institute of Physics, Slovak Academy of Sciences, Bratislava, Slovak Republic

b) Dept. of Theor. Physics, Comenius University, Bratislava, Slovak Republic

Abstract

The non-dipole behavior of $G_{Ep}(Q^2)$ in the space-like region with the zero around $Q^2 = 13GeV^2$ and the charge proton *rms* radius to be compatible with the value obtained in a spectroscopy of the muon hydrogen atom is confirmed in a global analysis of all reliable nucleon electromagnetic form factors data by means of a sophisticated nine resonance analytic model of nucleon electromagnetic structure, which respects the $SU(3)$ symmetry.

1. Introduction

The nucleon electromagnetic (EM) structure is completely described by electric $(G_{Ep}(t), G_{En}(t))$ and magnetic $(G_{Mp}(t), G_{Mn}(t))$ form factors (FFs) where $t = -Q^2$ is squared momentum transferred by the virtual photon γ^*.

The corresponding charge distribution within the proton and the neutron is defined as the Fourier transformation of the proton and neutron electric FFs, respectively

$$\rho_{ch_p}(\mathbf{r}) = \frac{1}{(2\pi)^3} \int G_{Ep}(Q^2) e^{i\mathbf{Qr}} d^3r. \tag{1}$$

$$\rho_{ch_n}(\mathbf{r}) = \frac{1}{(2\pi)^3} \int G_{En}(Q^2) e^{i\mathbf{Qr}} d^3r. \tag{2}$$

The size of the proton EM structure in a specific (Breit) reference frame is described by the proton charge root-mean-square (*rms*) radius $r_p = \sqrt{< r_{Ep}^2 >}$ where the mean-square-radius is defined as

$$< r_{Ep}^2 >= \int_0^\infty r^2 \rho_{ch_p}(r) 4\pi r^2 dr \tag{3}$$

[1] E–mail: dubnickova@fmph.uniba.sk

or equivalently

$$< r_{Ep}^2 >= 6\frac{dG_{Ep}(t)}{dt}|_{t\to 0} \tag{4}$$

We would like to note that one can not define neutron charge *rms* radius as its mean-squared-radius is appeared to be negative.

From Eqs. (1), (3), (4) it follows that the proton charge *rms* radius can be determined if one knows proton electric FF $G_{Ep}(t)$ with sufficient precision.

There are two substantially different approaches in a determination of the proton charge mean-square-radius $< r_{Ep}^2 >$.

- For its determination [1], [2] the data on $G_{Ep}(t)$ to be obtained in unpolarized elastic electron-proton scattering for very low values of t just below the normalization point are used.

  A sophisticated data analysis, based on a continued-fraction expansion of $G_{Ep}(t)$, was carried out, however, very large value

  $$r_p = 0.895(18) fm \tag{5}$$

  of the proton charge *rms* radius has been found, which is even larger than the newest Review of Particle Physics value [3]

  $$r_p = \sqrt{< r_{Ep}^2 >} = 0.8768(69) fm \tag{6}$$

  based mainly on precision spectroscopy of electron hydrogen atom and a calculation of bound state in QED.

- We, however, defend different approach in a determination of the proton charge mean-square-radius.

  The reason is that the proton electric FF $G_{Ep}(t)$ is correlated at least with the proton magnetic FF $G_{Mp}(t)$ in the measured electron-proton scattering cross-section and if we consider the proton and neutron to be two isotopic states of the nucleon then $G_{Ep}(t)$ is correlated even with the neutron electric $G_{En}(t)$ and the neutron magnetic $G_{Mn}(t)$ FFs.

  In other words the behavior of the proton electric FF $G_{Ep}(t)$ and as a result also the value of the proton charge mean-square-radius depends on behaviors of all other nucleon EM FFs.

  Therefore the most reliable value of the proton charge *rms* radius can be determined only from the behavior of the proton electric FF $G_{Ep}(t)$ [4],[5], [6],[7] to be obtained from the simultaneous analysis of all existing data on nucleon EM FFs.

From the proton EM structure discovery in the middle of 50's of the last century until 2 000 plenty of data on proton (equally well on neutron, however, in a more complicated way) EM FFs in space-like region by the so-called Rosenbluth technique were experimentally determined. They manifest a smooth falling, i.e. the dipole behavior.

However, starting from 2000 in JLab the polarization components [8] P_t

$$P_t = \frac{h}{I_0}(-2)\sqrt{\tau(1+\tau)}G_{Ep}G_{Mp}tan\theta/2 \tag{7}$$

and P_l

$$P_l = \frac{h(E_e + E_{e'})}{I_0 m_p}\sqrt{\tau(1+\tau)}G^2_{Mp}tan^2\theta/2 \tag{8}$$

of the recoil proton have been measured [9], [10], [11] simultaneously in the polarization transfer process $\vec{e}p \rightarrow e\vec{p}$, from which one can determine the ratio

$$\frac{G_{Ep}}{G_{Mp}} = -\frac{P_t}{P_l}\frac{(E_e + E_{e'})}{2m_p}tan\theta/2 \tag{9}$$

indicating for the proton electric FF $G_{Ep}(t)$ to have no more dipole behavior (see Fig.1)

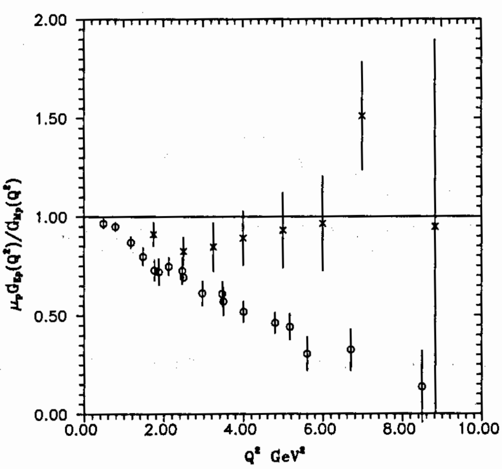

FIG. 1: New JLab polarization data on the ratio $\mu_p G_{Ep}(t)/G_{Mp}(t)$. The crosses are calculated ratio points from data on $G_{Ep}(t)$ and $G_{Mp}(t)$ obtained by Rosenbluth technique

A distinction in two our subsequent analyses carried out in [4],[6] is that in the second one from (2005) in order to find the realistic behavior of $G_{Ep}(t)$ in the whole space-like region, we have looked for optimal description of all existing nucleon FF data by the 10 resonance *Unitary&Analytic* (*U&A*) model (5 iso-scalar and 5 iso-vector vector-mesons) of the nucleon EM structure excluding completely the Rosenbluth space-like $G_{Ep}(t)$ data and replacing them by JLab proton polarization data on the ratio $\mu_p G_{Ep}(t)/G_{Mp}(t)$.

As a result we have found the non-dipole behavior of $G_{Ep}(t)$ with a zero around $t = -13 \quad GeV^2$ and the proton charge rms radius

$$r_p = 0.84895(688) fm, \tag{10}$$

to be different from the value

$$r_p = \sqrt{< r_{Ep}^2 >} = 0.8768(69) fm \tag{11}$$

given by the Review of Particle Physics [3].

Five years there was a disappointment with this disagreement, but only until the muon hydrogen atom result has been obtained in 2010.

The latter method is based on a precision measurement of the Lamb shift i.e. the energy difference measurement between $2S_{1/2}^{F=1}$ and $2P_{3/2}^{F=2}$ states in muon hydrogen atom and its comparison with a theoretical formula for energy difference dependent explicitly on the proton charge rms radius r_p, to be calculated in the framework of QED.

The muon hydrogen spectroscopy gives 10-times more precise proton charge rms radius

$$r_p = 0.84184(67) fm, \tag{12}$$

which disproves the value of Review of Particle Physics (2010)

$$r_p = 0.87680(690) fm,$$

obtained by an electron hydrogen atom spectroscopy, and coincides with our proton charge rms radius value

$$r_p = 0.84895(688) fm. \tag{13}$$

obtained 5 years earlier.

A similar results have been found also in analyses of Hammer et al [5]

$$r_p = 0.848 fm. \tag{14}$$

and Belushkin et al [7]

$$r_p = 0.844(12) fm. \tag{15}$$

In this contribution a reanalysis of all existing nucleon EM FFs by the 9 resonance $U\&A$ model, however, respecting $SU(3)$ symmetry is carried out with the aim if it will be confirmed the previous result of 10 resonance $U\&A$ nucleon EM structure model, i.e. the zero of G_{Ep} and proton charge rms radius value.

I. NUCLEON EM FFS $U\&A$ MODEL RESPECTING $SU(3)$ SYMMETRY

Though Sachs electric and magnetic FFs, $G_E(t)$ and $G_M(t)$, are very suitable for extraction of experimental data from the measured differential cross-sections, for a construction of various nucleon EM structure models the iso-scalar and iso-vector parts of the Dirac and Pauli FFs, to be defined as

$< N|J_\mu^{EM}|N >= e\bar{u}(p')\{\gamma_\mu F_1^N(t) + \frac{i}{2m_N}\sigma_{\mu\nu}(p'-p)_\nu F_2^N(t)\}u(p)$

are more suitable.

Then the flavor independent parts of the latter $F_1^s, F_1^v, F_2^s, F_2^v$ are related with Sachs FFs by the Eqs.

$$\begin{aligned} G_E^p(t) &= [F_1^s(t) + F_1^v(t)] + \frac{t}{4m_p^2}[F_2^s(t) + F_2^v(t)] \\ G_M^p(t) &= [F_1^s(t) + F_1^v(t)] + [F_2^s(t) + F_2^v(t)] \\ G_E^n(t) &= [F_1^s(t) - F_1^v(t)] + \frac{t}{4m_n^2}[F_2^s(t) - F_2^v(t)] \\ G_M^n(t) &= [F_1^s(t) - F_1^v(t)] + [F_2^s(t) - F_2^v(t)] \end{aligned}$$

By means of the iso-scalar and iso-vector parts of the Dirac and Pauli FFs are included all required properties of the nucleon $U\&A$ model like experimental fact of a creation of unstable vector-meson resonances in e^+e^- annihilation processes into hadrons and the analytic properties, the reality conditions, unitarity conditions, normalizations and asymptotic behaviors of FFs.

Consideration of the $SU(3)$ symmetry in EM structure model means that always complete trinity of vector-mesons $(\rho, \omega, \phi; \rho', \omega', \phi'$; etc.) with photonic quantum numbers has to be taken into account.

The newest Review of Particle Physics [3] provides just 3 complete trinities of such vector-meson resonances

$\rho(770), \omega(782), \phi(1020);\ \omega'(1420), \rho'(1450)), \phi'(1680);\ \omega''(1650), \rho''(1700), \phi''(2170)$.

Then one can write the 9-resonance zero-width VMD parametrization of iso-scalar and iso-vector parts of the Dirac and Pauli FFs

$$F^s_{1N}(t) = \frac{1}{2}\frac{m^2_\omega m^2_\phi}{(m^2_\omega - t)(m^2_\phi - t)} +$$

$$+\left\{\frac{m^2_\phi m^2_{\omega'}}{(m^2_\phi - t)(m^2_{\omega'} - t)}\frac{(m^2_\phi - m^2_{\omega'})}{(m^2_\phi - m^2_\omega)} + \frac{m^2_\omega m^2_{\omega'}}{(m^2_\omega - t)(m^2_{\omega'} - t)}\frac{(m^2_\omega - m^2_{\omega'})}{(m^2_\omega - m^2_\phi)} - \right.$$

$$\left. - \frac{m^2_\omega m^2_\phi}{(m^2_\omega - t)(m^2_\phi - t)}\right\}(f^{(1)}_{\omega' NN}/f_{\omega'}) +$$

$$+\left\{\frac{m^2_\phi m^2_{\phi'}}{(m^2_\phi - t)(m^2_{\phi'} - t)}\frac{(m^2_\phi - m^2_{\phi'})}{(m^2_\phi - m^2_\omega)} + \frac{m^2_\omega m^2_{\phi'}}{(m^2_\omega - t)(m^2_{\phi'} - t)}\frac{(m^2_\omega - m^2_{\phi'})}{(m^2_\omega - m^2_\phi)} - \right.$$

$$\left. - \frac{m^2_\omega m^2_\phi}{(m^2_\omega - t)(m^2_\phi - t)}\right\}(f^{(1)}_{\phi' NN}/f_{\phi'}) +$$

$$+\left\{\frac{m^2_\phi m^2_{\omega''}}{(m^2_\phi - t)(m^2_{\omega''} - t)}\frac{(m^2_\phi - m^2_{\omega''})}{(m^2_\phi - m^2_\omega)} + \frac{m^2_\omega m^2_{\omega''}}{(m^2_\omega - t)(m^2_{\omega''} - t)}\frac{(m^2_\omega - m^2_{\omega''})}{(m^2_\omega - m^2_\phi)} - \right.$$

$$\left. - \frac{m^2_\omega m^2_\phi}{(m^2_\omega - t)(m^2_\phi - t)}\right\}(f^{(1)}_{\omega'' NN}/f_{\omega''}) +$$

$$+\left\{\frac{m^2_\phi m^2_{\phi''}}{(m^2_\phi - t)(m^2_{\phi''} - t)}\frac{(m^2_\phi - m^2_{\phi''})}{(m^2_\phi - m^2_\omega)} + \frac{m^2_\omega m^2_{\phi''}}{(m^2_\omega - t)(m^2_{\phi''} - t)}\frac{(m^2_\omega - m^2_{\phi''})}{(m^2_\omega - m^2_\phi)} - \right.$$

$$\left. - \frac{m^2_\omega m^2_\phi}{(m^2_\omega - t)(m^2_\phi - t)}\right\}(f^{(1)}_{\phi'' NN}/f_{\phi''}).$$

$$F^v_{1N}(t) = \frac{1}{2}\frac{m^2_\rho m^2_{\rho'}}{(m^2_\rho - t)(m^2_{\rho'} - t)} +$$

$$+\left\{\frac{m^2_{\rho'} m^2_{\rho''}}{(m^2_{\rho'} - t)(m^2_{\rho''} - t)}\frac{(m^2_{\rho'} - m^2_{\rho''})}{(m^2_{\rho'} - m^2_\rho)} + \frac{m^2_\rho m^2_{\rho''}}{(m^2_\rho - t)(m^2_{\rho''} - t)}\frac{(m^2_\rho - m^2_{\rho''})}{(m^2_\rho - m^2_{\rho'})} - \right.$$

$$\left. - \frac{m^2_\rho m^2_{\rho'}}{(m^2_\rho - t)(m^2_{\rho'} - t)}\right\}(f^{(1)}_{\rho'' NN}/f_{\rho''}).$$

$$F^s_{2N}(t) = \frac{1}{2}(\mu_p + \mu_n)\frac{m^2_\omega m^2_\phi m^2_{\omega'}}{(m^2_\omega - t)(m^2_\phi - t)(m^2_{\omega'} - t)} +$$

$$+\left\{\frac{m^2_\phi m^2_{\omega'} m^2_{\phi'}}{(m^2_\phi - t)(m^2_{\omega'} - t)(m^2_{\phi'} - t)}\frac{(m^2_\phi - m^2_{\phi'})(m^2_{\omega'} - m^2_{\phi'})}{(m^2_\phi - m^2_\omega)(m^2_{\omega'} - m^2_\omega)} + \right.$$

$$+\frac{m^2_\omega m^2_{\omega'} m^2_{\phi'}}{(m^2_\omega - t)(m^2_{\omega'} - t)(m^2_{\phi'} - t)}\frac{(m^2_\omega - m^2_{\phi'})(m^2_{\omega'} - m^2_{\phi'})}{(m^2_\omega - m^2_\phi)(m^2_{\omega'} - m^2_\phi)} +$$

$$+\frac{m^2_\omega m^2_\phi m^2_{\phi'}}{(m^2_\omega - t)(m^2_\phi - t)(m^2_{\phi'} - t)}\frac{(m^2_\omega - m^2_{\phi'})(m^2_\phi - m^2_{\phi'})}{(m^2_\omega - m^2_{\omega'})(m^2_\phi - m^2_{\omega'})} -$$

$$\left. -\frac{m^2_\omega m^2_\phi m^2_{\omega'}}{(m^2_\omega - t)(m^2_\phi - t)(m^2_{\omega'} - t)}\right\}(f^{(2)}_{\phi' NN}/f_{\phi'}) +$$

$$+\left\{\frac{m^2_\phi m^2_{\omega'} m^2_{\omega''}}{(m^2_\phi - t)(m^2_{\omega'} - t)(m^2_{\omega''} - t)}\frac{(m^2_\phi - m^2_{\omega''})(m^2_{\omega'} - m^2_{\omega''})}{(m^2_\phi - m^2_\omega)(m^2_{\omega'} - m^2_\omega)} + \right.$$

$$+\frac{m^2_\omega m^2_{\omega'} m^2_{\omega''}}{(m^2_\omega - t)(m^2_{\omega'} - t)(m^2_{\omega''} - t)}\frac{(m^2_\omega - m^2_{\omega''})(m^2_{\omega'} - m^2_{\omega''})}{(m^2_\omega - m^2_\phi)(m^2_{\omega'} - m^2_\phi)} +$$

$$+\frac{m^2_\omega m^2_\phi m^2_{\omega''}}{(m^2_\omega - t)(m^2_\phi - t)(m^2_{\omega''} - t)}\frac{(m^2_\omega - m^2_{\omega''})(m^2_\phi - m^2_{\omega''})}{(m^2_\omega - m^2_{\omega'})(m^2_\phi - m^2_{\omega'})} -$$

$$\left. -\frac{m^2_\omega m^2_\phi m^2_{\omega'}}{(m^2_\omega - t)(m^2_\phi - t)(m^2_{\omega'} - t)}\right\}(f^{(2)}_{\omega'' NN}/f_{\omega''}) +$$

$$+\left\{\frac{m^2_\phi m^2_{\omega'} m^2_{\phi''}}{(m^2_\phi - t)(m^2_{\omega'} - t)(m^2_{\phi''} - t)}\frac{(m^2_\phi - m^2_{\phi''})(m^2_{\omega'} - m^2_{\phi''})}{(m^2_\phi - m^2_\omega)(m^2_{\omega'} - m^2_\omega)} + \right.$$

$$+\frac{m^2_\omega m^2_{\omega'} m^2_{\phi''}}{(m^2_\omega - t)(m^2_{\omega'} - t)(m^2_{\phi''} - t)}\frac{(m^2_\omega - m^2_{\phi''})(m^2_{\omega'} - m^2_{\phi''})}{(m^2_\omega - m^2_\phi)(m^2_{\omega'} - m^2_\phi)} +$$

$$+\frac{m^2_\omega m^2_\phi m^2_{\phi''}}{(m^2_\omega - t)(m^2_\phi - t)(m^2_{\phi''} - t)}\frac{(m^2_\omega - m^2_{\phi''})(m^2_\phi - m^2_{\phi''})}{(m^2_\omega - m^2_{\omega'})(m^2_\phi - m^2_{\omega'})} -$$

$$\left. -\frac{m^2_\omega m^2_\phi m^2_{\omega'}}{(m^2_\omega - t)(m^2_\phi - t)(m^2_{\omega'} - t)}\right\}(f^{(2)}_{\phi'' NN}/f_{\phi''})$$

$$F^v_{2N}(t) = \frac{1}{2}\frac{m^2_\rho m^2_{\rho'} m^2_{\rho''}}{(m^2_\rho - t)(m^2_{\rho'} - t)(m^2_{\rho''} - t)}$$

to be automatically normalized and governing the asymptotic behaviors as predicted by the quark model of hadrons.

An unitarization of the model is achieved by the non-linear transformations

$t = t^s_0 + \frac{4(t^{1s}_{in} - t^s_0)}{[1/V(t) - V(t)]^2}$; $t = t^v_0 + \frac{4(t^{1v}_{in} - t^v_0)}{[1/W(t) - W(t)]^2}$;

$t = t_0^s + \frac{4(t_{in}^{2s}-t_0^s)}{[1/U(t)-U(t)]^2}; \quad t = t_0^v + \frac{4(t_{in}^{2v}-t_0^v)}{[1/X(t)-X(t)]^2}.$

and a subsequent inclusion of the nonzero values of vector-meson widths.

In non-linear transformations $t_0^s = 9m_\pi^2$, $t_0^v = 4m_\pi^2$, $t_{in}^{1s}, t_{in}^{1v}, t_{in}^{2s}, t_{in}^{2v}$ are the square-root branch points, as it is transparent from the inverse transformations

$$V(t) = i\frac{\sqrt{(\frac{t_{in}^{1s}-t_0^s}{t_0^s})^{1/2} + (\frac{t-t_0^s}{t_0^s})^{1/2}} - \sqrt{(\frac{t_{in}^{1s}-t_0^s}{t_0^s})^{1/2} - (\frac{t-t_0^s}{t_0^s})^{1/2}}}{\sqrt{(\frac{t_{in}^{1s}-t_0^s}{t_0^s})^{1/2} + (\frac{t-t_0^s}{t_0^s})^{1/2}} + \sqrt{(\frac{t_{in}^{1s}-t_0^s}{t_0^s})^{1/2} - (\frac{t-t_0^s}{t_0^s})^{1/2}}} \tag{16}$$

and similarly for $W(t)$, $U(t)$, and $X(t)$.

As a result for every iso-scalar and iso-vector Dirac and Pauli FF one obtains just one analytic and smooth from $-\infty$ to $+\infty$ function in the forms

$$F_{1N}^s[V(t)] = \left(\frac{1-V^2}{1-V_N^2}\right)^4 \left\{\frac{1}{2}L_\omega(V)L_\phi(V) + \right.$$
$$+\left[L_\phi(V)L_{\omega'}(V)\frac{(C_\phi^{1s}-C_{\omega'}^{1s})}{(C_\phi^{1s}-C_\omega^{1s})} + L_\omega(V)L_{\omega'}(V)\frac{(C_\omega^{1s}-C_{\omega'}^{1s})}{(C_\omega^{1s}-C_\phi^{1s})} - \right.$$
$$\left. - L_\omega(V)L_\phi(V)\right](f_{\omega' NN}^{(1)}/f_{\omega'}) +$$
$$+\left[L_\phi(V)H_{\phi'}(V)\frac{(C_\phi^{1s}-C_{\phi'}^{1s})}{(C_\phi^{1s}-C_\omega^{1s})} + L_\omega(V)H_{\phi'}(V)\frac{(C_\omega^{1s}-C_{\phi'}^{1s})}{(C_\omega^{1s}-C_\phi^{1s})} - \right.$$
$$\left. - L_\omega(V)L_\phi(V)\right](f_{\phi' NN}^{(1)}/f_{\phi'}) +$$
$$+\left[L_\phi(V)H_{\omega''}(V)\frac{(C_\phi^{1s}-C_{\omega''}^{1s})}{(C_\phi^{1s}-C_\omega^{1s})} + L_\omega(V)H_{\omega''}(V)\frac{(C_\omega^{1s}-C_{\omega''}^{1s})}{(C_\omega^{1s}-C_\phi^{1s})} - \right.$$
$$\left. - L_\omega(V)L_\phi(V)\right](f_{\omega'' NN}^{(1)}/f_{\omega''}) +$$
$$+\left[L_\phi(V)H_{\phi''}(V)\frac{(C_\phi^{1s}-C_{\phi''}^{1s})}{(C_\phi^{1s}-C_\omega^{1s})} + L_\omega(V)H_{\phi''}(V)\frac{(C_\omega^{1s}-C_{\phi''}^{1s})}{(C_\omega^{1s}-C_\phi^{1s})} - \right.$$
$$\left.\left. - L_\omega(V)L_\phi(V)\right](f_{\phi'' NN}^{(1)}/f_{\phi''})\right\}$$

$$F^v_{1N}[W(t)] = \left(\frac{1-W^2}{1-W_N^2}\right)^4 \left\{ \frac{1}{2} L_\rho(W) L_{\rho'}(W) + \right.$$

$$+ \left[L_{\rho'}(W) H_{\rho''}(W) \frac{(C^{1v}_{\rho'} - C^{1v}_{\rho''})}{(C^{1v}_{\rho'} - C^{1v}_{\rho})} + L_\rho(W) H_{\rho''}(W) \frac{(C^{1v}_{\rho} - C^{1v}_{\rho''})}{(C^{1v}_{\rho} - C^{1v}_{\rho'})} - \right.$$

$$\left. \left. - L_\rho(W) L_{\rho'}(W) \right] (f^{(1)}_{\rho'' NN}/f_{\rho''}) \right\}$$

$$F^s_{2N}[U(t)] = \left(\frac{1-U^2}{1-U_N^2}\right)^6 \left\{ \frac{1}{2}(\mu_p + \mu_n) L_\omega(U) L_\phi(U) L_{\omega'}(U) + \right.$$

$$+ \left[L_\phi(U) L_{\omega'}(U) H_{\phi'}(U) \frac{(C^{2s}_\phi - C^{2s}_{\phi'})(C^{2s}_{\omega'} - C^{2s}_{\phi'})}{(C^{2s}_\phi - C^{2s}_{\omega})(C^{2s}_{\omega'} - C^{2s}_{\omega})} + \right.$$

$$+ L_\omega(U) L_{\omega'}(U) H_{\phi'}(U) \frac{(C^{2s}_\omega - C^{2s}_{\phi'})(C^{2s}_{\omega'} - C^{2s}_{\phi'})}{(C^{2s}_\omega - C^{2s}_{\phi})(C^{2s}_{\omega'} - C^{2s}_{\phi})} +$$

$$+ L_\omega(U) L_\phi(U) H_{\phi'}(U) \frac{(C^{2s}_\omega - C^{2s}_{\phi'})(C^{2s}_{\phi} - C^{2s}_{\phi'})}{(C^{2s}_\omega - C^{2s}_{\omega'})(C^{2s}_{\phi} - C^{2s}_{\omega'})} -$$

$$\left. - L_\omega(U) L_\phi(U) L_{\omega'}(U) \right] (f^{(2)}_{\phi' NN}/f_{\phi'}) +$$

$$+ \left[L_\phi(U) L_{\omega'}(U) H_{\omega''}(U) \frac{(C^{2s}_\phi - C^{2s}_{\omega''})(C^{2s}_{\omega'} - C^{2s}_{\omega''})}{(C^{2s}_\phi - C^{2s}_{\omega})(C^{2s}_{\omega'} - C^{2s}_{\omega})} + \right.$$

$$+ L_\omega(U) L_{\omega'}(U) H_{\omega''}(U) \frac{(C^{2s}_\omega - C^{2s}_{\omega''})(C^{2s}_{\omega'} - C^{2s}_{\omega''})}{(C^{2s}_\omega - C^{2s}_{\phi})(C^{2s}_{\omega'} - C^{2s}_{\phi})} +$$

$$+ L_\omega(U) L_\phi(U) H_{\omega''}(U) \frac{(C^{2s}_\omega - C^{2s}_{\omega''})(C^{2s}_{\phi} - C^{2s}_{\omega''})}{(C^{2s}_\omega - C^{2s}_{\omega'})(C^{2s}_{\phi} - C^{2s}_{\omega'})} -$$

$$\left. - L_\omega(U) L_\phi(U) L_{\omega'}(U) \right] (f^{(2)}_{\omega'' NN}/f_{\omega''}) +$$

$$+ \left[L_\phi(U) L_{\omega'}(U) H_{\phi''}(U) \frac{(C^{2s}_\phi - C^{2s}_{\phi''})(C^{2s}_{\omega'} - C^{2s}_{\phi''})}{(C^{2s}_\phi - C^{2s}_{\omega})(C^{2s}_{\omega'} - C^{2s}_{\omega})} + \right.$$

$$+ L_\omega(U) L_{\omega'}(U) H_{\phi''}(U) \frac{(C^{2s}_\omega - C^{2s}_{\phi''})(C^{2s}_{\omega'} - C^{2s}_{\phi''})}{(C^{2s}_\omega - C^{2s}_{\phi})(C^{2s}_{\omega'} - C^{2s}_{\phi})} +$$

$$+ L_\omega(U) L_\phi(U) H_{\phi''}(U) \frac{(C^{2s}_\omega - C^{2s}_{\phi''})(C^{2s}_{\phi} - C^{2s}_{\phi''})}{(C^{2s}_\omega - C^{2s}_{\omega'})(C^{2s}_{\phi} - C^{2s}_{\omega'})} -$$

$$\left. \left. - L_\omega(U) L_\phi(U) L_{\omega'}(U) \right] (f^{(2)}_{\phi'' NN}/f_{\phi''}) \right\}$$

$$F^v_{2N}[X(t)] = \left(\frac{1-X^2}{1-X_N^2}\right)^6 \left\{ \frac{1}{2}(\mu_p - \mu_n) L_\rho(U) L_{\rho'}(U) H_{\rho''}(U) \right\}$$

where

$$L_r(V) = \frac{(V_N - V_r)(V_N - V_r^*)(V_N - 1/V_r)(V_N - 1/V_r^*)}{(V - V_r)(V - V_r^*)(V - 1/V_r)(V - 1/V_r^*)},$$
$$C_r^{1s} = \frac{(V_N - V_r)(V_N - V_r^*)(V_N - 1/V_r)(V_N - 1/V_r^*)}{-(V_r - 1/V_r)(V_r - 1/V_r^*)}, r = \omega, \phi, \omega'$$

$$H_l(V) = \frac{(V_N - V_l)(V_N - V_l^*)(V_N + V_l)(V_N + V_l^*)}{(V - V_l)(V - V_l^*)(V + V_l)(V + V_l^*)},$$
$$C_l^{1s} = \frac{(V_N - V_l)(V_N - V_l^*)(V_N + V_l)(V_N + V_l^*)}{-(V_l - 1/V_l)(V_l - 1/V_l^*)}, l = \phi', \omega''\phi''$$

$$L_k(W) = \frac{(W_N - W_k)(W_N - W_k^*)(W_N - 1/W_k)(W_N - 1/W_k^*)}{(W - W_k)(W - W_k^*)(W - 1/W_k)(W - 1/W_k^*)},$$
$$C_k^{1v} = \frac{(W_N - W_k)(W_N - W_k^*)(W_N - 1/W_k)(W_N - 1/W_k^*)}{-(W_k - 1/W_k)(W_k - 1/W_k^*)}, k = \rho, \rho'$$

$$H_{\rho''}(W) = \frac{(W_N - W_{\rho''})(W_N - W_{\rho''}^*)(W_N + W_{\rho''})(W_N + W_{\rho''}^*)}{(W - W_{\rho''})(W - W_{\rho''}^*)(W + W_{\rho''})(W + W_{\rho''}^*)},$$
$$C_{\rho''}^{1v} = \frac{(W_N - W_{\rho''})(W_N - W_{\rho''}^*)(W_N + W_{\rho''})(W_N + W_{\rho''}^*)}{-(W_{\rho''} - 1/W_{\rho''})(W_{\rho''} - 1/W_{\rho''}^*)},$$

$$L_r(U) = \frac{(U_N - U_r)(U_N - U_r^*)(U_N - 1/U_r)(U_N - 1/U_r^*)}{(U - U_r)(U - U_r^*)(U - 1/U_r)(U - 1/U_r^*)},$$
$$C_r^{2s} = \frac{(U_N - U_r)(U_N - U_r^*)(U_N - 1/U_r)(U_N - 1/U_r^*)}{-(U_r - 1/U_r)(U_r - 1/U_r^*)}, r = \omega, \phi, \omega'$$

$$H_l(U) = \frac{(U_N - U_l)(U_N - U_l^*)(U_N + U_l)(U_N + U_l^*)}{(U - U_l)(U - U_l^*)(U + U_l)(U + U_l^*)},$$
$$C_l^{2s} = \frac{(U_N - U_l)(U_N - U_l^*)(U_N + U_l)(U_N + U_l^*)}{-(U_l - 1/U_l)(U_l - 1/U_l^*)}, l = \phi', \omega''\phi''$$

$$L_k(X) = \frac{(X_N - X_k)(X_N - X_k^*)(X_N - 1/X_k)(X_N - 1/X_k^*)}{(X - X_k)(X - X_k^*)(X - 1/X_k)(X - 1/X_k^*)},$$
$$C_k^{2v} = \frac{(X_N - X_k)(X_N - X_k^*)(X_N - 1/X_k)(X_N - 1/X_k^*)}{-(X_k - 1/X_k)(X_k - 1/X_k^*)}, k = \rho, \rho'$$

$$H_{\rho''}(X) = \frac{(X_N - X_{\rho''})(X_N - X^*_{\rho''})(X_N + X_{\rho''})(X_N + X^*_{\rho''})}{(X - X_{\rho''})(X - X^*_{\rho''})(X + X_{\rho''})(X + X^*_{\rho''})},$$

$$C^{2v}_{\rho''} = \frac{(X_N - X_{\rho''})(X_N - X^*_{\rho''})(X_N + X_{\rho''})(W_X + X^*_{\rho''})}{-(X_{\rho''} - 1/X_{\rho''})(X_{\rho''} - 1/X^*_{\rho''})}.$$

II. ANALYSIS OF EXISTING DATA

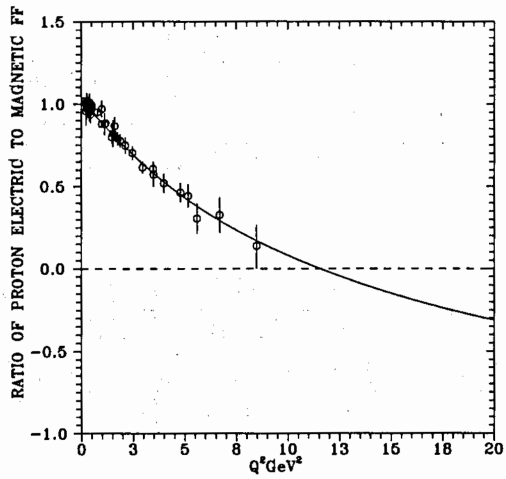

FIG. 2: Prediction of proton electric to magnetic FFs ratio behavior by $U\&A$ model respecting $SU(3)$ symmetry

There are 10 different nucleon EM FFs data at our disposal.

Proton polarization data on the ratio $G_{Ep}(t)/G_{Mp}(t)$ in $t < 0$ region.

The data on $G_{Ep}(t)$ in $t < 0$ region.

The data on $G_{Ep}(t)$ in $t > 0$ region.

The data on $G_{Mp}(t)$ in $t < 0$ region.

The data on $G_{Mp}(t)$ in $t > 0$ region.

The data on $G_{En}(t)$ in $t < 0$ region.

The data on $G_{En}(t)$ in $t > 0$ region.

The data on $G_{Mn}(t)$ in $t < 0$ region.

The data on $G_{Mn}(t)$ in $t > 0$ region.

Neutron polarization data on the ratio $G_{En}(t)/G_{Mn}(t)$ in $t < 0$ region.

However, not all data are equally reliable.

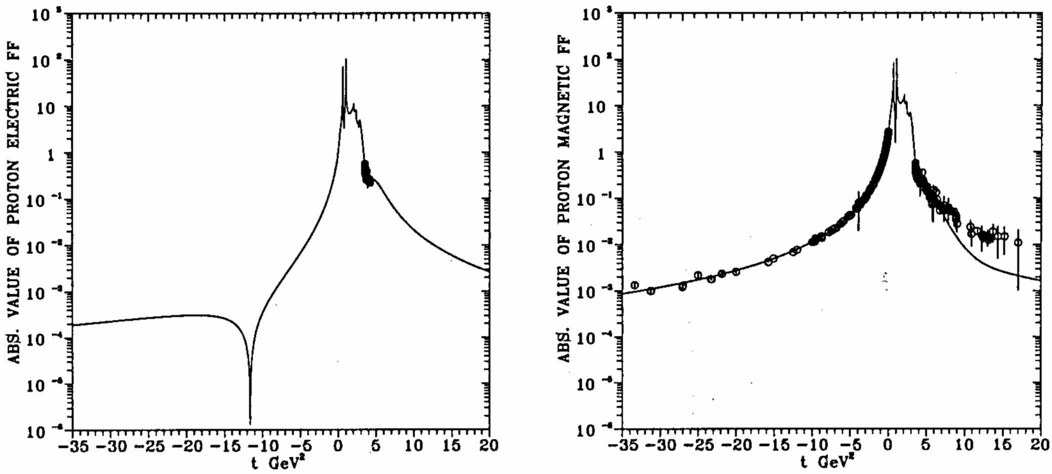

FIG. 3: Prediction the proton electric and magnetic FF behavior by $U\&A$ model respecting $SU(3)$ symmetry

III. RESULTS

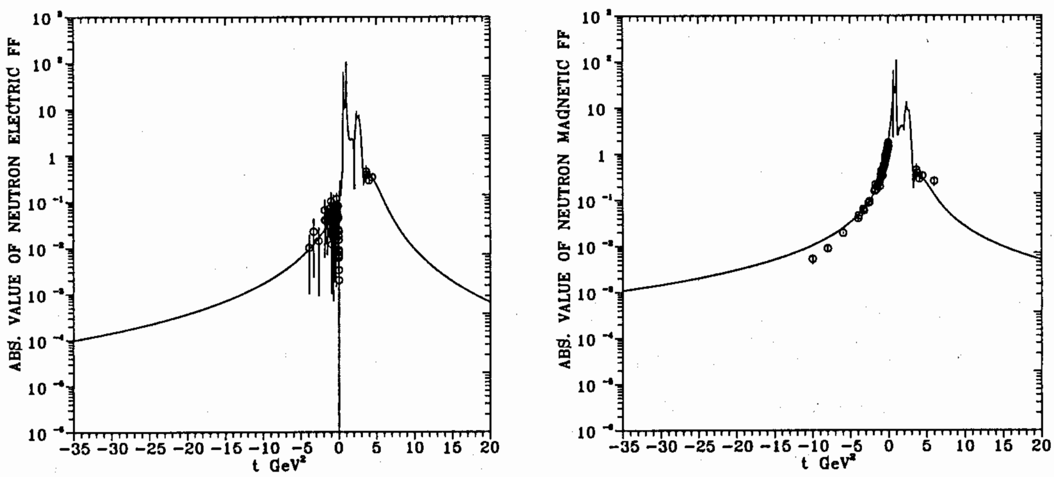

FIG. 4: Prediction of the neutron electric and magnetic FF behavior by $U\&A$ model respecting $SU(3)$ symmetry

By means of the analysis of the data with the $U\&A$ model we have achieved preliminary:

- description of existing data (see Figures 2-5)
- reproduction of the zero of $G_{Ep}(t)$ at the interval from $10GeV^2$ up to $15GeV^2$
- the proton charge rms radius from the interval $0.843fm$ up to $0.860fm$.

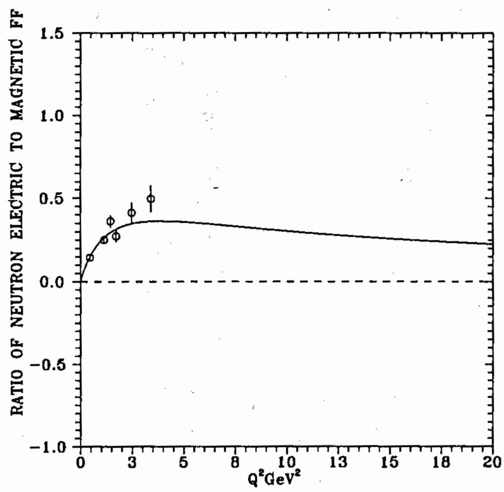

FIG. 5: Prediction of neutron electric to magnetic FFs ratio behavior by $U\&A$ model respecting $SU(3)$ symmetry

IV. ACKNOWLEDGEMENT

The support of the Slovak Grant Agency for Sciences VEGA under the Grant No: 2/0009/11 is acknowledged.

---

[1] I.Sick, Phys. Lett B576 (2003) 62

[2] P.G.Blunden, I.Sick, Phys. Rev. C72 (2005) 057601

[3] K.Nakamura et al (Particle Data Group), J. Phys G37 (2010) 075021

[4] S.Dubnicka, A.Z.Dubnickova, P.Weisenpacher, J. Phys. G29 (2003) 405

[5] H.-W.Hammer, U.-G.Meissner, Eur. Phys. J. A20 (2004) 469

[6] C.Adamuscin, S.Dubnicka, A.Z.Dubnickova, P.Weisenpacher, Prog. Part. Nucl. Phys. 55 (2005) 228

[7] M.A.Belushkin, H.-W.Hammer, U.-G.Meissner, Phys. Rev. C75 (2007) 035202

[8] A.I.Akhiezer, M.P.Rekalo, Sov. J. Part. Nucl. 4 (1974) 277.

[9] M.K.Jones et al, Phys. Rev. Lett. 84 (2000) 1398.

[10] O.Gayon et al, Phys. Rev. Lett. 88 (2002) 092301.

[11] V.Panjabi et al, Phys. Rev. C71 (2005) 055202.

Symmetry energy and nucleon-nucleon cross sections

M. Veselsky

Institute of Physics, Slovak Academy of Sciences, Bratislava

Y.G. Ma

Shanghai Institute of Applied Physics, Chinese Academy of Sciences

Abstract

The extension of the Boltzmann-Uehling-Uhlenbeck model of nucleus-nucleus collision is presented. The isospin-dependent nucleon-nucleon cross sections are estimated using the proper volume extracted from the equation of state of the nuclear matter transformed into the form of the Van der Waals equation of state. The results of such simulations demonstrate the dependence on symmetry energy which typically varies strongly from the results obtained using only the isospin-dependent mean-field. The evolution of the n/p multiplicity ratio with angle and kinetic energy, in combination with the elliptic flow of neutrons and protons, provides a suitable set of observables for determination of the density dependence of the symmetry energy. The model thus provides an environment for testing of equations of state, used for various applications in nuclear physics and astrophysics.

1 Introduction

One of the main goals of intermediate-energy heavy-ion collisions (HIC) is to study properties of nuclear matter, especially to determine the nuclear equation of state (EoS). HIC provide a unique possibility to compress nuclear matter to a hot and dense phase within a laboratory environment. The pressures that result from the high densities achieved during such collisions strongly influence the motion of ejected matter and are sensitive to the EoS. Within the hard work of the researchers over the three decades, the EoS of symmetric nuclear matter was studied in detail by the study of giant dipole resonances, collective flow as well as multifragmentation [3, 4, 5, 6]. The EoS of isospin asymmetric nuclear matter is recently underway, particularly, for the density dependence of symmetry energy. Considerable progress has been made in determining the sub- and supra-saturation density behavior of the symmetry energy [7, 8, 9, 10, 11, 12, 13, 14]. The later part is still an unanswered question in spite of recent findings in term of neutron-proton elliptic flow ratio and difference [12, 13]. However, the former one is understood to some extent [7, 8, 9, 10], although, more efforts are needed for precise measurements.

Transport model is very useful to treat heavy ion collision dynamics and obtain important information of nuclear matter EoS as well as the symmetry energy. In intermediate energy heavy ion collisions, the Boltzmann-Uehling-Uhlenbeck model is an extensively useful tool [1], which takes both Pauli blocking and mean field into consideration. The BUU equation reads

$$\frac{\partial f}{\partial t} + v \cdot \nabla_r f - \nabla_r U \cdot \nabla_p f = \frac{4}{(2\pi)^3} \int d^3p_2 d^3p_3 d\Omega$$
$$\frac{d\sigma_{NN}}{d\Omega} v_{12} \times [f_3 f_4 (1-f)(1-f_2) - f f_2 (1-f_3)(1-f_4)]$$
$$\delta^3(p + p_2 - p_3 - p_4), \tag{1}$$

where f=$f(r,p,t)$ is the phase-space distribution function. It is solved with the method of Bertsch and Das Gupta [2]. In Eq.(1), $\frac{d\sigma_{NN}}{d\Omega}$ and v_{12} are in-medium nucleon-nucleon cross section and relative velocity for the colliding nucleons, respectively, and U is the single-particle mean field potential including the isospin-dependent term:

$$U = a\rho + b\rho^\kappa + 2a_s(\frac{\rho}{\rho_0})^\gamma \tau_z I, \tag{2}$$

where $I = (\rho_n - \rho_p)/\rho$, ρ_0 is the normal nuclear matter density; ρ, ρ_n, and ρ_p are the nucleon, neutron and proton densities, respectively; τ_z assumes value 1 for neutron and -1 for proton, coefficients a, b and κ represent properties of the symmetric nuclear matter while the last term, which describes the influence of the symmetry energy, can be obtained e.g. from simple Weizsacker formula, where a_s represents the coefficient of the symmetry energy term. Typical sets of mean field parameters cover substantial range, between the soft EoS with the compressibility K of 200 MeV ($\kappa = 7/6, a\rho_0=$ -356 MeV, $b\rho_0^\kappa = 303$ MeV), and the hard EoS with K of 380 MeV ($\kappa = 2$, $a\rho_0 =$ -124 MeV, $b\rho_0^\kappa = 70.5$ MeV).

It is the aim of the present work to estimate the effect of the symmetry energy parametrization within the equation of the state on the crucial component of the transport simulations, namely the in-medium nucleon-nucleon cross section.

2 Isospin-dependent nucleon-nucleon cross sections

When considering influence of the symmetry energy on emission rates of nucleons in nucleus-nucleus collisions, one needs to understand whether and how the medium represented by the equation of state can influence relative probabilities of emission of protons and neutrons. Theoretical investigations of the density-dependence of in-medium nucleon-nucleon cross section were carried out for symmetric nuclear matter [15, 16], and significant influence of nuclear density on resulting in-medium cross sections was observed in their density, angular and energy dependencies. Using momentum-dependent interaction, ratios of in-medium to free nucleon-nucleon cross sections were evaluated via reduced nucleonic masses [17] and used for transport simulations. Still, transport simulation are mostly performed using parametrizations of the free nucleon-nucleon cross sections, eventually scaling them down empirically or using simple prescriptions for density-dependence of the scaling factor [18]. In the present work, a prescription for estimation of the density-dependence of the in-medium nucleon-nucleon cross sections corresponding to the specific form of phenomenological nuclear equation of state will be presented. Such possibility to establish a simple dependence of nucleon-nucleon cross sections on density, temperature and symmetry energy is potentially important for a wide range of problems in nuclear physics and astrophysics.

2.1 Equation of state of nucleonic matter

Based on the single-particle potential, shown in Eq. (2), one can construct corresponding equation of the state. Change of the pressure in thermodynamical equation of state, which is also a measure of non-ideality of a neutron or a proton gas, can be evaluated as

$$\Delta p_{non-ideal} = -\frac{d\mathcal{U}}{dV}|_{T=const} \tag{3}$$

where $\mathcal{U}$ is the thermodynamic potential, V is the volume and T is the temperature. When evaluating the thermodynamic potential $\mathcal{U}$ as a sum of single-particle contributions of neutrons and protons, given by equation (2), one arrives to expression

$$\begin{aligned} p &= x_n(\rho T + a\rho^2 + b\kappa\rho^{1+\kappa} + 2\gamma a_s \rho_0 (\frac{\rho}{\rho_0})^{1+\gamma} I) \\ &+ x_p(\rho T + a\rho^2 + b\kappa\rho^{1+\kappa} - 2\gamma a_s \rho_0 (\frac{\rho}{\rho_0})^{1+\gamma} I). \end{aligned} \tag{4}$$

where $x_n = \rho_n/\rho$ and $x_p = \rho_p/\rho$ are neutron and proton concentrations. This expression appears to provide separate terms for pressure of neutrons and protons, which however can be combined to obtain the typical quadratic dependence on isospin asymmetry I. The resulting pressure is the weighted average between two terms, which can be, in similar manner to equation (2), summarily expressed as

$$p = \rho T + a\rho^2 + b\kappa\rho^{1+\kappa} + 2\gamma a_s \rho_0 (\frac{\rho}{\rho_0})^{1+\gamma} \tau_z I. \tag{5}$$

These terms can be interpreted as the equation of state of the system of particles with the corresponding single-particle potential, given by the equation (2).

2.2 Proper volume in the Van der Waals equation of state

In order to find relation between equation of state and nucleon emission rates one can turn attention specifically to the Van der Waals equation of state. It can be written, using particle density ρ,

$$(p + a'\rho^2)(1 - \rho b') = \rho T, \tag{6}$$

where the parameter a' is related to attractive interaction among particles and b' represents the proper volume of the constituent particles. In geometrical picture the proper volume of the particle can be directly related to its cross section for interaction with other particles. It is possible to formally transform the above equations of state for neutrons and protons (5) (and practically any other equation of state) into the form analogous to the Van der Waals equation. Then, by comparison, one obtains values of coefficients

$$a' = -a, \tag{7}$$

and

$$b' = \frac{b\kappa\rho^{\kappa} + 2\gamma a_s (\frac{\rho}{\rho_0})^{\gamma} \tau_z I}{p - a\rho^2} = \frac{b\kappa\rho^{\kappa} + 2\gamma a_s (\frac{\rho}{\rho_0})^{\gamma} \tau_z I}{\rho T + b\kappa\rho^{1+\kappa} + 2\gamma \rho_0 a_s (\frac{\rho}{\rho_0})^{1+\gamma} \tau_z I}, \tag{8}$$

where the latter provides a measure of the proper volume of the constituents, nucleons in this case, as a measure of deviation from the behavior of the ideal gas. The proper volume of nucleon can be used to estimate its cross section within the nucleonic medium

$$\sigma = (\frac{9\pi}{16})^{1/3}\, b'^{2/3}, \tag{9}$$

which can be implemented into the collision term of the Boltzmann equation.

Concerning the physical meaning of this procedure, for each point in the ρ-T plane the Van der Waals equation of state is found which behaves identically to the nuclear equation of state (5) in the vicinity of that point. Thus the dynamics of the system can be described using the two parameters of the Van der Waals EoS, of which one provides a measure of the effective volume of the constituent at a given density and temperature. The variation of the constituent volume reflects the interplay of the long-range attractive interaction, leading to its apparent increase, with the short-range repulsive interaction, leading to its apparent decrease.

The trend of the estimated values of nucleus-nucleus cross sections, obtained using the soft parametrization of symmetry energy with $\rho^{2/3}$-dependence is shown in the Figure 1 for the temperature 20 MeV. The extracted values of the cross sections are surprisingly close to the expected value of geometric cross sections. With increasing isoscalar density the values of cross sections initially grow until they reach maximum values in the region around half of saturation density and then monotonously decrease. The increase at low densities possibly describes gradual deviation from the equation of state of ideal gas due to increasing attractive potential while at higher densities the decreasing trend may indeed represent the properties of short-range repulsive interaction. At high densities, with increasing isoscalar density the sensitivity to symmetry energy tends to decrease and around the density $2\rho_0$ it is practically lost, which however can be preserved using harder parametrizations of the symmetry energy.

It is worth mentioning that a similar rise and fall of nucleon-nucleon cross sections was observed by the Alm, Ropke and Schmidt [16] and it was explained as a precursor effect of super-fluid phase-transition. Also in the present case this effect can be related to the phase transition in the nuclear matter, since it is caused by the same interplay of attractive and repulsive interaction which influences also the proper volume and thus extracted cross sections.

2.3 Implementation into the Boltzmann equation

While the Boltzmann equation (1) is formulated in terms of density, it does not explicitly consider temperature. Therefore temperature T needs to be estimated independently. It is possible to estimate temperature using the Maxwellian momentum distribution of nucleons

$$f(\vec{p}) = \frac{1}{(2\pi m T)^{3/2}} e^{-\frac{p_x^2+p_y^2+p_z^2}{2mT}}, \tag{10}$$

where m is the nucleon mass. Using this formula, local temperature can be estimated from momentum distribution in the c.m. frame by evaluating the momentum variance. At early stages of collision this can be done primarily for transverse momentum since

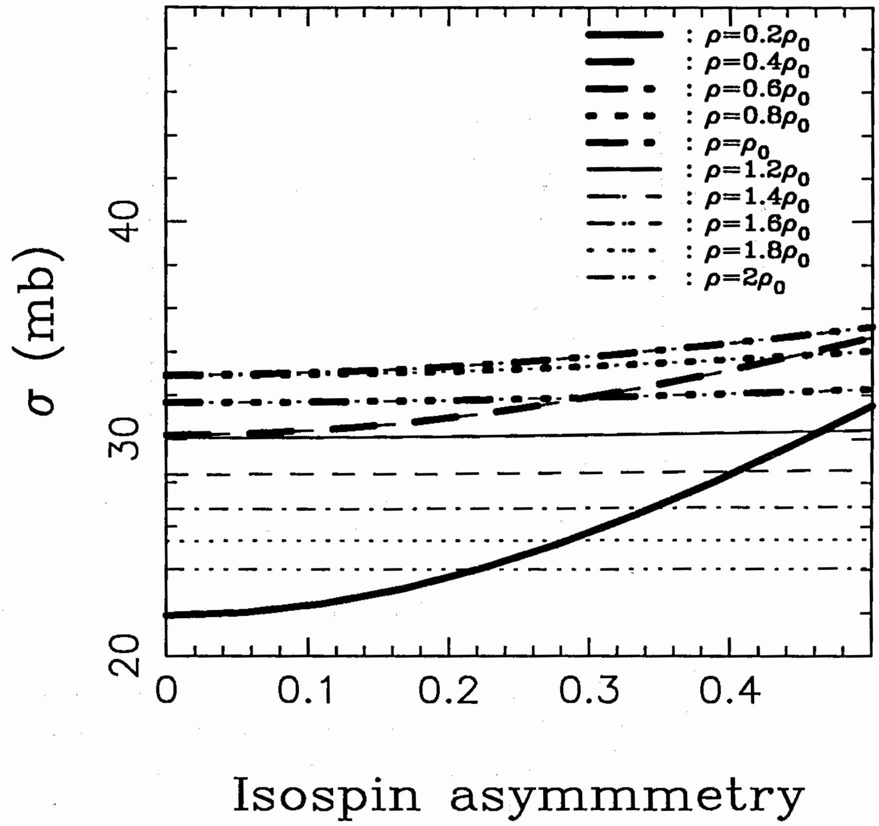

Figure 1: Extracted isospin dependencies of nucleon-nucleon cross sections for temperature 20 MeV and various densities.

it provides a measure of mutual thermalization of particles from the projectile and target, which proceeds by distant elastic collisions generating the transverse momentum. More violent collisions would lead to emission of colliding nucleons and thus would not contribute to thermalization of the source. This temperature estimate can be done without requiring stopping and formation of the source equilibrated in all three dimensions, closer analogue would be the friction of two dilute gas clouds passing through each other.

Evolution of average temperature of the fireball with the time is shown in Fig. 2. The results were obtained using the Boltzmann-Uehling-Uhlenbeck equation (BUU) [1] in reaction ^{48}Ca+^{48}Ca at 400 AMeV using the impact parameter 1 fm. Temperature was evaluated for each time step in the cubic cells with the side of 1 fm. Average temperature was determined as a mean value of temperature over all cells where number of nucleons was sufficient (corresponding to density of $\rho_0/10$) and temperature thus could be evaluated. The total volume of this fireball is shown in Fig. 2 in arbitrary scale as dash-dotted line. Dotted line shows the estimate of fireball temperature for a given beam energy obtained from the systematics of pre-equilibrium spectra [19]. One can see that the average temperature over the fireball at its peak value exceeds the estimate from the systematics, while the value averaged over the lifetime of the hot fireball (between 10 – 30 fm/c) appears to correspond to the value from the systematics. Thus it appears that the procedure introduced here leads to reasonable estimate of local temperature.

Once the local temperature is determined, it is possible to implement the isospin-

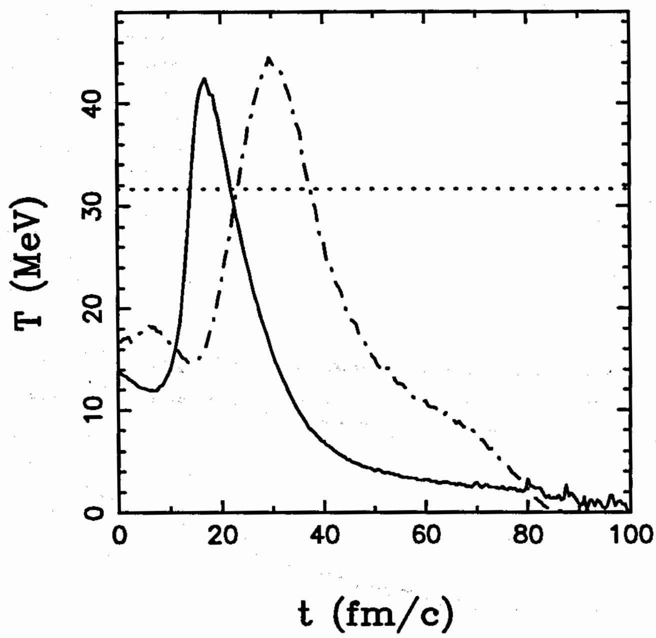

Figure 2: (Color online) Evolution of average temperature of the fireball (solid line) with the time. The total volume of the fireball is shown in arbitrary scale as dash-dotted line. The results were obtained using the BUU in reaction ^{48}Ca+^{48}Ca at 400 AMeV using the impact parameter 1 fm. Dotted straight line shows the fireball temperature estimate for a given beam energy obtained from the systematics of pre-equilibrium spectra [19].

dependent nucleon-nucleon cross section, obtained using the formula (9), to the reaction simulation which can be used for determination of collision rate. The results for solution of such fully isospin-dependent version of Boltzmann-Uehling-Uhlenbeck equation will be presented in the next section.

3 Reaction simulations

The behavior of the in-medium nucleon-nucleon cross sections was investigated using the already mentioned reaction ^{48}Ca+^{48}Ca at 400 AMeV using the impact parameter 1 fm. The soft equation of state was used, leading to incompressibility coefficient K=200 MeV. For the isospin asymmetric part the "asystiff" parametrization was used with two symmetry energy terms with parameters a_{s1}= 12.5 MeV and $\gamma_1 = 2/3$ and a_{s2}= 17.5 MeV and $\gamma_2 = 2$, respectively.

Fig. 3 shows a comparison of the nucleon-nucleon cross sections in two variants of the Boltzmann-Uehling-Uhlenbeck simulations. On the left panel are shown, as a function of density, the isospin-dependent nucleon-nucleon cross sections, obtained using the proper volume of the Van der Waals-like equation of state. On the right panel are shown the corresponding free nucleon-nucleon cross sections, obtained as energy dependent parametrization of measured nucleon-nucleon cross sections [20]. It is apparent that while the isospin-dependent nucleon-nucleon cross sections essentially follow the $1/\rho^{2/3}$-dependence, the nucleon-nucleon cross section parametrization of Cugnon et al. leads to much larger spread, mostly due to its explicit energy dependence. Nev-

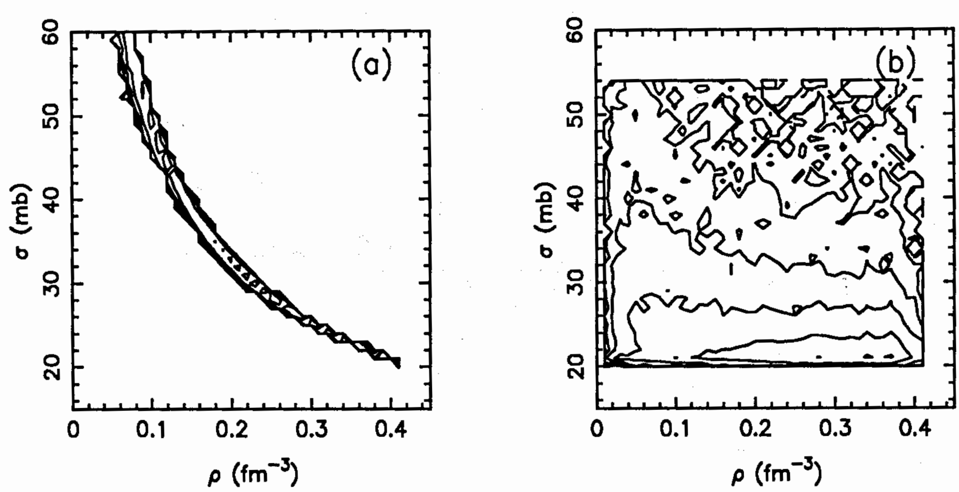

Figure 3: (Color online) Comparison of the nucleon-nucleon cross sections in two variants of the BUU calculations. On the left panel are the isospin-dependent nucleon-nucleon cross sections, obtained as the proper volume of the Van der Waals form of the equation of state, as a function of density, while on the right panel are shown the corresponding nucleon-nucleon cross sections, obtained using standard energy dependent parametrization, used in BUU calculation. The results were obtained using the BUU in reaction ^{48}Ca+^{48}Ca at 400 AMeV using the impact parameter 1 fm.

ertheless, it is interesting to observe that both parametrization cover essentially the same range of values of the nucleon-nucleon cross sections. In general, it is remarkable, that the in-medium nucleon-nucleon cross sections can be possibly directly related to the equation of state of the isospin asymmetric nuclear matter. This offers a more consistent description of the nuclear reactions and various astrophysical objects and processes in term of properties of nucleonic matter, expressed using the corresponding equation of state.

The magnitude of the effect of isospin asymmetry on the nucleon-nucleon cross sections can be judged from Fig. 4, which shows the relative difference of the isospin-dependent neutron-neutron and proton-proton cross sections as a function of isospin asymmetry of the volume cell. The results were again obtained using the BUU in reaction ^{48}Ca+^{48}Ca at 400 AMeV using the impact parameter 1 fm. One can see that the relative magnitude does not reach very high values even for most isospin-asymmetric cells, and the sensitivity of the Boltzmann-Uehling-Uhlenbeck simulation to the isospin-dependent nucleon-nucleon cross sections will result from the cumulative effect of large amount of nucleus-nucleus collisions.

The behavior observed in Figures 3 and 4 appears to be consistent with the behavior shown in Figure 4 of the work [17]. In both cases the absolute values of cross sections decrease monotonously with increasing density while the relative difference of the neutron-neutron and proton-proton cross sections increases with increasing asymmetry. Thus it appears that the procedure used to extract in-medium nucleon-nucleon cross sections by determining the parameters of corresponding Van der Waals EoS reflects the same physics, which is encoded even to a phenomenological equation of state such as Equation (2).

Figure 5 shows evolution of the difference of n/p multiplicity ratios between Boltzmann-

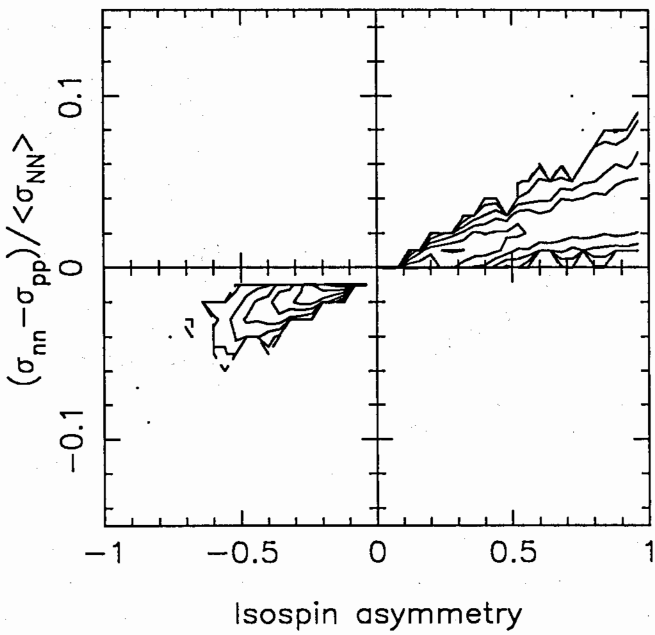

Figure 4: (Color online) Relative difference of the isospin-dependent neutron-neutron and proton-proton cross sections as a function of isospin asymmetry of the volume cell. The results were obtained using the BUU in reaction ^{48}Ca+^{48}Ca at 400 AMeV using the impact parameter 1 fm.

Uehling-Uhlenbeck simulation with both isospin-dependent mean-field and nucleon-nucleon cross sections which are correlated to each other by the Eq. 9 (based on the analogy with the van der Waals equation of state, thereafter we call this simulation as VdWBUU) and Boltzmann-Uehling-Uhlenbeck simulation with isospin-dependent mean-field and free nucleon-nucleon cross sections (thereafter we call it fBUU), for three angular ranges as a function of the kinetic energy in the center-of-mass system. The results were obtained using the BUU simulation in reactions ^{124}Sn+^{124}Sn and ^{112}Sn+^{112}Sn at 400 AMeV using the impact parameter 1 fm at the stopping time 200 fm/c. Squares show the result with stiff symmetry energy parametrization (a_{s1}= 12.5 MeV, $\gamma_1 = 2/3$, $a_{s2} = 17.5$ MeV and $\gamma_2 = 2$) while triangles show results for with soft symmetry energy parametrization ($a_{s1} = 12.5$ MeV, $\gamma_1 = 2/3$, $a_{s2} = 17.5$ MeV and $\gamma_2 = 1/2$). Soft nuclear equation of state ($K = 200$ MeV) is used in this case. Particles are considered as emitted when they are separated in the phase-space from any other particle and separation is large enough to assure that two particles are not part of a cluster (a condition $\Delta\vec{p}\Delta\vec{r} > 2h$ is implemented). One can see that implementation of isospin-dependent nucleon-nucleon cross sections leads to significant variation of n/p multiplicity ratio and this effect appears to evolve with both kinetic energy and polar angle. Variation of n/p multiplicity ratio is more significant for the more neutron-rich system, which offers a strong argument for the use of neutron-rich exotic beams for studies of density dependence of the symmetry energy in the future.

Figure 6 again shows evolution of the difference of n/p multiplicity ratio between VdWBUU calculation and fBUU calculation, in this case using stiff nuclear equation of state ($K = 380$ MeV). Also in the case of stiff nuclear equation of state one can see that implementation of isospin-dependent nucleon-nucleon cross sections leads to consider-

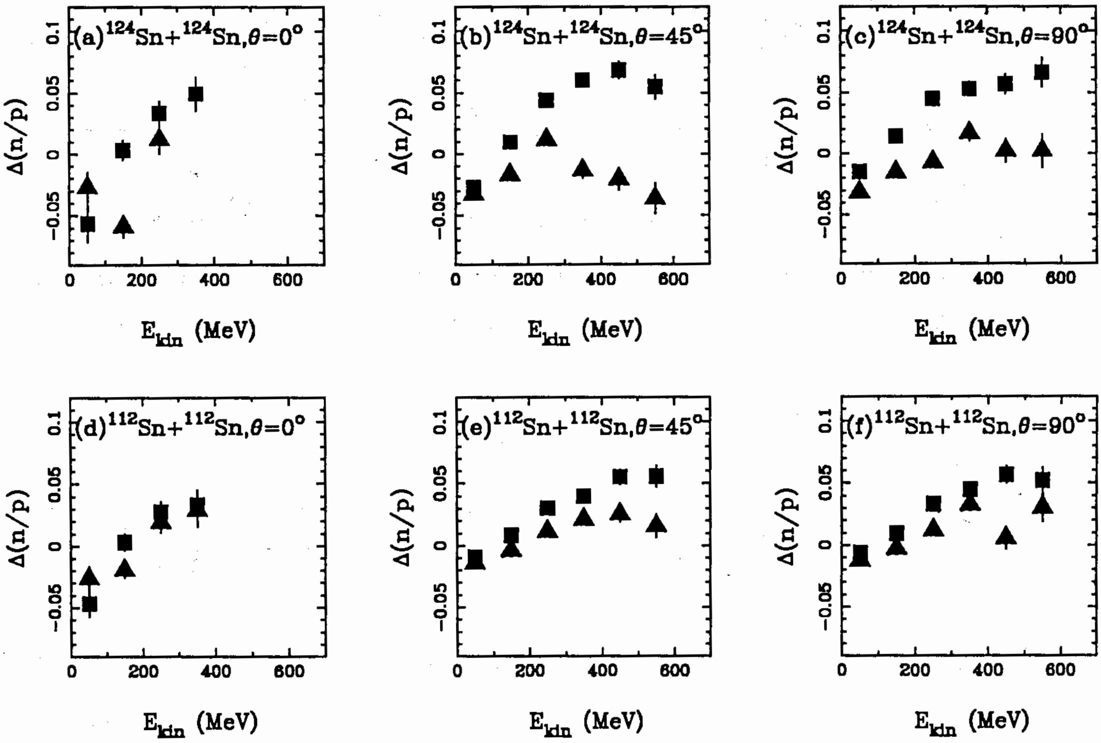

Figure 5: (Color online) Evolution of the difference of n/p multiplicity ratio between VdWBUU and fBUU calculations for three angular ranges. The results were obtained in reactions ^{124}Sn+^{124}Sn and ^{112}Sn+^{112}Sn at 400 AMeV using the impact parameter 1 fm at the time 200 fm/c. Squares show the result with stiff symmetry energy while triangles show results for soft symmetry energy. Soft nuclear equation of state is used.

able variation of n/p multiplicity ratio, which again evolves with both kinetic energy and polar angle. Also here the variation of n/p multiplicity ratio is more significant for the more neutron-rich system. It thus appears that variation of n/p multiplicity ratio between VdWBUU calculation and fBUU calculation provides a robust signal of the density dependence of nuclear symmetry energy.

Figures 7 and 8 show results for difference of n/p multiplicity ratio between VdWBUU calculation and fBUU calculation analogous to figures 5 and 6, with the impact parameter set to be 6 fm. It can be seen that the effect of isospin-dependent nucleon-nucleon cross sections persists, with comparable magnitude, even in peripheral collisions. This offers possibility to study such signal of the density-dependence of the symmetry energy in a wide range of centralities and thus eventually to provide a strong signal of the density-dependence of the symmetry energy in a wider range of nuclear density.

The fact, that the isospin-dependent nucleon-nucleon cross sections, obtained using the proper volume of the Van der Waals–like equation of state, need to be introduced in order to fully explore the isospin dependence in the Boltzmann-Uehling-Uhlenbeck simulations, directly affects the applicability of the symmetry energy parametrizations to the study of astrophysical objects such as neutron stars or supernovae. Due to increased sensitivity to isospin due to isospin-dependent nucleon-nucleon cross sections, the symmetry energy parametrizations may change significantly and that will affect

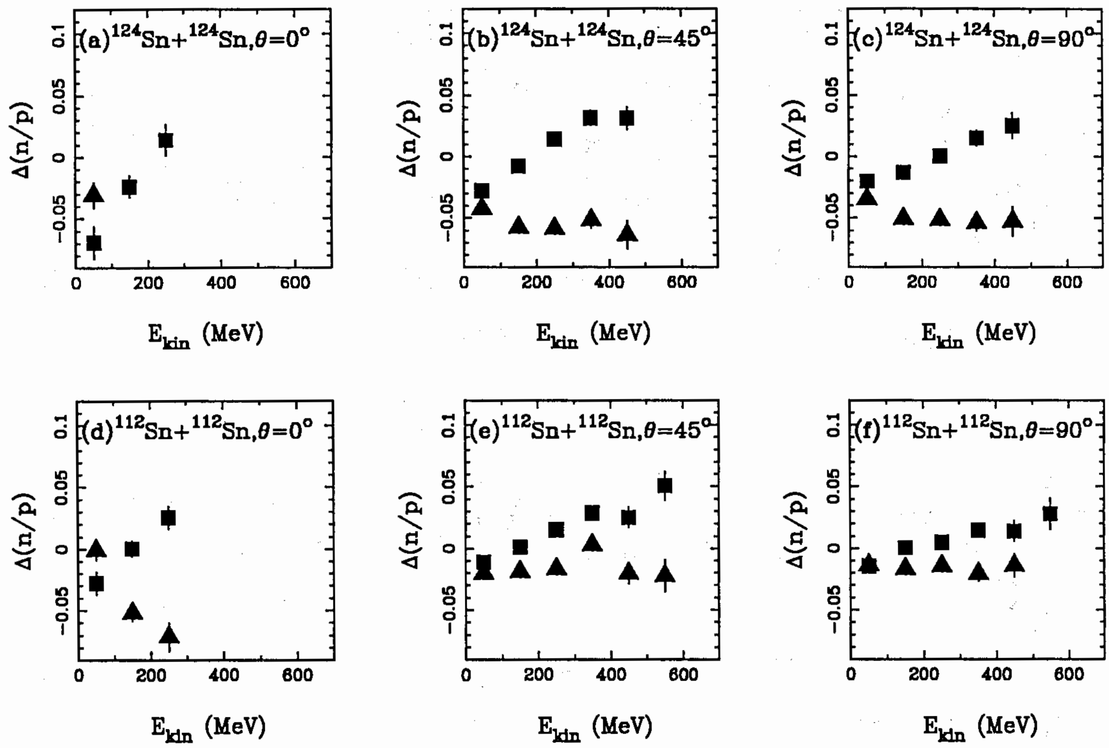

Figure 6: (Color online) Same as Figure 5 but for stiff nuclear equation of state.

the extrapolations toward the nuclear densities, typical for neutron stars and similar objects. On the other hand, increased sensitivity may offer more possibilities for the simulations of reactions of exotic nuclear beams, with the possible observation of stronger isospin-dependent signals.

The recently performed simulations based on the Ultrarelativistic Quantum Molecular Dynamics model (UrQMD) suggest that one of the most promising probe of the strength of the symmetry energy at supra-saturation densities is the difference of the neutron and proton (or hydrogen) elliptic flows [11, 12, 21, 22]. The simulations were performed using both stiff (γ= 1.5) and soft (γ =0.5) symmetry energy parametrizations. An inversion of the relative strengths of the elliptic flow for neutrons and protons is observed when the symmetry energy parametrization is changed from the stiff behavior to the soft behavior. Neutron and proton directed and elliptic flows were measured a decade ago in ^{197}Au +^{197}Au collisions at beam energies from 400 to 800 AMeV using the LAND neutron detector and the FOPI Phase 1 forward wall [24, 25]. Comparison of predictions of the UrQMD model [26] provided a constraint on symmetry energy at supra-saturation densities from transverse momentum dependence of the neutron and hydrogen's elliptic flow parameter v_2 measured in the ^{197}Au +^{197}Au system with FOPI+LAND, suggesting a value of $\gamma = 0.9 \pm 0.4$ [12], in agreement with findings at sub-saturation densities. However the statistics of these data set severe limits on the conclusions that can be drawn by comparison to transport model calculations. The promising results of re-analysis of FOPI+LAND experiment initiated proposal for a new experiment [27], which is one of the first dedicated explorations of the symmetry energy at high densities. The experiment uses the LAND calorimeter for neutron and charged particle detection, and the impact parameter is determined with a detection

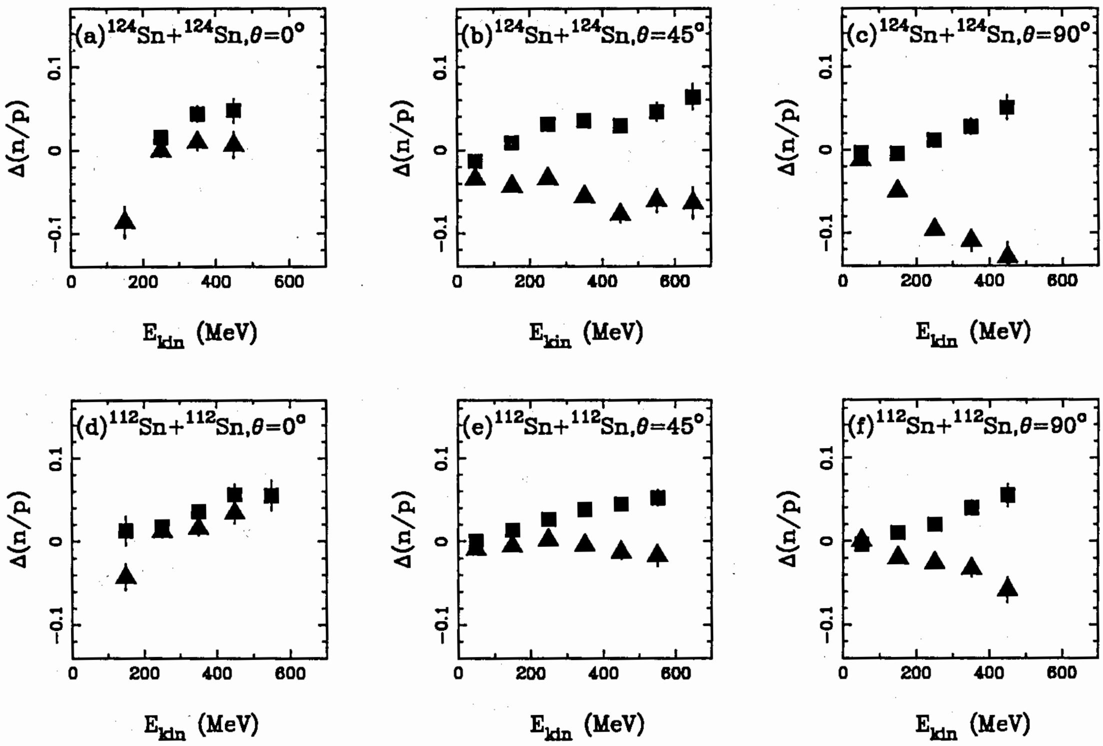

Figure 7: (Color online) Evolution of the difference of n/p multiplicity ratio between VdWBUU and fBUU calculations for three angular ranges. The results were obtained in reactions ^{124}Sn+^{124}Sn and ^{112}Sn+^{112}Sn at 400 AMeV using the impact parameter 6 fm at the time 200 fm/c. Squares show the results with stiff symmetry energy while triangles show results for soft symmetry energy. Soft nuclear equation of state is used.

system with high effective granularity at forward angles consisting of several CsI rings of the CHIMERA multi-detector [28] and the ALADIN Time-Of-Flight wall [29]. In addition, flow of light fragments are measured with the Krakow telescope [30] array positioned opposite from LAND. Uncertainties are expected to be reduced by a factor of 4-5, thus allowing to constrain theoretical calculations. Expected results of this experiment will provide a welcome testing-ground for the model calculations introduced in the present work.

It is of interest to estimate what effect will the introduction the isospin-dependent nucleon-nucleon cross sections, obtained as the proper volume of the Van der Waals–like equation of state, have on the resulting elliptic flow of neutrons and protons. Figure 9 shows calculated values of the elliptic flow of neutrons and protons (determined conventionally as second Fourier coefficient of the invariant triple differential distribution v_2 relative to reaction plane) in reactions ^{124}Sn+^{124}Sn and ^{112}Sn+^{112}Sn at 400 AMeV at the impact parameter 6 fm. Solid and open squares show results of VdWBUU calculation and fBUU calculation, respectively, with soft symmetry energy parametrization. Solid and open asterisks show analogous results with stiff symmetry energy parametrization. One can see that introduction of isospin-dependent nucleon-nucleon cross sections, varying the ratio of neutron-neutron and proton-proton collision rates and thus modifying the in-plane/out-of-plane emission ratios, influences the resulting values of the elliptic flow, and since the effect appears to vary between neu-

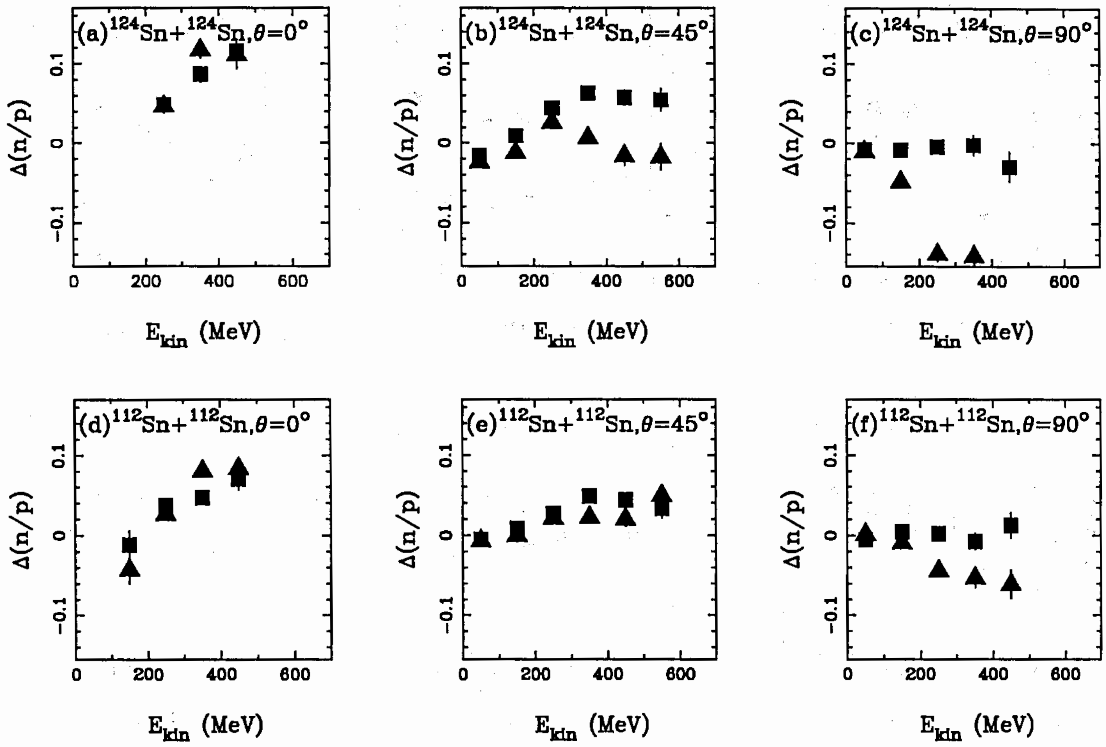

Figure 8: (Color online) Same as Figure 7 but for stiff nuclear equation of state.

trons and protons, it will strongly influence the differential elliptic flow, thus making it a strong signature of the nuclear equation of state, as suggested in the work [12]. However, since the effect of symmetry energy on such differential elliptic flow tends to vary also with isoscalar part of the nuclear equation of state, it appears necessary to study differential elliptic flow in combination with other observables, such as the evolution of n/p multiplicity ratio at different polar angles and kinetic energies. Such a study, carried out on sufficiently neutron-rich system, can provide a good sensitivity to both isoscalar and isovector part of the nuclear equation of state.

4 Conclusions

The extension of the Boltzmann-Uehling-Uhlenbeck model of nucleus-nucleus collision is presented. The isospin-dependent nucleon-nucleon cross sections are estimated using the proper volume extracted from the equation of state of the nuclear matter transformed into the form of the Van der Waals equation of state. The results of such simulations demonstrate the dependence on symmetry energy which typically varies strongly from the results obtained using only the isospin-dependent mean-field. The evolution of the n/p multiplicity ratio with angle and kinetic energy, in combination with the elliptic flow of neutrons and protons, provides a suitable set of observables for determination of the density dependence of the symmetry energy. The model thus provides an environment for testing of equations of state, used for various applications in nuclear physics and astrophysics.

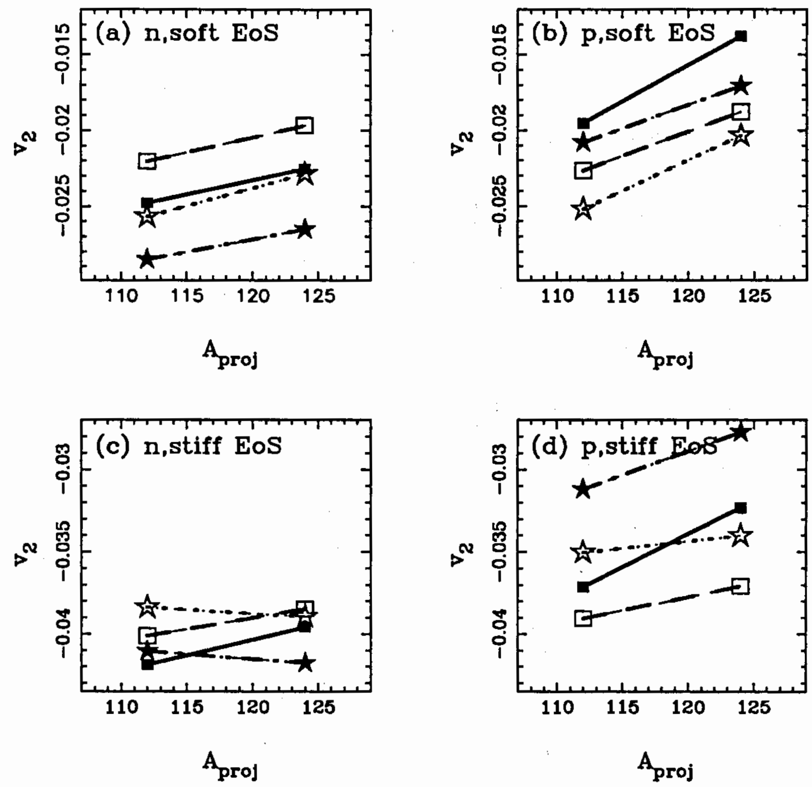

Figure 9: (Color online) Elliptic flow of neutrons and protons in reactions ^{124}Sn+^{124}Sn and ^{112}Sn+^{112}Sn at 400 AMeV at the impact parameter 6 fm. Solid and open squares show results of VdWBUU calculation and fBUU calculation, respectively, with soft symmetry energy. Solid and open asterisks show analogous results with stiff symmetry energy.

Acknowledgments: This work is supported in part by the Chinese Academy of Sciences Fellowships for the international scientists under the Grant No. 2011T2J13 (M.V.), and by NSFC of China under contract Nos. 11035009, 10979074, the Knowledge Innovation Project of CAS under Grant No. KJCX2-EW-N01 (Y.G.M.). M.V. has been also supported by the Slovak Scientific Grant Agency under contract 2/0105/11, and by the Slovak Research and Development Agency under contract APVV-0177-11.

References

[1] W. Bauer, G.F. Bertsch, W. Cassing, and U. Mosel, Phys. Rev. C **34**, 2127 (1986).

[2] G. F. Bertsch, and S. Das Gupta, Phys. Rep. **160**, 189 (1988).

[3] D. H. Youngblood, H. L. Clark, and Y.-W. Lui, Phys. Rev. Lett. **82**, 691 (1999).

[4] J. B. Natowitz *et al.*,Phys. Rev. Lett. **89**, 212701 (2002).

[5] P. Danielewicz, R. Lacey, and W. G. Lynch, Science **298**, 1592 (2002).

[6] W. Reisdorf *el al.,* Nucl. Phys. A **876**, 1 (2012).

[7] M. B. Tsang *et al.*, Phys. Rev. Lett. **92**, 062701 (2004).

[8] M. A. Famiano *et al.*, Phys. Rev. Lett. **97**, 052701 (2006).

[9] M. B. Tsang *et al.*, Phys. Rev. Lett. **102**, 122701 (2009).

[10] S. Kumar *et al.*, Phys. Rev. C **84** , 044620 (2011).

[11] B. A. Li, L.W. Chen, and C. M. Ko, Phys. Rep. **464**, 113 (2008).

[12] P. Russotto *et al.*, Phys. Lett. B **697**, 471 (2011).

[13] M. D. Cozma, Phys. Lett. B **700**, 139 (2011).

[14] S. Gautam *et al.*, Phys. Rev. C **83**, 034606 (2011).

[15] G.Q. Li, and R. Machleidt, Phys. Rev. C **48**, 1702 (1993); Phys. Rev. C **49**, 566 (1994).

[16] T. Alm, G. Ropke, and M. Schmidt, Phys. Rev. C **50**, 31 (1994); T. Alm, G. Ropke, W. Bauer, F. Daffin, and M. Schmidt, Nucl. Phys. A **587**, 815 (1995).

[17] B.-A. Li, and L.-W. Chen, Phys. Rev. C **72**, 064611 (2005).

[18] D. Klakow, G. Welke, and W. Bauer, Phys. Rev. C **48**, 1982 (1993).

[19] C.K. Gelbke, and D.H. Boal, Prog. Part. Nucl. Phys. **19**, 33 (1987).

[20] J. Cugnon, T. Mizutani, and J. Vandermeulen, Nucl. Phys. A **352**, 505 (1981).

[21] W. Trautmann *et al.*, Prog. Part. Nucl. Phys **62**, 425 (2009).

[22] W. Trautmann *et al.*, Int. J. Mod. Phys. E **19**, 1653 (2010).

[23] V. Baran *et al.*, Phys Rep **410**, 335 (2005).

[24] Y. Leifels *et al.*, Phys. Rev. Lett. **71**, 963 (1993).

[25] D. Lambrecht *et al.*, Z. Phys. A **350**, 115 (1994).

[26] Q. Li *et al.*, Phys. Rev. C **73**, 051601(R) (2006) .

[27] R.C. Lemmon, P. Russotto *et al.*, Constraining the Symmetry Energy at Supra-Saturation Densities with Measurements of Neutron and Proton Elliptic Flows, GSI experiment S394.

[28] A. Pagano *et al.*, Nucl. Phys. A **734**, 504 (2004) .

[29] A. Schüttauf *et al.*, Nucl. Phys. A **607**, 457 (1996).

[30] J. Lukasik *et al.*, KRATTA, a triple telescope array for charged reaction products, EPJ Web of Conferences **31**, 00032 (2012).

PROPOSAL OF THE DAQ SYSTEM FOR THE BM@N PROJECT

A.Yu.Isupov[a,1], V.P.Ladygin[a], S.G.Reznikov[a]

a) JINR, 141980, Dubna, Moscow region, Russia

Abstract

The proposal of the DAQ architecture for the BM@N setup is described. The requirements to the DAQ, Trigger, and Slow Control hardware suitable for this architecture are issued. The DAQ software will be responsible for the managing of the experimental data transportation and processing. This software implementation is proposed on the base of the *ngdp* (for NetGraph Data Processing) framework, which allows us to:
— use the already implemented OS kernel modules for the data streams handling and control (***netgraph(4)*** package);
— implement the DAQ specific kernel modules in the uniform object–oriented style, which provides the high scalability and the easy remote distribution;
— execute the ***netgraph(4)***–style code out of the regular scheduling scope (with the very high, practically realtime performance);
— reduce the data copying over the context boundaries;
— eliminate the intermediate storages on the media slower than memory.

1. Introduction

The Baryonic Matter at the Nuclotron (BM@N) project is approved in 2012 for the comprehensive technical design report preparation. The present proposal is written in the frame of these efforts. According to the BM@N Letter of Intent the BM@N setup will contain approximately 370000 channels of the front–end electronics (see Table 1). The Au beam intensity of 10^7 Hz and the Au target with 1% nuclear interaction length leads to the mean interactions rate 10^5 Hz. The detectors occupancy from this Table accounts (as the most severe case) the average event multiplicity 164 from the minimal bias collision into the 82.5 msr around the forward direction, excluding 1.4 msr around the beam direction (for T0 — 10^7 Hz Au). This assumption allows us to estimate the average single event size as 44100 bytes and leads to the up to 40 Gbit/s data flow. The transportation of this data bandwidth through the 10 Gbit/s Ethernet requires 4 or more (for 1 Gbit/s Ethernet — more than 40) such Ethernet channels. On the other hand, the whole dataset belonging to some physical event should at some processing stage to appear on the single computer for the full event building. This requirement is true for the each event. So the system should contain more than one Event Builder (EvB) in principle. This fact requires to solve the nontrivial questions related with the data streams organization and management.

The proposed technical design has potential to be used by the larger experiments like MPD, SPD. It seems reasonable to implement and debug both hardware and software components of this design for the BM@N setup to obtain experience with the corresponding technologies. Anyway, the large scale DAQ system design is inevitable step for the upcoming NICA experiments.

[1]E–mail: isupov@moonhe.jinr.ru

Table 1: Data flows estimations

Digitization types legend: T — time, Q — charge, A — amplitude, c — coordinate (=channel number, embedded if we use hptdc).
Per each Ethernet frame 1500 bytes we have overhead: 40 bytes of *ngdp* packet header + 38 bytes Ethernet overhead = 78 bytes (∼6%).

subdet	number of channels / number of stations / number of planes	digitization type	digitization time required, ns	required for precision / really acquired value, bit/channel (assuming hptdc)	dynamic range	detector occupancy (per event per plane)	synchronous trigger producer	synchronous trigger consumer	full data stream, bit per event / Mbit per second (w/o 6% overhead)	channels per board × boards per subdet
T0	64/1/2	T+Q	≤?30	/64×?3 + 32, 16(?8)		100/32	yes	yes	15584+1024 (512) / 1661 [a]	32 × 2
ZDC	300/1/1	A(?Q)	<120..150	/64(32)		1.0	?yes	yes	19200(9600) / 1920(960)	128 × 3
DTE	64/1/1	A(?Q)	<120..150	/64(32)		1.0	?yes	yes	4096(2048) / 410(205)	64 × 1..2
RPC	1200/1/1	T+Q(+c)	≤100	12+?(+0) / ?64(32)	0..64 ns	0.16	yes	yes	12288(6144) / 1229(615)	256 × 5..6
DC	4000/2/8	(c+)T	≤111	(11+)?/?32	0..128 ns	0.66	no	yes	84480 / 8448	256 × 16..20
ST	7000/1/3	(c+)T		(13+)?/?32		≤0.16	no	yes	35904 / 3590	256 × 28..30
Sum:	∼16000								172580/17258	
IT (STS)	350000/4/2 (450000/5/2)	c+A		/ 24+8		0.016	no	could	180000(225280) / 18000(22528)	16384 × (3×8(10))
Sum:	∼370000								352580/35258	

[a] 6% overhead included.

2. Overview

Logically the whole proposed DAQ system for the BM@N setup could be subdivided by the three big subsystems:

- the Data AcQuisition subsystem itself (Fig. 1);
- the Fast Control and Trigger (**FC+T**) subsystem, which intended to produce and handle all the synchronous signals in the setup (Fig. 2);
- the Slow Control (**SC**) subsystem (Fig. 3).

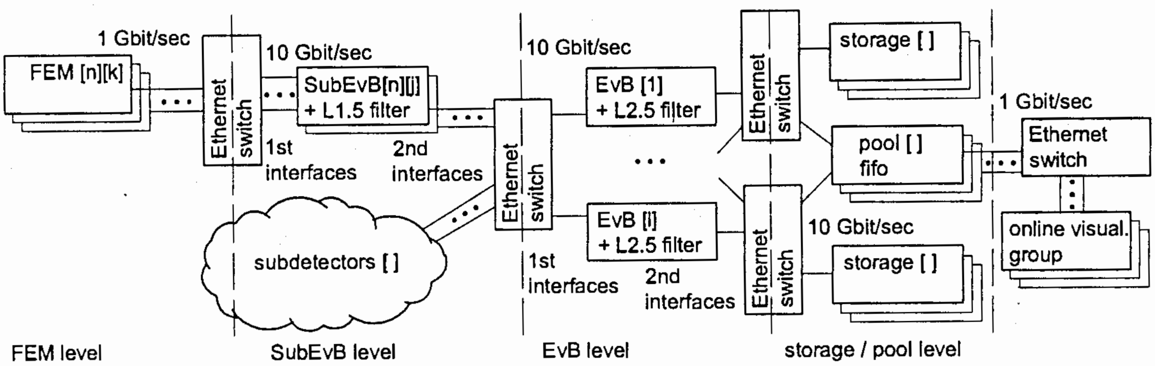

Figure 1: The levels of the DAQ system.

- FEM[n][k] — k-th entity of the n-th subdetector;
- SubEvB[n][j] — j-th computer belonging to the n-th subdetector;
- EvB[l] — l-th computer of the Event Builders level;
- L1.5 — software filter on the SubEvB level;
- L2.5 — software filter on the EvB level;
- pool[] — computers of the pool level;
- storage[] — computers of the storage level.

Of course, the same hardware card or board physically could contain parts of more than one subsystem due to the high electronics integration.

There are many reasons to functionally subdivide the hierarchy of the DAQ hardware units by the logical levels along the data stream, e.g.:

- to formalize and simplify the interactions between the DAQ elements,
- to provide for each subdetector the standalone working mode,
- to allow easy reconfiguration of the active subdetectors' set,
- to allow easy hardware replacement, etc.

We propose, that at least the four logical levels of the data processing (see Fig. 1) are needed:

- FEM level implements at least the queues of ready data fragments produced by the Dig[][] cards;
- SubEvB level — data preprocessing computers grouped by the subdetectors. SubEvB level requests the L1[] trigger packets and the corresponding ready data fragments from the FEM level, merges the sub–events, implements the queues of ready sub–events, and possibly the L1.5[] software filters for the sub–events rejection;
- EvB level – full events building computers. EvB level requests the L1<t> / L2<t> trigger packets and the corresponding ready sub–events from the SubEvB level, merges the full events, implements the queues of ready full events, and possibly the L2.5 software filters for the full events rejection;
- pool level — data postprocessing computers. Pool level requests the ready events subset from the EvB level, converts their from a native binary format to some ROOT

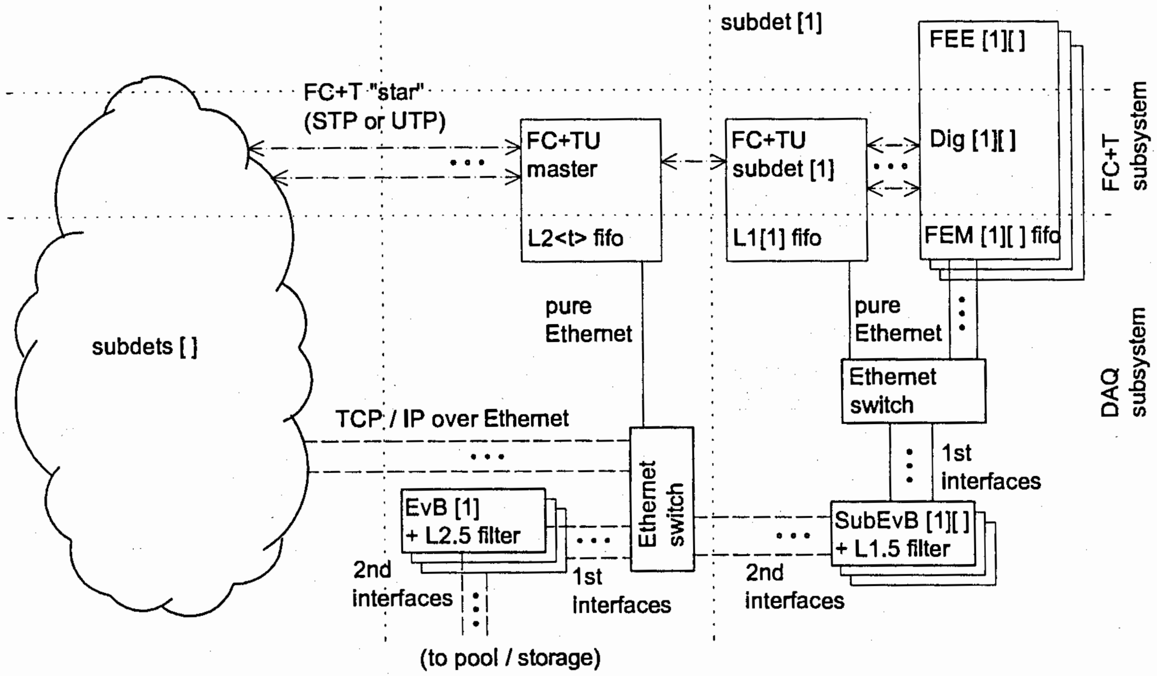

Figure 2: The Fast Control and Trigger (FC+T) subsystem.
• FC+TU — Fast Control and Trigger Unit card, the basic hardware unit of the FC system, which are master (1 per setup) and subdet[n] (1 per n-th subdetector);
• Dig[n][m] — m–th Digitizer card of the n–th subdetector;
• For other elements see legend in Fig. 1.
These elements are interconnected by the:
• dedicated lines of the trigger production ("ascending") path;
• dedicated lines of the trigger distribution ("descending") path;
• "pure" Ethernet lines;
• TCP/IP network over Ethernet lines.

[1] class representation, implements the queues of ROOT events, and provides their to clients for the online analysis and visualization. Also the ROOT events are histogrammed and these histograms are provided to clients for the online analysis and visualization;
• storage level (parallel to the pool level) — computers, which request the ready events from the EvB level and write their into the intermediate (HDD) storage. The storage level consists of some identical computer groups switchable while the data taking, so one group obtains the events from the EvB level while the other groups transfer the obtained data from the intermediate into the final storage, possibly slower than HDD.

Each intermediate level behaves as a server for the downstream level and as a client for the upstream level. This approach simplifies algorithms of inter–level interactions, which will be reduced to the ones only between neighbour levels.

In addition, some computer groups can be outside of the data stream:
• Fast Control and Trigger group — computers, which implement the FC+TU subsystem: trigger queues (see also chapter 4) and the corresponding GUI;
• Slow Control group — computers, which implement the SC subsystem (see also chapter 3) and the corresponding GUI;
• DAQ Operator group — computers, which perform the control over the DAQ software components and provide the user interface for them;

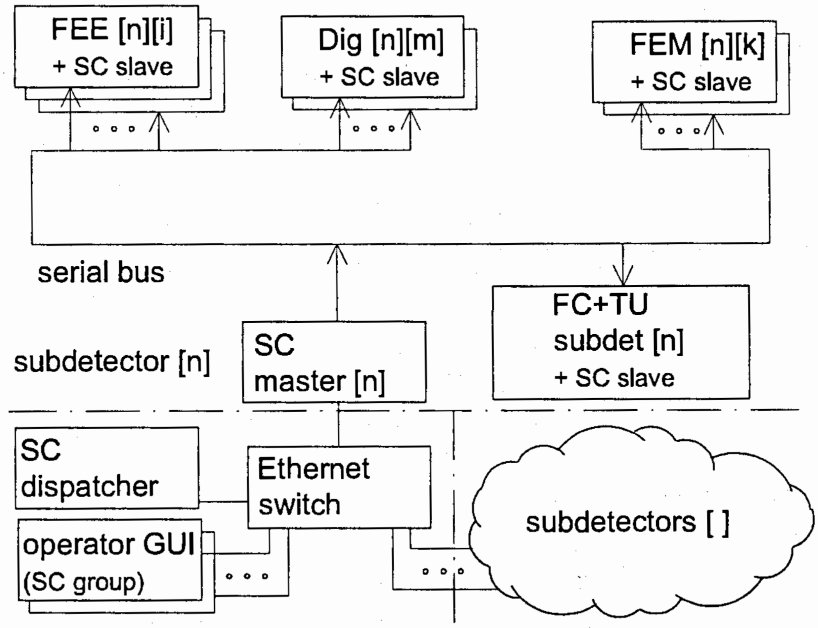

Figure 3: The Slow Control subsystem.

- FEE[n][i] — i-th Front–End Electronic card of the n-th subdetector, which prepares signals for the Dig[n][m] card;
- SC master[n] — Slow Control master card (1 per n-th subdetector), the basic hardware unit of the SC system;
- SC slave — peer part for the SC master (integrated into FEE, Dig, HV/LV, FC+TU cards);
- SC dispatcher — the computer (1 per setup), which obtains the operator GUI requests and forwards ones to the specific SC master[] according to their destination.

- online visualization group — clients of the pool level.

The requirements to the proposed levels are described in chapter 4. Lets also introduce some terms absent in Figs. 1–3 legends:

Packet — the sequence of bytes, which contains the fixed length packet header (with at least the ID string, type, timestamp, number, length, flags, CRC32) followed by the packet body of known length (see [2] and ***packet(3,5,9)***).

Event merging — simple kind of event building, which produces the new output packet to contain sequence of all the input packets (headers are preserved, the ID string reflects the encapsulation level). This operation performed on SubEvB and EvB levels leads to the full event's encapsulation level ≥ 2.

Trigger packet — the packet is produced by the FC+TU master or FC+TU subdet[] card and contains the reliable (sub)event merging tag (number and/or timestamp) for the (Sub)EvB.

Fragment, sub–event, full event — the packets represent the data and are produced by the Dig[][], SubEvB[][], EvB[], correspondingly.

Queue — the software buffer of packets with the FIFO (First In — First Out) nature and some rule set (discipline) of the packets getting.

L1[n], L1<t> / L2<t> **fifo** — queues of the L1[n] or L1<t> / L2<t> trigger packets supplied by the FC+TU subdet[n] or master card, respectively.

3. Hardware requirements

Here we describe requirements to the hardware proposed for development.

Currently we assume for the whole BM@N setup the L1 central synchronous ("live") single-stage trigger to be the only trigger implemented by the hardware. This hardware belongs to the FC+T subsystem. This approach solves the deadtime account issues in the straightforward and clear manner, and allows us to establish the reliable triggers (and *ngdp* data packets) numbering. Such numbering will be simple and single tag (however see also chapter 4) for the (sub)events merging: the data fragments / sub-events will be selected to belong to the same N-th sub-event / full event, if and only if their reliable numbers are match with (i.e. corresponding integers are equal to) the N-th trigger number. The overall architecture of the FC+T subsystem we can see in Fig. 2. With the L1<t> hardware trigger (possibly of some type t) the higher level triggers are assumed to be the software filters on the SubEvB (L1.5[]) and EvB (L2.5) levels.

The whole setup's L1<t> will be assembled from the subdetector's L1[n], while L1[n] — from the Dig[n][] card's preL1[n][] by the hierarchy of analog and/or digital summators (n corresponds to the trigger-producer subdetectors). This hierarchy could be implemented as parts of the FEE[][]s, Dig[][]s and FC+TU subdet[]s (see below), or as independent modules. Former option is preferable in respect of the power solution, cabling arrangement, SC implementation reasons (entia non sunt multiplicanda sine necessitate). The presence of the FC+TU subdet[] instances also allows to operate subdetectors easily in the standalone mode for test, calibration, etc. purposes (setup scalability providing). Currently the trigger-producer subdetectors are T0 (existence of the beam particle), RPC (number of fired pads as the multiplicity characteristic), and ZDC (possibly with DTE) (total energy deposition as the centrality characteristic). The signals sum is discriminated according to the preset trigger conditions by some controlled discriminators, possibly on the FC+TU master card.

The nominal (mean over time) event rate on BM@N equals to the interactions rate 10^5 Hz, i.e. 10 μs per event, during which we should provide the L1 trigger decision. Of course, the beam inhomogeneity in time tightens this requirement to $< 1..2$ μs. This requirement is reachable, if the FPGA processing (the main time consuming part of the trigger production) will be no longer than 0.5 μs (50 cycles at the 100 MHz). Note if we can use the trigger queues on the each involved digitizer chip type (hptdc has one of 16 triggers deep) and their possible trigger latency is > 10 μs (hptdc — up to 25..50 μs), this requirement could be softened.

The proposed FC+T hardware architecture is expected to support also the two-stage L2<t> triggers production. Possibly this will require the Trigger Protocol Messages (TPMs, see below) content expansions (e.g., to carry the reliable timestamps) and assortment additions, (sub)events merging tag change from the reliable numbers to timestamps, etc.

The FC+T subsystem is intended to produce and handle all the synchronous signals in the BM@N setup (L0 clock, L1<t> / L2<t> and L1[n] triggers, etc.), while the FC+TU cards are basic hardware unit of it.

The 40 MHz L0 clock is the single synchronization source for all setup elements — hptdc, FPGA, serdes of the TPMs transfer system, etc.

The **FC+TU master card** (1 per setup) should contain at least:

- 8..16 trigger (TPM) input/output downlink connectors (UTP/STP/optic);

• (at least for the FC+TU subdet[]s) one trigger (TPM) input/output uplink connector (UTP/STP/optic);
• Begin of Burst (BoB) input (and configurable burst length) to be able to produce BoB and End of Burst (EoB) triggers;
• 1 Gbit/s Ethernet port (RJ-45/optic);
• the FPGA, which:
† (re)distributes the direct signals — L0 clock (40 MHz), Reset, etc.;
† analyses the L1[n] trigger (TPM) inputs from FC+TU subdet[]s according to programmable (not wired) rules (trigger "ascending" path);
† produces the L1<t> / L2<t> trigger signals (of some type t) in form of the TPM (see below), delivers ones, and obtains the TPM responses (ackL1<t> / ackL2<t>) synchronously (trigger "descending" path);
† for each L1<t> / L2<t> trigger occurrence produces the trigger packet (of some type t, each packet is the Ethernet frame, which encapsulates the *ngdp* packet), supplies ones to the L1<t> / L2<t> fifo server, and obtains ACK / NAK responses in the same form (through the Ethernet port);
† implements the uniform SC slave (conversation with SC master through the Ethernet port);
• (at least for the FC+TU master) the hardware timeserver (GPS, etc.) with the ability to synchronize the L0 with the absolute time of the accelerator cycle begin and produce the absolute timestamp (struct timespec {sec; nsec}) for each trigger packet;
• the uniform power solution: single input (some of 12, 24, 48 V) and on–board converters;
• solution for the hardware reset (by power switching or FPGA reset).

The trigger *ngdp* packets produced by the FC+TU master should have both the reliable packet number and the absolute timestamp, as well as valid type, length, flags, CRC32 (i.e. the full packet header of 40 bytes), and possibly carry some information in the packet body. The trigger *ngdp* packets are used by the EvB[]s.

The **TPMs assortment** should be like the following:
• FC+TU subdet[n] ← Dig[n][]: preL1[n][] pre-triggers, ackL1 acknowledgments;
• FC+TU master ← FC+TU subdet[]: L1[] trigger, ackL1 acknowledgments;
• FC+TU master → FC+TU subdet[]: L1<t> / L2<t> trigger (of some type: BoB, EoB, some kinds of event), ?ackL1[] acknowledgments;
• FC+TU subdet[n] → Dig[n][]: L1<t> / L2<t> triggers (with types mapped according to FC+TU subdet[n] configuration: localized kinds of event, possibly BoB, EoB, some out of burst tests), ?ackpreL1[n][] pre-trigger acknowledgments.

The ACK / NAK scheme should be used for both the TPM and *ngdp* packet trigger exchange control. This means the future trigger production will be suspended until the proper acknowledgment obtaining. The TPM could be implemented as the fixed length transfer, the front of start bit is the time moment of the trigger (for the trigger input of the hptdc, etc.), the 32-bit value is the reliable trigger number (used by the FPGA), and some (?16) bits for trigger type (BoB, EoB, some kinds of event). (For the timestamps tag scheme of the (sub)events merging the two 32-bit values for sec and nsec should be transmitted by each TPM, too.) All cable lengths should be aligned for the simultaneous TPMs arrival at each FC+TU subdet[] and Dig[][]. Of course, the TPM assortment could be expanded over these mentioned above if needed. It is very likely that the switch to/from the test/imitation/calibration mode, the downscaling factor, BoR and End of Run (EoR), etc. should be distributed as TPMs.

The **FC+TU subdet** [n] (1 per n-th subdetector) should be similar or identical to the FC+TU master one. It:
• redistributes the L0, Reset, etc.;
• redistributes the trigger TPMs (and possibly produces local trigger TPMs: e.g., test/calibration between EoB and BoB) to the Dig[n][] cards (trigger "descending" path);
• analyses the preL1[n][] TPM inputs from Dig[n][] according to programmable (not wired) rules and produces the L1[n] trigger signal in the TPM form, delivers it, and obtains the TPM responses (?ackL1[]) synchronously (trigger "ascending" path);
• (in the reliable numbers tag scheme) for each L1<t> trigger TPM obtained produces the *ngdp* trigger packet with: the same reliable packet number as present in trigger TPM, the mapped type, valid length, flags, CRC32, the same timestamp as present in trigger TPM, or otherwise produced locally by the TPM arrival time;
• (in the timestamps tag scheme) for each L1<t> trigger TPM obtained / L1[n] trigger TPM issued produces the *ngdp* trigger packet with: the same timestamp as present in L1<t> TPM, or otherwise produced locally by the L1[n] TPM issuing time, the mapped type, valid locally produced number, length, flags, CRC32;
• supplies these packets to the L1[n] fifo server (or trigger input channel buffers of the SubEvB[n][]s) (through the Ethernet port).

The **Dig cards** are intended to the digital data preparation for the lower entities (FEM queues) of the DAQ subsystem. Such data (and possibly error) fragments are produced in form of the Ethernet frame, which encapsulates the *ngdp* packet with the full valid header of 40 bytes and the body, which contains the data fragment itself. Types for both data and error fragments (packets) are online configurable 16-bit constant integer offsets relative to the trigger TPM type values.

The Dig[][] hardware is responsible to produce the binary data in the reasonably compact format. Probably for the calorimeters (ZDC, DTE) we need the charge value only, so in the Q2T scheme the common FPGA of Dig cards should calculate the difference between trailing and leading signal edges, i.e. produce 32 bits per hit instead of 64 ones preserving the same precision 100 ps/bin.

The Dig cards location on setup is probably near the corresponding subdetector (1..3 m), while its shape should be suitable for both the Euromechanics crate (6U/9U) and standalone positioning.

The Dig cards use some ready digitization chips: hptdc [3] (TDC, QDC through Q2T conversion), n–XYTER or something other (coordinate), etc. under the common FPGA control, so it is possible to have a very few (2..3) slightly different Dig card types per BM@N setup. The common requirements for each of these types are to contain:
• connectors (with or without cables) or conductors (on the same printed circuit) to input data signals from the FEEs;
• the FC slave implementation in the common FPGA (see below for details);
• connector(s) (1 Gbit/s Ethernet) for the bidirectional conversations under the FPGA control:
† output — *ngdp*-packetized digital data fragments with the nanosecond precision timestamp (to FEM fifo), possibly SC responses (to SC master), etc.;
† input — backward ACK / NAK *ngdp* control packets to acknowledge the data fragments acception (from FEM fifo), possibly SC commands (from SC master), etc.;
• the uniform SC slave implemented by the common FPGA;
• the means to support the test/imitation/calibration mode (not yet understood in

details, however should not be forgotten);
• the uniform power input (some of 12, 24, 48 V) and on–board converters;
• solution for the hardware reset (by power switching or FPGA reset).

In respect of the FC+T subsystem the Dig cards should contain also:
• up to 8 signals sum inputs (UTP/STP/optic for digital) from the FEE[][]s;
• one trigger (TPM) input/output uplink connector (UTP/STP/optic);
• the common FPGA should in particular implement:
† the digital summator to produce the preL1[n][] TPMs (as part of the trigger production "ascending" path);
† the L1[] trigger TPM obtaining and the ackL1 acknowledge TPM sending (trigger "descending" path);
† the different behaviour at arrival the different trigger TPM types (BoB/EoB, some kinds of event or test / calibration);
† the data fragments production (see above), where the *ngdp* packet has: the body, which contains the data fragment itself, and the full packet header of 40 bytes, namely:
* (in the reliable numbers tag scheme) the reliable packet number (from the L1<t> trigger TPM), timestamp (from the trigger TPM, if present, or otherwise produced locally by TPM arrival time), type mapped according to Dig[n][] configuration, valid length, flags, CRC32;
* (in the timestamps tag scheme) the timestamp (from trigger L1<t> TPM, if present, or otherwise produced locally by theL1[n] TPM arrival time), type mapped according to Dig[n][] configuration, valid length, number (locally produced), flags, CRC32.

The Dig card with hptdc chips for the TDC and QDC is probably suitable for work with all but the STS subdetector and could be considered now in details.

The maximal capacity of the hptdc read–out token ring is 16 chips, so we can have no more than 512 channels per Dig card. However the reasonable size of the Dig card (6U) as well as the data flow issues (see below) restricts us by 8 hptdc chips (256/64 channels in 100/25 ps/bin modes). To reduce the data flow we should not produce the local (slave) header and trailer hptdc words. Some subdetector variants of the hptdc handling should be used:
• RPC mode: leading and trailing edges (100 or ?25 ps/bin), 64 bit/hit;
• T0 mode: leading and trailing edges (25 ps/bin), 64 bit/hit, without hptdc trigger matching ;
• Q2T mode: leading and trailing edges (100 ps/bin), 64 bit/hit, or with subtraction by the common FPGA, 32 bit/hit;
• DC/ST mode: leading edge (100 ps/bin) + width (more rough like 1.6 ns/bin), 32 bit/hit.

The common FPGA of the Dig card should for each obtained trigger TPM:
† read–out and buffer the data fragment according to the trigger TPM type for further Ethernet transfer,
† account the data fragment length;
† save the data fragment nanosecond timestamp (number of L0 clock pulses from start multiplied by 25), it is assumed the times for the same trigger in different hptdc are differ no more than by single L0 clock;
† fill in the 40 bytes of the *ngdp* packet header and store it in the 0th..9th words of the buffer;
† produce the summary error word using all encountered hptdc error words (if any, or fill by zeros otherwise) and store it in the 10th word of the buffer;

† produce the data fragment packet mentioned above;
† (as the online configurable option) produce separate packet of all hptdc error words, if their are encountered for current trigger.

We assume the data fragment should always be carried by single Ethernet frame to avoid the nontrivial reassembling algorithms on the obtaining side (FEM fifo). So, the data buffer size should be $\leq$ MTU = 1500 bytes, i.e. $\leq$ 187.5 bytes per event per chip. Note the maximal hits number per event could be enforced by the hptdc as power of 2, so we can guarantee that for each event the data fragment will fit into the single Ethernet frame. With up to $2^5(2^4$ for 64-bit hits) hits/event/chip the data of $(2^5 \times 8 + 2) \times 4 = 1032$ bytes $(2^4 \times 8 \times 8 + 2 \times 4 = 1032$ bytes) accompanied by the *ngdp* and Ethernet overheads of 40 and 38 bytes at the events rate of 10^5 Hz leads to the data flow of up to yet acceptable 888 Mbit/s.

The alternative for the hptdc usage is the TDC implementation on base of the dedicated FPGAs.

Probably the T0 Dig card should have the separate version of the FPGA firmware to produce also both hit counts per each trigger[2] and per each time slice (of the configurable duration, 5..10000 μs) for each T0 channel. This will require to perform the trigger matching (in the hptdc manner with configurable trigger latency and time window) by the Dig FPGA itself, because each produced hit (i.e. detected beam particle) should be evaluated for these counts calculation. At least the following trigger TPMs should be recognized: BoB, EoB, some kinds of event.

The **FEE cards** are intended to the signals (possibly always logical: LVDS / LVTTL) preparation for the Dig card. The FEE cards are located on the corresponding subdetector and possibly do not require the crate-suitable shape.

The FEE cards are specific for the serviced subdetector (here we can not essentially reduce entities to be designed), however in general each of them should contain and implement:
• the uniform SC slave (or be controlled through Dig);
• the means to support the test/imitation/calibration mode;
• the means to feed output signals to the Dig card(s);
• power supply: the uniform power input (some of 12, 24, 48 V) and on–board converters (or obtains the ready voltages from the Dig card);
• solution for the hardware reset (by power switching or FPGA reset).

In respect of the FC+T subsystem the FEE cards should provide:
• the branching of the analog signals from the detector to feed both the main (digitization) dataway and the trigger production "ascending" path;
• the analog (?or digital) summator, ADC, and single digital output as part of the trigger production path.

The FEE cards in the TDC chains probably will use the NINO chips [4] to produce the logical output signals for the hptdc [3].

The FEE cards in the QDC chains probably will use the Q2T converters to produce the logical output signals for the hptdc, too.

All the **SC master units** (typically 1 per n-th subdetector, see Fig. 3) should be similar or identical and contain at least:
• the standalone or Single Board computer (SBC, see also below): 1 Gbit/s Ethernet,

[2]Really between BoB and the first trigger, between two consequent ones, and between the last one and EoB.

network bootable (PXE), optional local flash memory as the permanent storage, the proper heat sink by the low–profile passive cooler;
• the means to converse (connector of Ethernet and/or some standard serial bus (RS-485, etc.)) with SC slave parts;
• the uniform power input (some of 12, 24, 48 V) and on–board converters to ATX voltages.

All the hardware **SC slaves** embedded into the FEE, Dig, HV/LV, FC+TU cards should be uniform, i.e. contain the same connector(s) and intellect (FPGA, etc.), which implements the same protocol. The only SC function should be hardware implemented for the SubEvB, EvB level computers is a remote reset solution (by power switching or motherboard reset).

Also we should choose a **hardware architecture of the standalone computers** to be used in all but FEM levels of the DAQ system and for the DAQ software design and implementation purposes. On the one hand, we have no special requirements to these computers hardware — other than performance and reliability. On the other hand, the big DAQ system can require from tens to some hundreds of units of such hardware with corresponding maintenance, etc. So, we should choose the most standard and generic hardware reasonably cheap due to a great volume of production. This architecture is called `AMD64/EM64T`, previously known also as `x86-64` and `IA-32e`, and should be used currently and in the near future. For the embedded SBCs involved in the BM@N DAQ they will be very desirable to have the same architecture (or the 32–bit `x86`). Note the SBC is preferable over the System–on–Chip (SoC) due to flexibility, replaceability, low integration efforts (printed circuit design is not required).

4. Software requirements

The operating system (OS) used on the online computers determines the DAQ system design and organization, consequently the inadequate OS selection is sure to strongly complicate implementation, maintenance, and using of the DAQ system. The OS itself should have adequate technical abilities for easy multiple installations, remote maintenance and backup, read–only boot filesystem and diskless network boot, boot without input and output devices, easy and centralized startup customization, etc.

UNIX–like OSs are optimal for the above requirements. UNIX is a multiprocess and multiuser OS with powerful mechanisms for interprocess and inter–computer communications, a very advanced virtual memory subsystem, support of sophisticated networking and graphics interfaces, extended tools for the software design. Costs for UNIX working itself are practically negligible on the modern hardware. Availability of the OS sources is a mandatory requirement for the present developments, while the freely distributable nature of some UNIX–like OSs is highly desirable. After all, high portability of UNIX programming and approximately unlimited quantity of the existing software are also very attractive.

To achieve the reasonable performance, we should choose C programming language (or C++ — only in such cases, where we can neither avoid an object–oriented design nor implement it using C) and ultimately avoid interpreted languages like Perl or CINT.

Because the FPGA firmware responsibilities are described above, here we formulate our requirements to the DAQ software modules only, which should be executed by CPUs of the standalone computers and/or SBCs.

In the proposed design we could use two **(sub)events merging schemes** based on the reliable trigger numbers or the timestamps as the (sub)event merging tags. The former is suitable for the central L1<t> trigger only, while the latter — for any trigger architecture, however requires more expensive TPMs for timestamps propagation from the FC+TU master in the central L1<t> case. In case of the two-stage L2<t> trigger the timestamp is the only possible merging tag, however should be produced locally by each Dig card instead of propagated from the FC+TU master. Anyway, the synchronization issues should be addressed by the FC+T subsystem. Note the packet queues implementation seems to be simpler for the timestamping scheme (see chapter 5 for details). Anyway we require the proper merging tag to be present on the each produced data fragment / sub-event and trigger packet. For the timestamps tag this means each data fragment packet should be timestamped by the Dig with the enough (practically nanosecond) precision: really ones could be the 64–bit numbers of the L0 clock pulses[3] from some start time moment (e.g., BoB), for which the absolute time ats with the nanosecond precision is saved (in the struct timespec form) by the FC+TU master.

The fragment searching in the queues by the corresponding merging tag will be the only method to obtain all the fragments belonging to each the full event. For the reliable numbers the correspondence means their equality. For the timestamping it is the falling of the data fragment timestamp tsd into the time window, defined by the reference timestamp ts, parameter twin, and twin's usage policy. For example, for BOTH policy the $\texttt{ts}-\texttt{twin} \leq \texttt{tsd} \leq \texttt{ts}+\texttt{twin}$ means tsd is corresponded to the reference ts. The time window possibly should be: $\texttt{twin} \leq 1/(2F_{\mathrm{L0}})$ s, namely ≤ 12.5 ns for the clock L0 with $F_{\mathrm{L0}} = 40$ MHz frequency. After merging the sub-events are stamped by the reference timestamp ts of the L1[n] trigger packet, while the full events — by the absolute event time $\texttt{ets} = \texttt{ats}+\texttt{ts}$, where ts is the reference timestamp of the L1<t> / L2<t> trigger packet and the described above ats is carried in the L1<t> / L2<t> packet body. Anyway the strictly no more than one L1<t> / L2<t> trigger instance should be produced for each L0 clock pulse, because otherwise we will have uncertainty in the full event merging. The same sub–event could be collected into ≥ 1 full event(s), if this required by the L1<t> / L2<t> triggers of the different types t. Alternatively (not so easy to implement) the trigger of type t, which represents the more complicated conditions (i.e., more sophisticated and rare physical event), should have precedence over the simpler ones in the L1<t> / L2<t> production to resolve EvB[]s competition for the same sub–events. On the other hand, the most simple L1<t> / L2<t> trigger type could appear as often as the L0 clock. This means, in principle (too huge data flow should be processed!) we can exploit the whole setup in the almost free–streaming mode to accept any hits in the inner tracker.

The software on the L1[n] **fifo server** will behave as follows:

• some driver in the OS kernel:

† for each Ethernet frame arrival from the FC+TU subdet[n] card on the dedicated interface decodes this frame and obtains the trigger packet, which carries the merging tag (i.e. it is reliably numbered and/or timestamped with the nanosecond precision);

† puts this packet into the tail of L1[n] queue in the OS kernel;

• this queue:

† answers the SubEvB[n][] client(s) requests by sending the next packet of the corresponding type from the queue, or by sending the answer packet in the absence case;

† responds by ACK / NAK packets to the FC+TU subdet[n] card to propagate the "full" state on the lower DAQ levels and prevent the queue overfull;

[3]L0 pulse counts of 40 MHz possibly should be multiplied by 25 to express time in nanoseconds.

† supports the garbage collection to remove from the queue packets, which already obtained by all the connected clients;
† supports the queue cleaning — full or on the packet type basis.

The software of the **FEM fifo** will behave as follows:

• some driver in the OS kernel:
† for each Ethernet frame arrival from the Dig[][] card on the dedicated interface decodes this frame and obtains the data fragment packet, which is reliably numbered and/or timestamped with the nanosecond precision;
† puts this fragment into the tail of FEM queue in the OS kernel;
• this queue:
† answers the SubEvB[n][] client(s) requests by sending the data fragment(s) of the corresponding type and number (and/or timestamp) from the queue, or by sending the answer packet in the absence case;
† responds by ACK / NAK packets to the Dig[n][] card to propagate the "full" state on the lower DAQ levels and prevent the queue overfull;
† supports the queue cleaning — full or on the packet type basis.

The software on the L1<t> / L2<t> **fifo server** will behave as follows:

• some driver in the OS kernel:
† for each Ethernet frame arrival from the FC+TU master card on the dedicated interface decodes this frame and obtains the trigger packet, which is reliably numbered and/or timestamped with the nanosecond precision;
† puts this packet into the tail of L1<t> / L2<t> queue in the OS kernel;
• this queue:
† answers the EvB[] clients requests by sending the next packet of the corresponding type from the queue, or by sending the answer packet in the absence case;
† responds by ACK / NAK packets to the FC+TU master card to propagate the "full" state on the lower DAQ levels and prevent the queue overfull;
† supports the queue cleaning — full or on the packet type basis.

The software on the **SubEvB[n][] computers** will behave as follows:

• sub-event merger entity in the OS kernel:
† requests the FEM queues for data fragments and L1[n] queue for trigger packets according to own configuration, obtains their, matches merging tags, and merges packets to produce the sub-event packet;
† puts this packet into the tail of SubEvB[n][] queue in the OS kernel, possibly through some filter facility, which implements the L1.5[n] software trigger;
• this queue:
† answers the EvB[] clients requests by sending the sub–event of the corresponding type from the queue, or by sending the answer packet in the absence case;
† responds by ACK / NAK packets to the sub-event merger to propagate the "full" state on the lower DAQ levels and prevent the queue overfull;
† supports the queue cleaning — full or on the packet type basis.

The software on the **EvB[] computers** will behave as follows:

• full event merger entity in the OS kernel:
† requests the L1<t> / L2<t> queue for trigger packets and SubEvB[][] queues for sub-events according to own configuration, obtains their, matches merging tags, and merges packets to produce the full event packet;
† puts this packet into the tail of EvB[] queue in the OS kernel, possibly through some filter facility, which implements the L2.5 software trigger;

• this queue:
† answers the pool[] client(s) requests by sending each N–th full event of the corresponding type from the queue (this packet is kept in the queue for the storage client), or by sending the answer packet in the absence case;
† answers the storage[] client requests by sending the next full event of the corresponding type from the queue (this packet is removed from the queue), or by sending the answer packet in the absence case;
† responds by ACK / NAK packets to the event merger to propagate the "full" state on the lower DAQ levels and prevent the queue overfull;
† supports the queue cleaning — full or on the packet type basis.

The software on the **pool[] computers** will behave as follows:
• event pool entity in the OS kernel:
requests the EvB[] queues for the representative subset of full events according to own configuration, obtains these full events, and puts into the tail of pool[] queue in the OS kernel through the filter facility;
• this filter:
converts each of these full event packets into the representation by the corresponding ROOT class, which is serialized and packetized again;
• this queue:
† answers the visualization group client(s) requests by sending the next ROOT packet of the corresponding type from the queue (this packet is kept in the queue for other clients), or by sending the answer packet in the absence case;
† supports the garbage collection to remove from the queue packets, which are already obtained by all the connected clients;
† supports the queue cleaning — full or on the packet type basis;
† provides two policies of the full queue handling: the cleaning of the oldest possibly not yet read packet (default) and the newcomer packet dropping.

For the proposed histogramming server and client see chapter 5.

The **storage[] computers** possibly should be equipped by:
• the ***writer(1)*** utility [2];
• some network demultiplexer with the requests sending ability like the pool entity described above (possibly ported into the user context) to feed ***writer(1)***.

In Fig. 3 we can see main elements of the SC subsystem. The SC dispatcher and SC master[]s should contain CPUs and execute **SC software**. The SC dispatcher obtains operator commands from the operator GUI and forwards their to the specific subdetector's SC master[], which interacts with SC slaves to perform the corresponding actions. The correspondence between operator command and actions to be performed is established by the SC master[] local configuration. The remote network interactions between SC elements should be implemented by the standard client-server model (possibly using RPC) over TCP/IP or UDP/IP.

The SC slaves integrated into FEE, Dig, HV/LV, FC+TU cards are controlled by their firmware, while on SubEvB, EvB computers the SC slaves should be implemented by software (with exclusion of the remote reset solution, see chapter 3).

5. Software implementation

The key features of the proposed DAQ software, which are natural for the UNIX–like OS, are the following:
• splitting into the software modules interconnected by the experimental data streams;

• spreading of these modules over CPUs and networked computers easily;
• experimental data representation in the unified form of *ngdp* packets (see [2] and ***packet(3,5,9)***);
• experimental data transportation by the streams of these packets, which (without using the media slower than memory) can:
† be buffered, copied, filtered, demultiplexed in a different manner;
† to cross the context boundaries from the kernel space to the user one and vice versa;
† be transferred between software modules locally and/or remotely, etc.
• software modules implementation in form of the user context processes or, in the kernel context, — the so called loadable kernel modules (KLD);
• implementation of the packet streams between the processes:
† locally — by the unnamed pipes and
† remotely — by the TCP/IP socket pairs;
• using the kernel threads to implement the process–like activity in the kernel context allows us:
† to avoid the preemptive scheduling;
† to reduce the unnecessary data copying in the memory at the context boundary crossing;
• using the ***netgraph(4)*** package [5] to implement the packet streams between the ***netgraph(4)***-style kernel modules (nodes):
† locally — by the ***netgraph(4)*** data messages along the graph edges and
† remotely — by the TCP/IP ***ng_ksocket(4)*** pairs;
• high and easy scalability due to the object–oriented programming (OOP) style of the ***netgraph(4)*** package.

One of the freely distributable open source UNIX–like OSs with the ***netgraph(4)*** support, enough stable, reliable, modern, and dynamically developed simultaneously due to its very weighted up design policy, is FreeBSD.

The *netgraph(4)* package [5] provides the following entities of our interest:
• ***ng_ksocket(4)*** socket for the remote data exchange by IP protocol (TCP, UDP, etc.);
• ***ng_ether(4)*** interface for the remote data exchange by Ethernet protocol;
• ***ng_socket(4)*** socket for data and control messages interchange between the kernel context graph and the user context process;
• means for building the graph itself: ***ngctl(8)***, ***nghook(8)*** utilities;
• service nodes for data flow managing: ***ng_tee(4)***, ***ng_one2many(4)***, ***ng_split(4)***;
• nodes for debugging: ***ng_source(4)***, ***ng_hole(4)***, ***ng_echo(4)***.

The ***netgraph(4)*** could be improved [6] in some aspects:
• the remote delivering of the ***netgraph(4)*** control messages is introduced;
• the function for the node insertion between the two already connected nodes is implemented (very useful for the software filters implementation);
• some additions for the ***ngctl(8)***'s scripting language are implemented;
• the maximum data message size could be tuned by changing some OS kernel variables (without the kernel recompile).

The *ngdp* framework [6] was implemented to be used for a big DAQ system software building and provides the following ***netgraph(4)***-style node types:
• ***ng_fifo(4)*** supports the packets buffer with some queuing disciplines;
• ***ng_em(4)*** implements the SubEvB and EvB algorithms of the event merging;
• ***ng_pool(4)*** implements the pool level functionality according to the above require-

ments (see chapter 4);
• ***ng_filter(4)*** supports (chain of) KLD plug–in(s) with the filter procedure(s) and/or the external filter implemented by the (pipe of) user context process(es) or the (chain of) netgraph node(s);
• ***ng_defrag(4)*** reassembles the big *ngdp* packets obtained from the ***ng_ksocket(4)*** after passing through network, which unavoidably fragments their to fit into the TCP/IP packets;
• ***ng_mm(4)*** (for Memory Mapping) provides the more efficient mechanism for the *ngdp* packets exchange between the kernel context graph and the user context process as the alternative to the standard ***ng_socket(4)***;
• ***ng_sv(4)*** (for SuperVisor) delivers the ***netgraph(4)*** control messages remotely, also could be used to automatize the remote ***netgraph(4)*** graph building;
• ***ng_mysource(4)*** and ***ng_kthsource(4)*** produce the packets stream for debugging.
The *ngdp* framework provides the following user context utilities:
• ***ngput(1)*** injects the ***pipe(2)***d packets into the graph;
• ***ngget(1)*** extracts the packets from the graph into the ***pipe(2)***;
• ***b2r(1)*** (for "binary–to–ROOT") converts the packetized binary data into the packetized ROOT class instances;
• ***r2h(1)*** (for "ROOT–to–histograms") is the runtime configurable histogramming server;
• ***histGUI(1)*** is the client for the ***r2h(1)***.

As we can see from the chapter 4 requirements, the SubEvB, EvB, and pool levels could be implemented by the very similar graphs like the following:

```
ng_ksocket ↘                                                      ↗ ng_ksocket
...             ng_em(ng_pool) → [ ng_filter → [...]] ng_fifo          ...
ng_ksocket ↗                                                      ↘ ng_ksocket
```

Of course, the queue and event merger nodes functionalities are slightly variated on the different levels. The FEM fifo as well as the `L1[n]` and `L1<t>` / `L2<t>` queues on the dedicated network nodes could be represented by the following scheme:

```
                       ↗ ng_ksocket
ng_ether →  ng_fifo       ...
                       ↘ ng_ksocket
```

For SubEvB level there is also option to implement FEM and `L1[n]` queues as the input channels of the event merger and, subsequently, use more fast medium (memory instead of network) to request and obtain the data packets, which should provide some performance benefit. This will lead to the following scheme, which requires to implement some configurable multiplexor `ng_mux` and essentially revise the event merger to be `ng_eml`:

```
            ↘                                               ↗ ng_ksocket
ng_ether → ng_mux → ng_eml → [ ng_filter → [...]] ng_fifo      ...
            ↗                                               ↘ ng_ksocket
```

The further details about the *ngdp* provided entities can be found in [6, 7].

The **queue node type** (let it name as ***ng_fifo(4)***) according to the chapter 4 requirements could be implemented with two mutually exclusive assumptions about the (sub)event merging tag will be used, namely:
• the reliable packet numbers. This requires the following modes (i.e. buffer disciplines) of the packet extraction from the queue:
† "N": provides packet of the defined type `type`: `GETPACK(type)`. Needed by `L1<t>` /

L2<t>, EvB, and pool queues.
† "T": provides packet of the defined type type without removing it from the queue: COPYTRIG(type). Needed by L1[n] queue, if it is not embedded into SubEvB, otherwise replaced by "N".
† "G": provides packet of the defined type type by its number num: GETNTHPACK(num,type). Needed by FEM and SubEvB queues.
† "O": provides one of each N^{th} packets of the defined type type without removing it from the queue: COPY1OFN(N,type). Needed by EvB and pool queues.
• the timestamps. This requires the following buffer disciplines:
† "N". Needed by L1<t> / L2<t>, EvB, and pool queues.
† "T": provides packet of the defined type type without removing it from the queue: COPYTRIG(type). Needed by L1[n] queue if it is not embedded into SubEvB, otherwise replaced by "N".
† "S": provides packet(s) of the defined type type from the time window [ts−twin, ts+twin]: GETTSPACK(ts,twin,type). Needed by FEM and SubEvB queues.
† "O". Needed by EvB and pool queues.

Both "nNTGO" [6] and "NTSO" set of the buffer disciplines are implemented now by two separate versions of ***ng_fifo(4)*** node type. It seems the latter one is more simple.

The FEM level could be partially based on the CAMAC hardware. For the CAMAC hardware the number of DAQs are already built in this way using the *camac* package [8] and the ***ng_camacsrc(4)*** node [7] from the *ngdp* framework, e.g., SPILL DAQ, QUADRO DAQ [9], and IntTarg CDAQ [10], [11]. DAQ architectures like these are practically ready for the BM@N DAQ integration.

The **event merger** ***ng_em(4)*** for both the SubEvB and EvB levels should work very similar for the timestamps merging tag scheme. The "SubEvBT" mode should (with some simplifications) behave as follows. The ***ng_em(4)*** node makes one loop over the configured merging rules (and corresponding requests) array and launches the kernel thread (see ***kthread(9)***) for each configured index, so each thread serves only its "own" request. Each request has the so called trigger input channel and is handled in two phases:
• In the first (Trig) phase each thread emits the COPYTRIG(type) ("T") control packet to the L1[n] trigger fifo through the hook of the trigger input channel and waits for a positive or negative response up to obtaining one or corresponding (trigger) timeout expiration. If the answer packet is obtained, the thread analyses the error code and repeats the request after either the same or increased trigger timeout. If the trigger input channel does not respond at all before the trigger timeout expiration, the thread repeats the request and waits during the increased trigger timeout. The trigger timeout can be increased up to the limit only. If the data packet from the L1[n] trigger fifo is successfully obtained, the ***ng_em(4)*** node extracts the ts timestamp[4] and goes to the second phase, which for each request index is handled by the same thread as the first phase. Note the FEM and L1[n] queues implementation as the SubEvB input channels will simplify this behaviour and replace the "T" request by the "N" one, however leads to essentially revised node type ng_eml (not implemented yet) and very high requirements to the memory size available for SubEvB.
• In the second (afterTrig) phase the thread emits the GETTSPACK(ts, twin, type) ("S") control packets to the FEM queues through all the hooks of the involved input

[4] T type is also extracted and checked against the resulting type of the corresponding merging rule.

channels (other than trigger one) using the `ts` trigger timestamp obtained in first phase. After that each thread waits for positive and/or negative responses up to obtaining all the required packets or regular timeout expiration. If all the required data packets are obtained, the ***ng_em(4)*** node merges their (preserving the headers) into the sub-event packet of resulting type and with the number and timestamp of the trigger packet, and sends it to the `output` hook, if it exists, or drops packet otherwise.
After that the thread sets a regular timeout to the nominal value, sends the full request again, and so on.

The "EvBT" mode for the timestamps merging tag uses the `L1<t>` / `L2<t>` fifo server in the trigger input channel and requests it by the `GETPACK(type)` ("`N`") control packets, while the regular inputs — by the `GETTSPACK(ts,twin,type)` ("`S`") ones like the "SubEvBT" mode.

For the reliable numbers tag merging we have two-phase "EvBt" algorithm (like described in [6]) with "`N`" trigger and "`G`" regular requests. The SubEvB algorithm could be implemented as the single-phase "SubEvBt" one (see [6]), where `L1[n]` fifo has not dedicated meanings (it is simply one of the FEM queues, which requested by "`N`"), or like the two-phase "SubEvBT" algorithm described above, however uses the afterTrig phase "`G`" requests. The latter option seems preferable, because the two-phase algorithm should be more robust and less CPU-intensive. Anyway the existing ***ng_em(4)*** implementation [6] should be revised for BM@N purposes.

The *ngdp* framework implements the **pool level functionality** by the ***ng_pool(4)*** node separately from the very similar ***ng_em(4)***. The existing ***ng_pool(4)*** algorithm [6] seems suitable for us. The production of the events in a ROOT class representation from the full events in a native binary format will be done by the ***ng_filter(4)*** node type using the ***b2r(1)*** utility [7].

The ***r2h(1)*** **histogramming server** [7] could be executed to fill the ROOT histograms from the ROOT events. The ***r2h(1)*** could be fed by some network demultiplexer with the requests sending ability (e.g. the pool node ***ng_pool(4)***), as it proposed above for the ***writer(1)***.

The ***r2h(1)*** histograms assortment and parameters could be online configured using the ***histGUI(1)*** histogram visualization client [7] with the read–write access. This (single per server) client as well as many read–only ***histGUI(1)*** clients will be executed on the visualization group computers.

Note also some entities are inherited by the *ngdp* from the *qdpb* framework [2]:
• the application program interfaces (APIs):
† the ***packet(3,9)*** for the packet making, reading, writing, merging, etc.
† the ***pack_types(3)*** to deal with the packet types and corresponding attributes;
• the ***writer(1)*** utility to write the packet stream as the regular files on the HDD.
Some improvements for our needs are possible:
• the packet header could be improved by enlarging some existing fields and introducing the new ones (without keeping the backward compatibility);
• the packet body compression by the *zlib* or XZ Embedded package could be provided.

6. Conclusions

The basic principles and overall architecture of the DAQ system for the BM@N setup are described. The requirements to the DAQ, Trigger, and Slow Control hardware suitable for this architecture are issued. The *ngdp* framework [6, 7] seems to be suitable for needs of the BM@N DAQ due to the high scalability, easy remote distribution, and the high performance of execution out of the scheduling scope. The *ngdp* nodes implementation should be adopted for the event merging scheme, which will be chosen. Possibly the present design can be used also by the upcoming NICA experiments, so the essential experience can be obtained during implementation and debugging of the proposed hardware and software.

Acknowledgments

The authors have a pleasure to thank T.A.Vasiliev for the very preliminary simulation results about the BM@N subdetectors occupancy and S.N.Basilev for the fruitful discussions about the hardware DAQ part.

References

[1] R. Brun and F. Rademakers. ROOT – An Object Oriented Data Analysis Framework. In *Proc. of the AIHENP'96 Workshop*, volume **A**(389) of Nucl.Instr.and Meth.in Phys.Res. (1997), pages 81–86, Lausanne, Switzerland, (1996). See also `http://root.cern.ch/`.

[2] K. I. Gritsaj and A. Yu. Isupov. A Trial of Distributed Portable Data Acquisition and Processing System Implementation: the *qdpb* – Data Processing with Branchpoints. JINR Communications, **E10–2001–116**, 1–19, (2001).

[3] J.Christiansen. *HPTDC. High Performance Time to Digital Converter. Ver.2.2 for HPTDC ver.1.3.* CERN/EP-MIC, March (2004).

[4] F.Anghinolfi et al. NINO, an ultra-fast, low-power, front-end amplifier discriminator for the Time-of-Flight detector in ALICE experiment. IEEE Trans. Nucl. Science, **51**(5), 1974–1978, (2004).

[5] `http://www.freebsd.org/cgi/man.cgi?query=netgraph&sektion=4` (2008).

[6] A. Yu. Isupov. The *ngdp* framework for data acquisition systems. JINR Communications, **E10–2010–34**, 1–20, (2010).

[7] A. Yu. Isupov. CAMAC subsystem and user context utilities in *ngdp* framework. JINR Communications, **E10–2010–35**, 1–20, (2010).

[8] K. I. Gritsaj and V. G. Olshevsky. Software package for work with CAMAC in Operating system FreeBSD (in Russian). JINR Communications, **P10–98–163**, 1–16, (1998).

[9] A. Yu. Isupov, V. E. Kovtun, and A. G. Foshchan. Implementation trial of the DAQ system for the compact physics setup on base of the *ngdp* framework (in Russian). In A. K. Vlasnikov, editor, *Fundamental problems and applications of nuclear physics: from space to nanotechnologies. Book of Abstracts*, 59 International Meeting on Nuclear Spectroscopy and Nuclear Structure (NUCLEUS-2009), page 346, Cheboksary, Russia, (2009). Saint-Petersburg, 2009.

[10] A. Yu. Isupov. New software of the control and data acquisition system for the Nuclotron internal target station. JINR Communications, **E10–2012–32**, 1–20, (2012).

[11] A. Yu. Isupov, V. A. Krasnov, V. P. Ladygin, S. M. Piyadin, and S. G. Reznikov. The Nuclotron Internal Target Control and Data Acquisition System. Nucl. Instr. and Meth. in Phys. Res., **A**(698), 127–134, (2013).

RELATIVISTIC PARTICLES PRODUCED IN ^{197}Au INDUCED NUCLEAR COLLISIONS AT 11.6 A GeV/c

S. Vokál[a,1] and J. Vrláková[a]

a) Faculty of Science, P. J. Šafárik University, Košice, Slovakia

Abstract

The angular structures of relativistic particles produced in $^{197}Au + Ag(Br)$ collisions in emulsion detector at 11.6 AGeV/c have been studied. Two different methods of analysis have been used - a scaled factorial moments and parameter S_2. An evidence for nonstatistical fluctuations has been shown using the method of scaled factorial moments in pseudorapidity phase space. The comparative study has been done for different beam energies and masses and $Au + Em$ events with different degree of centrality. No clear minimum has been found in the dependence of intermittency parameter λ_q on q. Inverse dependence of the parameter φ_2 on pseudorapidity density was confirmed. The nonstatistical ring-like structures of produced particles in azimuthal plane of a collision have been found using the S_2 method.

1 Introduction

One of the proposed signals for collective phenomena in relativistic nuclear interactions is large fluctuation in the number of produced particles in local regions of phase space. As an example, the transition from the QGP (quark-gluon plasma) back to the normal hadronic phase is predicted to give rise to such fluctuations [1, 2].

The goal of our work was to study the emission of relativistic particles emitted in $^{197}Au + Ag(Br)$ interactions at 11.6 A GeV/c using emulsion technique. Some new results of the search for fluctuations of relativistic particles produced in ^{197}Au induced interactions with $Ag(Br)$ targets at the BNL AGS energy obtained during last decade are presented.

There are many methods which have been proposed to analyze such effects in relativistic nuclear interactions. For our analysis we used two methods: S_2 - parameter [3] and scaled factorial moments [4] methods. Both methods are described briefly, some new results are presented.

Experimental data sample was collected by the EMU01 Collaboration [5, 6]. Comparison of experimental data with model calculations for different centrality groups of events and for different beam nuclei have been made using the modified FRITIOF [7, 8] and cascade models [9].

[1]E–mail: stanislav.vokal@upjs.sk

2 Experiment

Nuclear emulsions were irradiated horizontally by 11.6 A GeV/c ^{197}Au beam at the BNL AGS accelerator - experiment E863/EMU01. Experimental details about measurements and selection criteria can be found in [5, 6].

In the measured interactions all charged secondary particles were classified according to the commonly accepted emulsion experiment terminology into b-, g-, s- and f- particles. The target fragments include b- and g-particles with the velocity $\beta < 0.7$. The relativistic (shower) s-particles were those with $\beta \geq 0.7$ emitted outside the fragmentation cone. This group includes particles produced in the interactions as well as those knocked-out from the target nucleus. The projectile fragments (f-particles) have $\beta \sim 0.99$. The schematic view of our experimental setup is shown in Fig.1.

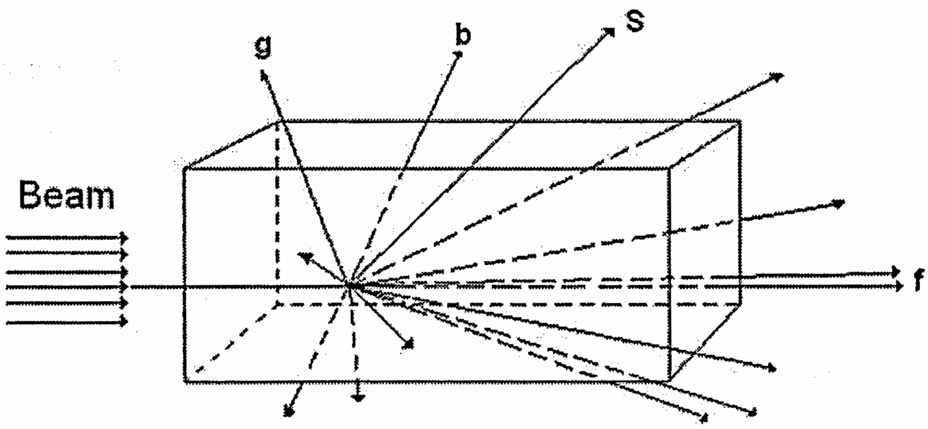

Figure 1: The experimental setup.

The polar (θ) and azimuthal (Ψ) emission angles of all tracks were measured. The pseudorapidity η was calculated for each relativistic particle:

$$\eta = -ln[\tan \frac{\theta}{2}] \tag{1}$$

The photography of the fragmentation of ^{197}Au into relativistic fragments in emulsion detector is shown in Fig.2.

The dependence of the number of produced particles (N_s) on the impact parameter (b_{imp}) calculated by the FRITIOF model for $^{197}Au + Em$ collisions at 11.6 A GeV/c is shown in Fig.3 for different emulsion targets. On can see that interactions with $N_s > 100$ are interactions of gold nuclei with the heavy emulsion targets Ag and Br. The group with $N_s > 300$ comprises the central $Au + Ag(Br)$ interactions with impact parameter $b_{imp} \sim (0 - 4)\ fm$, this is shown in Fig.3, also.

The multiplicity and pseudorapidity spectra of s-particles measured in Au induced collisions with emulsion targets are shown in Fig.4 [10]. The mean

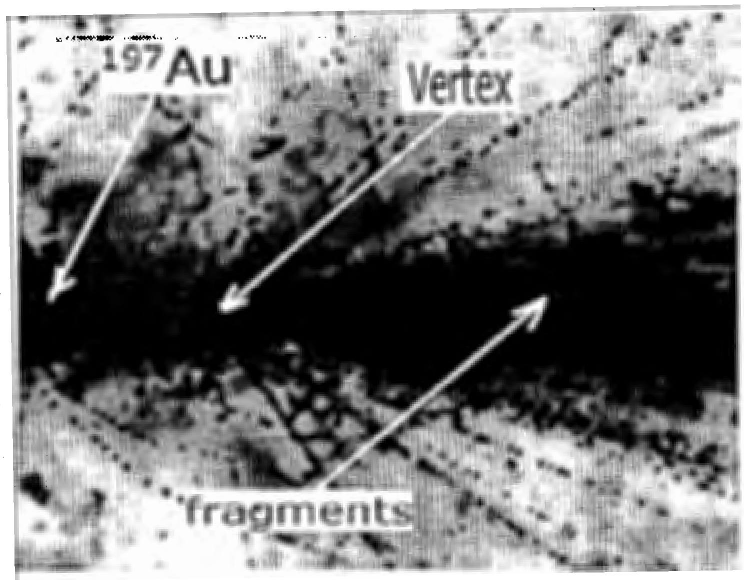

Figure 2: Fragmentation of the ^{197}Au nucleus into relativistic fragments.

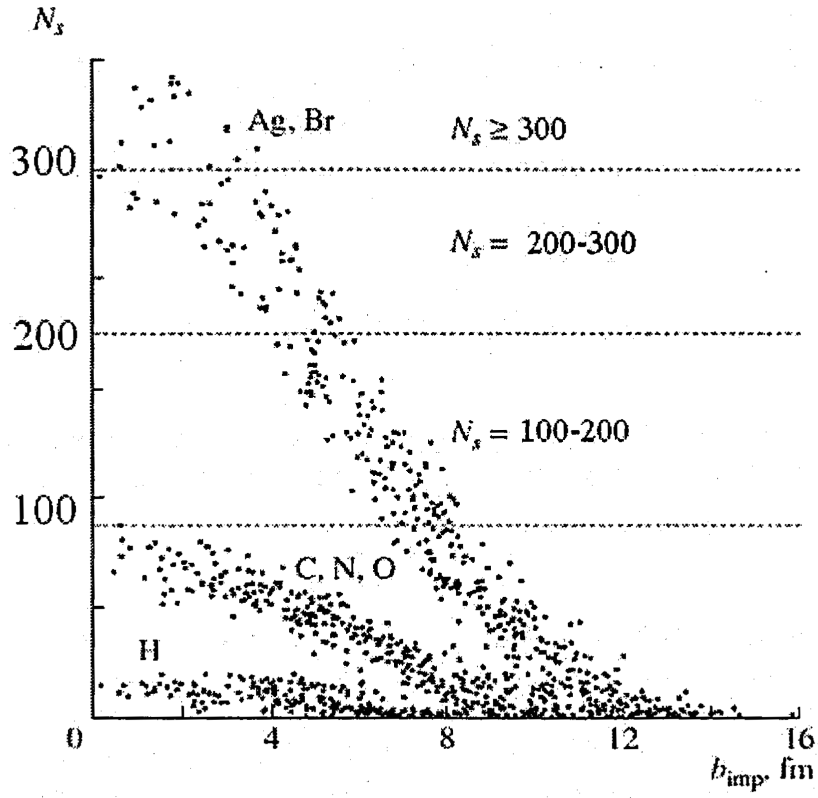

Figure 3: The dependence of multiplicity of produced particles N_s on the impact parameter b_{imp} for $^{197}Au+Em$ collisions at 11.6 A GeV/c for different emulsion targets calculated by the FRITIOF model.

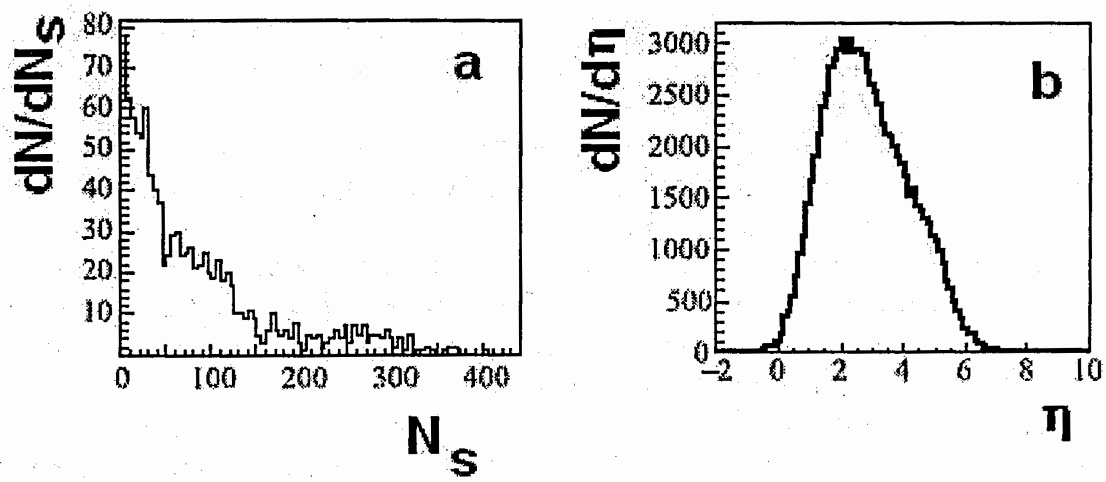

Figure 4: The multiplicity (a) and pseudorapidity (b) spectra of produced particles for minimum bias sample of $^{197}Au + Em$ interactions at 11.6 A GeV/c.

number of produced shower particles in $Au + Em$ interactions is $< N_s >=$ 66.3 ± 2.3.

In our work the multiplicity of relativistic s - particles was adopted as a criterion for the centrality of the collisions. As one can see from Fig.4.a, the highest multiplicity of s - particles are above 300.

From the total number of 1185 measured events of $^{197}Au{+}Em$ interactions at 11.6 A GeV/c, 261 collisions with the number of relativistic particles $N_s > 100$ have been selected. The interactions with $N_s > 100$ are those of gold nuclei with heavy emulsion targets Ag and Br. The group of the central $Au + Ag(Br)$ events with $N_s > 300$ includes 21 events.

3 Methods of analysis

In our present investigations two different methods of analysis have been used - S_2-parameter [3] and scaled factorial moments [4], both methods are described briefly. As was mentioned above in the introduction the main aim of this paper is to present some new results of the search for fluctuations of relativistic particles produced in ^{197}Au induced interactions with $Ag(Br)$ targets at the BNL-AGS energy.

3.1 Method of the S_2-parameter

The method was proposed by E. Stenlund (EMU01 Collaboration) and the first detailed study of the average values of the parameter S_2 was made in [3]. The azimuthal substructure of particles produced in ultra-relativistic heavy-ion collisions was investigated. It was find out that the observed substructure seems to be of stochastic nature and the features of the experimental data can be understood when effects like gamma-conversion and particle interference (HBT) are taken into account.

How it was find out in [3]? When azimuthal spectra of particles from relativistic heavy-ion collisions, produced within a narrow region of pseudorapidity, are studied, two classes of spectra are seen.

The jet-class consists of cases where several particles seem to form clusters in the azimuthal plane, clusters which are separated with rather large void regions. The ring-class consists of cases where the particles are distributed almost regularly as the spokes in a wheel.

In the S_2-method [3] the multiplicity N_d of the analyzed subgroup from an individual event is kept fixed. Each N_d tuple of consecutive particles along the η axis of individual event can then be considered as a subgroup characterized by a size

$$\Delta\eta_d = \eta_{max} - \eta_{min}, \tag{2}$$

where η_{min} and η_{max} are the pseudorapidity values of the first and last particles in the subgroup, density $\rho_d = N_d/\Delta\eta_d$ and average pseudorapidity (or subgroup position) $\eta_m = \sum \eta_i/N_d$.

To parametrize the azimuthal structure of the subgroup in a suitable way, a parameter S_2 of the azimuthal structure has been suggested

$$S_2 = \sum(\Delta\phi_i)^2, \tag{3}$$

where $\Delta\phi$ is the difference between azimuthal angles of two neighboring particles in the investigated group (starting from the first and second and ending with the last and first).

The parameter S_2 is small ($S_2 \to 1/N_d$) for the particle groups with the ringlike structure and is large ($S_2 \to 1$) for the particle groups with the jetlike structure.

The expectation value for the parameter S_2, in the case of a stochastic scenario with independent particles in the investigated group, was analytically expressed [3] as $\langle S_2 \rangle = 2/(N_d + 1)$. This expectation value can be derived from the distribution of gaps between neighbors.

Fig.5 shows the results of the analysis of the generated FRITIOF+HBT sample, with and without gama-conversion, compared with the results obtained from the data. From these results was conclude that the HBT-effect qualitatively explains the general trend of the data.

One can see, that except for some additional jet-structure seen by the S_2 parameter for the dilute groups, the features of the data can be understood as a superposition of stochastic fluctuations, γ-conversion and particle interference.

Finally it was conluded in [3] that jet-like and ring-like events do not exhibit significant deviations from what can be expected from stochastic emission. Such average value studies do not give a full information about an effect. Next step was performed in 2002 [11] when the systematic study of the S_2-spectra for subgroups of the particles produced in ^{197}Au induced collisions with heavy targets (Ag, Br) in emulsion detector has started. Nonstatistical ring-like substructures

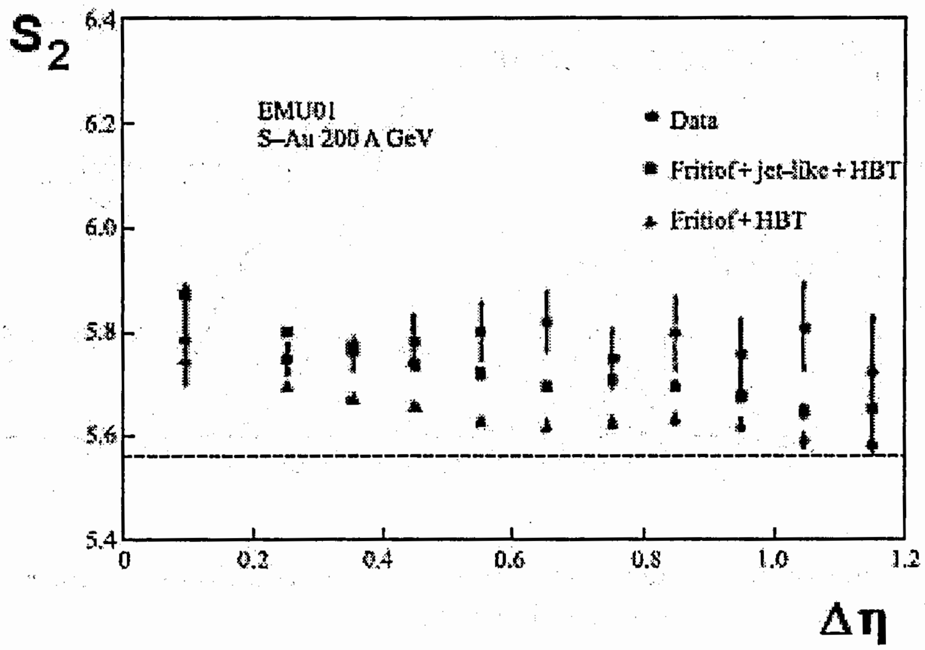

Figure 5: The dependence of the parameter S_2 on group size for central 200 A Gev $S + Ag(Br)$ interactions. The dashed line indicates the expectation values for purely stochastic emission.

have been found and cone emission angles as well as other parameters have been determined.

What we can expect to see in the experimental $S_2/\langle S_2 \rangle$ distributions in different scenarios was shown in 2004 [12]. It is illustrated schematically in Fig.6 using for example Gauss distributions. In case of a pure stochastic scenario the distribution would have a peak position at 1. The existence of the jet-like structures in collisions results to appearance of additional S_2 distribution from this effect, but shifted to the right side in comparison with stochastic distribution. Analogously, the existence of the ring-like structures results to appearance of additions to S_2 distribution from this effect but shifted to the left side. As a result, the summary S_2 distribution from these three effects may have different form and depends on mutual order and sizes.

The S_2 distributions for subgroups with $N_d = 35$ and different groups of shower particles multiplicity N_s in $Au + Ag(Br)$ collisions at 11.6 AGeV/c are shown in Fig.7. As one can see at all three cases of different centralities the S_2 distributions have peak position around the value corresponding to the stochastic scenario ($\langle S_2 \rangle = 0.056$) for Au and tails at the right side. In order to study the ring-like structures the only left part of the S_2 distribution, where a signal of ring-like structure may be expected, is essential.

Comparison of the S_2 distributions for subgroups with $N_d = 90$ and 35 in the Pb and Au induced collision with heavy $Ag(Br)$ targets is shown in Fig.8.

The only central collisons ($N_s > 1000$ in Pb- and $N_s > 300$ in Au-induced

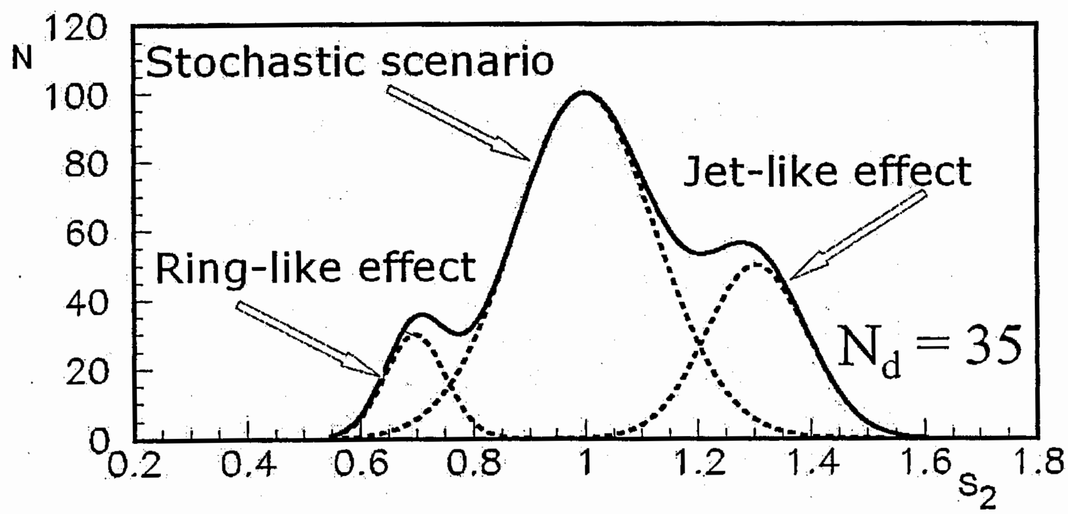

Figure 6: The example of possible summary S_2-distribution from three effects : stochastic + ring- like + jet- like distribution.

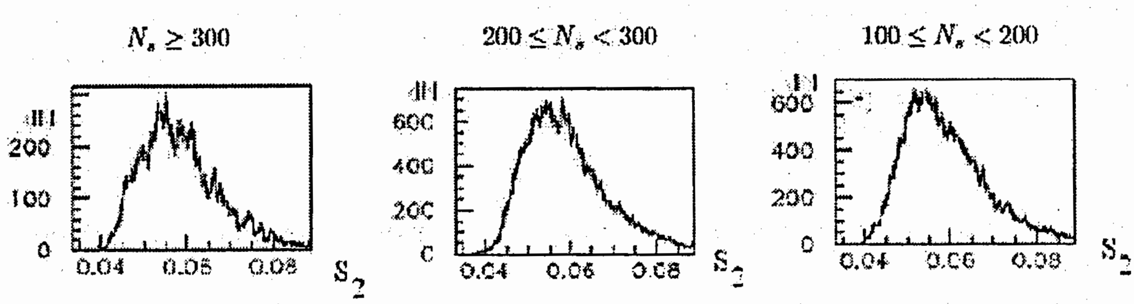

Figure 7: The S_2 distributions for subgroups with $N_d = 35$ and different groups of shower particles multiplicity N_s in $Au + Ag(Br)$ collisions at 11.6 AGeV/c .

collisions with $Ag(Br)$ targets) have an designation on additional peak on the left part at $S_2 \sim 0.021$ and $S_2 \sim 0.050$, respectively. For smaller multiplicities it is complicated to prove or to refute an existence of additional peaks on the left part at S_2 distribution. This indicates that a certain ring-like structures are present at these two experiments.

To estimate the reliability of the existence of additional peak on the left part at S_2 distribution the experimental normalized $S_2/\langle S_2 \rangle$ distribution compared with the calculated one by the FRITIOF model for the most central groups of events measured in ^{197}Au induced collisions with $Ag(Br)$ nuclei at 11.6 A GeV/c is presented on the Fig.9a. The model spectra were aligned according to the position of the peak with the experimental one. The FRITIOF includes neither the ringlike nor the jetlike effects, so the model spectra are used like the statistical background. Except this, in [3], it was shown that the S_2 distribution for the FRITIOF model coincides with the calculated distribution in the case

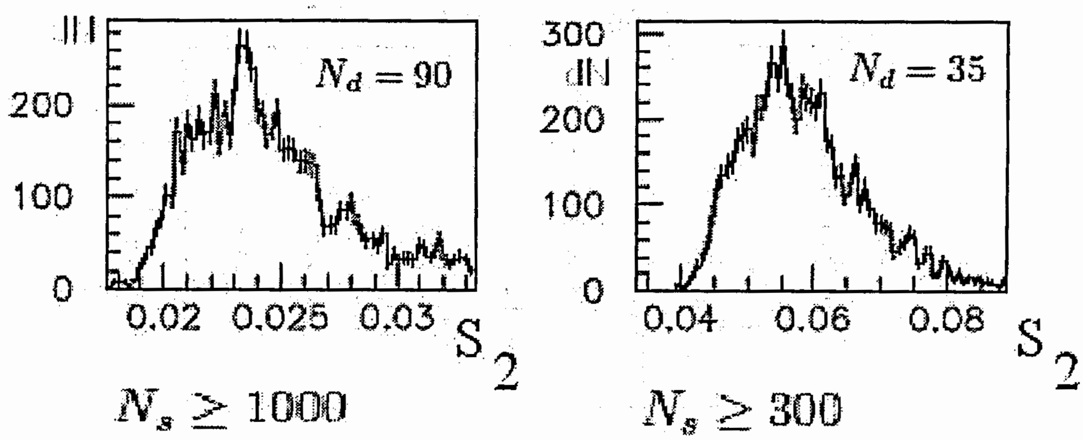

Figure 8: The S_2 spectra for subgroups with N_d = 90(35) in $Pb(Au) + Em$ collisions at 158(11.6) AGeV/c .

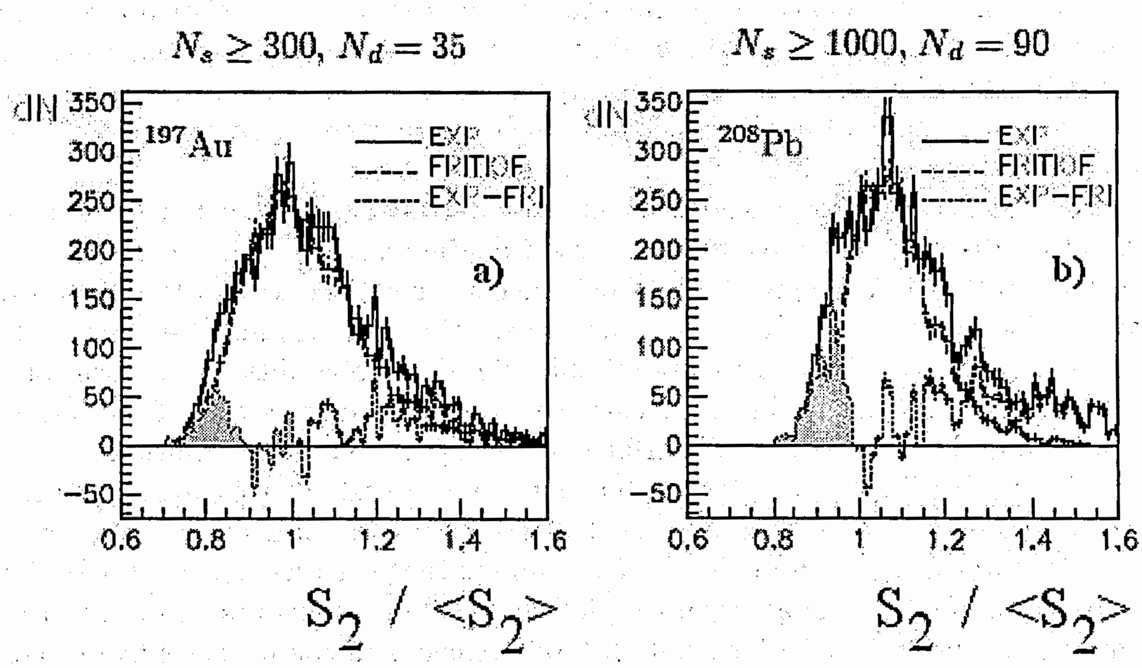

Figure 9: The experimental $S_2/\langle S_2 \rangle$ distributions after subtraction of the FRITIOF ones for Au and Pb+ $Ag(Br)$ central collisions with N_d = 35 and 90, respectively.

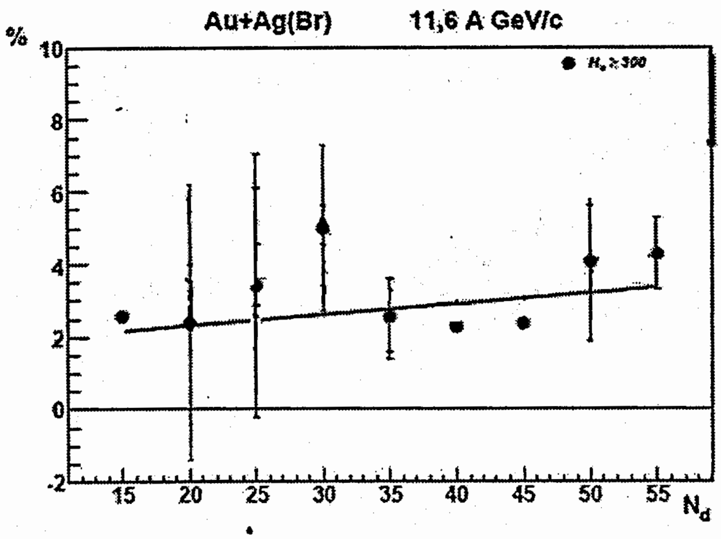

Figure 10: The probability of the formation of the nonstatistical ring-like structures on the number N_d for central $Au + Ag(Br)$ interactions at 11.6 A GeV/c.

of the stochastic scenario with independent particles in the investigated group.

The difference between experimental and model spectra is shown also. One can see that the experimental distributions are broader than the spectra calculated by the FRITIOF model. The experimental distributions have a surplus of events on both sides of the center. Such a situation takes place for all N_s groups and any N_d meanings which were examined.

The comparison with lead data is presented in Fig.9b. In both cases the resultant distributions have two very good distinguishable hills, the first in the region $S_2/\langle S_2 \rangle < 1$, where the ring-like effects are expected, and the second in the jet-like region ($S_2/\langle S_2 \rangle > 1$). One can see that the surplus of events in the region $S_2/\langle S_2 \rangle < 1$ is statistically reliable. So, the probability of the formation of the nonstatistical ring-like structures can be estimated as a rate of the surface of the ring-like part to the full surface of the experimental distribution.

The probability of the formation of the nonstatistical ring-like structures on the number N_d for the most central group in Au induced collisions with $Ag(Br)$ targets is shown in Fig.10. One can see that the estimated contribution of the events with nonstatistical ring-like structure in the emission of produced particles is about 2 - 5 % for $Au + Ag(Br)$ collisions in the most central group. This value is less as in our previous $Pb + Ag(Br)$ experiment at 160 A GeV/c, where the estimation of the probability of the formation of the nonstatistical ring-like structures is about 10 - 12 % [13].

Our result is that the azimuthal structures of produced particles from collisions induced by the 11.6 A GeV/c ^{197}Au beams with $Ag(Br)$ targets in the emulsion detector have been investigated and the additional groups of produced particles in the region of the ring-like structures ($S_2/\langle S_2 \rangle < 1$) and the jet-like structures ($S_2/\langle S_2 \rangle > 1$) in comparison to the FRITIOF model calculations have been observed [11, 12]. Analogical situation have been observed in the interactions of 158 A GeV/c ^{208}Pb beams with heavy targets in the emulsion detector [13, 14].

3.2 Scaled factorial moments method analysis

Search for nonstatistical fluctuations of particle production in heavy ion collisions has been done using the scaled factorial moments method proposed by Bialas and Peschanski [15, 16]. They suggested to study the dependence of factorial moments F_q, where q is the order of the moment, as a function of the bin width $\delta\eta$. In the case of nonstatistical fluctuations in particle emission it is expected a power law dependence

$$F_q \propto (\frac{\Delta\eta}{\delta\eta})^{\varphi_q}, \varphi_q > 0 \tag{4}$$

where $\Delta\eta$ is the pseudorapidity interval of produced relativistic particles.

Our analysis is based on the method of horizontal factorial moments (HFM) proposed in [4]. The standard horizontal factorial moments $F_e^{(H)}$ characterizing the $e-th$ event are defined by the following formula:

$$F_e^{(H)}(q) = M^{q-1} \sum_{m=1}^{M} \frac{F(n_{me};q)}{[N_e^{(H)}]^q}, \tag{5}$$

where M is the number of equal bins of size $\delta\eta$ into which the pseudorapidity interval $\Delta\eta$ has been divided, n_{me} is the number of shower particles in the $m-th$ bin. Non averaging and non normalized factorial moments are given by $F(n;q) = n(n-1)...(n-q+1)$. Vertical averaging of $F_e^{(H)}$ gives the full form

$$F^{(H)}(q) = \frac{1}{E}\sum_{e=1}^{E} F_e^{(H)}(q), \tag{6}$$

where E is the total number of events. Denominator of the horizontal moment (5) is $N_e^{(H)} = \sum_{m=1}^{M} n_{me}$.

The intermittent behaviour, or self similarity of the production mechanism, should lead to a power law dependence of the factorial moments on the size of the phase space domain (or number of bins) [15, 16] (illustrated on Fig.11):

$$ln\langle F_q\rangle = \alpha_q + \varphi_q.lnM \tag{7}$$

For a random uncorrelated particle production $\langle F_q\rangle$ should be constant for all values of q [17]. In case of effect (correlated particle production) $\langle F_q\rangle$ should increase with increasing order q of the moment and the exponent $\varphi_q > 0$ for $\delta \to 0$ [17].

The dependences of $ln\langle F_q\rangle$ on lnM for our $Au + Ag(Br)$ experimental data sample [18] is presented on the Fig.12. The analysis was performed for central

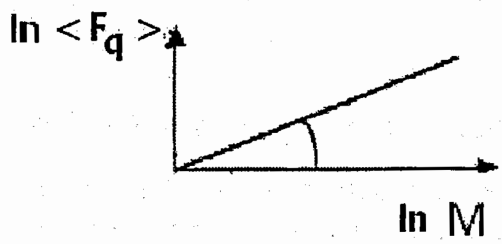

Figure 11: Illustration of the intermittent behaviour of factorial moments on the number of bins M.

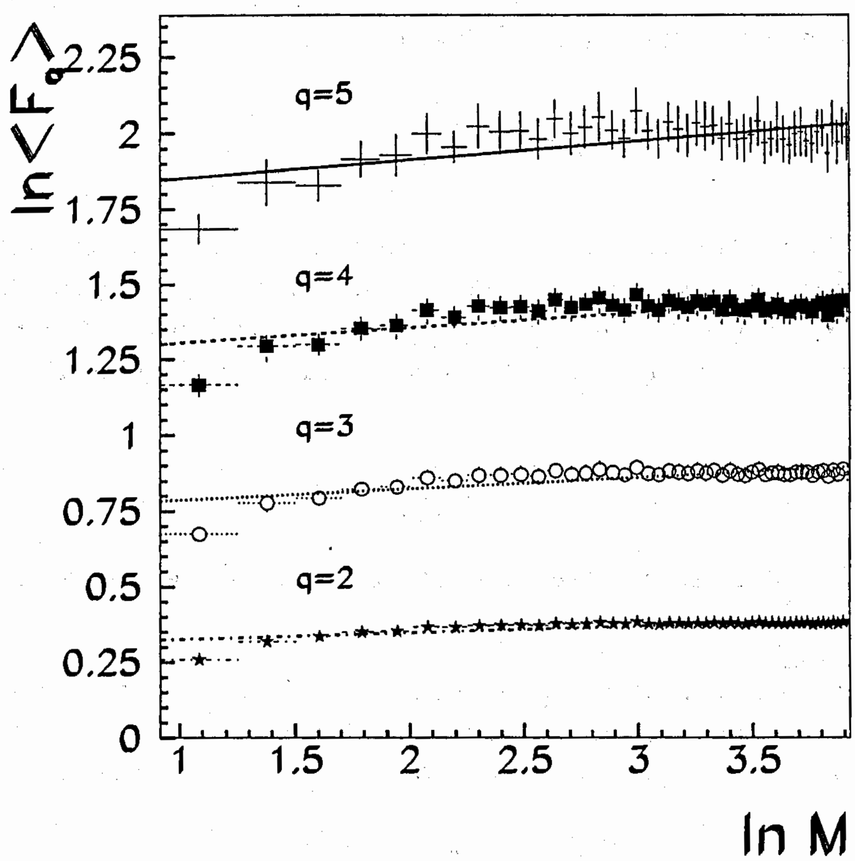

Figure 12: The dependences of $ln\langle F_q \rangle$ on lnM for $Au + Ag(Br)$interactions at 11.6 A GeV/c.

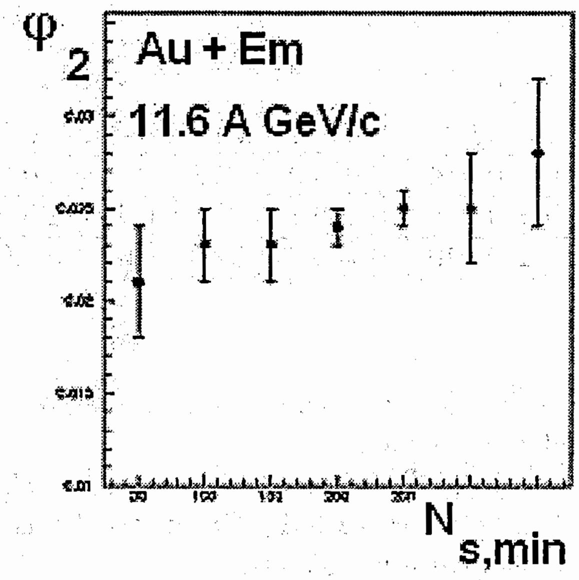

Figure 13: The φ_2 dependence on degree of centrality characterized by minimal number of s-particles $N_{s,min}$ produced in $Au + Em$ interactions.

$Au + Ag(Br)$ interactions at 11.6 A GeV/c (with $N_s \geq 300$) in the full pseudorapidity window $\Delta\eta = 0 - 5$ with M varied from 3 till 50 using the HFM method. The scaled factorial moments F_q of the order q have been studied as a function of the pseudorapidity bin size $\delta\eta = 0.1 - 1.67$.

The preliminary results of this analysis have been published [18] and compared with calculations made by other methods (vertical and mixed factorial moments) not presented here. It was shown that the values of slopes φ_q obtained by all these methods are similar for $q = 2 - 5$.

The φ_2 dependence on degree of centrality of measured events is shown in Fig.13. The values of slopes for $ln\langle F_q \rangle$ dependence on lnM were calculated for events with different centrality degree. The number of events and mean multiplicities of s-particles are $N_e = 507$ and $< N_s >= 132$ for minimal number of s-particles $N_{s,min} = 50$ produced in $Au + Em$ interactions. For central events with $N_{s,min} = 300$ these values are : $N_e = 21$ and $< N_s >= 329$. One can see that the value of φ_2 increases with increasing of centrality degree of selected events.

The comparison was made with other experiments performed by the unique emulsion technique at similar energies. The values of slopes of $ln\langle F_q \rangle$ dependences on lnM are presented in Tab.1 for different beam nuclei at similar momenta from 11.6 to 14.6 A GeV/c. The calculations were done by the HFM method, in the same pseudorapidity window $\Delta\eta = 0 - 4.75$ and for same number of bins $M = 4 - 25$. The values of slopes φ_q obtained for different beam nuclei at momenta 11.6 - 14.6 A GeV/c are similar. The same trend was shown in [19], where the ^{22}Ne,^{28}Si and ^{32}S interaction with emulsion have been studied at Dubna energy region (momenta 4.1 - 4.5 A GeV/c).

Table 1: The parameters φ_q for different primary nuclei at BNL energy range.

	^{16}O	^{28}Si	^{197}Au
φ_2	0.036 ± 0.005	0.029 ± 0.004	0.032 ± 0.001
φ_3	0.085 ± 0.014	0.063 ± 0.010	0.063 ± 0.005
φ_4	0.149 ± 0.026	0.100 ± 0.018	0.101 ± 0.012
φ_5	0.224 ± 0.040	0.133 ± 0.027	0.147 ± 0.024

The comparison with $^{208}Pb + Em$ collisons is presented in Fig.14 for the most central group of selected events.

The steepest dependence was found for the most central Pb induced interactions. The slope values ($\varphi_q > 0$) for $Au + Ag(Br)$ interactions show an evidence for the presence of nonstatistical fluctuations.

The dependences of slopes φ_q on beam energy are presented in Tab.2 for $^{16}O + Em$ collisions 4,5, 14.6, 60, 200 A GeV/c and in Tab.3 for $^{28}Si + Em$ collisions at 4.5 and 14.6 A GeV/c [20]. Comparisons with calculations performed in the frame of the modified cascade code (CEM) [9] is shown in brackets.

Table 2: The values of slopes for $^{16}O + Em$ collisions at 4.5, 14.6, 60, 200 A GeV/c (rows 1.- 4.). The CEM values are shown in the brackets.

	φ_2	φ_3	φ_4	φ_5
1.	0.041 ± 0.006 (0.018 ± 0.003)	0.099 ± 0.015 (0.035 ± 0.004)	0.178 ± 0.029 (0.050 ± 0.019)	0.270 ± 0.048 (0.072 ± 0.033)
2.	0.040 ± 0.004 (0.018 ± 0.004)	0.094 ± 0.017 (0.026 ± 0.009)	0.163 ± 0.031 (0.021 ± 0.016)	0.236 ± 0.047 (0.017 ± 0.025)
3.	0.038 ± 0.004	0.073 ± 0.010	0.103 ± 0.017	0.128 ± 0.024
4.	0.043 ± 0.004	0.093 ± 0.010	0.148 ± 0.017	0.207 ± 0.025

Table 3: The values of slopes for $^{28}Si + Em$ collisions at 4.5 and 14.6 A GeV/c. The CEM values are shown in the brackets.

Momenta $[AGeV/c]$	φ_2	φ_3	φ_4	φ_5
14.6	0.037 ± 0.005 (0.023 ± 0.003)	0.076 ± 0.012 (0.045 ± 0.008)	0.112 ± 0.021 (0.063 ± 0.014)	0.145 ± 0.032 (0.076 ± 0.021)
4.5	0.044 ± 0.009 (0.008 ± 0.004)	0.117 ± 0.025 (0.023 ± 0.012)	0.224 ± 0.051 (0.032 ± 0.023)	0.336 ± 0.092 (0.040 ± 0.037)

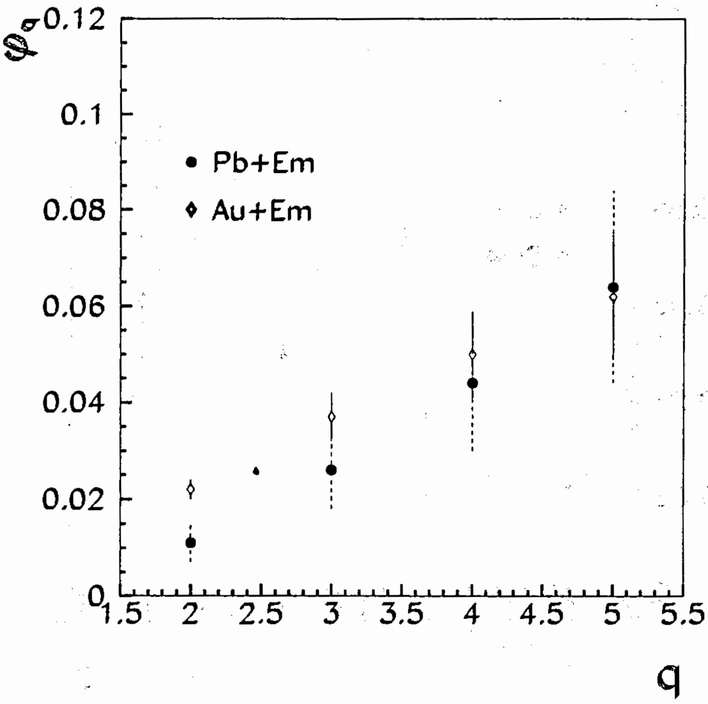

Figure 14: The φ_q dependence on q for Au and Pb induced interactions with $Ag(Br)$ targets.

One can see that the values of slopes for experimental samples are higher than calculated ones. This increase indicates the presence of dynamical fluctuations, while factorial moments independent of $\delta\eta$ (or lnM) are expected in the case of purely statistical fluctuations.

The dependences of slopes φ_q on q are compared with the CEM values for the most central events of the Au induced interactions with $Ag(Br)$ targets at the BNL energy. It is shown on the Fig.15 for events selected by the criteria $N_s \geq 300$ and $M = 3 - 50$. The number of events are equal $N_{EXP} = 21$ and $N_{CEM} = 37$. The mean multiplicities of s-particles are $< N_s >_{EXP}= 329$ and $< N_s >_{CEM}= 341$.

Experimental values of slopes are higher than calculated ones. The CEMs factorial moments are practically independent of $\delta\eta$ (or lnM) as can be expected in the case of purely statistical fluctuations.

The φ_q dependence on q for $Pb + Ag(Br)$ at 158 A GeV/c was compared with the MC calculations in [21]. For high energy collisions, the moments calculated in the one dimensional analysis of rapidity or azimuth satisfy a power law dependence over a large range of bin widths. They showed that the slopes φ_q increase with increasing order q of the moment and they are larger than those obtained from Monte Carlo simulations performed in the VENUS code (Fig.16). As one can see, our $Au+Ag(Br)$ results for the most central collisions, presented in Fig.15 showed the qualitative agreement of both analysis.

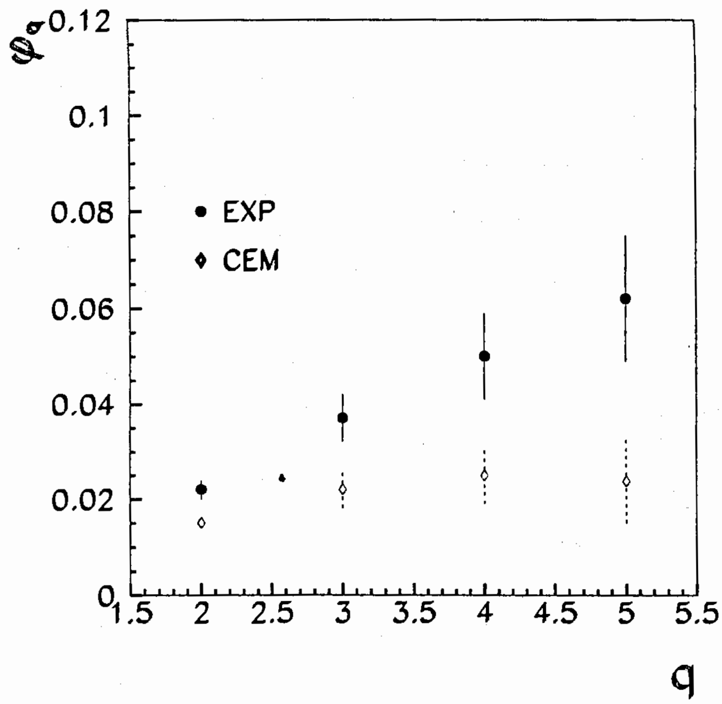

Figure 15: The slopes φ_q dependences on q compared with CEM for the most central $Au + Ag(Br)$ interactions at 11.6 A GeV/c.

In [4] was recommended to study the dependence of intercept parameter α_q on q. The result of this analysis is presented in Fig.17 for the most central $Au + Em$ collisions with $N_s > 300$, $M = 3 - 50$, $\delta\eta = 1.67 - 0.1$, $q = 2 - 5$. This dependence is similar as dependence for $Pb+Em$ interactions ($N_s > 1000$, $M = 7 - 74$, $\Delta\eta = 0 - 7.4$, $q = 2 - 6$) published in [14].

The dependences of intermittency parameter (λ_q) on the order of factorial moment q for ^{208}Pb at 158 A GeV/c and ^{16}O at 200 A GeV/c induced interactions have been studied in [22]. If the function

$$\lambda_q = \frac{\varphi_q + 1}{q}, \tag{8}$$

had a minimum at a certain $q = q_c$, there would be a possibility of observing a phase transition [22].

The dependences of parameter (λ_q) on the order of factorial moment q for different primary nuclei is presented in Fig.18. On can see that no minimum has been found in the dependences of (λ_q) on q. The dependences of parameter λ_q on the order of factorial moment q for ^{208}Pb at 158 A GeV/c ($M = 7 - 74$, $\Delta\eta = 0 - 7.4$) and ^{197}Au at 11.6 A GeV/c ($M = 3 - 50$, $\Delta\eta = 0 - 5$) for 2 groups of interactions are shown in Fig.19ab. No minimum has been found in the dependences of λ_q on q, also.

Finally, the dependence of φ_2 on the mean pseudorapidity density of s-

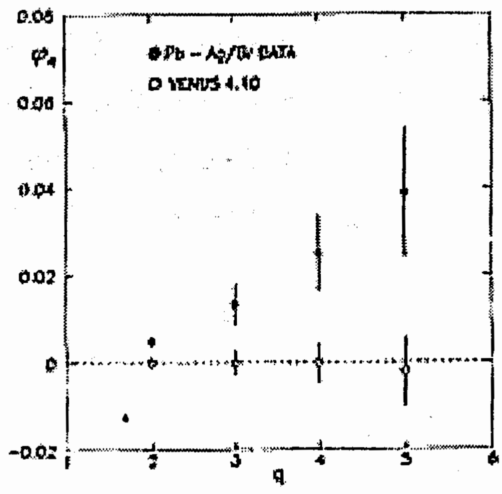

Figure 16: The φ_q dependence on q for Pb interactions with $Ag(Br)$ targets compared with VENUS model calculations [21].

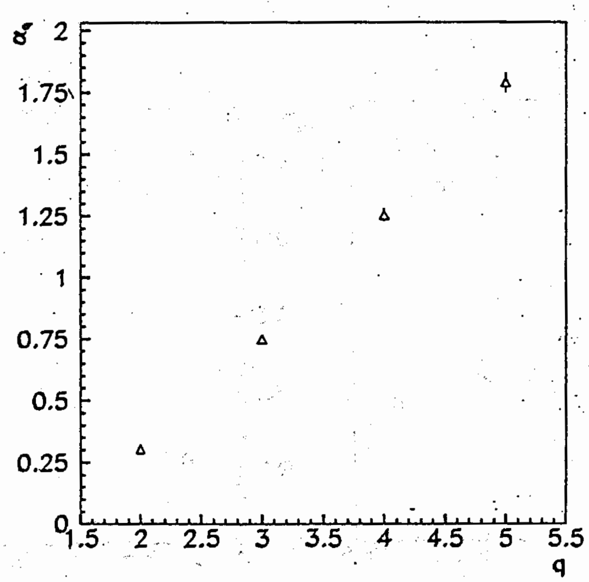

Figure 17: The intercept parameter α_q dependence on q for $Au + Em$ interactions.

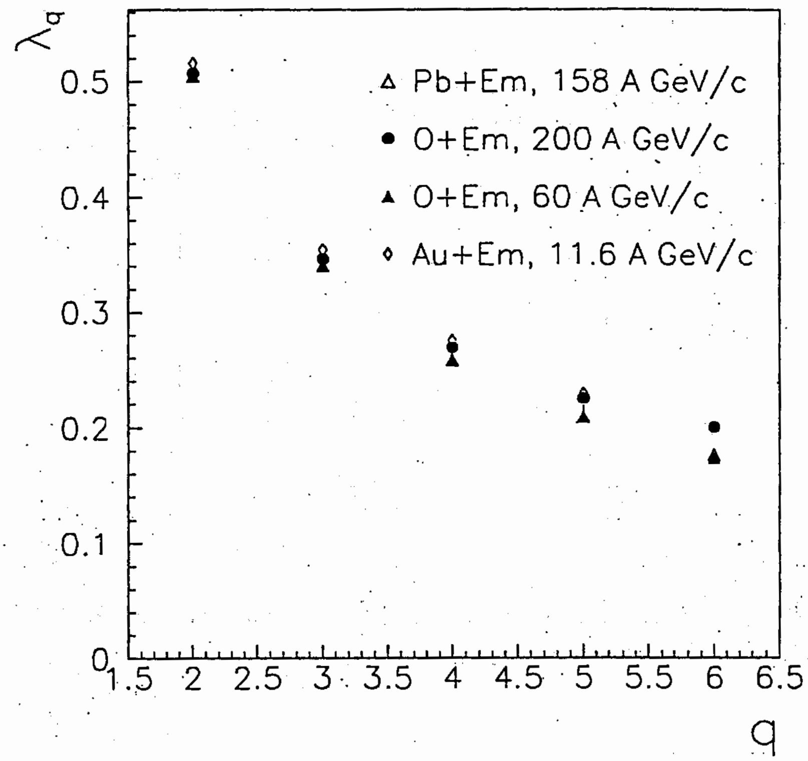

Figure 18: The parameter λ_q on q for different primary nuclei.

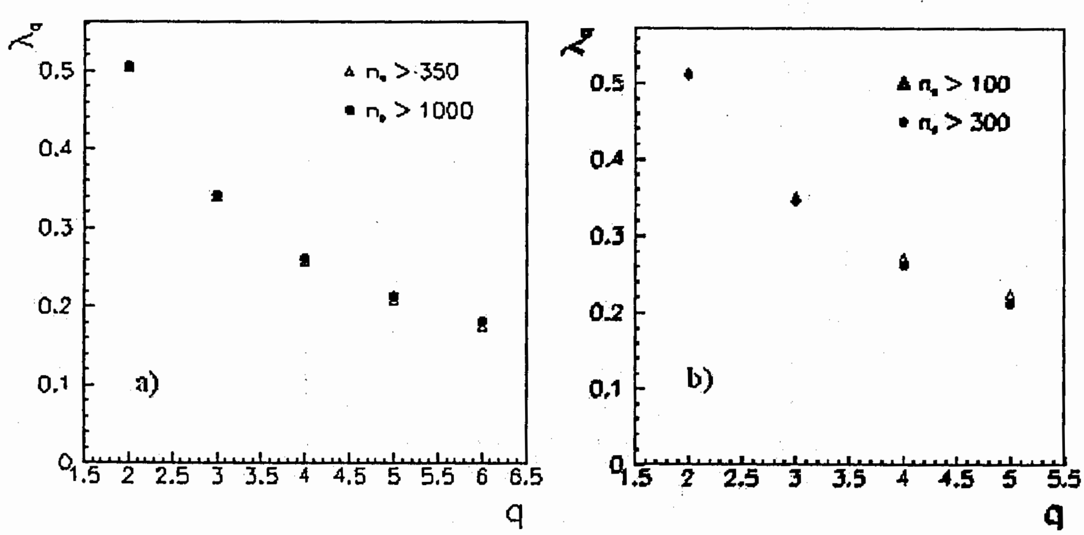

Figure 19: The dependences of parameter λ_q on q for (a) ^{208}Pb at 158 A GeV/c and (b)^{197}Au at 11.6 A GeV/c.

particles is presented in Fig.20. The values for $Au + Em$ and $Pb + Em$ interactions with different degree of centrality are shown. The comparison with other EMU01 results is shown also. It is clearly seen that the slopes show an inverse dependence upon pseudorapidity density.

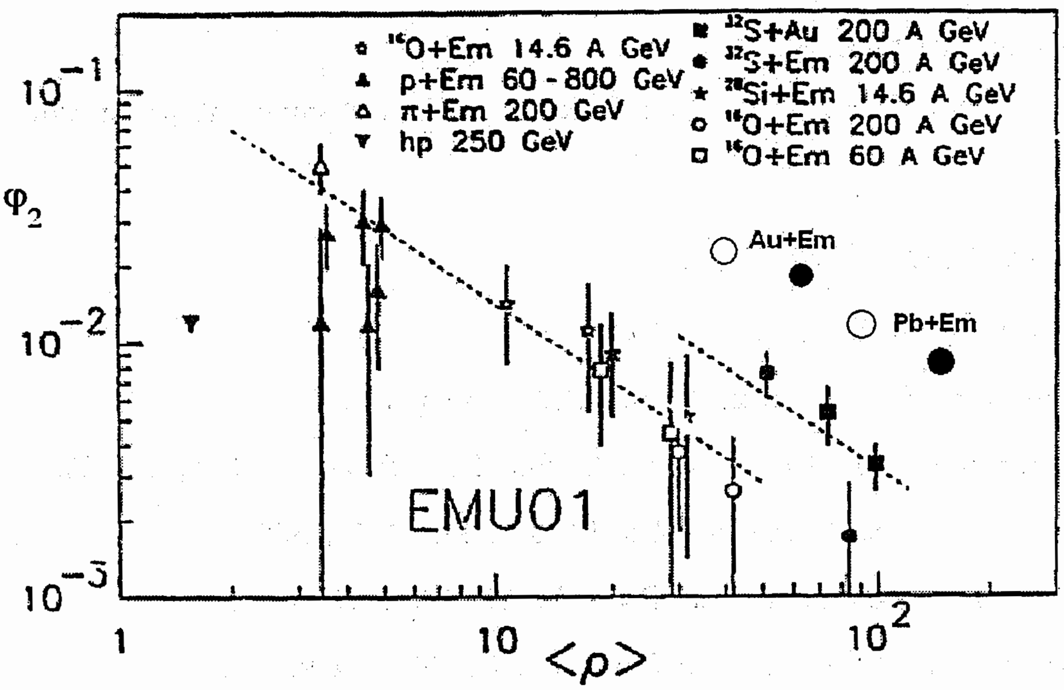

Figure 20: The dependence of φ_2 on the mean pseudorapidity density of s-particles measured in nuclear interactions with emulsion targets, for $Au + Em$: ∘ - events with $N_s > 100$, • - events with $N_s > 300$, for $Pb + Em$: ∘ - events with $N_s > 350$, • - events with $N_s > 1000$.

4 Conclusion

- Emission of relativistic particles produced in central ^{197}Au induced nuclear collisions at 11.6 A GeV/c has been studied using two different approaches - scaled factorial moments and parameter S_2 methods.
- The additional groups of produced particles in the region of the ring-like structures $(S_2/\langle S_2\rangle < 1)$ and the jet-like structures $(S_2/\langle S_2\rangle > 1)$ in comparison to the FRITIOF model calculations have been observed.
- An evidence for nonstatistical fluctuations has been shown using horizontal factorial moment method in pseudorapidity phase space.
  - The comparative study has been done for different beam energies and masses and for different centrality selection of Au events.

– No clear minimum has been found in the dependences of intermittency parameter λ_q on q.
– Inverse dependence of the parameter φ_2 on pseudorapidity density was confirmed.

Acknowledgments

This work was supported by Grants from the JINR Plenipotentiary of Slovak Republic.

References

[1] Van Hove L., Z. Phys. C21, 1984, p.93.

[2] Gyulassy M. et al., Nucl. Phys. B237, 1984, p.477.

[3] Adamovich M.I. et al., J. Phys. G: Nucl.Part. Phys., 19, 1993, p.2035.

[4] Blažek M., Int. Journal of Mod. Phys., A12, 1997, p.839.

[5] Adamovich M.I. et al., Eur. Phys. J., A1, 1998, p.77.

[6] Adamovich M.I. et al., Eur. Phys. J., A5, 1999, p.429.

[7] Nilsson-Almquist B., Stenlund E., Comp. Phys. Com., 43, 1987, p.387.

[8] Uzhinsky V., Preprint JINR, E2-96-192, Dubna, 1996.

[9] Musulmanbekov G., Preprint JINR, P2-99-59, Dubna, 1999; also in: AIP, 1995, 428.1.

[10] Fedorišin J., Vokál S., Preprint JINR, E1-2007-4, Dubna, 2007.

[11] Orlova G.I., Kravčáková A., Vokál S., Prosin V.V., Proc. of the Hadron Structure 2002, Herľany, Sept. 22-27, 2002, Košice, 2003, p.155.

[12] Vokál S., Vokálová A., Kravčáková A., Lehocká S., Orlova G.I., Preprint JINR, E1-2004-173, Dubna, 2004.

[13] Vokál S., Lehocká S., Orlova G.I., Preprint JINR, E1-2005-66, Dubna, 2005.

[14] Vokál S., Vrláková J., Preprint JINR, E1-2009-188, Dubna, 2009.

[15] Bialas A., Peschanski R., Nucl. Phys. B273, 1986, p.703.

[16] Bialas A., Peschanski R., Nucl. Phys. B308, 1988, p.857.

[17] Jain P.L. and Singh G.: Phys. Rev. C44, No.2, 1991, p.854.

[18] Vrláková J. et al.: Proc. of 12th Conf. of Slov. Phys., Smolenice, Slovakia, Sept.3 - 5, 2001, p.96.

[19] Vrláková J. et al.: Proc. of 11th Conf. of Slov. Phys., Zvolen, Slovakia, Sept.4 - 6, 2000, p.38.

[20] Adamovich M.I. et al., APH N.S., Heavy Ion Physics 13, 2001, p.213.

[21] Wosiek B., Acta Phys.Slov. 46, 1996, p.531.

[22] Ghosh G. et al., Europhys. Lett. 41, 1998, p.371.

SEARCH FOR η-MESIC NUCLEI AT THE NUCLOTRON

S.V. Afanasiev[a,1], Yu.S.Anisimov[a], R.N. Bekmirzaev[b], I.Cruceru[c], F.Constantin[c], M.Cruceru[c], M.Cruceru[c], L.Ciolacu[c], D.K. Dryablov[a], Z.A. Igamkulov[a], V.I. Ivanov[a], A.Yu. Isupov[a], J. Kliman[d], A.I. Lebedev[e], A.I. L'vov[e], A.I. Malakhov[a], V. Matousek[d], G.Niolescu[c], L.N. Pavlyuchenko[e], E.B. Plekhanov[a], V.V. Polyansky[e], S.S. Sidorin[e], M. Shpavorova[f], G.A. Sokol[e], I. Turzo[d], S. Vokal[f]

a) Joint Institute for Nuclear Research, 141980 Dubna, Moscow Region, Russia
b) Horia Hulubei National Institute of R&D for Physics and Nuclear engineering (IFIN-HH Bucharest, Romania
c) Jizzakh State Pedagogical Institute, Uzbekistan
d) Institute of Physics, Slovak Academy of Sciences, Bratislava, Slovak republic
e) Lebedev Physical Institute, Leninsky Prosect 53, Moscow 119991, Russia
f) Faculty of Science, University of P.J. Shafarik, Koshice, Slovak republic

Abstract

Results of a search for quasi-bound states of the η-meson and a target nucleus obtained during several years using an internal target at the Nuclotron d-beam are presented. Formation of the η-mesic nuclei was studied in the reaction $d + \mathrm{C}$ in the energy interval 1.5 to 2.1 GeV/nucl. Decay products of S_{11} resonances excited by η-mesons captured nucleons in the nuclear target have been analyzed. Measurements were performed with a scintillation spectrometer SCAN. Analysis of obtained data is presented.

1 Introduction

Properties of hadrons in the nuclear medium is one of interesting topics in modern hadron and nuclear physics. All nuclei have essentially smaller masses than the sum of masses of neutrons and protons forming the nucleus. This mass difference is a result of strong interaction between hadrons that form the nuclear composite system. One can think that other particles distinct from nucleons, such as pions or η-mesons, may also have smaller masses in the nuclear medium than those in the empty space. In the case of η this feature is supported by many theoretical analyses of ηN interaction.

Measurements of the meson masses and their interactions in finite nuclei provide valuable data for our understanding of dynamical symmetry breaking in low energy QCD [1]. The SCAN experiment at JINR was designed to study possible formation of η-meson bound states inside nuclei [1]-[10].

2 Requirements for experiment

The idea of that experiment is in observing decays of $S_{11}(1535)$ resonances excited in a target nucleus after capturing (binding) the η-meson. In the case of a recoilless reaction the rest of the target nucleus has a small momentum, so products of the

[1]E-mail: afanasev@jinr.ru

$S_{11}(1535)$ resonance decay are emitted to nearly back-to-back directions. Detection of the emitted back-to-back particles is the main idea for separation of the wanted $S_{11}(1535)$ decays in nuclei from another ones.

A good candidate for the primary reaction is $d + {}^{13}C$ interaction. ${}^{13}C$ is a halo nucleus. It has an outer neutron that can be easily removed from the nucleus. The reaction $d + {}^{13}C = t + {}^{12}C + \eta + Q$ has a positive energy balance Q and a big cross section.

We choose the primary deuteron energy to satisfy a recoilless kinematics for η-meson production in nuclei. In this kinematics the produced η-mesons can be almost at rest in the nucleus. In Fig.1 we plot the minimal momentum transfer in the $A(d,X)(A-1)_\eta$ reaction as a function of the primary kinetic energy per nucleon. For the η momentum less than 100 MeV/c (this value is chosen according to a theoretically expected η binding energy) that reaction with $\Theta = 0$ has a magic value for the nucleon energy when a recoilless condition is satisfied. Some wider region of the primary energy from 1.6 to 2.7 GeV/nucl has been selected to take into account also a quasi free nucleon reaction $A(p,d)(A-1)_\eta$. Theoretical predictions for the s-wave ηN scattering amplitude

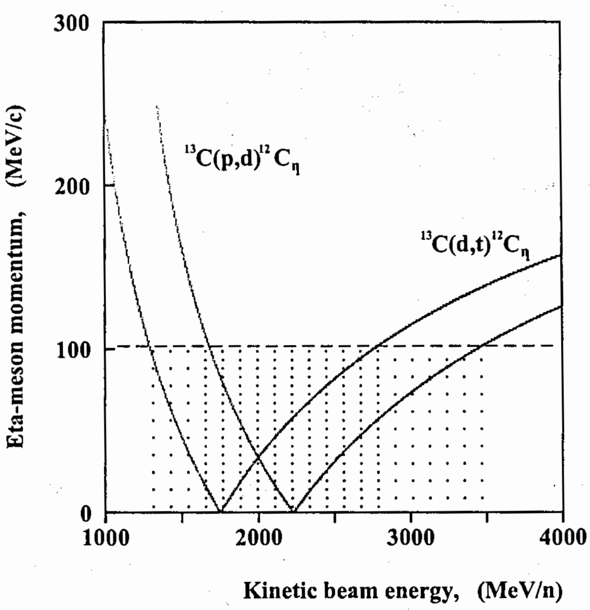

Figure 1: Minimal momentum transfer for the ${}^{13}C(p,d){}^{12}C$ and ${}^{13}C(d,t){}^{12}C$ reactions (right and left curves, respectively).

demonstrates an attraction between η and N at kinetic energies of the η meson less that 70 MeV. The captured η-meson can decay through the S_{11} resonance to a πN pair that can be detected in the experiment. Such πN pairs emitted from nuclei are correlated over the opening angle $\Theta(\eta, N) \approx 180°$.

In this paper we describe experimental results of a search for η-mesic nuclei at the internal deuteron beam of the Nuclotron in the reaction

$$d + \mathrm{C} \rightarrow (A_2)_\eta + \ldots \rightarrow \pi + p + \ldots \quad (1)$$

where the A_2-nucleus is part of ${}^{13}C$ formed in the $d + {}^{13}C$ collision. Hadrons emitted in transverse directions are detected by a two-arm spectrometer. The flow of particles includes πp pairs which are products of η-nuclei decays. A bound state of η is expected to be seen as a peak in the total energy spectrum of these pairs.

3 Experimental setup

The setup for study of η-nuclei is shown in Fig. 2. It has two sets of counters located to the left (P-arm) and right (K-arm) side of the target for back-to-back coincidence measurement and also a two-ring array of scintillators (H_M) near forward direction to cover a solid angle for particles emitted in the primary collision. Each of the coincidence counter sets consists of fast timing counters ($P_1 \div P_3$; $K_1 \div K_3$), a large volume counter (P_4; K_4), a high-momentum particles detector (P_5; K_5), and a threshold Cherenkov counter (C_P; C_K) for pions separation. Four sets of counters (B_L, F_L, B_R, F_R) are added to the setup for monitoring the collision rate.

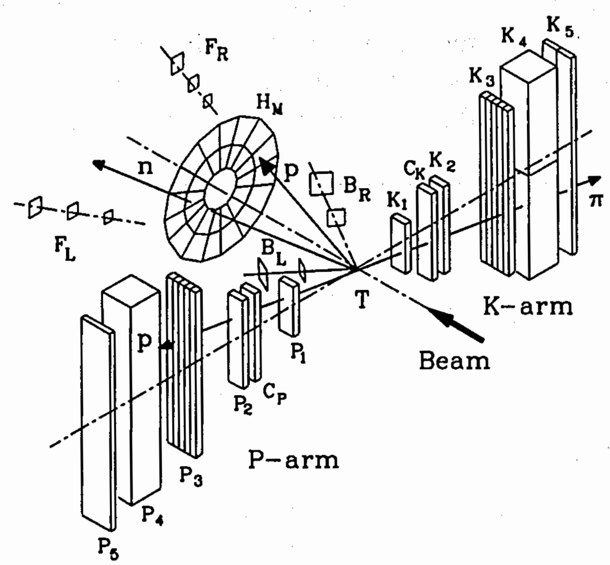

Figure 2: The experimental setup for studying in-medium properties of hadrons.

Charged particles are identified using three measured quantities: 1) ΔE, the energy loss per unit length measured by all counters, 2) TOF, time of flight between $P_1(K_1)$ and $P_3(K_3)$, and 3) E, the ADC sum of sequentially fired counters. Protons and pions were clearly identified, and the proton contamination in the pion gate was less than 5%. The threshold Cherenkov counter reduced this contamination by up to 10 times. Detection thresholds were 40 MeV/c for pions and 230 MeV/c for protons. Efficiency of the counter system was Monte Carlo calculated using the GEANT code. These particle counters are described in more detail in Ref. [11].

4 Event reconstruction and data selection

The experiment was carried out at the internal deuteron beam of the accelerator Nuclotron with the primary beam energy T_d between 1.5 and 2.2 GeV/nucl. In order to achieve aims of the experiment it is important to unambiguously identify two-body decays of the S_{11} resonance. This identification has been realized by measuring velocities and angles of emitted particles. We measured in coincidence two charged particles emitted in back-to-back directions from the target, with the angle between two arms of the setup near the open angle ($\Theta_{PK} = 180°$). Also a background was measured in another kinematic, with the angle $\Theta_{PK} = 170°$. Collected data have been converted to DST using a procedure described in [11] and then analyzed as follows. Types of particles were determined by evaluating their masses. The latter was done be measuring two independent kinematic quantities related to the particle mass, namely the velocity β and the kinetic energy T. The velocity was found from the time of flight. The kinetic energy of a charged particle, being proportional to its ionization losses in detectors, was found through a light yield from fired detectors:

$$\beta = \frac{L_{\text{start-stop}}}{c\, t_{\text{tof}}}; \quad T = \sum_{i=1}^{4} k_i \cdot (dE/dx)_i.$$

Here c is the speed of light, $L_{\text{start-stop}}$ is a time-of-flight base, and i numerates activated detectors. Finally, the particle mass was reconstructed as

$$M_{\text{rec}} = T \frac{\sqrt{1-\beta^2}}{1-\sqrt{1-\beta^2}}.$$

All particles with $0 < M_{\text{rec}} < 500$ MeV were then considered as pions ($M_{\text{rec}} \to m_\pi$);

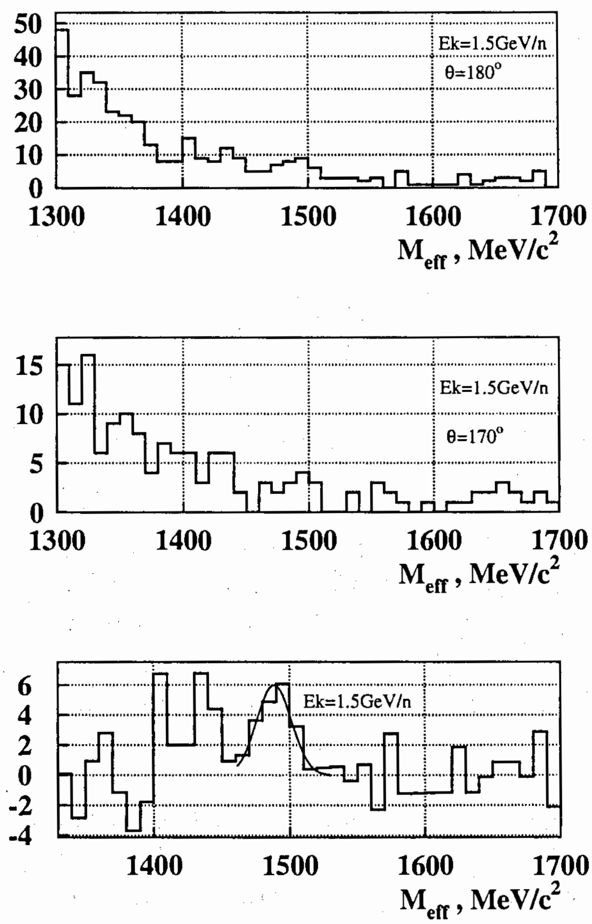

Figure 3: The effective mass in the region of the S_{11} resonance for $T_d = 1.5$ GeV/nucl.

particles with $500 < M_{\text{rec}} < 1500$ MeV were counted as protons ($M_{\text{rec}} \to m_p$), and those with $M_{\text{rec}} > 1500$ MeV were counted as deuterons. Thus found masses of two identified particles in both arms, m_1 and m_2, have then been applied to reconstruction of the effective mass M_{eff} (or the energy sum E_{sum}) of the pair,

$$M_{\text{eff}} = \frac{m_1}{\sqrt{1-\beta_1^2}} + \frac{m_2}{\sqrt{1-\beta_2^2}}.$$

As a result, three well separated peaks in M_{eff} were found corresponding to $\pi^{\pm}\pi^{\pm}$, $\pi^{\pm}p$ and pp pairs.

We performed coincidence measurements of yields of πN pairs emitted in the reaction (1) for two angles: $\Theta_{\pi N} = 180°$ and $\Theta_{\pi N} = 170°$. Found distribution of the yields over M_{eff} between 1300 and 1700 MeV/c^2 is shown in Fig. 3 using mass bins of 10 MeV/c^2. Only pairs in which each particle had the energy above 50 MeV were counted there. Top part of Fig. 3 corresponds to back-to-back correlated pairs ($\Theta = 180°$), middle part of the figure shows contaminations observed at the angle $\Theta = 170°$, and the bottom part gives the difference.

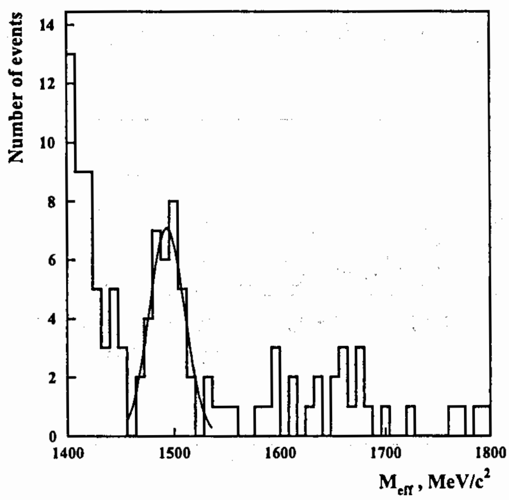

Figure 4: The effective mass in the region of the S_{11} resonance for $T_d = 1.9$ GeV/nucl (the difference of 180° and 170° yields).

The ratio of the pair yields with $\Theta = 170°$ and 180° was $N_{170}/N_{180} = 0.42 \pm 0.08$(stat) in the mass region of $1450 < M_{\text{eff}} \leq 1550$ MeV/c^2 at $T_d = 1.5$ GeV/nucl. It was $N_{170}/N_{180} = 0.11 \pm 0.04$(stat) at $T_d = 1.9$ GeV/nucl (Fig. 4).

Gaussian fits to the difference histograms give peaks at $M_{\text{eff}} = 1480 \pm 18$ MeV/c^2 with the width (sigma) of 23 MeV/c^2 for $T_d = 1.5$ GeV/nucl and $M_{\text{eff}} = 1493 \pm 4$ MeV/c^2, $\sigma = 38.3$ MeV/c^2 for $T_d = 1.9$ GeV/nucl. Within errorbars peak's parameters are identical.

Given the estimated energy-sum resolution of the setup for πp pairs, $\sigma(E_{\text{sum}}) \approx 10$ MeV, one can conclude that a peak at $E_{sum} \approx 1500$ MeV is seen as anticipated. Meanwhile the free $S_{11}(1535)$ state is not clearly observed. We can also conclude that the number of events recorded in the open angle geometry greatly exceeds the number of events recorded in the background position of detectors.

A much more statistically significant results were recently obtained for $d + A$ reactions at the beam energy $T_d = 2.1$ GeV/nucl. The geometry and other experimental conditions were the same as in the previous runs. Analysis of these data used dE-E and

TOF techniques and also information from Cherenkov counters to select π-mesons. In the region of $M_{\text{eff}} \approx 1450$ MeV/c^2 a peak is visible above a monotonically decreasing spectrum. A fit of the data with an exponent plus a gaussian function gives the peak position at 1447.8 ± 3.6 MeV/c^2 with the width 38.8 ± 10.4 MeV/c^2. Fig. 5 shows these data after subtraction of background. Given the energy resolution of the spectrometer, $\sigma(M_{\text{eff}}) = 10$ MeV/c^2, and systematic errors estimated as 10 MeV/c^2, we find these results consistent with those obtained previously at a lower energy of the accelerated beam.

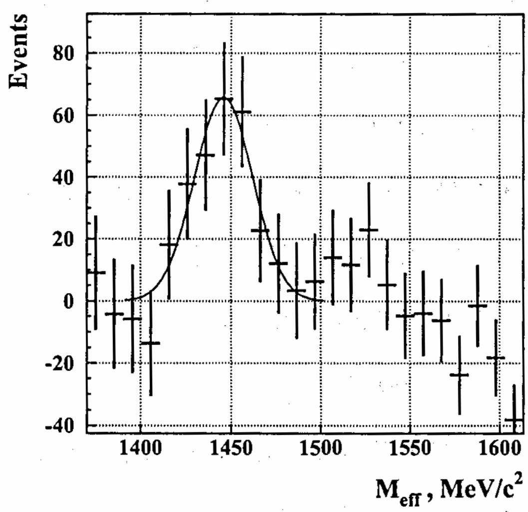

Figure 5: The effective mass of correlated πp pairs after background subtraction for $T_d = 2.1$ GeV/nucl.

The value of the total cross section can be estimated from the number of inelastic interactions $d + \mathrm{C}$. This number is determined from counts of the monitor telescopes and comparison with simulation results of the GEANT and RQMD codes. Histograms shown in Fig. 4 correspond to $N_{\text{in}} = (1.5 \div 2.2) \times 10^9$ inelastic interactions. Using the solid angle of the spectrometer ($\Omega \approx 8 \times 10^{-3}$ ster) and the cross section of inelastic dC interaction ($\sigma_{\text{in}} = 426 \pm 22$ mb for the energy 2.1 GeV/nucleon), one can roughly estimate the total cross section of πN production through intermediate η-nucleus formation as

$$\sigma(A_\eta) \approx \frac{4\pi}{\Omega} \frac{N_{\text{effect}} - N_{\text{backgr}}}{N_{\text{in}}} \sigma_{\text{in}} \approx 11 \pm 8\ \mu\text{b}.$$

This value is ~ 100 times smaller than expected in [6].

5 Summary

We have measured the energy-sum distribution of angular-correlated πp pairs emitted in the $d + \mathrm{C}$ reaction. We have clearly observed a distinct πp back-to-back correlation that may be associated with a two-body decay of η-mesic nuclei through the S_{11} resonance.

The resonance-like peak was observed in the spectrum of effective masses in the range 1400-1500 MeV/c^2. This peak is slightly different depending on the energy of the primary beam but the difference does not exceed experimental uncertainties. The resulting cross section was found to be considerably smaller than expected.

The obtained data is a good base for further studies of η-mesic nuclei at the internal beam of the Nuclotron.

References

[1] T. Hatsuda and S.H. Lee, Phys. Rev. C46 (1992), R34-R38

[2] C.J. Batty et al., Phys. Rep. 287, 385 (1997) 63-68

[3] A.I. L'vov, nucl-th/9809054 (1998).

[4] R.S. Hayano, S. Hirenzaki and A. Gillitzer, Eur. Phys. J. A6, 99 (1999)

[5] M. Pfeiffer et al., Phys.Rev.Lett. 92, 252001 (2004)

[6] M.Kh. Anikina et al., nucl-ex/0412036 (2004)

[7] G.A. Sokol et al., nucl-ex/0011005 (2001)

[8] T. Falter et al., Progress in Particle and Nuclear Physics 53 (2004) 25-44

[9] D. Jido, H. Nagahiro and S. Hirenzaki, Nucl. Phys., A 721 (2003) 665-668

[10] S.V. Afanasev et al., JINR Rapid. Comm., 5[91]- 98(1988) 25-28

[11] S.V. Afanasev and D.K. Dryablov, Particles and Nuclei, Letters 2[125](2005) 82-90

SHORT RANGE CORRELATIONS IN EXPERIMENTS WITH DEUTERONS AT INTERMEDIATE ENERGIES

M. Janek[a,1], V.P.Ladygin[b], L.S.Azhgirey[b], T.Uesaka[c], Yu.V.Gurchin[b], M.Hatano[d], K.Itoh[e], A.Yu.Isupov[b], J.-T.Karachuk[a,f], H.Kato[d], T.Kawabata[c], V.A.Krasnov[a,g], A.N.Khrenov[b], A.S.Kiselev[b], V.A.Kizka[b], J.Kliman[a,h], A.K.Kurilkin[b], P.K.Kurilkin[b], N.B.Ladygina[b], A.N.Livanov[a,g], Y.Maeda[c], A.I.Malakhov[b], V.Matousek[h], M.Morhach[a,h], J.Nishikawa[e], Yu.K.Pilipenko[b], T.Ohnishi[i], H.Okamura[j], S.M.Piyadin[b], S.G.Reznikov[b], T.Saito[d], S.Sakaguchi[c], H.Sakai[c,d], N.Sakamoto[i], S.Sakoda[d], Y.Sasamoto[c], Y.Satou[k], K.Sekiguchi[i], K.Suda[c], M.A.Shikhalev[b], A.Tamii[l], B.Trpisova[a], I.Turzo[h], N.Uchigashima[d], T.A.Vasiliev[b], K.Yako[d] and L.S.Zolin[b]

a) Physics Department, University of Zilina, Zilina, Slovakia
b) Joint Institute for Nuclear Research, Dubna, Russia
c) Center for Nuclear Study, University of Tokyo, Tokyo, Japan
d) Department of Physics, University of Tokyo, Tokyo, Japan
e) Department of Physics, Saitama University, Urawa, Japan
f) Advanced Research Institute for Electrical Engineering, Bucharest, Romania
g) Institute for Nuclear Research, Moscow, Russia
h) Institute of Physics Slovak Academy of Sciences, Bratislava, Slovakia
i) RIKEN (the Institute for Physical and Chemical Research), Saitama, Japan
j) CYRIC, Tohoku University, Sendai, Japan
k) Department of Physics, Tokyo Institute of Technology, Tokyo, Japan
l) Research Center for Nuclear Physics, Osaka University, Ibaraki, Japan

Abstract

Polarisation observables, vector and tensor analyzing powers obtained in experiments with deuterons at intermediate energies are presented. Obtained data are compared with different theoretical calculations. The simulation of dp breakup reaction is also presented.

1. Introduction

To describe the properties of nuclei and their reactions, the detailed knowledge about nuclear force is needed. The main goal of collaboration in investigation of the reaction induced by the deuterons is to investigate the nature of two nucleon (NN) and three nucleon (3N) forces, the role of the relativistic effects and nonucleon degrees of freedom.

The progress in exploring the nuclear force in both the theoretical and experimental investigations is remarkable. From the theoretical side, different theoretical approaches such as Chiral-Perturbation Theory (χPT), partial-wave analysis, and meson-exchange potentials are available.

Yukawa explained the pair-wise NN force as an exchange of a pion [1]. The attractive long range NN force is due to the exchange of pion. The exchange of two pions and heavier mesons (σ, ρ, ω, ...) is due to repulsive short range force.

The high precision measurements on few nucleon systems provide large sets of data which allow a systematic study. The modern NN potentials (e.g. CD-Bonn [2]) reproduced the NN scattering data up to 350 MeV with very good accuracy. But,

[1]E-mail: janek@fyzika.uniza.sk

these NN potentials, underestimate the binding energies of the three-nucleon systems ^{3}H and ^{3}He by about 0.5-1 MeV [3].

The investigation of the nd scattering at energies below 30 MeV has shown that the vector analyzing power A_y couldn't be described using any known NN potential. The inclusion of the 3N forces did not improve the situation either, leading to the well known A_y puzzle.

It has also been demonstrated that the cross section data of the pd elastic scattering obtained at 250 MeV cannot be reproduced by the Faddeev calculations [4]. The reason of this discrepancy can be neglecting of new type of short-range 3N force. These forces can be built within approaches beyond one-boson-exchange. In the dressed bag model [5] 3N force comes from the interaction between intermediate six-quark state dressed by σ-field and the third nucleon.

The cross sections and tensor analyzing powers of the of dp breakup reaction have been measured at 130 MeV [6]. There have been found large discrepancies between experimental data and calculations based on various NN and 3N potentials giving evidence of 3N force effects. It was shown that theoretical calculations based on χPT are able to describe data. But at this moment, this approach can be applied up to 100 MeV/nucleon. The description of NN and 3N correlations at the energies higher than several hundreds MeV/nucleon should be obtained within QCD.

2. dp elastic scattering

The vector A_y and tensor analyzing powers A_{yy} and A_{xx} for the dp elastic scattering have been measured at Internal Target Station at the Nuclotron at deuteron energy of 880 MeV (Figure. 1) and 2000 MeV (Figure. 2) in angular range from 60° to 140° in c.m.

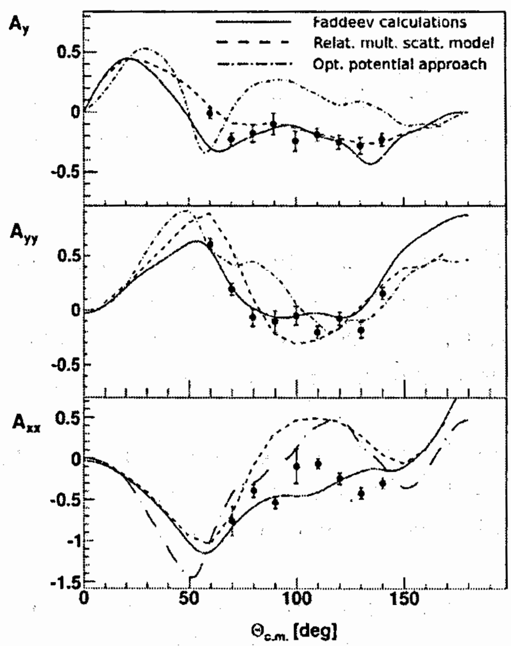

Figure 1: The angular dependencies of the vector A_y and tensor analyzing powers A_{yy} and A_{xx} for dp elastic scattering at energy 880 MeV.

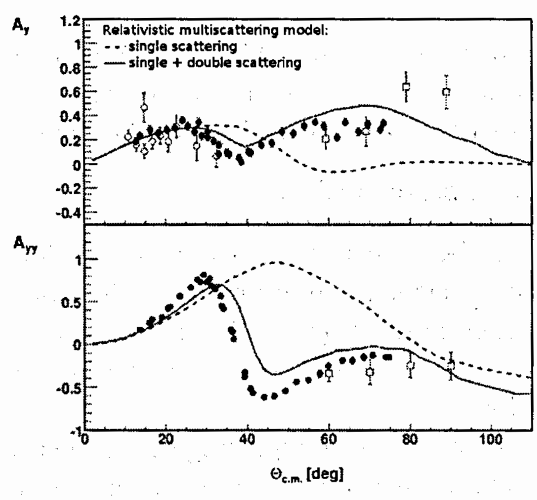

Figure 2: Vector A_y and tensor A_{yy} analyzing powers in dp-elastic scattering at 2000 MeV. The solid symbols represent the data obtained at ANL [7]. Open squares and circles are the data obtained at Internal Target Station [8] and at hydrogen bubble chamber at JINR, respectively.

The beam polarisation measurements has been performed at 270 MeV where the precise data on the vector and tensor analyzing powers exist. Results on the tensor analyzing powers at 880 MeV indicate strong deviations from the predictions of the relativistic phenomenological approaches [9, 10] based on the use of the NN forces only. The nonrelativistic Faddeev calculations [11] using CD-Bonn NN force [12] describe only the angular behavior of the new data for the analyzing powers. Differential cross section data obtained in earlier experiments [13, 14] cannot be described in full angular range. Deficiencies in the description of the differential cross section and the deuteron analyzing powers at 880 MeV obtained at quite large transverse momenta require the consideration of additional mechanisms of reaction. Such candidate can be 3N force.

The results on the vector A_y and tensor A_{yy} analyzing powers obtained at 2000 MeV are shown in Figure. 2. The solid (dashed) lines are the results of the relativistic multiple scattering model [15] with inclusion of single scattering term and with (without) the inclusion of the double scattering term. The reasonable agreement between data and calculations with the inclusion of the double scattering term is obtained.

3. dp breakup reaction

The dp breakup reaction will be investigated by the registration of two protons in coincidence by two detectors positioned at different angles with respect to the direction of motion of the deuteron beam at Nuclotron. The energies of the deuterons will be ranging from 300 MeV to 500 MeV. Eight ΔE–E detectors are planned. Each detector consists of two scintillators, thin – ΔE and thick – E. Both scintillators are of a tube shape, the thin one of a height of 1 cm, the thick one of a 20 cm height, with the diameter of the cross section 8 cm and 10 cm, respectively.

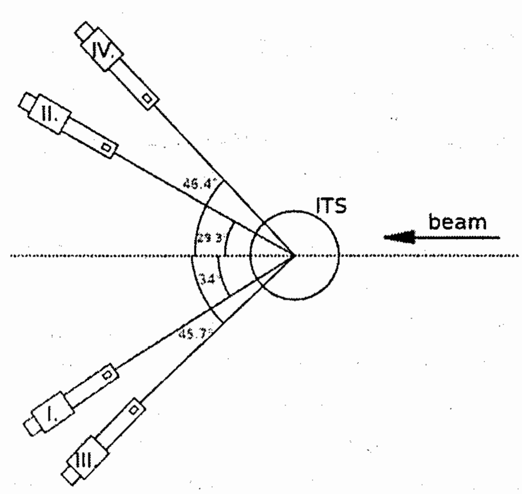

Figure 3: Position of the detectors at Internal Target Station at Nuclotron in the test run.

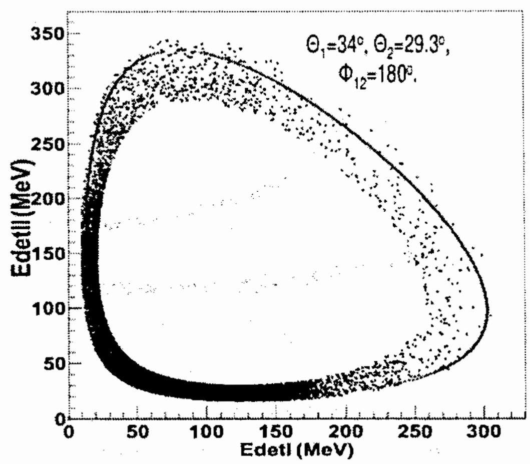

Figure 4: Energy correlation for two particles with the cut on neutron missing mass in case of configuration 12 (see Table. 1). Curve denotes the kinematic locus for the deuteron breakup reaction at 500 MeV deuteron energy.

configuration	Θ_1	Θ_2	Φ
12	31.7 – 36.3	27.0 – 31.6	180°
14	31.7 – 36.3	44.1 – 48.7	180°
23	27.0 – 31.6	43.4 – 48.0	180°

Table 1: Detector configurations description.

Two Photomultiplier tubes PMTs-85 will be positioned opposite to each other at the outside cylindrical surface of the thin scintillator At the free bottom of the E scintillator a photomultiplier tube PMT-63 will be positioned. The details of the ΔE–E detector construction are presented in [16]. Three configurations of the two ΔE–E detectors used in test run are presented in Table. 1. Θ_1 and Θ_2 denote azimuthal angles, Φ is polar angle. All detectors are located in the horizontal plane containing the mean orbit of the accelerator. Two targets, CH_2 and Carbon $10\mu m$ thick were used. The experiment with 4 ΔE-E detectors at Internal Target Station has been performed at the initial deuteron kinetic energy of 500 MeV on CH_2 target (Figure. 3). The calibration of ΔE+E detectors has been performed using cosmic muons just after the experiment at Nuclotron. The correlation of the particle energies are ploted with condition on mass of neutron $\pm$20 MeV (Figure. 4). Curve denotes kinematic locus for deuteron breakup reaction at 500 MeV of deuteron energy. Detector configuration is 12 (see Table. 1).

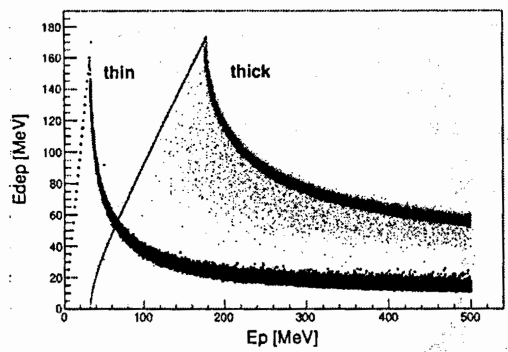

Figure 5: Dependence of deposited energy of protons on their incoming energy for the ΔE (thin) and E (thick) scintillator. For better clarity the data corresponding to the thin scintillator is ploted with five times enlarged values.

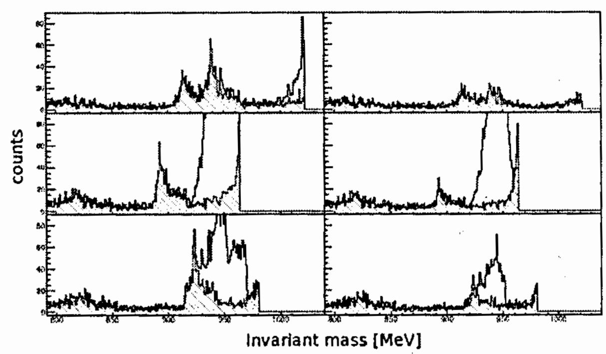

Figure 6: Invariant mass distribution of two particles obtained for CH_2 (black) and Carbon target (hatched) that were bombarded by deuterons of energy 500 MeV. The detector configurations are 12 (first row), 14 (second row) and 23 (third row), respectively. First (second) column is without (with) TOF cut applied.

The goal of simulation is to find criteria how to select our signal events and this should be done for various detector configurations at energies of 300 MeV, 400 MeV and 500 MeV. To accomplish this goal we have performed computer modelling using the GEANT4 toolkit [17]. In Figure. 5, the correlation of the energy of protons deposited in a ΔE–E detector and the energy with which they hit the detector, *i. e.* their incoming energy is presented.

To separate the signal from the background, we calculated the invariant mass of two particles. This resulted in most cases into a clear peak at about 940 MeV – the rest mass of neutron – in our dCH_2 spectra. To remove the background, we also performed simulations using a target made from Carbon. Thus by subtracting the dC spectra from the dCH_2 spectra the signal events could be selected. Signal events can be obtained in case of the deuteron energy of 300 MeV for different detector configurations. With increasing energy of deuteron beam, the energy of outgoing particles increased. Particles which have the energy larger than about 180 MeV imitates lower energy ones (see Figure. 5). Such particles occured mainly for the 400 MeV and 500 MeV of deuteron energy. One can applied time-of-flight cut in order to remove this events, but this approach mostly remove signal events (see right column in Figure. 6). Second approach is based on localisation of dp breakup events which don't have invariant mass around of 940 MeV (particles which have energy larger than 180 MeV) from simulation and than extract them by subtraction procedure with normalisation in regions where only Carbon content is located. As conclusion, both approaches are applicable, second approach can be used in low yields.

4. d d → ^{3}He n and d d → ^{3}H p reaction

The data on the analyzing powers in d d → ^{3}He n and d d → ^{3}H p reaction obtained at 270 and 200 MeV [18] are shown in Figure. 7. The curves are the calculation

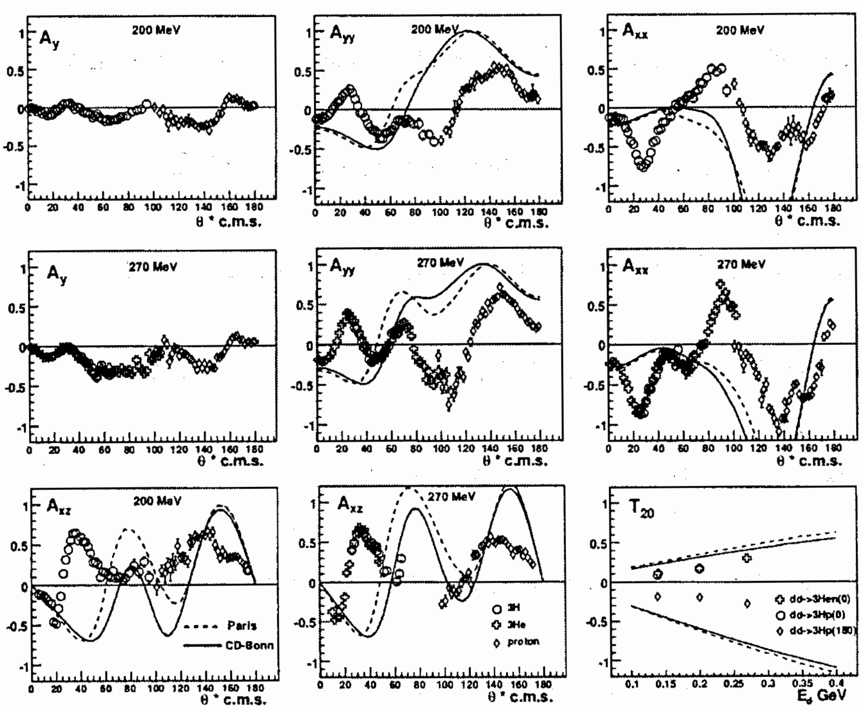

Figure 7: The analyzing powers data from d d → ^{3}He n and d d → ^{3}H p at 270 and 200 MeV [18]. The curves are the calculation within one nucleon exchange approximation [19].

within one-nucleon-exchange approximation using standard deuteron and ^{3}He (^{3}H) wave functions [20]. The data demonstrate the sensitivity to the D/S waves ratio in these light nuclei at short internucleonic distances. However, the calculations [20] fail to reproduce the data. The reason of the discrepancy can be in the non-adequateness of the 3N-bound state spin structure and/or more complicated reaction mechanism. The multiple scattering calculations are in progress now [19].

5. Conclusion and future plans

Important data on the short range correlations were obtained at Nuclotron. Future plans are connected with the construction of the new polarized deuteron source [21] with larger variety of the spin modes than POLARIS. With using polarized deuteron beam from new polarized deuteron source, the energy dependence of the polarization observables for the dp elastic and dp nonmesonic breakup reaction will be investigated. The $d^3He \to p^4He$ reaction is also interest. Polarization correlation coefficient $C_{//}$ in the energy region of 1.0 – 1.75 GeV is sensitive to deuteron D-state contribution. Strange structure in dp backward elastic scattering can be investigated with this setup.

References

[1] H. Yukawa, Proc. Phys. Math. Soc. Jap. **17**, 48, 1935.

[2] R. Machleidt, F. Sammarruca, and Y. Song, Phys. Rev. **C53**, R1483, 1996.

[3] A. Nogga, D. Huber, H. Kamada, and W. Glockle, Phys. Lett. **B409**, 19, 1997.

[4] K. Hatanaka, Y. Shimizu et al., Phys.Rev. **C66**, 044002, 2002.

[5] V.I. Kukulin et al., J. Phys. G: Nucl. Part. Phys. **30**, 287, 2004.

[6] St. Kistryn, A. Micherdzinska, R. Bieber et al., Phys. Rev. **C68**, 054004, 2003.

[7] M. Bleszynski et al., Phys.Lett. **B87**, 178, 1979.

[8] P. K. Kurilkin et al., Int.J.Mod.Phys. **A24**, 530, 2009.

[9] N. B. Ladygina, Phys. Atom. Nucl. **71**, 2039, 2008.

[10] M. A. Shikhalev, Phys. Atom. Nucl. **72**, 588, 2009.

[11] H. Witala, W. Glockle, J. Golak, A. Nogga, H. Kamada, R. Skibinski, J. Kuros-Zolnierczuk, Phys. Rev. **C63**, 024007, 2001.

[12] R. Machleidt, Phys. Rev. **C63**, 024001, 2001.

[13] N.E. Booth, et al., Phys. Rev. **D4**, 1261, 1971.

[14] J.C. Alder, et al., Phys. Rev. **C6**, 2010, 1972.

[15] N. B. Ladygina, Phys. Atom. Nucl. **71**, 2039, 2008.

[16] S. M. Piyadin et al., Physics of Particles and Nuclei Letters, Vol. **8**, no. 2, pp. 107-113, 2011.

[17] S. Agostinelli et al., Geant4 - a simulation toolkit, Nucl. Instrum. Meth. A, vol. **506**, no. 3, pp. 250-303, 2003.

[18] A.K. Kurilkin et al., Eur.Phys.J. **ST162**, 133, 2008; V. P. Ladygin et al., Phys.Lett. **B589**, 47, 2004; M. Janek et al., Eur.Phys.J. **A33**, 39, 2007.

[19] N. B. Ladygina, Eur.Phys.J. **A42**, 91, 2009.

[20] N. B. Ladygina, private communication.

[21] V. V. Fimushkin et al., Eur. Phys. J. **ST162**, 275, 2008.

NEW DATA OF THE $dp \to ppn$ REACTION AT 500 MEV ENERGY OF DEUTRON AT ITS AT NUCLOTRON.

S.M. Piyadin[a,1], M. Janek[a,b], B. Trpišová[b], Yu.V. Gurchin[a], A.Yu. Isupov[a], J.-T. Karachuk[a,c], A.N. Khrenov[a], V.A. Krasnov[a], A.K. Kurilkin[a], P.K. Kurilkin[a], V.P. Ladygin[a], A.N. Livanov[a], G. Martinska[d], S.G. Reznikov[a], A.A. Terekhin[a], T.A. Vasiliev[a].

a) LHEP-JINR, 141-980 Dubna, Moscow region, Russia
b) Physics Department, University of Žilina, Univerzitná 1, 010 26 Žilina, Slovakia
c) Advanced Research Institute for Electrical Engineering, Bucharest, Romania
d) P.J.Safarik University, Kosice, Slovakia

Abstract

The first results on the study of the dp-breakup reaction with 500 MeV unpolarized deuteron beam at Internal Target Station at Nuclotron-M are discussed. Selection procedure of useful events for the $dp \to ppn$ reaction with the registration of two protons is shown. Further scientific program with polarized and unpolarized deuterons is discussed.

1. Introduction

The purpose of Deuteron Spin Structure experimental program is to obtain the information on the spin dependent parts of 2-nucleon and 3-nucleon forces from two processes: *dp*-elastic scattering in a wide energy range and *dp* non-mesonic breakup with two protons detection at energies 200 - 500 MeV[1].

Properties of few-nucleon system at moderate energies are determined mainly by pairwise nucleon-nucleon(NN) interactions. Models of NN forces describe the long range interaction part according to the meson-exchange, while the short range is based on phenomenology, adjusted by fitting a certain number of parameters to the NN scattering data. Nowadays a new generation of the NN potentials (AV-18[2], CD-Bonn[3], Nijmegen[4] etc.) was obtained. They reproduce data on the nucleon-nucleon scattering up to 350 MeV with very good accuracy. However, these modern 2N forces fail to provide the experimental binding energies of few-nucleon systems. Moreover, the data on the *dp*- elastic scattering and deuteron breakup are not described properly.

Precise predictions for observables in the $3N$ system can be obtained via exact solutions of the $3N$ Faddeev equations for any nucleon-nucleon (NN) interaction, even with the inclusion of a 3 nucleon forces($3NF$) model[5]. Incorporation of the $3NF$ makes it possible to reproduce the binding energy of the three-nucleon bound systems and also data on unpolarized *dp*- interaction. Nevertheless, polarization data for the reactions with participation of three and more nucleons are not described even with inclusion of $3NF$. Therefore, the obtaining of the additional polarization data in the *dp*- interaction in the wide energy range more is very desirable for the study of the spin structure of $2N$ and $3N$ forces[6]. To investigate the details of the dynamics of the $3N$ system, in addition to elastic Nd scattering data, reliable deuteron breakup data sets, covering large regions of the available phase space, are needed.

The experimental data on the deuteron analyzing powers for large phase space were obtained at 130 MeV at KVI[7]. The predictions for analyzing powers and differential

[1]E-mail: piyadin@jinr.ru

cross section in the selected *dp*-breakup configurations at 200 MeV were obtained in [8]. It was shown large sensitivity of these observables to the model of $3NF$. The cross section, A_y, A_{yy} and A_{xx} analyzing powers in *dp*-breakup will be measured at Internal Target Station(ITS) at Nuclotron at 200-500 MeV [9].

2. The experimental setup.

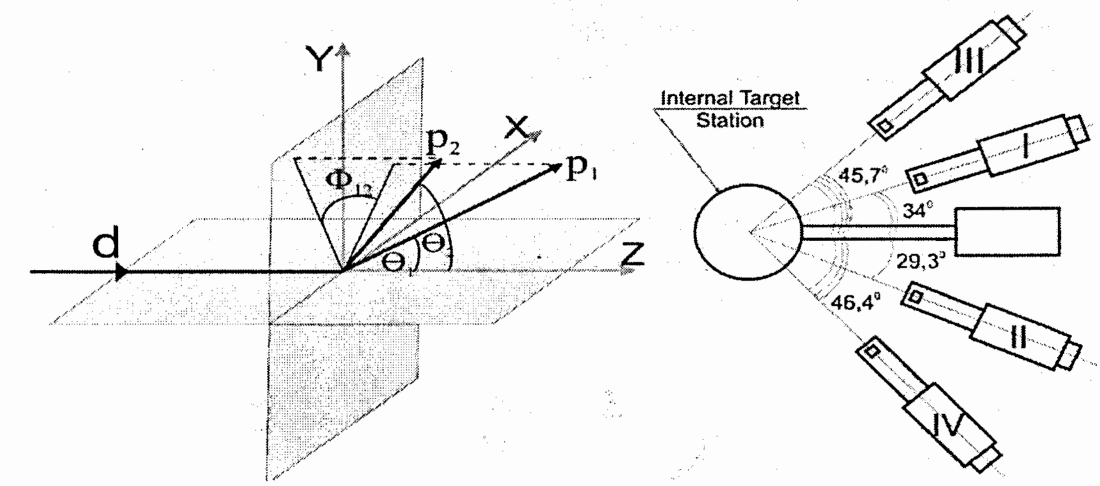

Figure 1: Detection angles for registration of two protons and the position of the detectors at Internal Target Station at Nuclotron.

The *dp* breakup reaction will be investigated using ΔE-E techniques for the detection of protons. 8 detectors of this kind are planned to be used in the experiment. The details of the ΔE-E detector construction are presented in [9].

The experiment with 4 ΔE-E detectors at ITS has been performed at the initial deuteron kinetic energy of 500 MeV on CH_2 target. During this experiment the DAQ-system based on the VME - standard has been used. The detection angles for registration of two protons and the position of the detectors at Internal Target Station at Nuclotron for study reaction $dp \to ppn$ are presented in Fig.1.

All detectors were located in the horizontal plane containing the mean orbit of the accelerator. The correlations of ΔE+E energies depositions in MeV in different detectors for 6 possible kinematics configurations are presented in Fig.2. The calibration of ΔE+E detectors has been performed using cosmic muons just after the experiment at Nuclotron. ΔE energies were obtained as a half-sum of the integrated amplitudes from 2 PMTs-85 viewing the thin scintillator.

2. Results at 500 MeV.

The energy losses of the protons which passes through the scintillators are presented in Fig3. In (b) figure the energy losses of the proton in thin scintillator are plotted

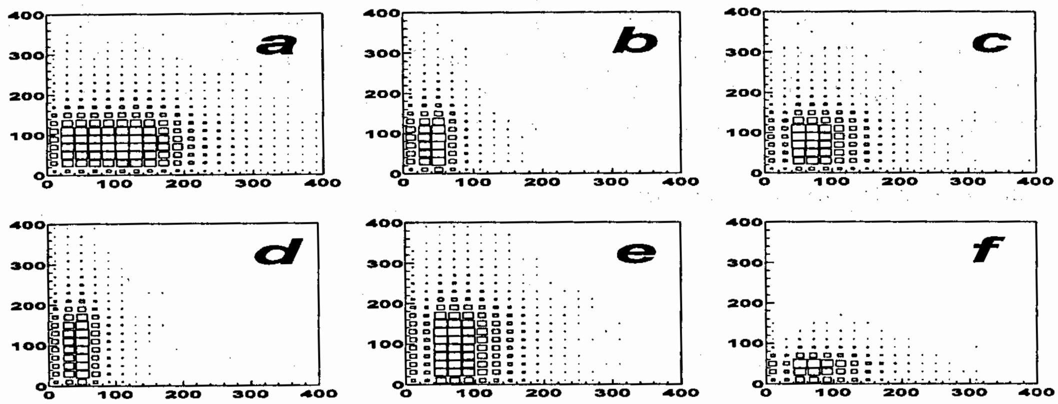

Figure 2: The correlations of the energies from 4 ΔE-E-detectors. a) - $\Theta_1 = 34^o$, $\Theta_2 = 29{,}3^o$, $\Phi_{12} = 180^o$. b) - $\Theta_1 = 34^o$, $\Theta_2 = 45{,}7^o$, $\Phi_{12} = 0^o$. c) - $\Theta_1 = 34^o$, $\Theta_2 = 46{,}4^o$, $\Phi_{12} = 180^o$. d) - $\Theta_1 = 29{,}3^o$, $\Theta_2 = 45{,}7^o$, $\Phi_{12} = 180^o$. e) - $\Theta_1 = 29{,}3^o$, $\Theta_2 = 46{,}7^o$, $\Phi_{12} = 0^o$. f) - $\Theta_1 = 45{,}7^o$, $\Theta_2 = 46{,}4^o$, $\Phi_{12} = 180^o$.

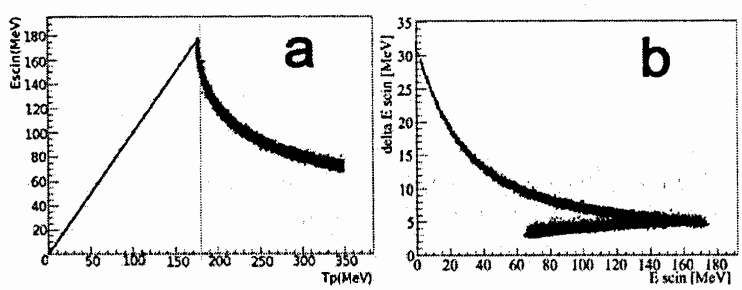

Figure 3: The energy losses of the protons passed through ΔE and E scintillators. a - energy losses of the proton when the length of a scintillator is 21 cm ($\Delta E + E$). b - energy losses of protons presented in thin scintillator versus thick.

versus ones the thick scintillator. For selects of linear dependence are imposed the following conditions on the ΔE and E information ($5 < \Delta E < 35$ and $0 < E < 180$).

The procedure of the useful events separation for $dp \rightarrow ppn$ reaction was established as following. The missing mass of the neutron has been obtained by kinematic formulas. Fig.4 presents the neutron missing mass for detectors pairs in this the angular configuration ($\Theta_1 = 34^o$, $\Theta_2 = 46{,}4^o$, $\Phi_{12} = 180^o$.) with imposing of the cut on amplitudes. The correlation of the energies were plotted with the criteria on mass of neutron ($\pm$ 10 MeV).

Correlation of the proton energies with the cut on missing mass of the neutron is presented in Fig 5. Black curve is the kinematic locus for the deuteron breakup reaction at 500 MeV energy for the kinematic configuration ($\Theta_1 = 34^o$, $\Theta_2 = 46{,}4^o$,

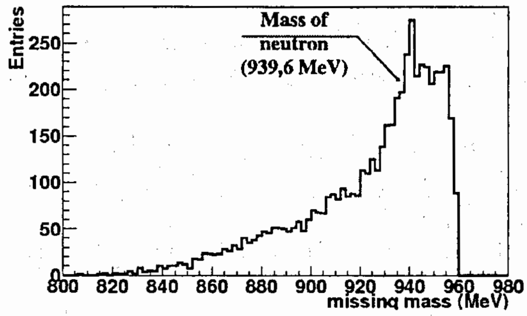

Figure 4: Missing mass of the neutron for the kinematical configuration $\Theta_1 = 34^o$, $\Theta_2 = 46{,}4^o$, $\Phi_{12} = 180^o$.

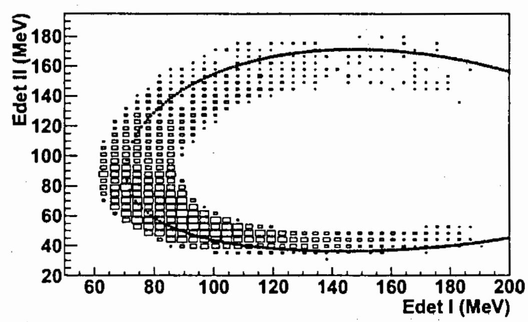

Figure 5: Correlation of the proton energies with the cut on the missing mass of the neutron ± 10 MeV.

$\Phi_{12} = 180^o$).

3. Conclusion.

The setup on the study of deuteron non-mesonic breakup reaction was put into operation. The first results for $dp \longrightarrow ppn$ reaction at 500 MeV for the complanar geometry at Internal Target Station at Nuclotron were obtained. The procedure of the useful events separation for $dp \longrightarrow ppn$ reaction was established.

The future plans are to increase the number of detectors up to 8 and to obtain the data on the deuteron breakup reaction at energy 300 - 500 MeV at Nuclotron.

The work has been supported in part by RFBR under grant N^o 10-02-00087a.

References

[1] V.P. Ladygin et al., EPJ Web Conferences 3, **3**, (2010), 04004

[2] R.B. Wiringa, V.G.J. Stoks, and R. Schiavilla., Rhys. Rev. **C51**, (1995) 38.

[3] R. Machleidt, Phys.Rev. **C63**, (2001) 024001.

[4] V.G.J. Stoks, R.A.M. Klomp, C.P.F. Terheggen, and J.J. de Swart., Rhys. Rev. **C49**, (1994) 2950.

[5] W. Glockle, H. Witala, D. Huber, H. Kamada, and J.Golak, Phys. Rep. **274**, (1996), 107.

[6] T. Uesaka, V.P. Ladygin, et al., Phys.Part.Nucl.Lett. **3**, (2006) 305.

[7] St. Kistryn et al., Phys.Rev. **C72**, (2005), 044006.

[8] J. Kuros-Zolnierczuk et al., Phys.Rev., (2005), 044006

[9] S.M. Piyadin et al., Phys.Part.Nuc.Lett., **8**, (2011), 107

NEW DATA OF THE $dp \to ppn$ REACTION AT 500 MEV ENERGY OF DEUTRON AT ITS AT NUCLOTRON.

S.M. Piyadin[a,1], M. Janek[a,b], B. Trpišová[b], Yu.V. Gurchin[a], A.Yu. Isupov[a], J.-T. Karachuk[a,c], A.N. Khrenov[a], V.A. Krasnov[a], A.K. Kurilkin[a], P.K. Kurilkin[a], V.P. Ladygin[a], A.N. Livanov[a], G. Martinska[d], S.G. Reznikov[a], A.A. Terekhin[a], T.A. Vasiliev[a].

a) LHEP-JINR, 141-980 Dubna, Moscow region, Russia
b) Physics Department, University of Žilina, Univerzitná 1, 010 26 Žilina, Slovakia
c) Advanced Research Institute for Electrical Engineering, Bucharest, Romania
d) P.J.Safarik University, Kosice, Slovakia

Abstract

The first results on the study of the dp-breakup reaction with 500 MeV unpolarized deuteron beam at Internal Target Station at Nuclotron-M are discussed. Selection procedure of useful events for the $dp \to ppn$ reaction with the registration of two protons is shown. Further scientific program with polarized and unpolarized deuterons is discussed.

1. Introduction

The purpose of Deuteron Spin Structure experimental program is to obtain the information on the spin dependent parts of 2-nucleon and 3-nucleon forces from two processes: *dp*-elastic scattering in a wide energy range and *dp* non-mesonic breakup with two protons detection at energies 200 - 500 MeV[1].

Properties of few-nucleon system at moderate energies are determined mainly by pairwise nucleon-nucleon(NN) interactions. Models of NN forces describe the long range interaction part according to the meson-exchange, while the short range is based on phenomenology, adjusted by fitting a certain number of parameters to the NN scattering data. Nowadays a new generation of the NN potentials (AV-18[2], CD-Bonn[3], Nijmegen[4] etc.) was obtained. They reproduce data on the nucleon-nucleon scattering up to 350 MeV with very good accuracy. However, these modern 2N forces fail to provide the experimental binding energies of few-nucleon systems. Moreover, the data on the *dp*- elastic scattering and deuteron breakup are not described properly.

Precise predictions for observables in the $3N$ system can be obtained via exact solutions of the $3N$ Faddeev equations for any nucleon-nucleon (NN) interaction, even with the inclusion of a 3 nucleon forces($3NF$) model[5]. Incorporation of the $3NF$ makes it possible to reproduce the binding energy of the three-nucleon bound systems and also data on unpolarized *dp*- interaction. Nevertheless, polarization data for the reactions with participation of three and more nucleons are not described even with inclusion of $3NF$. Therefore, the obtaining of the additional polarization data in the *dp*- interaction in the wide energy range more is very desirable for the study of the spin structure of $2N$ and $3N$ forces[6]. To investigate the details of the dynamics of the $3N$ system, in addition to elastic Nd scattering data, reliable deuteron breakup data sets, covering large regions of the available phase space, are needed.

The experimental data on the deuteron analyzing powers for large phase space were obtained at 130 MeV at KVI[7]. The predictions for analyzing powers and differential

[1]E–mail: piyadin@jinr.ru

cross section in the selected dp-breakup configurations at 200 MeV were obtained in [8]. It was shown large sensitivity of these observables to the model of $3NF$. The cross section, A_y, A_{yy} and A_{xx} analyzing powers in dp-breakup will be measured at Internal Target Station(ITS) at Nuclotron at 200-500 MeV [9].

2. The experimental setup.

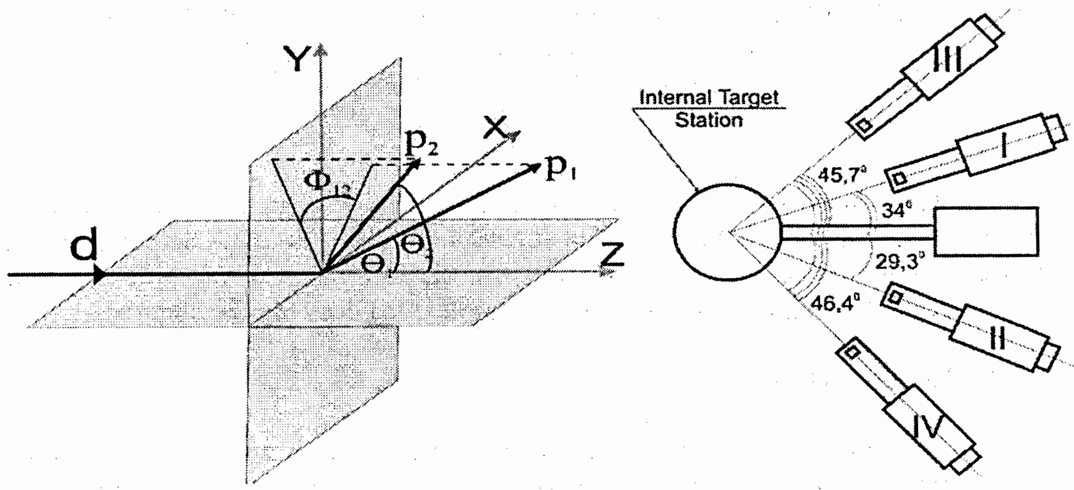

Figure 1: Detection angles for registration of two protons and the position of the detectors at Internal Target Station at Nuclotron.

The dp breakup reaction will be investigated using ΔE-E techniques for the detection of protons. 8 detectors of this kind are planned to be used in the experiment. The details of the ΔE-E detector construction are presented in [9].

The experiment with 4 ΔE-E detectors at ITS has been performed at the initial deuteron kinetic energy of 500 MeV on CH_2 target. During this experiment the DAQ-system based on the VME - standard has been used. The detection angles for registration of two protons and the position of the detectors at Internal Target Station at Nuclotron for study reaction $dp \to ppn$ are presented in Fig.1.

All detectors were located in the horizontal plane containing the mean orbit of the accelerator. The correlations of ΔE+E energies depositions in MeV in different detectors for 6 possible kinematics configurations are presented in Fig.2. The calibration of ΔE+E detectors has been performed using cosmic muons just after the experiment at Nuclotron. ΔE energies were obtained as a half-sum of the integrated amplitudes from 2 PMTs-85 viewing the thin scintillator.

2. Results at 500 MeV.

The energy losses of the protons which passes through the scintillators are presented in Fig3. In (b) figure the energy losses of the proton in thin scintillator are plotted

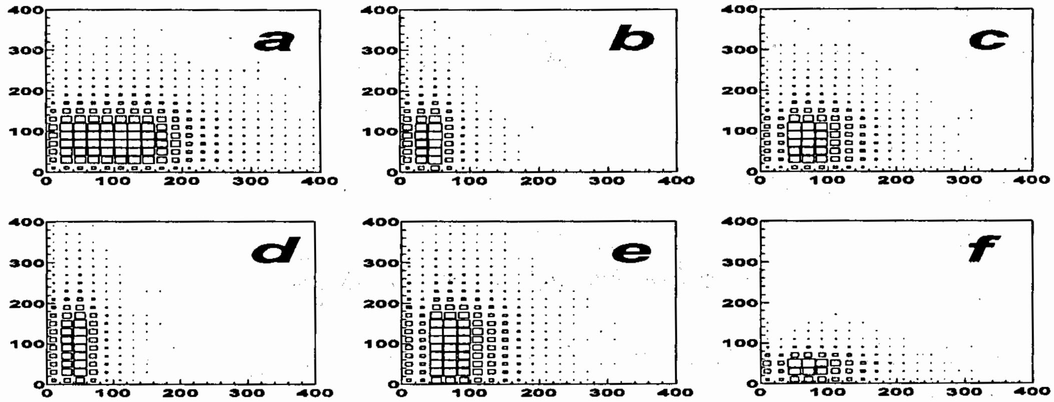

Figure 2: The correlations of the energies from 4 ΔE-E-detectors. a) - Θ_1 = 34°, Θ_2 = 29,3°, Φ_{12} = 180°. b) - Θ_1 = 34°, Θ_2 = 45,7°, Φ_{12} = 0°. c) - Θ_1 = 34°, Θ_2 = 46,4°, Φ_{12} = 180°. d) - Θ_1 = 29,3°, Θ_2 = 45,7°, Φ_{12} = 180°. e) - Θ_1 = 29,3°, Θ_2 = 46,7°, Φ_{12} = 0°. f) - Θ_1 = 45,7°, Θ_2 = 46,4°, Φ_{12} = 180°.

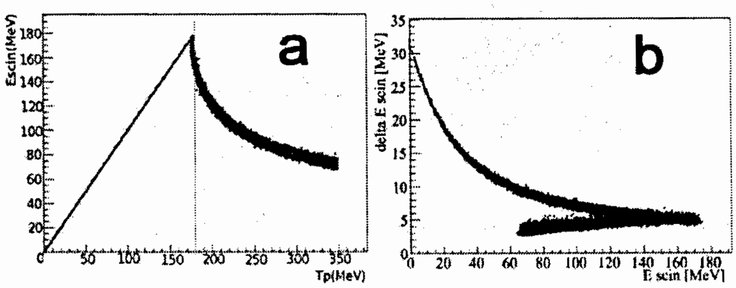

Figure 3: The energy losses of the protons passed through ΔE and E scintillators. a - energy losses of the proton when the length of a scintillator is 21 cm (ΔE + E). b - energy losses of protons presented in thin scintillator versus thick.

versus ones the thick scintillator. For selects of linear dependence are imposed the following conditions on the ΔE and E information ($5 < \Delta E < 35$ and $0 < E < 180$).

The procedure of the useful events separation for $dp \rightarrow ppn$ reaction was established as following. The missing mass of the neutron has been obtained by kinematic formulas. Fig.4 presents the neutron missing mass for detectors pairs in this the angular configuration (Θ_1 = 34°, Θ_2 = 46,4°, Φ_{12} = 180°.) with imposing of the cut on amplitudes. The correlation of the energies were plotted with the criteria on mass of neutron (± 10 MeV).

Correlation of the proton energies with the cut on missing mass of the neutron is presented in Fig 5. Black curve is the kinematic locus for the deuteron breakup reaction at 500 MeV energy for the kinematic configuration (Θ_1 = 34°, Θ_2 = 46,4°,

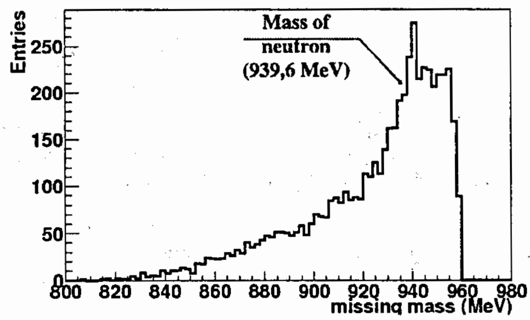

Figure 4: Missing mass of the neutron for the kinematical configuration $\Theta_1 = 34^o$, $\Theta_2 = 46{,}4^o$, $\Phi_{12} = 180^o$.

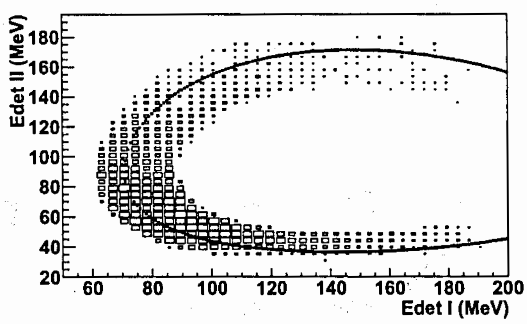

Figure 5: Correlation of the proton energies with the cut on the missing mass of the neutron ± 10 MeV.

$\Phi_{12} = 180^o$).

3. Conclusion.

The setup on the study of deuteron non-mesonic breakup reaction was put into operation. The first results for $dp \rightarrow ppn$ reaction at 500 MeV for the complanar geometry at Internal Target Station at Nuclotron were obtained. The procedure of the useful events separation for $dp \rightarrow ppn$ reaction was established.

The future plans are to increase the number of detectors up to 8 and to obtain the data on the deuteron breakup reaction at energy 300 - 500 MeV at Nuclotron.

The work has been supported in part by RFBR under grant N^o 10-02-00087a.

References

[1] V.P. Ladygin et al., EPJ Web Conferences 3, **3**, (2010), 04004

[2] R.B. Wiringa, V.G.J. Stoks, and R. Schiavilla., Rhys. Rev. **C51**, (1995) 38.

[3] R. Machleidt, Phys.Rev. **C63**, (2001) 024001.

[4] V.G.J. Stoks, R.A.M. Klomp, C.P.F. Terheggen, and J.J. de Swart., Rhys. Rev. **C49**, (1994) 2950.

[5] W. Glockle, H. Witala, D. Huber, H. Kamada, and J.Golak, Phys. Rep. **274**, (1996), 107.

[6] T. Uesaka, V.P. Ladygin, et al., Phys.Part.Nucl.Lett. **3**, (2006) 305.

[7] St. Kistryn et al., Phys.Rev. **C72**, (2005), 044006.

[8] J. Kuros-Zolnierczuk et al., Phys.Rev., (2005), 044006

[9] S.M. Piyadin et al., Phys.Part.Nuc.Lett., **8**, (2011), 107

EXPERIMENTS TO STUDY THE DENSE BARYONIC MATTER AT NUCLOTRON

A.ATerekhin[1], S.M.Piyadin,V.P.Ladygin, A.N.Khrenov, A.Yu.Isupov, Yu.V.Gurchin, V.A.Krasnov, A.K.Kurilkin, P.K.Kurilkin, S.G.Reznikov, T.A.Vasiliev.

JINR, 141980, Dubna, Moscow region, Russia

Abstract

The results of preparation of the experiments at extracted beam and internal target station at Nuclotron-JINR are reported. First extraction of the 3.42 A·GeV carbon beam and of the 4 A·GeV deuteron beam at Nuclotron and their transportation to the beam experimental area as well as the measurements of dp-elastic scattering, dW- and dAg- quasi-elastic scattering at internal target station at Nuclotron are performed.

The study of the strange matter in heavy-ion collisions at the beam energies from 2 to 6 A·GeV is main direction of BM@N project [1]. Installation of experimental setup at the 6V beamline in the fixed-target hall at Nuclotron is proposed. The basic setup will include the set of magnets and detector system. Namely small and large-acceptance dipole magnets, tracking detector modules, trigger and time-of-flight systems. The researches at this setup are focused to understanding the strange matter.

The goal of DSS project [2] is the systematic study of the polarization observables in hadronic reactions by using polarized deuteron beam and polarized ^3He - target [3] at intermediate and high energies. The experiment to measure T_{20} and C_{yy} for the $^3He(d,p)^4He$ - reaction at 1.0-2.0 GeV deuterons energy is planned. The results of this experiment will help to understand the short-range deuteron spin structure. In addition the study of deuterons interaction with protons and nuclei is included in DSS project.

In this paper the results of first extraction of the 3.42 A·GeV carbon beam and of the 4 A·GeV deuteron beam [4] at Nuclotron and their transportation to the beam experimental area are reported. The measurements of dp-elastic scattering, dW- and dAg- quasi-elastic scattering at internal target station at Nuclotron are presented.

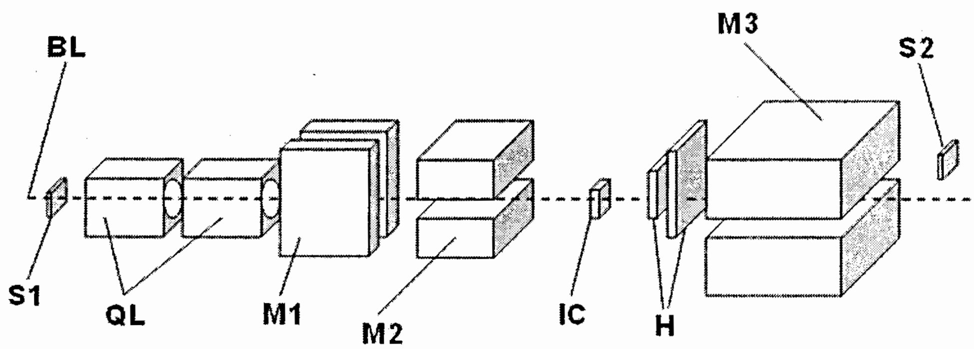

Figure 1: The layout of the experiment. **BL** is the optical axis of the 6V beam line, **QL** and **M1-M3** are the quadrupole and dipole magnets, respectively. **IC** is the coordinate ionization chamber, **S1** and **S2** are the start- and stop- scintillation counters, respectively, **H** are 2 planes of the scintillation counters hodoscopes.

[1]E–mail: aterekhin@jinr.ru

The magnetic scheme of the 6V line is shown in Fig. 1. The experimental setup of the experiment is placed at the distance of about 110 m from the ring of Nuclotron. The doublet of quadrupole magnets (QL) allows to focus the beam. Two small dipole magnets M1 and M2 can deflect the beam in the horizontal and vertical directions. The large aperture magnet SP41 (GIBS magnet, M3) can be used as an analyzing magnet.

The start scintillation counter S1 is based on the use of XP2020 PMT. The stop scintillation counter S2 is based on the use of PMT FEU-87. The additional multi-wire ionization chamber (IC) and two scintillation hodoscopes (H) are installed in the experimental area.

The first and second hodoscopes provided the coordinate measurements in the horizontal and vertical planes, respectively. Each hodoscope (see Fig. 2) consist of 8 scintillators with the size of 400x40x4 mm^3 viewed by PMTs FEU-85 from both sides each [5].

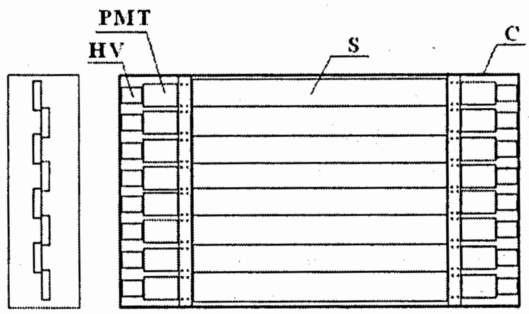

Figure 2: The scheme of the hodoscope. Left: profile of the hodoscope. Right: the layout of the hodoscope. **C**-case, **HV**-cells of high-voltage power,**PMT** - photomultipliers FEU-85, **S**-scintillation plates

The VME based data acquisition system was used for the data taking from scintillation detectors. 16 - channel time and charge digitizer (TQDC16) allows to measure the amplitude and time appearance of the signal [6].

The carbon- and deuteron- beams with energies 3.42 and 4 A·GeV respectively were successfully transported to 6V - area. The correlation of the signal amplitudes taken from the both sides of one of the scintillation detector of hodoscope for carbon nuclei beam is shown in Fig. 3.

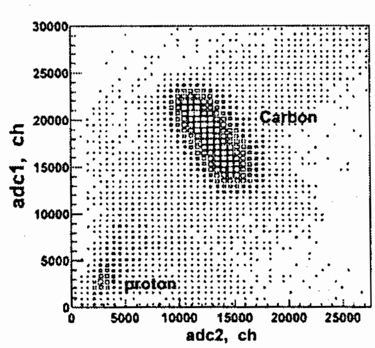

Figure 3: The signal amplitudes correlation for carbon nuclei beam for one of the scintillation detector of the hodoscope.

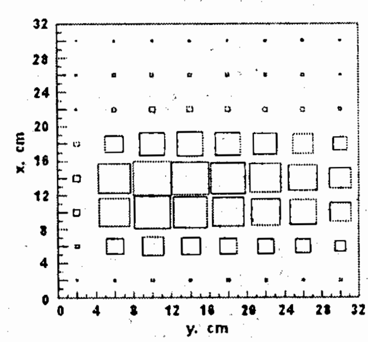

Figure 4: The X-Y coordinates correlation for carbon nuclei.

One can see the clean separation of the primary carbon nuclei and background single charged particles. The X-Y coordinates correlation for carbon nuclei was plotted (see Fig. 4). One can see that the size of the carbon beam in Y- direction is wider. The amplitude distribution for the deuteron beam (see Fig. 5) is corresponded to amplitude distribution for the single charged particles in Fig.3. The inclusion of quadrupole magnetic lenses allowed to reduce the size of the beam (see. Fig 6).

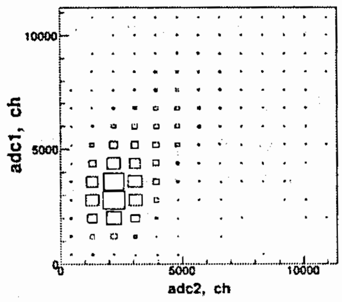

Figure 5: The signal amplitudes correlation for deuteron beam for one of the scintillation detector of the hodoscope.

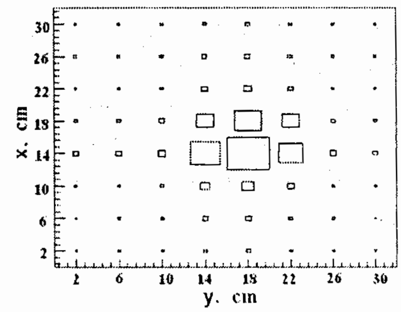

Figure 6: The X-Y coordinates correlation for deuteron beam.

In addition the methodical measurements to obtain of the differential cross section for dp-elastic scattering at the ITS was performed. The measurements have been performed by using CH_2-target and deuteron beam at 1GeV/nucleon energy. The dp- and pp-detectors were mounted at angle $\theta^* = 75^o$ and $\theta^* = 90^o$ in the c.m.s., respectively. Subtraction of the time signal taken from the D- and P- detectors for counters based on the FEU -85 and counters based on the Hamamatsu H7416MOD is shown in Fig.7 and Fig. 8 respectively. One can see, that the dp-elastic scattering events and background are not selected in the case of the measurements with the counters based on the FEU -85 unlike the counters based on the Hamamatsu H7416MOD.

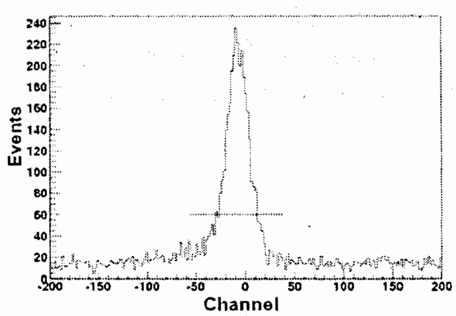

Figure 7: Subtraction of the time signal from D- and P- counters. The data were obtained by using the counters based on the FEU-85.

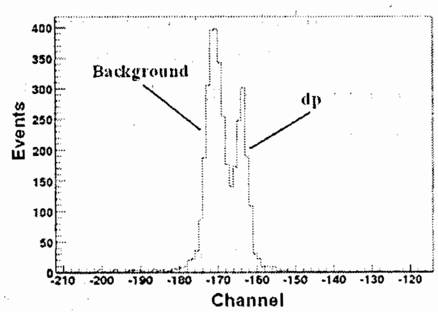

Figure 8: The subtraction of the time signal from D- and P- counters. The data were obtained by using the counters based on the Hamamatsu H7416MOD.

The anomalous pion yield is observed in the interaction of protons and deuterons with nuclei [7]. The experiment at ITS with DELTON setup [8] on the measurement of the pion yield in the interact of deuterons with W and Ag nuclei was performed in 2011 - 2012 years. During these experiments the energy dependence of the dp- and pp-yield in dW and dAg - interactions have been measured. The reaction products were registered by the scintillation counters. Each counter consist of two detectors with thin and thick scintillators [9]. First particle passes in a thin plastic scintillator and then in thick plastic scintillator. The thin scintillator is used to clean background. The set of detectors to register reaction products is placed in horizontal plane. D- and P- counters are to register dp-elastic scattering. PPL and PPR - to register pp- quasi-elastic scattering. The monitor-counters are mounted in the vertical plane. The results of these measurements are shown in Fig. 9 and Fig 10, respectively. Any anomalous effect isn't observed for studied channels.

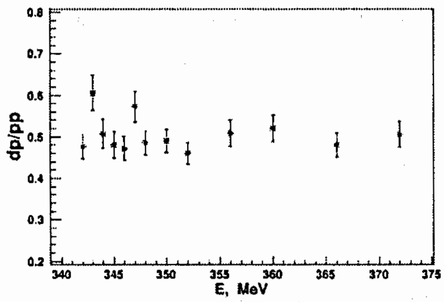

Figure 9: Energy dependences of the dp- to pp-quasi-elastic yields ratio for dW-interaction.

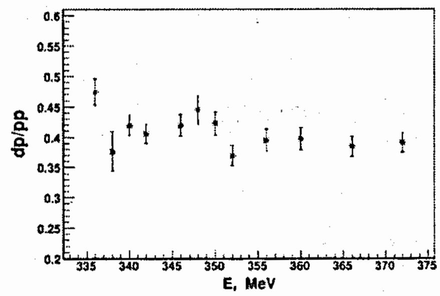

Figure 10: Energy dependences of the dp- to pp-quasi-elastic yields ratio for dAg-interaction.

Measurements with the omission of target cycles was performed in regime of the simultaneous run at ITS and at the extracted beam setup. The target was injected out from the beam every third, every second and every fourth cycle. One can see in Fig.11 the statistic of the extracted beam setup is increased when the target doesn't cross beam, unlike the statistic of ITS setup.

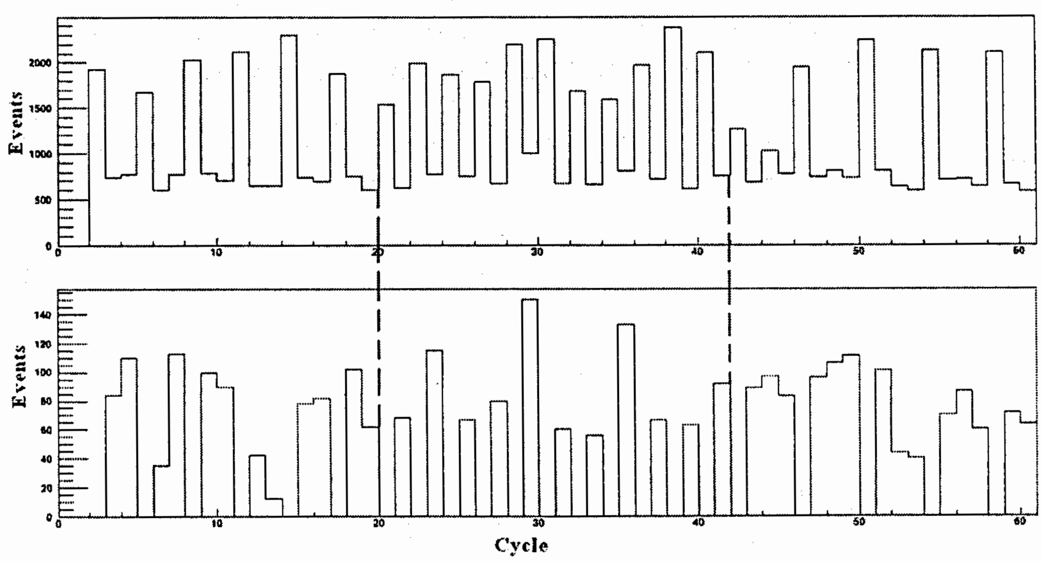

Figure 11: Distribution of events over cycles recording. Upper - for extracted beam setup, bottom - for ITS

In summary, first extraction of the 3.42 A·GeV carbon beam and 4 A·GeV deuteron beam at Nuclotron and their transportation to the BM@N experimental area are performed. The measurements of dp-elastic scattering, dW- and dAg- quasi-elastic scattering at internal target station at Nuclotron are performed. Energy dependences of dp- and pp-quasi-elastic scattering yields ratio are measured. Any anomalous effect isn't observed for these channels. The regime of the beam sharing between the experiment at ITS and extracted beam is realized. The simultaneous work of the ITS and extracted beam setup is demonstrated.

We thanks J.Lukstins and A.N. Livanov for their help during preparation of the experiment.

The work has been supported in part by the RFBR grant 10-02-00087a.

References

[1] http://nica.jinr.ru

[2] V.P. Ladygin et al. *Short-range correlation studies in collisions of polarized nuclei at Nuclotron-M*, *EPJ* Web of Conferences 2010. **3**. 04004.

[3] T. Uesaka et al. Nucl.Instr.Meth. in Phys.Res. **A402** (212) 1998.

[4] S.M. Piyadin et al. *First extraction of the 3.42 AGeV C beam for studies of baryonic matter at Nuclotron*, JINR Preprint **E1-2012-17** 2012.

[5] A.A. Terekhin et al. *Scintillation hodoscope for experiments at extracted beam at Nuclotron JINR*, BSU Scientific bulletin, MathematicsPhysics **11(130)** (207) 2012.

[6] http://afi.jinr.ru/TQDC-16

[7] V.A. Krasnov et al. *Search for resonant structure in the pion production reaction on the Nuclotron internal beam*, Int.J.Mod.Phys. **A22** (604) 2007

[8] V.A. Krasnov et al. *Multilayer Scintillation Charge Pions Spectrometer*, JINR Preprint **P13-2011-135** 2011.

[9] Yu.V. Gurchin et al. *Study of the possibility to use d p-elastic scattering for the nuclotron external deuteron beam polarimetry*, Phys.Part.Nucl.Lett. **8** (566) 2011.

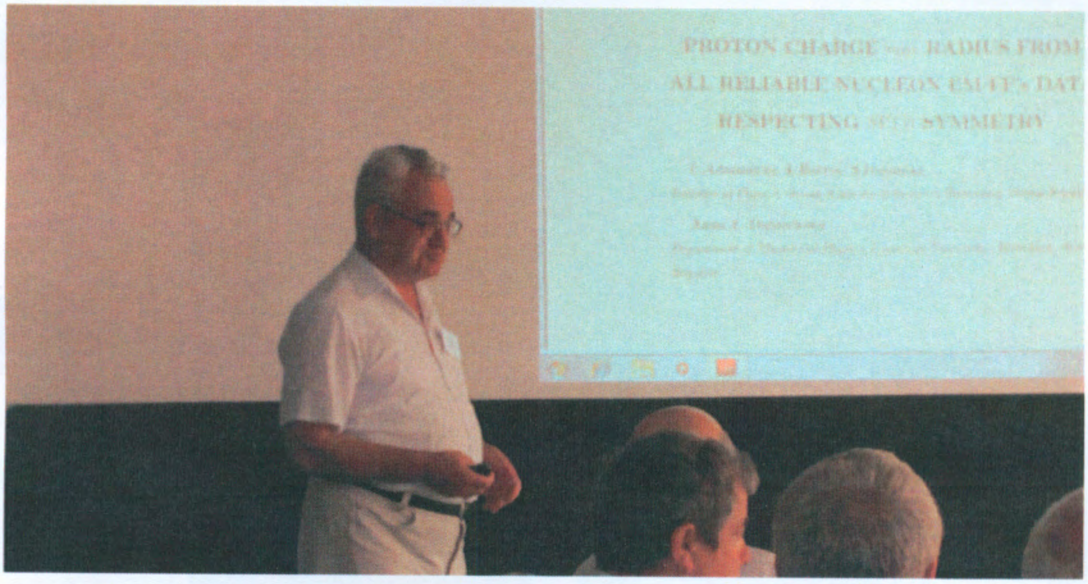
PROTON CHARGE RADIUS FROM
ALL RELIABLE NUCLEON
RESPECTING SYMMETRY

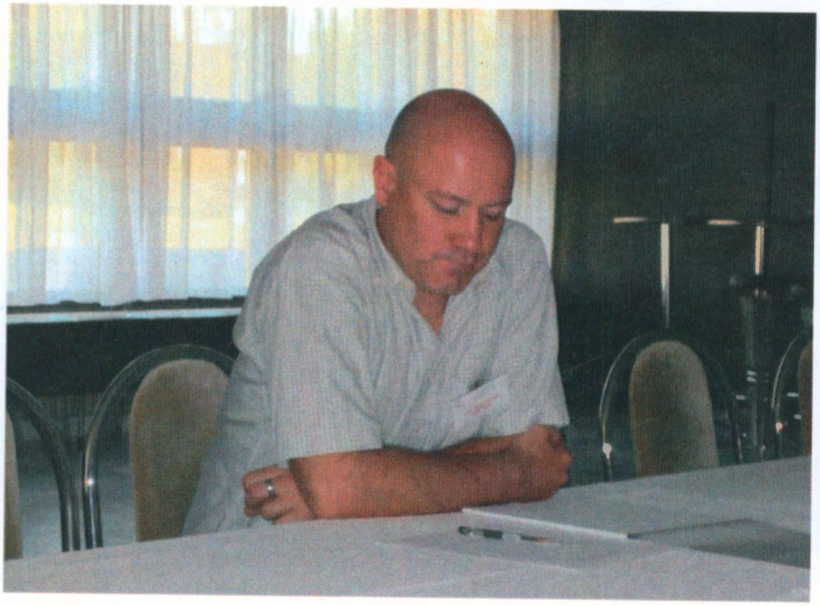


PEPSI


KRATTA, a triple telescope array for
the ASY-EOS experiment


Study of dense


Covariant separable potential of nucleon-nucleon
interaction in the Bethe-Salpeter approach


2 minutes


DELL

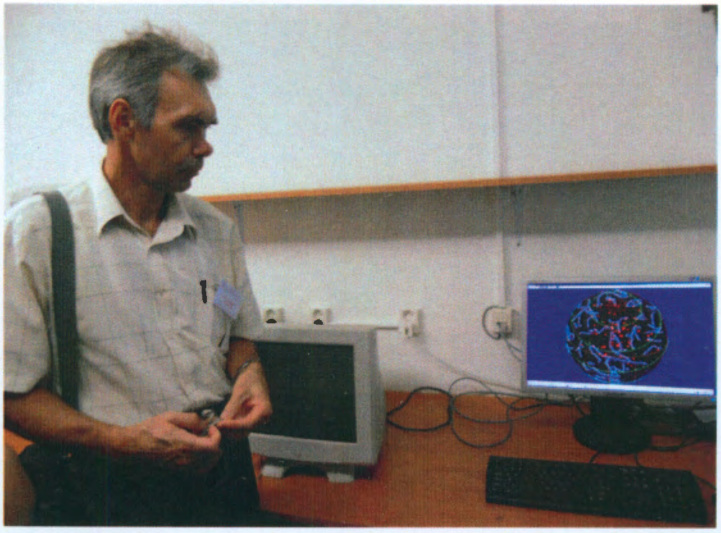

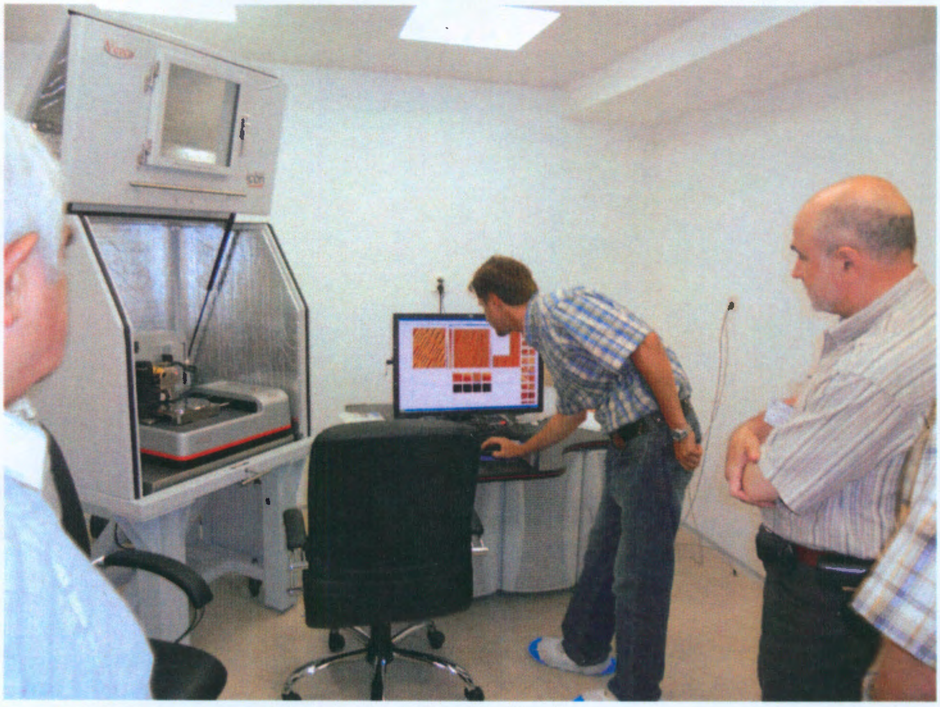


max.12 cestujúcich
SK-6-76080

Ground-state Properties of Nuclei and Initial state in Relativistic Heavy Ion Collisions

P.Filip[1]

Institute of Physics, Slovak Academy of Sciences
Dúbravská cesta 9, Bratislava 845 11, Slovakia

Abstract

We discuss why ground state deformation of nuclei may influence the energy density and elliptic flow in relativistic heavy ion collisions. Besides the static quadrupole deformation we consider dynamic variations of deformation parameter β_2 and also other properties of the ground-state wave function of nucleus. Collisions of specific isotopes of Sm, Nd, Zr, and Ru nuclei are proposed to verify our understanding of elliptic flow and chiral magnetic effect.

1. Introduction

Ground-state deformation of nuclei in heavy ion collisions is often neglected, or it is considered to be an unnecessary complication. However, interactions of significantly deformed nuclei have already been studied experimentally (e.g. by HELIOS experiment [1] at SPS/CERN and on relativistic collider RHIC at BNL). Therefore, deformation effects need to be well understood.

For example, a moderate prolate deformation [2] of ^{115}In (or ^{113}In) nuclei ($\beta_2 \approx 0.1$) might slightly influence the energy density and consequently also J/ψ suppression [3] in the most central In+In collisions studied at CERN/SPS [4]. Assuming ^{197}Au and In nuclei (with measured quadrupole moments Q_{Au}=0.5 b and Q_{In}=0.8 b) to be spherical in Glauber Monte-Carlo simulations, may introduce a systematical bias, which can possibly distort the interpretation of specific experimental results.

We shall discuss here, why deformation of nuclei influences the average eccentricity of the interaction zone and how much the energy density achieved in central collisions gets increased due to the deformation. Additionally, enhanced elliptic flow fluctuations at given fixed centrality are expected in collisions of deformed nuclei, due to the increased fluctuations of the initial eccentricity.

Although simulations of the elliptic flow in Au+Au and Pb+Pb collisions [5] reproduce experimental data observed at RHIC and LHC satisfactorily, the magnitude of elliptic flow measured in Cu+Cu collisions at $\sqrt{s} = 22.4$GeV/n is two times larger than expected [6]. Is there something in the initial state geometry of Cu+Cu interaction zone which is not taken into account properly, or we do not fully understand mechanism of the elliptic flow generation during the expansion of hot QCD matter?

We suggest here, that by studying the elliptic flow in collisions of selected isotopes of Sm (or Nd) elements one can test and improve our understanding of the elliptic flow and charged particle multiplicity generation processes. Additionally, in ^{96}Zr+^{96}Zr and ^{96}Ru+^{96}Ru collisions one can verify the existence of chiral magnetic effect [7].

2. Initial energy density in collisions of deformed nuclei

It has been suggested a long time ago [8], that energy density achieved in nucleus-nucleus collisions can get substantially increased for certain orientations of colliding

[1]E-mail: peter.filip@savba.sk

heavy deformed nuclei. The reason for the increase of energy density is two-fold: a) transverse area of the interaction zone gets smaller for tip-tip collisions of prolate nuclei if compared to spherical nuclei with similar number of participating nucleons. b) number of binary nucleon-nucleon interactions N_{coll} is higher for tip-tip configuration, as will be discussed later. As a result of these two effects combined together it appears, that in ^{165}Ho+^{165}Ho collisions the maximal energy density can become higher than in ^{208}Pb+^{208}Pb collisions (see Fig.1).

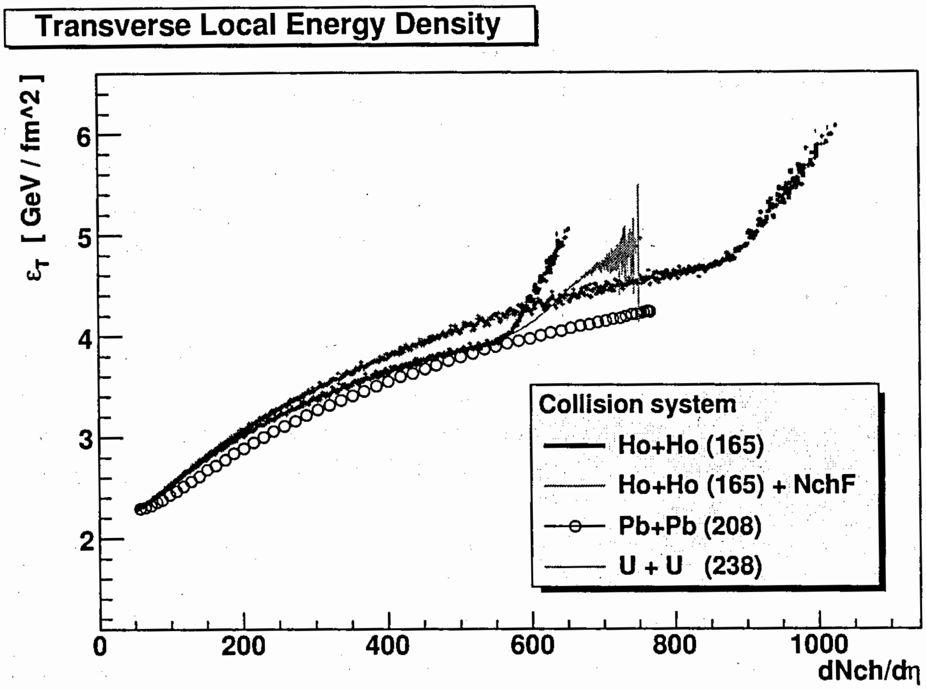

Figure 1: Transverse energy density calculated by optical Glauber Model [9].

Transverse energy density ε_T shown in Fig.1 as a function of charged particle multiplicity density $dN_{ch}/d\eta$ has been obtained for typical RHIC energy (200GeV/n) by Optical Glauber Model simulation [9] in the following way: multiplicity $dN_{ch}/d\eta$ per unit od pseudorapidity has been calculated using two-component model of particle production [10]

$$dN_{ch}/d\eta = (1-x)\cdot n_{pp}\frac{N_{part}}{2} + x\cdot n_{pp}N_{coll} \tag{1}$$

where N_{part} (number of participants) and N_{coll} (number of binary N-N interactions) quantities are evaluated using Glauber model [11] from the transverse nucleon densities of the interacting parts of nuclei. For a given impact parameter b, the orientations of nuclei are sampled (varied) by small $(\pi/6)$ steps in azimuthal and polar angles θ_1, ϕ_1 and θ_2, ϕ_2 independently, to simulate interactions of unpolarized nuclei. Energy density ε_T is proportional to charged multiplicity $dN_{ch}/d\eta$ multiplied by average transverse energy $\langle E_T\rangle/dN_{ch} \approx$ 0.8GeV (see Fig.5 in Ref.[12]), divided by transverse interaction area A_T

$$\varepsilon_T = \langle\varepsilon_T^j\rangle = \left\langle\frac{dN_{ch}^j/d\eta}{A_T^j}\right\rangle\cdot\langle E_T\rangle/dN_{ch} \tag{2}$$

on event-by-event basis. Different impact parameters with various angles $\theta_1, \phi_1, \theta_2, \phi_2$ contribute to given multiplicity $dN_{ch}/d\eta$ bin in Fig.1, showing average ε_T values.

Additionally, to test the influence of stochastic nature of secondary particle production, for each $dN_{ch}/d\eta$ value obtained at given $b, \theta_1, \phi_1, \theta_2, \phi_2$ a fluctuation of charged multiplicity is introduced and histograms are filled using fluctuating $d\tilde{N}_{ch}/d\eta$ values with Poisson probability distribution. Influence of fluctuating $dN_{ch}/d\eta$ is shown for collisions of ^{165}Ho nuclei in Fig.1 (green line "Ho+Ho(165)+NchF"). Maximal energy density gets reduced and it is shifted to higher multiplicities. Nevertheless, transverse energy density obtained for Ho+Ho collisions is still higher compared to Pb+Pb collisions, which is a surprising result. Collisions of prolate deformed nuclei with proton number $Z > 90$ allow one to achieve energy densities substantially higher than those obtained in Pb+Pb collisions (see Fig.1).

Average transverse area $\langle A_T \rangle$ of interaction zone corresponding to given multiplicity $dN_{ch}/d\eta$ is shown in Fig.2. In the region of very high multiplicities (VHM), area $\langle A_T \rangle$ decreases due to the effective self-orientation effect, which enhances a probability of tip-tip collisions of prolate deformed nuclei in VHM events sample (see next section).

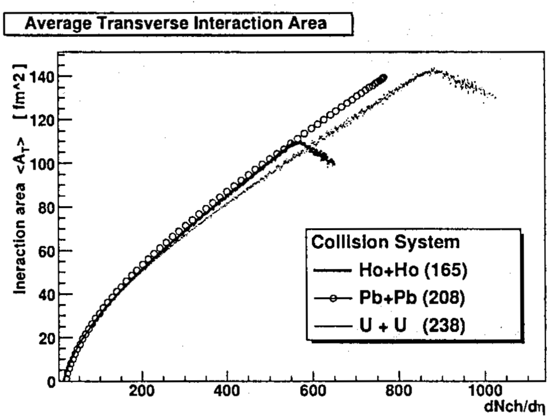

Figure 2: Transverse interaction area $\langle A_T \rangle$.

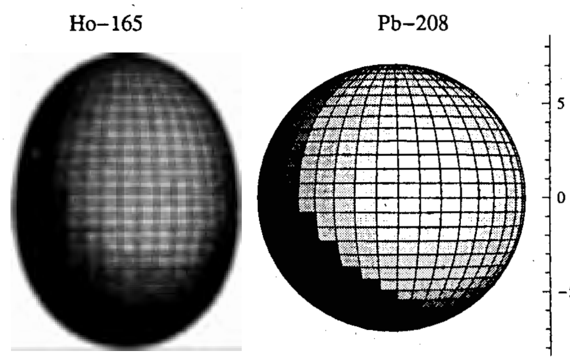

Figure 3: The size and shape of ^{165}Ho (deformed) and ^{208}Pb (spherical) nuclei.

Slightly different slopes of rising data values observed in Fig.1 and Fig.2 are (most likely) a consequence of small differences in density $\varrho(r = 0)$ of nucleons in the simulated nuclei, determined by R_o radius parameter in our Optical Glauber simulation [9]. Using Woods-Saxon density [13]: $\varrho(r, \theta, \phi) = \varrho_o/(1 + e^{(r - R_o(1+\beta_2 Y_{20}+\beta_4 Y_{40}))/a})$, deformation parameters were chosen: $\beta_2 = 0.3$ for ^{165}Ho, $\beta_2 = 0.27$ for ^{238}U and for spherical (β_2=0) nucleus ^{208}Pb we have used $R_o = 6.68$fm with diffuseness parameter $a = 0.55$fm.

2. Initial eccentricity in deformed nuclei collisions

Spatial orientation of deformed nuclei colliding at given impact parameter directly affects the initial eccentricity ε_2 of the interaction zone. In Fig.4 we show 2-dim plot of initial eccentricity ε_2 and $dN_{ch}/d\eta$ values obtained in our Optical Glauber simulation of ^{150}Nd+^{150}Nd collisions for typical RHIC energy ($\approx$200 GeV/n). The eccentricity ε_2 is calculated according to formula

$$\varepsilon_2 = \frac{\sqrt{(\sigma_y^2 - \sigma_x^2)^2 + 4\sigma_{xy}^2}}{\sigma_x^2 + \sigma_y^2} \tag{3}$$

from transverse density of participants $\rho_p(x, y)$ (see explanation in [14]), and Eq.(1) was used to obtain $dN_{ch}/d\eta$. One observes large fluctuations of initial eccentricity at given

$dN_{ch}/d\eta$, which correspond to prolate deformation $\beta_2 \approx 0.24$ of ^{150}Nd nucleus. For collisions of ^{142}Nd nuclei (spherical according to Ref.[2]) the Optical Glauber Model gives a single value of eccentricity ε_2 at given $dN_{ch}/d\eta$. However, in Monte-Carlo Glauber simulations, the eccentricity at fixed $dN_{ch}/d\eta$ fluctuates even for spherical nuclei due to fluctuating positions of nucleons within volume of nucleus and due to stochastic nature of particle production. Eccentricity values calculated using Eq.(3) are always positive, which corresponds to the evaluation in Participant plane [15].

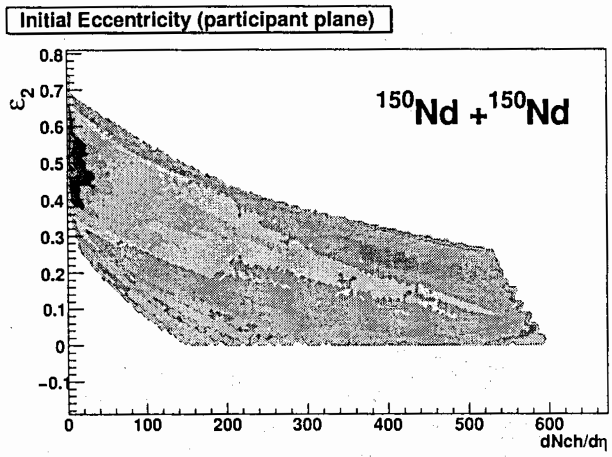

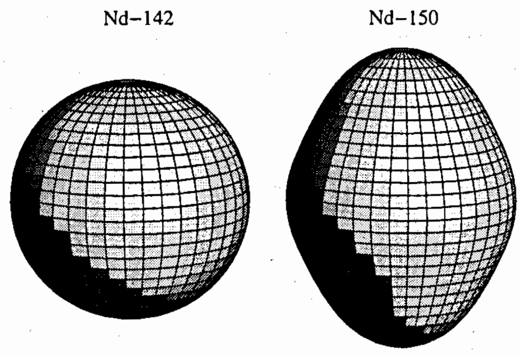

Figure 4: Eccentricity values for collisions of ^{150}Nd nuclei from Optical Glauber simulation [9].

Figure 5: Nuclei ^{142}Nd and ^{150}Nd.

One observes a sudden drop of fluctuation width σ_{ε_2} and of mean eccentricity $\langle\varepsilon_2\rangle$ for $dN_{ch}/d\eta > 540$ in the Optical Glauber simulation (see Fig.4). This happens, because the region of the highest multiplicities is populated mainly by central collisions of longitudinally oriented (tip-tip) prolate deformed nuclei. In such configuration, multiplicity of secondary charged particles is enhanced due to the contribution of binary interactions N_{coll} term in Eq.(1). Therefore, by selecting central collisions of prolate nuclei with very-high multiplicity (VHM region) one effectively enhances the fraction of events with longitudinally oriented nuclei in such data sample, which corresponds to the "effective orientation". The exaggerated situation is shown in Fig.6 for the clarity of explanation.

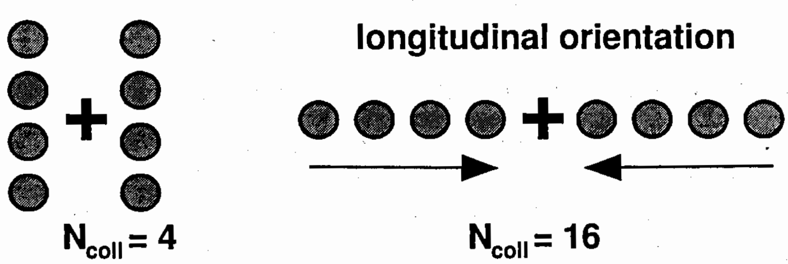

Figure 6: Number of nucleon-nucleon collisions for different orientations of extremely deformed nuclei. Participant number is the same, while N_{coll} differs by factor 4.

Full Monte-Carlo Glauber simulation [14] also predicts a drop of initial eccentricity $\langle\varepsilon_2\rangle$ and consequently of the elliptic flow magnitude v_2 in the VHM region for U+U collisions. Similar behavior of elliptic flow should be observable in ^{150}Nd+^{150}Nd and ^{154}Sm+^{154}Sm (see Fig.8) interactions at energies for which two-component model of secondary particle production [10] is applicable (see Eq.1).

Since elements of Sm and Nd contain also stable isotopes ^{144}Sm and ^{140}Nd which are expected to be spherical [2], the Nature gives us the opportunity to verify our understanding of elliptic flow using beams of spherical and deformed nuclei of the same element. This guaranties almost identical influence of huge electromagnetic fields (in the interaction zone) generated by spectator protons moving at relativistic speeds.

For example, comparing elliptic flow fluctuations σ_{v_2} in collisions of ^{140}Nd nuclei to width σ_{v_2} measured in collisions of ^{152}Nd nuclei one can verify, to what extent the elliptic flow fluctuation at given centrality (fixed by N_{ch} and/or ZDC energy) is driven by the initial eccentricity fluctuation σ_ε. For ^{152}Nd+^{152}Nd collisions width σ_{v_2} of the elliptic flow fluctuation should increase as $\sigma_{v_2} \approx \lambda \cdot \sqrt{\tilde{\sigma}_\varepsilon^2 + \sigma_\beta^2}$, where $\tilde{\sigma}_\varepsilon$ is the eccentricity fluctuation present also for spherical (^{140}Nd) nuclei collisions (originating from all other sources except a static deformation), and σ_β denotes the eccentricity fluctuation width due to β_2 deformation of ^{152}Nd. Factor $\lambda \approx 0.18 = v_2/\varepsilon_2$ comes from hydrodynamic simulations of QCD matter expansion (see Fig.6 in [16]).

Sudden drop of the elliptic flow magnitude v_2 in ^{152}Nd+^{152}Nd collisions should not appear in ^{144}Nd+^{144}Nd (spherical nuclei) collisions.

Experimental verification of the above mentioned deformation effects and a their more detailed study by correlation methods [17] would convince heavy ion community, that our understanding of the initial eccentricity and the elliptic flow phenomenon are correct. Additionally, if deviations from the expected behavior are observed in collisions of heavy nuclei (U+U and Pb+Pb), while predictions meet the observations in collisions of light nuclei (Nd, Sm) one can claim that the equation of state of QCD matter has changed due to higher energy density and/or deconfinement.

One can argue also the other way around: If the equation of state of compressed QCD matter is known well enough, the phenomena described above may allow one to determine deformation parameters of nuclei from the measurement of elliptic flow v_2 behavior in relativistic heavy ion collisions. Since various theoretical calculations of deformation parameters differ (for some nuclei) by more than 20%, a possibility to determine deformation of nuclei from the elliptic flow measurement may be interesting[2].

3. Ground-state shape vibration

Our discussion so far, implicitly assumes a static quadrupole deformation for nuclei. However, it is expected [18] that deformation of some nuclei may oscillate (dynamically) due to quantum property of their ground state. Indeed, from molecular physics is is well known, that zero-point energy (ZPE) needs to be taken into account to understand quantum behavior of molecules. For example, understanding the catalysis of fusion reactions by μ-mesons in heavy hydrogen molecule [19] requires vibrational wave function (Eq.4 left, the harmonic case) in the ground state to be taken into account:

$$\psi_{vib}(x) = \left(\frac{2A_o}{\pi}\right)^{1/4} e^{-A_o(x-\langle x\rangle)^2}; \qquad \psi_{vib}(\beta_2) = \left(\frac{2A_o^\beta}{\pi}\right)^{1/4} e^{-A_o^\beta(\beta_2-\langle\beta_2\rangle)^2/2} \tag{4}$$

Similarly, nuclei in their ground state have a zero-point energy, which corresponds to the vibrational degrees of freedom. Quantum vibrations are carefully studied in molecular

[2] Quadrupole moment of s=1/2 or 0 nuclei cannot be determined by usual spectroscopy or NMR.

physics [20], and for C_{60} fullerene molecule a zero-point amplitude of individual atomic vibrations in the ground state, and shape vibrations of C_{60} have been calculated [21].

One is tempted to ask then, how large is zero-point amplitude (parameter A_o^β in Eq.4 right) of quadrupole shape vibrations in nuclei. Bohr and Mottelson [18] suggest, that the amplitude of β_2 ground state vibration can be as large as 0.2, which is comparable to the static deformation of some nuclei.

If nuclear (ground-state) shape vibrations are large enough they can effectively generate *dynamical* quadrupole moment even for almost spherical $\beta_2 \approx 0$ nuclei [22]. In Fig.7 we show a large quadrupole vibration, which can be expected in the ground state of some nuclei. Such dynamical deformation effects have not been taken into account in initial eccentricity and elliptic flow simulations so far. Since zero-point energy is expected to be larger for lighter molecules, it may well happen, that shape vibrations in ^{63}Cu nucleus are larger than one may expect for ^{196}Hg nuclei [23].

In Fig.8 we show potential energy surface for ^{63}Cu nucleus in the ground state as a function of deformation parameter β_2 (reproduced from Ref.1 database of [24]). It appears that ^{63}Cu nucleus can be found in oblate or prolate shape configuration with very similar probability. This suggests a coexistence of oblate-prolate shapes in ^{63}Cu and one may expect a large amplitude of zero-point quadrupole vibrations.

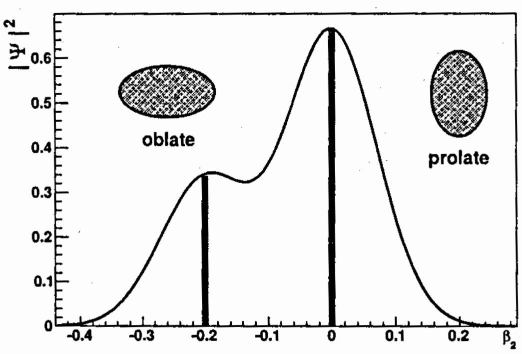

Figure 7: Probability distribution of β_2 quadrupole deformations of a nucleus [23].

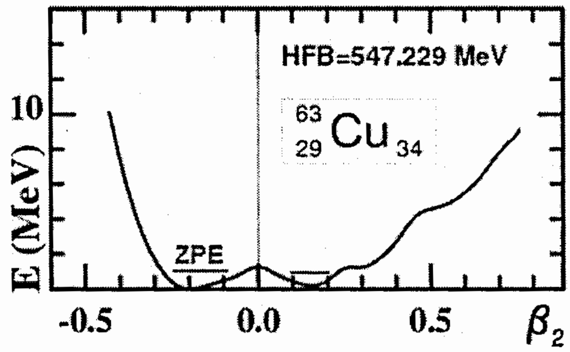

Figure 8: ^{63}Cu potential energy surface and ZPE energy reproduced from [24].

A quadrupole shape vibration of nuclear surface means also correlated "movement" of nucleons in radial direction, with opposite momenta (separated by 180 degrees in azimuthal angle ϕ). Therefore, in momentum space, the quadrupole vibration resembles the elliptic flow phenomenon of nucleons due to $\cos(2\phi)$ modulation of their momenta in a given transverse plane. Can such transverse momentum correlation of participating nucleons be significant in ^{63}Cu+^{63}Cu collisions [6] at energy $\sqrt{s_{NN}}$=22.4GeV? We shall leave this question open now. The existence of short-range-correlation (SRC) of p-n pairs in light nuclei has been addressed recently [25] again, and fraction of SRC pairs in ^{12}C was estimated to be 12%. However, here we discuss an intrinsic momentum-space correlation of a large number (e.g.40) of nucleons in the nucleus exhibiting quadrupole vibrational degrees of freedom. Cumulative effects studied 30 years ago [26] might be (possibly) somehow related.

Initial overlap time $\tau_o \leq 6\text{fm}/c$ for relativistic collisions of nuclei is shorter than period $T \approx 10^{-20}$s of zero-point shape vibrations ($h\nu \approx 1$MeV); and one can consider dynamic vibrational state to be frozen during the collision. All deformation values β_2

below curve shown in Fig.7 should be taken into account with corresponding weights.

4. Suggested collision systems

In the preceding sections we have suggested to study elliptic flow behavior in collisions of ^{140}Nd (spherical) and deformed ^{152}Nd nuclei (see Fig.5). Similar possibility exists with stable isotopes of Samarium element, which also contains spherical ^{144}Sm and strongly deformed (β_2=0.27) [2] prolate ^{154}Sm nuclei (see Fig.10). Verification of our understanding of the relation between initial eccentricity and the observed elliptic flow strength (and their fluctuations) can thus be done using single element (Nd or Sm) in the ion source of the collider. A cusp-like decrease of v_2 strength in VHM central collisions of ^{154}Sm nuclei should be observable at ultra-relativistic energies on LHC and RHIC colliders, if our understanding of the elliptic flow and mechanism of charged multiplicity generation (see Eq.1) are correct. A possibility to observe such effects at lower SPS and NICA energies requires additional considerations.

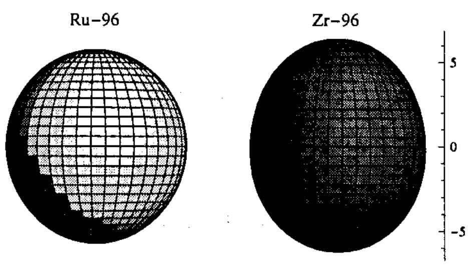

Figure 9: ^{96}Ru and ^{96}Zr nuclei.

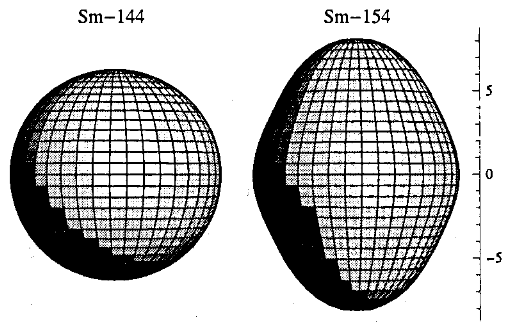

Figure 10: ^{144}Sm and ^{154}Sm nuclei.

Another interesting opportunity is to compare ^{96}Zr+^{96}Zr and ^{96}Ru+^{96}Ru collisions. These nuclei have the same mass number but their charge (number of protons) differs by 10%. Different electric charge of these nuclei allows one to study sensitivity of various measured quantities (also elliptic flow) to the extreme (B>10^{14}T) magnetic fields [27] created for a short time in non-central heavy ion collisions. One should keep in mind however, that ^{96}Ru nucleus is almost spherical (β_2 = 0.05) while ^{96}Zr has prolate (β_2 = 0.22) deformation [2]. It is therefore important to understand and subtract deformation effects (observed e.g. in ^{154}Sm+^{154}Sm collisions) from ^{96}Zr+^{96}Zr observables before chiral magnetic effect [7] (local strong Parity violation) or other initial state isospin-dependent phenomena are claimed to exist. Collisions of ^{96}Zr and ^{96}Ru nuclei have been studied successfully by FOPI collaboration [28] at GSI.

5. Summary

We have discussed the influence of static ground-state deformation of nuclei on the energy density and elliptic flow in relativistic heavy ion collisions. Dynamical degrees of freedom (quadrupole vibration and momentum-space correlation) in the ground-state wave function of nuclei have been considered. We suggest to study collisions of selected isotopes of Nd and/or Sm elements to improve our understanding of elliptic flow, and collisions of ^{96}Zr and ^{96}Ru nuclei to verify the existence of chiral magnetic effect [7].

Acknowledgments

This work was supported by Slovak grant agency VEGA under project 1/0171/11.

References

[1] J. Schukraft for HELIOS Collaboration, Nucl. Phys. **A498**, p.79c, 1989.

[2] J.Möller et al., Atomic Data Nucl. Data Tables, **59**, p.185, 1995.

[3] T.Matsui and H.Satz, Phys. Lett. **B178**, p.416, 1986.

[4] R.Arnaldi for NA60 Collaboration, Nucl. Phys. **A774**, p.711, 2006.

[5] H.Song, S.A.Bass and U.Heinz, Phys. Rev. **C83**, p.054912, 2011.

[6] G.Agakishiev and STAR Collaboration, Phys. Rev. **C85**, p.014901, 2012.

[7] K.Fukushima, D.E.Kharzeev, H.J.Warringa, Phys. Rev. **D78**, p.074033, 2008.

[8] E.V.Shuryak, Phys. Rev. **C61**, p.34905, 2000.

[9] P.Filip, Physics of Atomic Nuclei, **71**, p.1609, 2008.

[10] D.Kharzeev, M.Nardi, Phys. Lett. **B507**, p.121, 2001.

[11] M.L.Miller et al., Annual Rev. Nucl. Partic. Science **57**, p.205, 2007.

[12] A.Bazilevsky for PHENIX Collaboration, Nucl. Phys. **A715**, p.486, 2003.

[13] K.Hagino, N.W.Lwin, M.Yamagami, Phys. Rev. **C74**, p.17310, 2006.

[14] P.Filip, R.Lednicky, H.Masui, N.Xu, Phys. Rev. **C80**, p.054903, 2009.

[15] S.A.Voloshin, A.M.Poskanzer, A.Tang, G.Wang, Nucl. Phys. **B659**, p.537, 2008.

[16] H.Holopainen, H.Niemi, K.J.Eskola, Phys. Rev. **C83**, p.034901, 2011.

[17] R.S.Bhalearo, M.Luzum, J.-Y.Ollitrault, Phys. Rev. **C84**, p.034910, 2011.

[18] A.Bohr and B.R.Mottelson *Nuclear Structure* Vol. **II**, World Scientific, 1998.

[19] J.D.Jackson, Phys. Rev. **106**, p.330, 1957.

[20] H.A.Jahn and E.Teller, Proc. Roy. Soc. Lond. **A161**, p.220, 1937.

[21] M.C.Böhm and R.Ramírez, Jour. Phys. Chem. **99**, p.12401, 1995. J.Menéndez and J.B.Page, Topics in Applied Physics **76**, p. 27-95, 2000.

[22] I.Boboshin et al., in Proc. of Internat. Conf. on Nucl. Data for Science and Technology, April 22-27, 2007, France, (edit. Bersillon) EDP Sciences, p.65, 2008.

[23] Th.J.Köppel, A.Faessler and U.Götz, Nucl. Phys. **A403**, p.263, 1983.

[24] J.-P. Delaroche et al., Phys. Rev. **C81**, p.014303, 2010.

[25] E.Piasetzky, Journal of Physics Conference Series **381**, p.012005, 2012.

[26] V.V.Burov, V.K.Lukyanov, A.I.Titov, Phys. Lett. **B67**, p.46, 1977.

[27] V.Voronyuk et al., Phys. Rev. **C83**, p.054911, 2011.

[28] W.Reisdorf and FOPI Collaboration, Nucl. Phys. **A781**, p.495, 2007.

KRATTA, A TRIPLE TELESCOPE ARRAY FOR THE ASY-EOS EXPERIMENT

J. Łukasik[a,*], P. Pawłowski[a], A. Budzanowski[a,†], B. Czech[a], I. Skwirczyńska[a], J. Brzychczyk[b], M. Adamczyk[b], S. Kupny[b], P. Lasko[b], Z. Sosin[b], A. Wieloch[b], M. Kiš[c], Y. Leifels[c], W. Trautmann[c] and the ASY-EOS Collaboration

a) Institute of Nuclear Physics, IFJ-PAN, 31-342 Kraków, Poland
b) Institute of Physics, Jagiellonian University, 30-059 Kraków, Poland
c) GSI, D-64291 Darmstadt, Germany

Abstract

A new detection system KRATTA, Kraków Triple Telescope Array, is presented. This versatile, low threshold, broad energy range system has been built to measure the energy, emission angle, and isotopic composition of light charged reaction products. It has been equipped with fully digital chains of electronics. The array performed very well during the ASY-EOS experiment, conducted in May 2011 at GSI. The performance of the array is presented using the first experimental results, with the emphasis on the advantages of the pulse shape analysis.

1. Motivation and requirements

The main parameters of the KRATTA array have been motivated by the needs of the ASY-EOS experiment [1]. This experiment has been designed to study the density dependence of the nuclear symmetry energy by measuring flows and isotopic compositions of the reaction products from the ^{197}Au+^{197}Au, ^{96}Ru+^{96}Ru, and ^{96}Zr+^{96}Zr reactions at 400 MeV/nucleon. During the experiment the most relevant products, neutrons and Z=1 and 2 particles, have been measured by the LAND [2] detector and the direction and magnitude of the impact vector were estimated using the CHIMERA [3] and ALADIN ToF-Wall [4] detectors. The KRATTA array has been designed to complement the neutron and hydrogen detection with LAND by measuring the isotopic composition and flow of light charged reaction products up to atomic number $Z \lesssim 7$, and specially, to identify the hydrogen and helium isotopes with a resolution much better than achievable with LAND. The array was placed on the opposite side of the beam with respect to LAND, and covered approximately the same solid angle (160 msr). It has been designed to detect energetic particles emerging from the "mid-rapidity" region of the 400 MeV/nucleon reactions. Modular design, portability, low thresholds (below 3 MeV/nucleon) and high maximum energy (~260 MeV/nucleon for p and α), allow the array to be used in various configurations and experiments. In particular, it will very well suit the needs of the future cyclotron facility at IFJ-PAN in Kraków, planned for proton beams from 70 to 250 MeV.

2. Active elements and geometry

The modules of KRATTA are composed of three large area HAMAMATSU PIN photodiodes for direct detection [5] and of two CsI(Tl) crystals [6]. The layout and dimensions of these active elements are presented in Fig. 1 and their main characteristics are summarized in Table 1.

The first photodiode (PD0 in Fig. 1) serves as a Si ΔE detector providing the ionization

*E-mail: jerzy.lukasik@ifj.edu.pl
†Deceased.

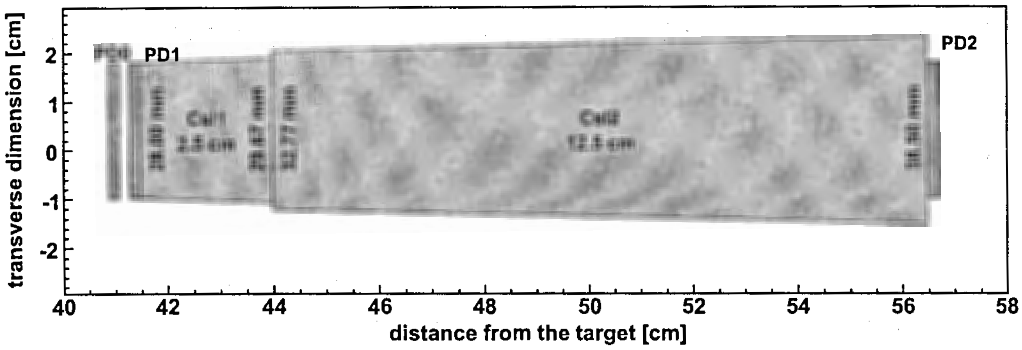

Figure 1: Schematic layout of the active elements.

Photodiodes [5]		**CsI(Tl) Crystals [6]**	
Active Area	28×28 mm^2	Tl concentration	1500 ppm
Thickness	500±15 μm	LO non-uniformity	< 7 %
Dead Layers	1.5 μm front	Shape	Truncated
	20 μm rear		pyramids
Full Depletion	120-135 V	Tolerance	±0.1 mm
Dark Current	6-16 nA	**Wrapping [8]**	
Rise Time	40 ns	Reflectance	> 98 %
Capacitance	190±3 pF	Thickness	65 μm

Table 1: Main characteristics of the active elements

signal alone. It has been "reverse mount", i.e. the ohmic side towards the incoming particles. The second photodiode (PD1), naturally "reverse mount", works in a "Single Chip Telescope", SCT [7], configuration and provides a composite signal combined of a direct (ionization) component and of a scintillation component coming from the thin crystal (CsI1). The third photodiode (PD2) reads out the light from the thick crystal (CsI2) and, in addition, provides an ionization signal for particles that punch through the crystal within its active area.

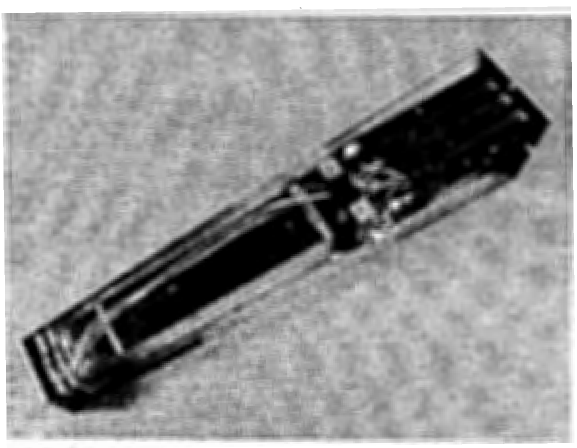

Figure 2: Single module content.

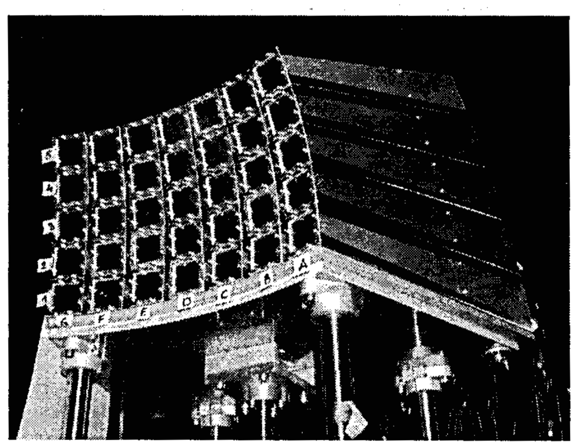

Figure 3: KRATTA in a 7×5 configuration.

The crystals have been polished and wrapped with a highly reflective ESR [8] foil, except

Fragment	E_{low}	E_{int}	E_{up}
^{1}H	8.3	89.6	254.4
^{4}He	8.3	89.4	253.9
^{7}Li	9.5	103.6	296.5
^{20}Ne	19.9	231.3	719.0
^{43}Ca	26.7	339.7	1134.2
^{91}Zr	34.0	513.9	1911.8
^{197}Au	38.6	775.8	3550.9

Table 2: Lower, E_{low} and intermediate, E_{int}, thresholds and upper limits, E_{up}, for selected species (in MeV/u). The thresholds correspond to the energy losses in 500 μm of Si, in 1000 μm of Si + 2.5 cm of CsI and in 1000 μm of Si + 15 cm of CsI, respectively. They have been calculated using the ATIMA tables [9].

for the front and back windows. The windows have been protected with 6 μm Mylar foils. The crystals were optically decoupled. The photodiode chips have been glued onto custom-made PCB frames and put in close optical contact with the crystal windows. The active elements have been placed inside aluminum boxes together with the charge preamplifiers (see Fig. 2). The photodiode frames and the aluminum housing reduced the geometric acceptance of a single module to about 54%. The active solid angle of a module amounts to 4.5 msr. The entrance window has been made of a 100 μm thick copper foil. During the experiment, 35 modules have been arranged in a 7×5 array (Fig. 3), all placed at a radial distance of 40 cm from the target, and operated in air. In a spherical coordinate system, with the origin at the target and the beam axis defining the reference equatorial plane, the columns follow the meridians from the beam level up to about 27° elevation (latitude) and the rows span the azimuth angles (longitude) between 21° and 64° with respect to the beam direction. The energy thresholds resulting from the thicknesses of the consecutive active layers are summarized in Table 2. As will be shown later on, the low threshold can be further reduced by applying a pulse shape analysis to the ionization signals of PD0.

3. Electronics and data acquisition

The main electronics and data acquisition functions are presented schematically in Fig. 4. The photodiodes (3 per module) have been reverse biased at 120 V, using the in-house made 120-channel, remote controlled, high voltage power supplies. The signal from each photodiode has been integrated with the own-design, low noise, charge preamplifier [10].

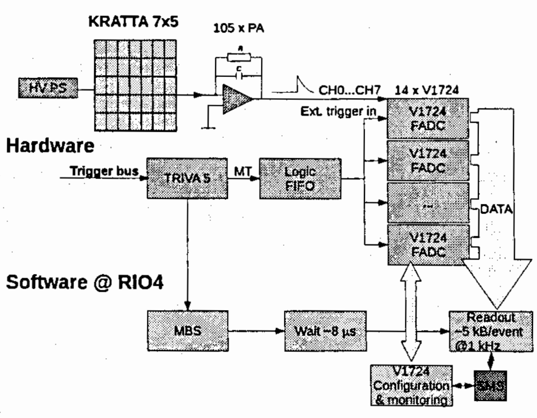

Figure 4: Analog, logical and digital signal flow chart. HV PS - high voltage power supply. PA - charge sensitive preamplifier. V1724 - CAEN digitizers. TRIVA5 - VME Trigger Synchronization Module [12]. MT - master trigger. FIFO - logical Fan-In Fan-Out module. RIO4 - VME controller board [13] running LynxOS. MBS - Multi Branch System, a GSI acquisition standard [14]. SMS - Shared Memory Segment.

The preamps were supplied with ±6 V and their dynamic range spanned about 3.6 V. Three nominal charge gains of the preamplifiers have been used, depending on the azimuthal angle of the module: 44.5, 22.2 and 13.5 mV/MeV, with 1, 2 and 3.3 pF feedback capacitors, respectively. After optional amplification, the signals have been digitized with the 100 MHz, 14 bit digitizers [11] and stored for the off line analysis. All logical and digital electronics modules shown in Fig. 4 have been controlled with the RIO4 board [13] within a single VME crate. During the experiment, the 14 Flash ADC boards have been triggered with an external trigger split and delivered into each FADC module. The stored waveforms spanned 5.12 or 10.24 μs (512 or 1024 time bins), with a 2 μs pre-trigger enabling a precise baseline estimation. The shorter samples have been sufficient for the first photodiode supplying the fast ionization signal alone. The expected data throughput amounted to about 5 MB/s, assuming 1 kHz single hit rate. The actual data rate did not go beyond this estimate during the experiment. The digitizers have been remotely set up and monitored using a self-developed software. The data flow has been controlled using the standard GSI MBS system [14].

4. Pulse shape analysis

The pulse shape analysis has two main purposes in the case of KRATTA data. First of all, it has to enable the decomposition of the signals from the middle photodiode, PD1 (SCT), into the ionization and scintillation components. Secondly, it is used to resolve masses of particles stopped in the first photodiode, PD0, utilizing the relation between the range of a particle and the time characteristics of the induced current signal [15].

The following assumptions have been made to accomplish these two goals. The preamplifier response has been modeled using a simple parallel RC circuit approximation [16]:

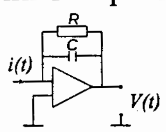

$$\frac{i(t)}{C} = \frac{dV(t)}{dt} + \frac{V(t)}{RC} \tag{1}$$

where, RC is the feedback coupling time constant, $i(t)$ is the induced current due to the carrier motion in the photodiode, and $V(t)$ is the measured voltage pulse. This relation assumes an infinite open loop gain, small detector capacitance and a zero rise time of the charge integrator, which is an idealization, but enables an analytical approach. The induced current has been approximated with one direct (ionization), $i_D(t)$, and two scintillation, $i_{Sk}(t)$, components, all of the same form:

$$i_D(t) = Q_D \frac{e^{-t/\tau_{RD}} - e^{-t/\tau_{FD}}}{\tau_{RD} - \tau_{FD}}, \tag{2}$$

$$i_{Sk}(t) = Q_{Sk} \frac{e^{-t/\tau_{RS}} - e^{-t/\tau_{Fk}}}{\tau_{RS} - \tau_{Fk}}, \quad k = 1, 2 \tag{3}$$

where Q's are the induced charges and the τ_{RD}, τ_{RS} and the τ_{FD}, τ_{Fk} are the rise and fall times for the respective component. The assumed shapes attempt to account for both, the complicated actual current pulse shape induced by the electrons and holes drifting in the photodiode [15], and for the instrumental rise time of the preamp. With the assumed preamplifier response (1) and the current shapes (2) and (3), it was possible to obtain the corresponding analytical model shapes of the waveforms, $V(t) = V_0 + V_D(t) + V_S(t)$, with:

$$V_D(t) = RCQ_D\left(\frac{e^{-\Delta t/RC}\,RC}{(RC-\tau_{RD})(RC-\tau_{FD})} + \frac{e^{-\Delta t/\tau_{RD}}\,\tau_{RD}}{(\tau_{RD}-RC)(\tau_{RD}-\tau_{FD})} + \frac{e^{-\Delta t/\tau_{FD}}\,\tau_{FD}}{(\tau_{FD}-\tau_{RD})(\tau_{FD}-RC)}\right) \tag{4}$$

$$V_S(t) = RC\sum_{k=1}^{2} Q_{Sk}\left(\frac{e^{-\Delta t/RC}\,RC}{(RC-\tau_{RS})(RC-\tau_{Fk})} + \frac{e^{-\Delta t/\tau_{RS}}\,\tau_{RS}}{(\tau_{RS}-RC)(\tau_{RS}-\tau_{Fk})} + \frac{e^{-\Delta t/\tau_{Fk}}\,\tau_{Fk}}{(\tau_{Fk}-\tau_{RS})(\tau_{Fk}-RC)}\right) \tag{5}$$

where, for generalization, V_0 is the baseline and $\Delta t = t - t_0$, with t_0 being the beginning of the pulse.

The two scintillation components (5) have been introduced to account for the fast and slow decay modes of the CsI(Tl) crystals. The rise times, τ_{RD} and τ_{RS}, account for the photodiode, scintillator and the preamp rise times. Overall, the model depends on 11 parameters listed in Table 3.

	Parameter	Value	
Q_D	Amplitude		fitted
τ_{RD}	Rise time	~90 ns	fixed/fitted
τ_{FD}	Fall time	<300 ns	fixed/fitted
Q_{S1}	Fast component amplitude		fitted
Q_{S2}	Slow component amplitude		fitted
τ_{F1}	Fast fall time	~650 ns	fitted
τ_{F2}	Slow fall time	~3.2 μs	fixed
τ_{RS}	Rise time	~140 ns	fixed
RC	Preamp fall time constant	~6 μs	fixed
t_0	Time offset	~2 μs	fitted
V_0	Baseline		fitted

Table 3: 11 parameters of the model waveforms.

The preamp fall time constant parameter RC has been determined individually for each chip by selecting the pulses with the fast ionization component alone. In order to describe precisely the shapes due to particles stopped in the first photodiode, PD0, both the time constants, τ_{RD} and τ_{FD}, were fitted and the scintillation components were obviously not used. In case of PD1 and PD2, the rise and fall times τ_{RD} and τ_{FD} were fixed. The fits were done using the FUMILI [17] minimization package, a relatively fast and precise implementation of the Gauss-Newton algorithm. Constraining some of the parameters was found inevitable, not only to obtain a good description of the waveforms (χ^2) but, at the same time, to maintain the global agreement between the reconstructed amplitudes of the three components and the predictions of the range-energy tables (see discussion of Figs. 16, 17).

An additional advantage of using the digitization of the signals and the fitting method, was the knowledge of the actual charges Q for each component, irrespectively of the substantial *ballistic deficit* (reduction of the amplitude) due to a relatively short discharge time of the preamps ($RC \simeq 6$ μs). For instance, the sum $Q_{S1} + Q_{S2}$ represents the total light produced in the scintillators. For typical values of the parameters presented in Table 3, the ballistic deficit amounts to about 5-15% for the ionization signal and to about 25 and 50% for the fast and slow CsI(Tl) components, respectively. Usually, the fall time constant of the preamp is a compromise between the level of pile-ups, the baseline variation, and the ballistic deficit. However, since ballistic deficit is not an issue in our approach, the short preamp fall times, of the order of the time span of the waveform and of the slow CsI(Tl) decay time, have the additional advantage of making the maximum and the tail of the pulse visible within the digitized sample.

Waveforms of low energy particles stopped in the first photodiode, PD0, have been fitted with a single component of the form (4), with the time constant parameters treated as free fit parameters. A more precise time characteristics of the associated current pulse (2) was needed to perform a pulse shape based identification (see discussion of Fig. 13).

The quality of the fits is demonstrated in Fig. 5. The ordinate represents the measured voltage, in the FADC channels. The hits corresponding to the selected waveforms are also marked in the identification maps presented in the next section.

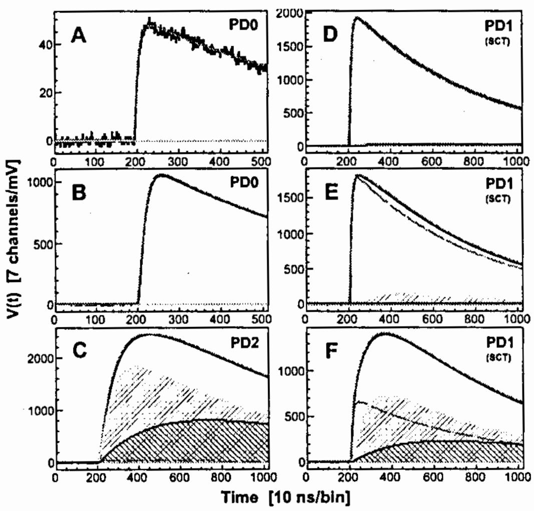

Figure 5: Example waveforms and their decomposition. Histogram (when visible): measured waveform. Solid line: sum of all fit components. Dashed line: ionization component. Hatched areas: fast and slow CsI(Tl) scintillation components. A: low-energy electron, particle or gamma ray, barely above the acquisition threshold, stopped in PD0 (see corresponding hit in Fig. 13). B: α particle stopped in PD0 (see Fig. 13). C: α particle stopped in CsI2 (see Fig. 7, 12). D: α particle stopped in PD1 (see Figs. 6, 8, 9,11). E: α particle barely punching through PD1 and stopped in CsI1 (see Figs. 6, 8, 10, 11). F: higher energy α particle stopped in CsI1 (see Figs. 6, 8, 10, 11.)

Panel A of Fig. 5 shows a waveform for a low energy electron, particle or gamma, registered barely above the acquisition threshold and stopped in PD0 (see also Fig. 13). Here the measured histogram is visible and the deviations from the smooth fit visualize the level of the total noise. The resultant signal distortions, including the photodiode, preamplifier, FADC and pickup noise sources, have been observed on the level of 0.4 mV rms, corresponding to about 30 keV.

Panel B of Fig. 5 presents the quality of the fit with the shape given by an ionization component alone (4), applied to particles stopped in PD0. Its location in the identification map is presented in Fig. 13. This fit allowed for derivation of both, the rise and fall times and, therefore, also of the *mode* (position of maximum) of the associated current signal (2):

$$mode = \frac{\tau_{RD}\,\tau_{FD}}{\tau_{RD} - \tau_{FD}} \log \frac{\tau_{RD}}{\tau_{FD}} \qquad (6)$$

Panel C of Fig. 5 shows the waveform of a high energy α particle stopped in the CSI2 crystal. The corresponding hit has been marked in Figs. 7 and 12.

Panels D-E-F of Fig. 5 show the evolution of the pulse shape of an α particle detected and stopped in the SCT as its energy increases. The corresponding hits have been marked, when possible, in Figs. 6, 8-11.

5. Performance

Figures 6-13 present various identification (ID) maps obtained by using the parameters of the reconstructed waveform components. The strongest lines in Figs. 6-13 correspond to p, d, t, ^3He, α, and so on, from bottom to top, respectively (see Fig. 16 for precise labeling).

The reconstructed amplitude maps for the first two and the last two photodiodes of the KRATTA module are presented in Figs. 6 and 7.

The identification map in Fig. 6 shows a complex spectrum with each "ID-line" composed of two parts: an ordinary Si-Si hyperbolic segment at low energies, for particles stopped in PD1, and a more curved part for particles punching through the PD1 photodiode and stopped in the CsI1 crystal. Due to line crossing and its complex structure, this kind of a map cannot be used for identification, however thanks to the presence of many characteristic punch-through points and curvatures, it is very well suited for energy calibration purposes.

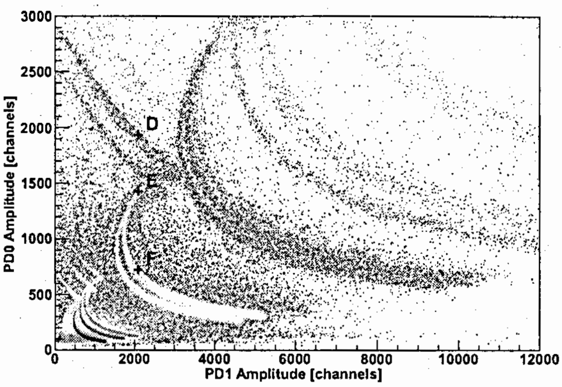

Figure 6: ΔE-E ID map for PD0 vs PD1(SCT), for particles stopped in PD1 or in CsI1.

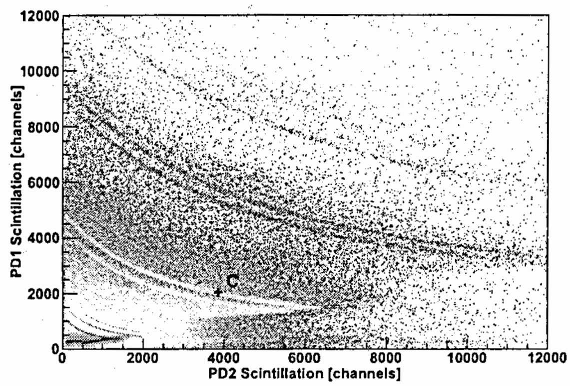

Figure 7: ΔE-E ID map of scintillation signals for CsI1 vs CsI2 detected by PD1 and PD2.

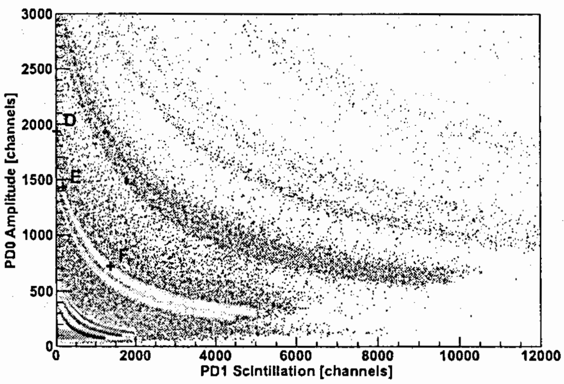

Figure 8: Decomposition of the map from Fig. 6. PD0 vs scintillation detected by PD1 - for particles stopped in CsI1.

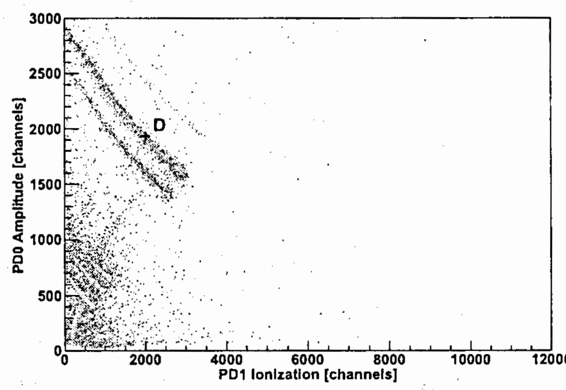

Figure 9: Decomposition of the map from Fig. 6. PD0 vs ionization signal from PD1 - for particles stopped in PD1 (producing no light).

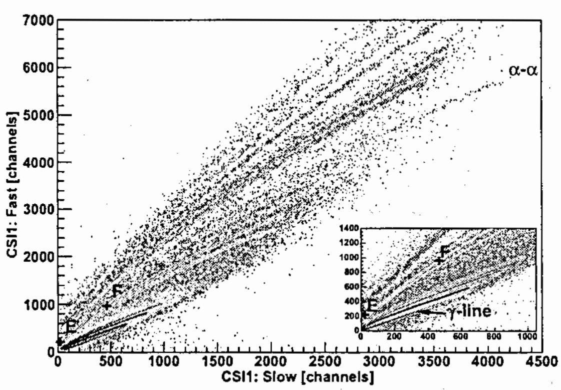

Figure 10: Fast vs Slow components of the scintillation in CsI1. The inset shows more clearly a γ–line and the p, d, t lines.

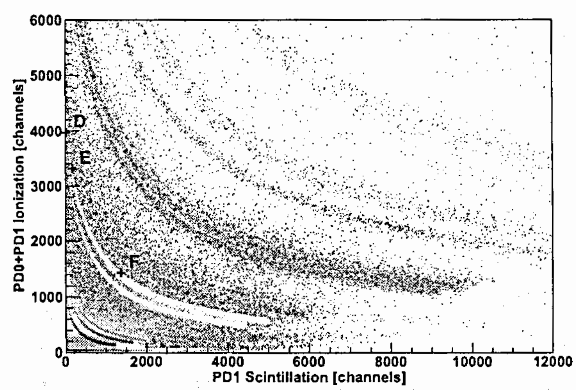

Figure 11: Summed PD0+PD1 ionization components vs scintillation in PD1 for particles stopped in CsI1.

Fig. 7 shows a ΔE-E map for scintillation signals detected by a second vs third photodiode. Apart from the very good isotopic resolution, one can see a substantial background from the secondary reactions/scatterings in the crystals and also from particles crossing the module at an angle and not originating from the target, as well as back-bendings corresponding to particles punching through the thick crystal (see discussion at the end of this section).

Thanks to the pulse shape decomposition, the ionization component for particles hitting the photodiode *(nuclear counter effect)* at the back of the thick crystal has been easily removed.

Using the individual reconstructed amplitudes for the ionization and for the scintillation components, the map of Fig. 6 can be decomposed into the PD0-PD1(Si) and PD0-PD1(CsI) components of the SCT segment (Figs. 9 and 8). This makes effectively KRATTA even a four-fold telescope.

The isotopic resolution visible from Fig. 8 can be improved by summing up the reconstructed ionization components from PD0 and PD1, and thus, increasing the effective thickness of the first ΔE layer to 1 mm of Si. See also inset in Fig. 14. Fig. 11 presents a classical ΔE-E ID map obtained from Fig. 6 thanks to the pulse shape decomposition (see discussion of Fig. 17 for more details on this transformation and Fig. 14 for the corresponding mass resolution.)

Figures 10 and 12 show the "Fast-Slow" ID maps for the CsI1 and CsI2 crystals, respectively. The latter represents a variant of the standard representation, using the total light vs the ratio Slow over Fast (see e.g. [18]). The Fast-Slow representation is very useful in many respects in addition to the standard ΔE-E one: One can observe a clear double alpha line (α-α in Figs. 10 and 12) which is hidden in the ΔE-E representation behind the Li isotope lines. The Fast-Slow map shows a clear "γ-line" - a strong line below the proton line due to γ-rays (see inset in Fig. 10), which can be precisely isolated and removed from the ΔE-E map. Last, but not least, as can be seen from Fig. 12, the punch through segments do not cross the lower lying isotope lines in a way they do in case of the ΔE-E maps (Fig. 7). Thus, the Fast-Slow maps allow to isolate the punch through segments in a much more precise way. Unfortunately, the punch through segments eventually merge with the γ-lines, which makes it difficult to discriminate between these two.

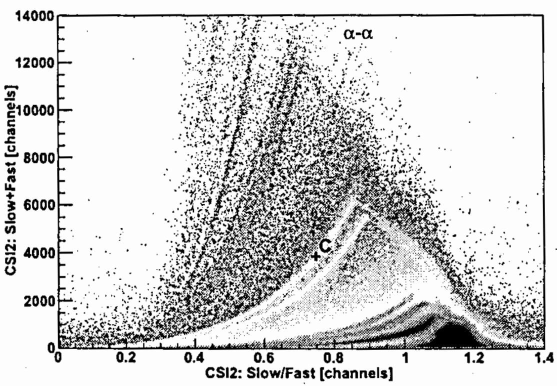

Figure 12: Total light vs Slow over Fast components of the scintillation in CsI2. Note, that unlike in Fig. 7, the punch through lines do not cross the lower lying isotope lines.

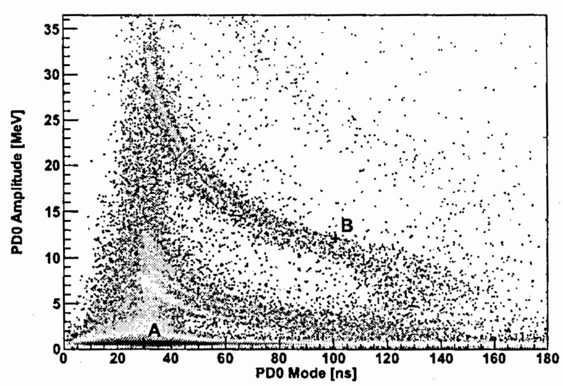

Figure 13: Amplitude vs mode of the current signal for particles stopped in PD0, obtained from a single Si chip.

Figure 13 demonstrates yet another powerful feature of the pulse shape analysis. It allowed to perform an identification of the majority of light particles stopped in the first photodiode by plotting the amplitude vs mode of the reconstructed current signal (6). Due to the constant value of the field within the intrinsic region of the PIN diode the enhancement of the resolution for stopped particles is not expected to be as pronounced as in the case of reverse mount PN detectors [19], nevertheless, the relation between the range and the carrier collection time seems to be still strong enough to enable the isotopic separation of light particles. This method allowed to reduce the lower identification threshold, due to the thickness of the first photodiode, (see Table 2) from 8.3 to about 2.5 MeV for protons, where they are still resolvable from deuterons (see two bottom lines in Fig. 13). This effectively corresponds to the reduction of the thickness of the first ΔE layer from 500 to about 65 μm of Si.

One should stress, that the time scale presented in Fig. 13 exceeds by about a factor of 3 the collection times estimated on the basis of the mobilities of the carriers alone, thus the plasma delay, or other effects, seem to be quite important in slowing down the collection process.

The mass resolution for particles stopped in the thin crystal (CsI1) and in the thick one (CsI2) can be viewed from Figs. 14 and 15, respectively.

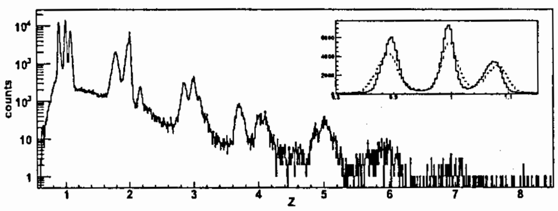

Figure 14: Particle identification spectrum (charge distribution) obtained from the map of Fig. 11, for particles stopped in CsI1.

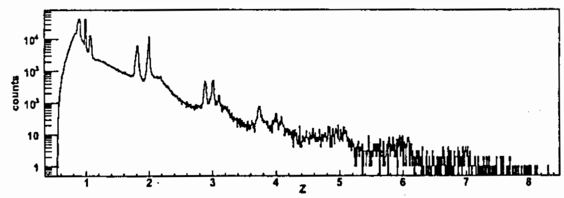

Figure 15: Same as Fig. 14, but obtained from the map of Fig. 7, for particles stopped in the thick crystal.

The background in Fig. 14, resulting mainly from the secondary reactions/scattering in the crystal, amounts to about 6% for the hits below the *p*, *d*, *t* peaks. For energetic $Z = 1$ particles traversing the thick crystal (12.5 cm of CsI) the secondary reaction probability amounts to about 46% (Fig. 15). These probabilities agree reasonably well with the simple estimates obtained using the nuclear collision length of 22.30 cm for CsI [20], which yields the probabilities of 11% and 43% for 2.5 and 12.5 cm of CsI, respectively. The background measured under the *p*, *d*, *t* lines includes also some contribution from the secondary reactions of neutrons and heavier charged particles, as well as from the accidental coincidences. The γ and punch-through hits have been removed from the background, in both cases. The high secondary interaction probability obviously deteriorates the identification quality and defines the limits for applying the telescope method to intermediate energies.

6. Discussion and remarks

Since the parametrization of the pulse shapes is only approximate and has no deep physical background, one can ask how precise is the decomposition into individual components and how physical they are. In order to address these questions, the ΔE-E map of the SCT (PD1+CsI1) has been compared to the predictions of the ATIMA range-energy tables. Such a comparison requires the knowledge of the energy calibration of both, the silicon photodiodes and of the CsI(Tl) light output. The calibration has been performed using the ID map of Fig. 6 (see Fig. 16) which is relatively insensitive to the details of the decomposition and is perfectly suited for the energy calibration due to its richness in characteristic punch-through points and curvatures.

The calibration routine allowed to adjust the thicknesses of the dead and active layers, the energy calibration parameters, as well as the light-energy conversion parameters. For the latter, a simple integrated Birks' formula (see e.g. [16]) has been used, with $dE/dx \propto A Z^2/E$, yielding a commonly applied two-parameter Light-Energy relation [21], applicable for particles stopped in the scintillator:

$$\text{Light} = a_1 \left(E - a_2 A Z^2 \log \left[1 + \frac{E}{a_2 A Z^2} \right] \right) \tag{7}$$

with E being the energy, A, Z - mass and atomic numbers of the stopped particle, a_1, a_2 - the gain and quenching parameters.

Having this (inverse) calibration it was possible to superpose the ATIMA lines on the decomposed ID map for the Single Chip Telescope segment of the KRATTA module. The result is presented in Fig. 17 and is worth a comment.

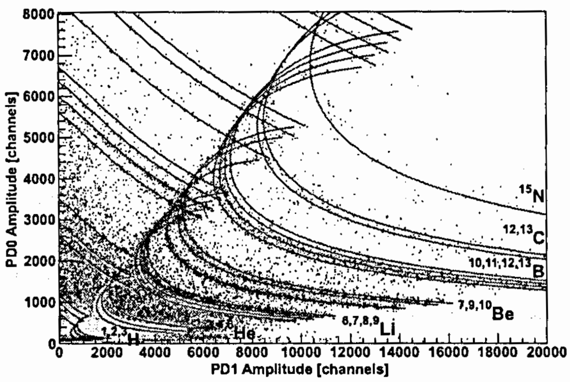

Figure 16: Same as Fig. 6 but with the superimposed ID lines calculated using the ATIMA range-energy tables.

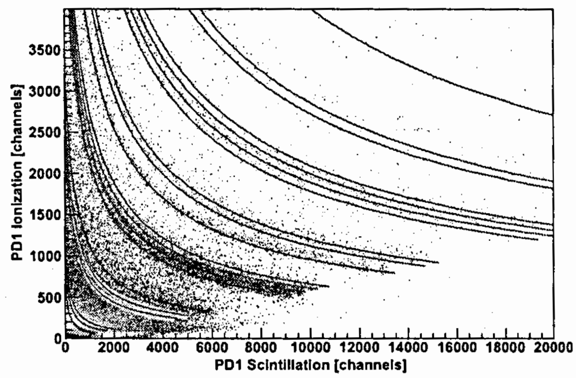

Figure 17: Decomposed SCT ΔE-E identification map with the superimposed ATIMA lines. The sequence of lines is the same as in Fig. 16.

The observed very good agreement between the reconstructed amplitudes and the range-energy table predictions is quite non-trivial taking into account the simplicity of the pulse shape parametrization. In order to obtain this kind of agreement, which is still a compromise, it was not enough to set all the parameters free and search for the minimum of the χ^2 distribution. Such an automatic procedure guarantees the best fit to the waveforms, but not necessarily guarantees the follow up of the trends defined by the range-energy tables. In general, an automatic procedure can lead, depending also on the starting values, to some local minima, produce discontinuities or lead in directions diverging from the ATIMA lines. The presented agreement has been obtained after searching for the optimal values and fixing some of the parameters (see Table 3). The agreement with the ATIMA lines could be made even better, for instance by freeing the τ_{RS} parameter, however at the expense of loosing completely the mass resolution in Fast-Slow representation (contrary to the case presented in Fig. 10). Thus, the presented agreement is a result of an iterative procedure of fixing some of the parameters and also of the energy calibration parameters, but once the crucial parameters are constrained the fitting proceeds automatically.

The whole procedure could probably be better automatized by using more realistic pulse shape parametrizations, especially for individual electron and hole components of the ionization signal, taking into account the plasma delay effects, interactions between carriers, diffusion effects, etc [15]. However, to our knowledge, such pulse shape parametrizations are still to be developed. Definitely, a more realistic preamplifier response function would improve the resolution and would allow for disentangling between physical and instrumental parameters. A more realistic parametrization and analysis would be worth the effort of implementing it to e.g. better understand the relation between the range and the charge collection times which enable the identification of the particles stopped in the silicon detectors.

Nevertheless, any more sophisticated analysis would definitely slow down even more the analysis.

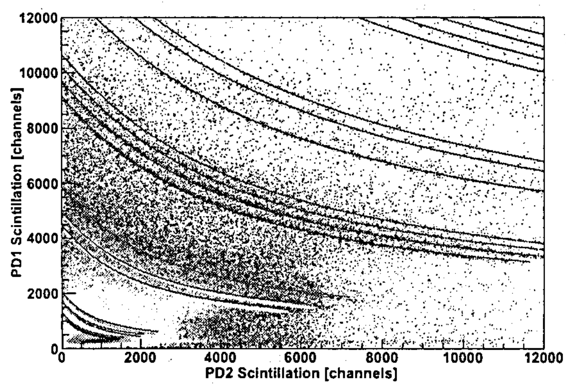

Figure 18: ΔE-E identification map for scintillation signals from CsI1 vs CsI2, with the superimposed ID lines calculated using the ATIMA tables. The sequence of lines is the same as in Fig. 16. The γ-line and punch-through hits have been removed (cf. Fig. 7).

Finally, Fig. 18 shows the calculated ATIMA lines superimposed on the ΔE-E identification map for scintillation signals from thin vs thick CsI(Tl) crystals. The slight overestimation of the ΔE component for $Z = 1$ particles results most probably from the simplicity of the Light-Energy conversion formula (7) and (or) from the light output non-uniformity of the crystals. The overall agreement is, nevertheless, quite satisfactory and the calculated lines can be used not only to derive the energy calibration parameters, but also for identification (see Fig. 15), after small manual adjustments.

The energy calibration routine based on the ATIMA range-energy tables operated on all three maps (Figs. 16-18) simultaneously, allowing for a consistent determination of the calibration parameters for all photodiodes and both crystals. Specifically, for the CsI(Tl) crystals with 1500 ppm of Tl concentration, the quenching parameter a_2 was found to be equal to 0.32, a value compatible with the one from [21] and about 20% larger than the average one quoted for the INDRA crystals [22]. The calibration of the SCT allowed also to estimate the efficiency of the scintillation. The combination of a relatively high Tl doping, high reflectance of the wrapping and large active area of the photodiode, resulted in a relatively high efficiency for energy-light conversion. It was found that only about 6 times more energy was needed to produce an electron-hole pair in the photodiode through a scintillation process in the CsI(Tl) crystal than in the direct ionization process in the photodiode. This fact is worth noting, since for the “good scintillators” quoted in [16] this factor amounts to 15-20.

Obviously, a drawback of the telescope method at high energies, is the high level of the secondary reactions. In order to handle this problem, a more sophisticated methods, neural networks and discriminant analysis are being tested, but this goes beyond the scope of this contribution.

Summary

A new, low threshold, broad energy range, versatile array of triple telescopes, KRATTA, has been constructed. The modules, equipped with digital electronics chains, allowed for isotopic identification of light charged reaction products.

Pulse shape analysis allowed for realistic decomposition of the complex SCT pulse shapes into individual ionization and scintillation components and eventually profit from the, otherwise harmful, nuclear counter effect. The isotopic resolution obtained using a single readout channel was found to compete very well with those obtained using the standard two channel readout. The applied pulse shape analysis permitted also the identification of particles stopped in the first photodiode and the reduction of the identification threshold, due to the thickness of the first photodiode, by a factor of three. Thanks to the pulse shape analysis, it was also possible to obtain the ballistic deficit free amplitudes, which allowed for easy energy calibration and identification based on the predictions of the range-energy tables.

The array has met the expectations, fulfilled the design requirements and performed very well during the ASY-EOS experiment at GSI.

Acknowledgments

Work made possible through funding by Polish Ministry of Science and Higher Education under grant No. DPN/N108/GSI/2009.

We (S.K.) acknowledge the support by the Foundation for Polish Science - MPD program, co-financed by the European Union within the European Regional Development Fund.

Stimulating discussions, expertise and help of Giacomo Poggi as well as of Marian Pârlog, Remi Bougault and Hector Alvarez Pol during the design and test phase of the prototypes are gratefully acknowledged.

References

[1] P. Russotto et al., IWM 2011 Proc., Conf. Proc. Vol. 105, p. 91. P. Russotto et al., IWM 2009 Proc., Conf. Proc. Vol. 101, p. 22. http://www.irb.hr/users/mkis. http://www.ct.infn.it/asyeos2010. P. Russotto et al., Phys. Lett. B 697 (2011) 471.

[2] Th. Blaich et al., Nucl. Instr. Meth. A 314 (1992) 136. P. Pawłowski et al., Nucl. Instr. Meth. A 694 (2012) 47.

[3] A. Pagano et al., Nucl. Phys. A 734 (2004) 504.

[4] A. Schüttauf et al., Nucl. Phys. A 607 (1996) 457.

[5] HAMAMATSU Si Photodiode for Direct Detection (S5377-0052(X)).

[6] Manufacturer: Institute of Modern Physics, Chinese Academy of Sciences, Lanzhou, China.

[7] G. Pasquali et al., Nucl. Instr. Meth. A 301(1991) 101.

[8] 3M Vikuiti^{TM} ESR foil, recommended by the crystal manufacturer.

[9] http://www-linux.gsi.de/~weick/atima

[10] Z. Sosin et al., in preparation.

[11] CAEN V1724 digitizer.

[12] http://www.gsi.de/informationen/wti/ee/elekt_entwicklung/triva_e.html

[13] RIO4-8072RE, CES, http://www.ces.ch

[14] http://www-win.gsi.de/daq/

[15] C.A.J. Ammerlaan et al., Nucl. Instr. Meth. 22 (1963) 189. A. Alberigi Quaranta et al., Nucl. Instr. Meth. 57 (1967) 131. G. Pausch et al., Nucl. Instr. and Meth. A 337 (1994) 573. M. Pârlog et al., Nucl. Instr. Meth. A 613 (2010) 290. Z. Sosin, Nucl. Instr. Meth. A 693 (2012) 170.

[16] G.F. Knoll, "Radiation Detection and Measurement", 4-th ed., Wiley (2010), Chapt. 9, 16.

[17] http://root.cern.ch. A.J. Ketikian et al., Nucl. Instr. and Meth. A 314 (1992) 578. S.N. Dymov et al., Nucl. Instr. and Meth. A 440 (2000) 431.

[18] F. Benrachi et al., Nucl. Instr. and Meth. A 281 (1989) 137.

[19] G. Pausch et al., Nucl. Instr. and Meth. A 365 (1995) 176. L. Bardelli et al., Nucl. Instr. and Meth. A 654 (2011) 272.

[20] http://pdg.lbl.gov/2012/AtomicNuclearProperties/HTML_PAGES/141.html

[21] D. Horn et al., Nucl. Instr. and Meth. A 320 (1992) 273.

[22] M. Pârlog et al., Nucl. Instr. and Meth. A 482 (2002) 693.

ONSET OF DECONFINEMENT AND SEARCH FOR CRITICAL POINT BY NA49 AND NA61 AT CERN SPS

G.L.Melkumov[1] (for the NA49 and NA61 Collaborations)

JINR, 141980, Dubna, Moscow region, Russia

Abstract

The NA49 results on hadron production obtained in Pb+Pb collisions at CERN SPS energies from $20A$ GeV to $158A$ GeV are shown and discussed as evidence for the onset of deconfinement. The signatures of the onset of deconfinement, found by the NA49 experiment at low SPS energies, are confronted with new results from the Beam Energy Scan program at BNL RHIC and CERN LHC results.

A possible indication of the QCD critical point signatures was investigated in the event-by-event fluctuations of various observables such as the mean transverse momentum, particle multiplicity and azimuthal angle as well as the chemical (particle ratio) fluctuations, intermittency of di-pions and net-protons are presented.

A primary conception and plans for continuation of this research program at the SPS by experiment NA61 are briefly discussed.

1 Introduction

It was early shown [1] that nucleus-nucleus collisions at the CERN SPS offered the possibility of reaching energy densities in excess of about 1 GeV$/fm^3$ during the early stage of the reaction. Under these conditions QCD predicts a phase transition between hadronic matter and state of quasifree quarks and gluons called the quark- gluon plasma (QGP).

Indeed, the predicted signatures of the QGP, e.g. strangeness enhancement, charmonia suppression and dilepton enhancement were observed in Pb+Pb collisions at the top SPS energy ($\sqrt{s_{NN}}$ = 17.3 GeV). Following these observations of a new state of matter [2], the energy dependence of inclusive hadronic observables, i.e. the K/π ratio, the total pion yield and the slope parameter of hadron transverse momentum spectra gave evidence that the predicted signatures of the onset of deconfinement transition [3] is observed at low SPS energies around $\sqrt{s_{NN}} = 8$ GeV [4, 5, 6, 7]. Final results from these studies will be reviewed.

Further insight into the early stage of nucleus-nucleus collisions was motivated by predictions from modern lattice QCD and the QCD model calculations indicating the primaty features of the phase diagram of strongly interacting matter (Fig.1). The QCD suggests that deconfined matter (QGP) is separated from hadron phase, hadron gas (HG), by a first order transition boundary at large bariochemical potential μ_B ending in a critical point E and then turning into a cross-over transition at low values of μ_B (low baryon density). A recent extension to the finite μ_B domain allowed to estimate the position of the critical point E [8].

The location of the hadron chemical freeze-out points of the high density fireball produced in nucleus-nucleus collisions shown in Fig.1. They are obtained from fits of a statistical hadron gas model to hadron abundandances [9, 10, 11]. It provides a good fit to the total yields of numerous particle species with 3 parametrs, namely a temperature T, a baryochemical potential μ_B and a strangeness saturation parameter γ_s. The resulting freeze-out points for central Pb+Pb collisions in the CERN SPS energy range are seen to approach the estimated phase boundary and the critical point E.

[1]E-mail: `Georgui.Melkoumov@cern.ch`

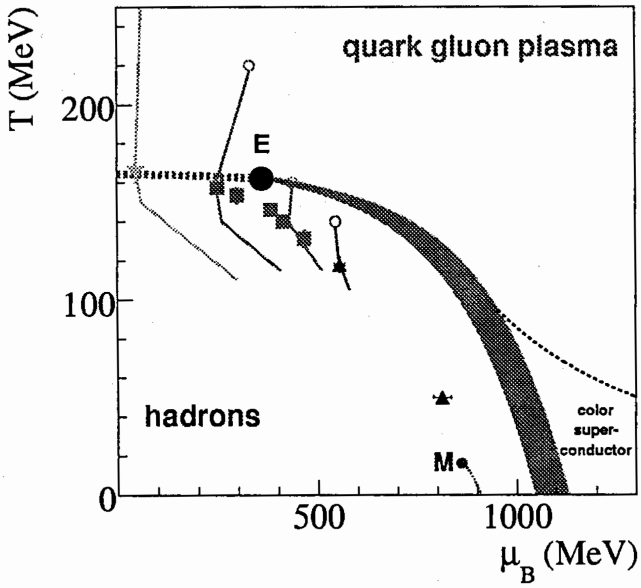

Figure 1: Phase diagram of strongly interacting matter in the plane temperature (T) versus barionic chemical potential (μ_B). The dark band is a lattice QCD estimate [8] of the first order phase boundary between quark-gluon plasma (OGP) and hadrons which ends in a critical point E and then proceeds to a crossover. Symbols denote the chemical freeze-out parameters of heavy ion collisions at different energies as extracted by statistical model fits [9, 10, 11] to the data of the hadron composition at RHIC (STAR), SPS (NA49), AGS and SIS. The open symbols schematically indicate possible values of initial parameters of the reaction systems, which then might evolve along paths as depicted by the vertical lines.

In the vicinity of the QCD critical point a large event-by-event fluctuations of various observables are expected [12, 13]. This paper reports the status of the search for such fluctuations. Results will be presented from analysis of central Pb+Pb collisions, which were recorded for SPS beam energies of 20A, 30A, 40A, 80A and 158A GeV ($\sqrt{s_{NN}}$ = 6.3, 7.6, 8.7, 12.3 and 17.3 GeV) as well as from p+p, C+C and Si+Si interactions at 158A GeV.

The experiment was carried out with the NA49 large acceptance hadron detector [14] employing a system of time projection chambers (TPCs) for efficient tracking in the forward hemisphere of the reactions, precise momentum reconstruction in the magnetic field with a resolution of $\sigma(p)/p^2 \cong (0.3 - 7) \cdot 10^{-4}$ (GeV/c)$^{-1}$ and particle identification using the energy loss dE/dx in the TPC gas. Two time of flight (TOF) walls of 900 scintillator pixels each situated symmetrically to the beam line behined TPCs augment particle identification near midrapidity. The typical dE/dx resolution was $\sigma(dE/dx)/\langle dE/dx\rangle \approx 0.04$ and for TOF resolution $\sigma(TOF) \approx 60$ ps.

2 Onset of deconfinement in hadron production

There is a firm notion that in central collisions of heavy nuclei at the top SPS energy ($\sqrt{s_{NN}}$ = 17.3 GeV) as well as at RHIC energies ($\sqrt{s_{NN}}$ = 130 and 200 GeV) a transient state of deconfined quarks and gluons (QGP) is produced. It is argued by the observation of the signatures predicted for the QGP.

In order to find out whether the early stage fireball actually reaches hadron deconfinement the energy dependence of the hadron production properties was studied [4]. This program was originally motivated by the predictions of the Statistical Model of the Early Stage (SMES) [3]

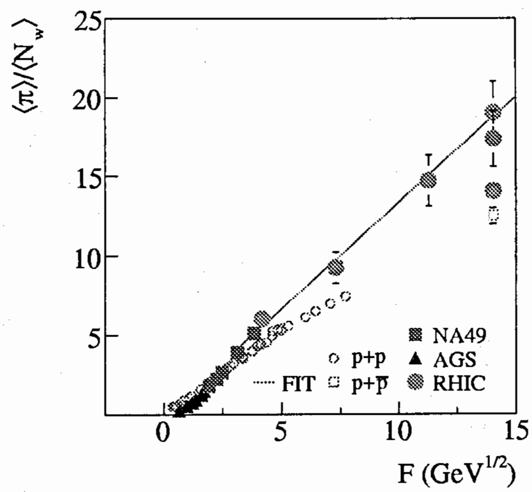

Figure 2: Total pion yield in a full phase space (4π) per wounded nucleons as a function of the Fermi variable $F = (\sqrt{s_{NN}} - 2m_N)^{3/4}/\sqrt{s_{NN}^{1/2}} \approx \sqrt{s_{NN}^{1/2}}$.

assuming that the energy threshold for deconfinement is located at low SPS energies. Several structures in excitation functions were expected within the SMES: a kink in the increase of the pion yield per participant nucleon (change of slope due to increased entropy as a consequence of the activation of partonic degrees of freedom), a sharp peak (horn) in the strangeness to entropy ratio, and a step in the inverse slope parameter of transverse mass spectra (constant temperature and pressure in a mixed phase). Such signatures were indeed observed in $A+A$ collisions by the NA49 experiment [14], thus locating the onset of deconfinement (OD) energy around 30A GeV ($\sqrt{s_{NN}} \approx 7.6$ GeV).

2.1 Charged pion yields

Fig.2 shows the pion yield in full phase space of central Pb+Pb collisions [4], normalized to the number of wounded nucleons N_w as a function of the collision energy expressed in a Fermi variable $F \approx \sqrt{s_{NN}^{1/2}}$.

The pions are the most abundantly produced particle species, therefore they measure the early stage entropy density created in the system as it stated in a statistical model approach. Compared to the same data in p+p interaction one can see that the energy dependence of the pion yield in A+A collisions changes its behaviour in the SPS energy region. It clearly steepens at low energies around 30A GeV and can be interpreted as an increase of the number of effective degrees of freedom by a factor ≈ 3 [3]. Such an increase may be considered as a consequence of the activation of partonic degrees of freedom when going from hadron gas to QGP.

2.2 Strangeness to pion ratio

Another remarkable observation is a pronounced sharp maximum of K^+/π^+ ratio in central Pb+Pb collisions at about 30A GeV beam energy [4] presented in Fig.3 (left). This feature is not seen in p+p interactions and not reproduced by the hadron-string models RQMD [15] , UrQMD [16] or HSD [17].

Since K^+ is by far the most abundant carrier of anti-strangeness at SPS energies, it provides a good measure of the total strangeness produced in the collisions. Thus, the K^+/π^+ ratio represents the strangeness to entropy ratio. A sharp maximum in this quantity was predicted by the SMES consideration as a consequence of the transition to a deconfined

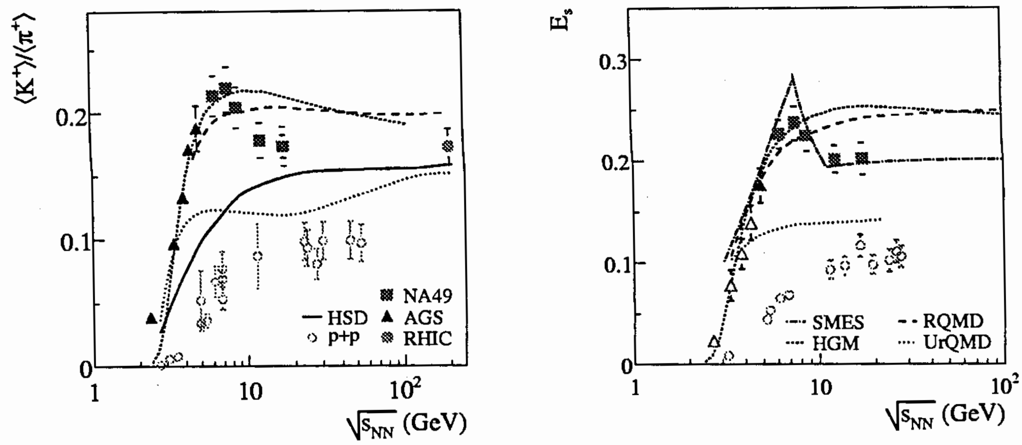

Figure 3: Energy dependence of the $\langle K^+\rangle/\langle\pi^+\rangle$ ratio in full phase space (left). Ratio $E_S = (\langle K + \bar{K}\rangle + \langle\Lambda\rangle)/\langle\pi\rangle$ of total number of strangeness carriers to entropy (pions) versus collision energy (right). NA49 results in Pb+Pb collisions are shown together with the data in A+A collisions at lower and higher energies, and compared to the measurements in p+p reactions. Curves show model predictions.

state [3]. The most relevant measure of the strangeness to entropy ratio used in this work is E_S calculated from π, K and Λ total yields in 4π acceptance. The energy dependence of E_S in central Pb+Pb collisions is plotted in Fig.3 (right).

2.3 Kaon transverse mass distributions

A phase transition was expected to also exhibit itself in the momentum distributions. Fig.4 shows the inverse slope parameters for K^+ and K^- [4] derived from transverse mass spectra of these particles at midrapidity as a function of the collision energy. One observes for slope parameter in A+A collisions a steep rise at lower AGS energies turning into plateau over the entire SPS energy range and then gradually increasing towards RHIC energies. This structure is not seen in p+p reactions and not reproduced by transport models UrQMD [16] and HSD [17].

Since the slope parameter measures both the local temperature and the pressure induced collective flow the step-like behaviour observed for the kaon slopes is consistent with the constant temperature and pressure, the features pecular for the mixed phase of a first-order phase transition. Indeed, a hydrodynamical model [18] incorporating a deconfimenent phase transition provides a satisfying description of the experimental data. The step-like behaviour was shown [4] to be a characteristic feature also for pions, protons and antiprotons.

Above feature attributed to the softest point of the equation of state as expected in the first order phase transition is also seen in the excitation function of sound velocity c_s [19], which has been derived from the width of the pion rapidity distributions of the NA49 using the Landau hydrodynamical model.

Finally, in conjuction with the transverse mass spectra, the fireball volume derived from the Bose-Einstein correlations allowed to extract the energy dependence the pion phase space density [20]. This quantity exhibits a plateau at SPS energies, which may also be related to the onset of deconfinement.

The NA49 data on hadron production at SPS energies have recently been confirmed by preliminary data from the STAR experiment at $\sqrt{s_{NN}} = 9.3$ and 19.6 GeV [21, 22, 23].

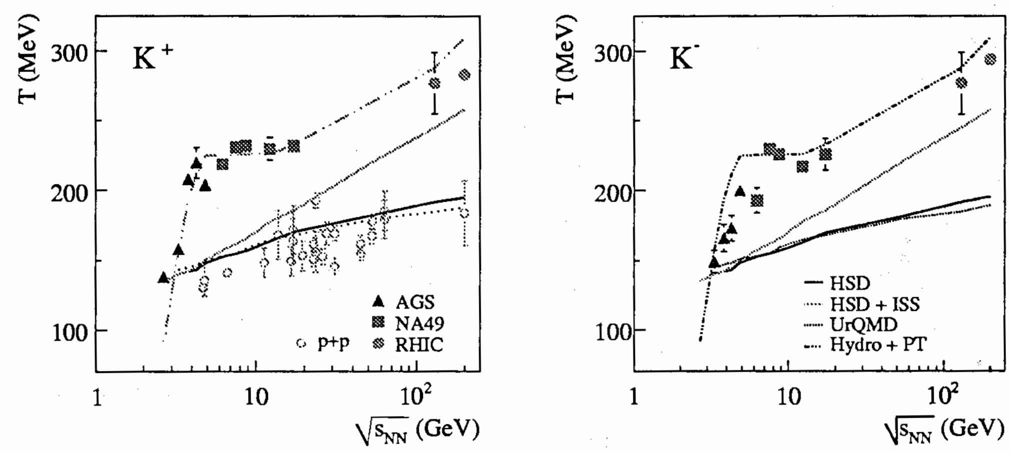

Figure 4: Energy dependence of the inverse slope parameter T of transverse mass spectra for K^+ (left) and K^- (right) [4]. The data are compared to results of UrQMD [16] and HSD [17] models, and hydrodynamical model (Hydro+PT) [18] incorporating the first order phase transition.

2.4 Verification of NA49 results by STAR and ALICE

Until now the evidence of the onset of deconfinement was based on the results of a single experiment. Recently new results on central Pb+Pb collisions at the LHC [24] and data on central Au+Au collisions from the RHIC BES (Beam Energy Scan) program [25] were released. Figure 5 (left) shows an update of the kink plot, where BES points follow the line for $A+A$ collisions and the LHC point [2], within a large error, does not contradict extrapolations from high SPS and RHIC energies.

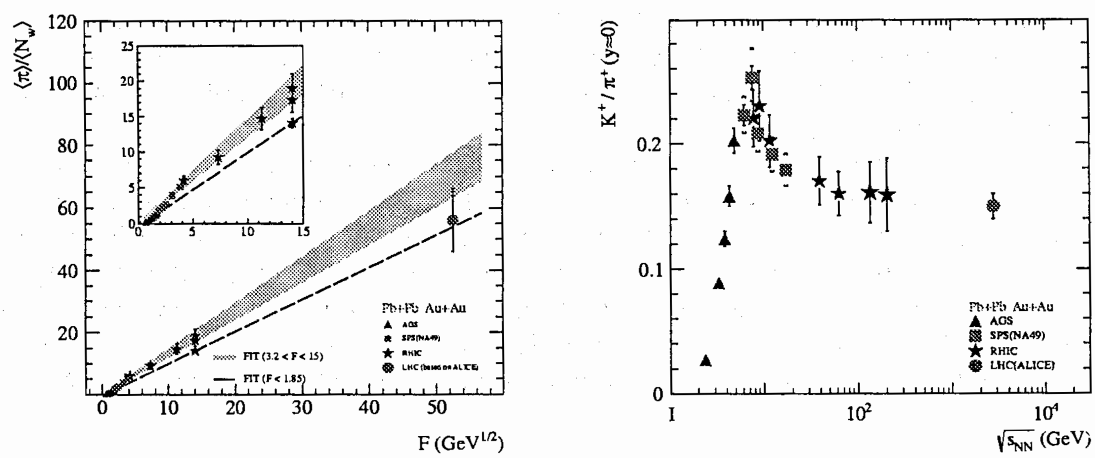

Figure 5: Mean pion multiplicity per participant nucleon (left). Kaon to pion yield near midrapidity (right). See [26] for details.

The K^+/π^+ yield (near midrapidity) is presented in Fig. 5 (right). Figure 6 shows inverse slope parameters of kaon transverse mass spectra. The LHC points and the RHIC BES points confirm the step structure expected for the onset of deconfinement. As seen, RHIC results confirm NA49 measurements at the onset of deconfinement. Moreover, LHC (ALICE) data demonstrate that the energy dependence of hadron production properties shows rapid changes

[2] the mean pion multiplicity at LHC was estimated based on the ALICE measurement of charged particle multiplicity, see [26] for details.

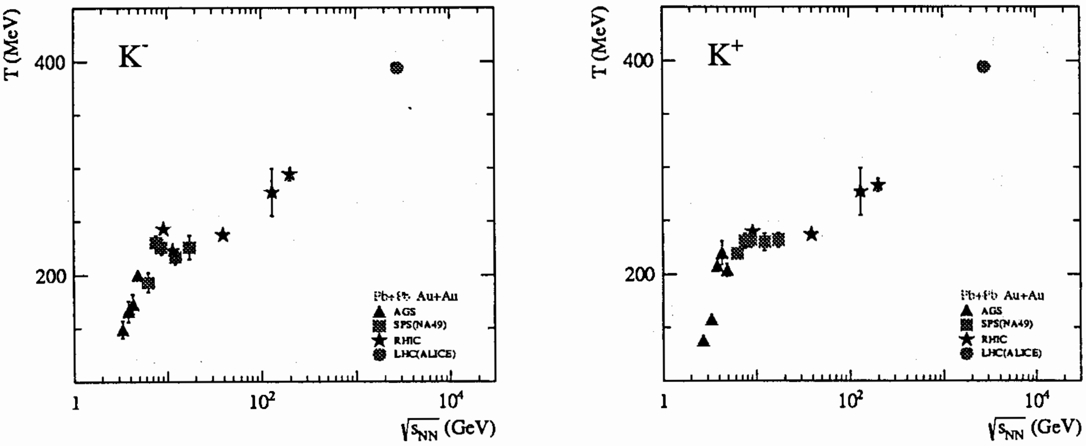

Figure 6: Inverse slope parameters of kaon transverse mass m_T spectra. See [26] for details.

only at low SPS energies, and a smooth evolution is observed between the top SPS (17.2 GeV) and the current LHC (2.76 TeV) energies. All three structures confirm that results agree with the interpretation of the NA49 structures as due to the onset of deconfinement. Above the onset energy only a smooth change of QGP properties with increasing energy is expected.

3 Critical point and phase transition in fluctuations

The QCD phase diagram [27] is often plotted in terms of tempeerature (T_{chem}) and baryochemical potential (μ_B). The lattice QCD calculations indicate that at small chemical potential ($\mu_B \approx 0$) the transition from hadronic to partonic matter is a crossover [28], while at larger values of μ_B the transition becomes first order [29]. Therefore, one expects the existence of a critical point at the end of first order transition. Several lattice QCD calculations suggest the existence of the critical point (CP) of strongly interacting matter in the SPS energy range [8, 30]

One of the characteristic signatures of the critical point is an increase in fluctuations of various event-by-event observables, in particular the particle multiplicity and transverse momentum fluctuatios [12, 13]. A signal of CP is expected to be maximal when freeze-out of the system created in the collision happens near critical point. These observations suggest that it might be possible to perform a 2-dimentional scan of the phase diagram of strongly interacting matter by changing $\sqrt{s_{NN}}$ (variation of μ_B) and the colliding system size A (variation of T_{chem}) and look for a maximum of fluctuations as a signature for the critical point.

3.1 Transverse momentum and multiplicity fluctuations

In NA49 the Φ_{p_T} measure [31, 32, 33] and the scaled variance ω [34, 35, 36] are used for studying the mean transverse momentum and particle multiplicity fluctuations, respectively.

The Φ_{p_t} measure is defined as

$$\Phi_{p_t} = \sqrt{\frac{\langle Z^2_{p_t}\rangle}{\langle N\rangle}} - \sqrt{\overline{z^2_{p_t}}}, \tag{1}$$

where $z_{p_t} = p_t - \overline{p_t}$ with the bar denoting the overall inclusive average and $Z_{p_t} = \sum_{i=1}^{N}(p_{ti} - \overline{p_t})$ with summation over the event multiplicity N. Thus, the Φ_{p_t} represents the difference between the event average of a quantity $\langle p_t\rangle$ and its ensemble average expressed by the first and second terms of Eq.1, respectivelly.

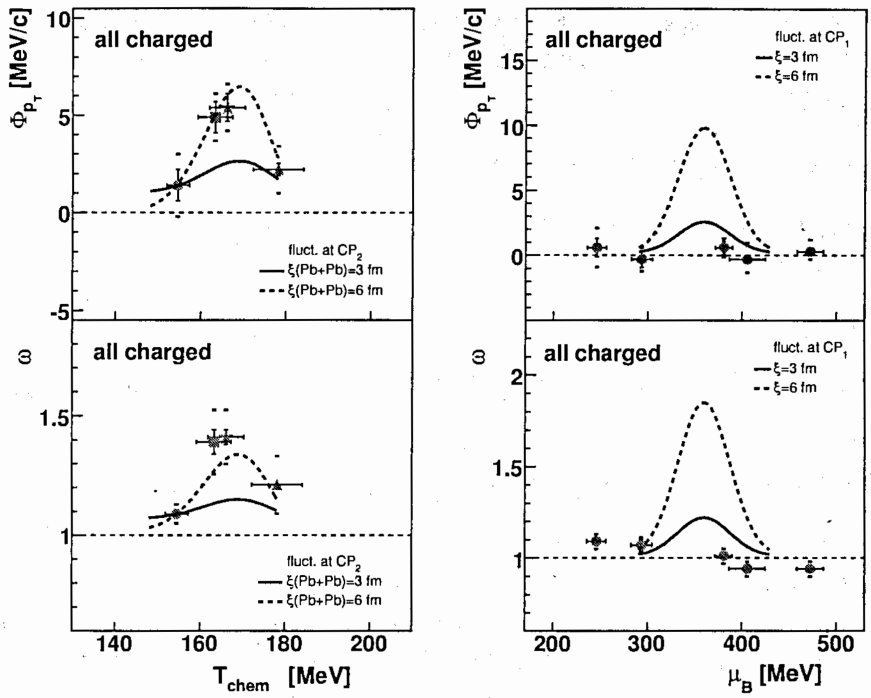

Figure 7: Fluctuation measures Φ_{p_t} of average transverse momentum and ω the scaled variance of the multiplicity distribution versus freeze-out temperature T (left) and baryochemical potential μ_B (right) measured by NA49. Dashed and solid lines indicate the estimated effects of the critical point for two values of the correlation lenght ξ (size of the fireball).

For multiplicity fluctuation the scaled variance ω (variance of the multiplicity distribution normalized by its mean value) is defined as

$$\omega = \frac{Var(n)}{\langle n \rangle} = \frac{\langle n^2 \rangle - \langle n \rangle^2}{\langle n \rangle} \tag{2}$$

The results of the NA49 study of transverse momentum [33] and multiplicity [35, 36] fluctuations are plotted in Fig.7 [37, 38].

It presents the energy (μ_B) and system size (T_{chem}) dependence of Φ_{p_t} and ω. The chemical freeze-out parameters, $T_{chem}(A, \sqrt{s_{NN}})$ and $\mu_B(A, \sqrt{s_{NN}})$ were taken from fits of the hadron gas model [10] to particle yields. The lines correspond to predictions for critical points CP_1 and CP_2 with estimated magnitude of the effect for Φ_{p_t} and ω taken from [12, 39, 40], assuming correlation lenghts ξ decreases monotonicaly with decreasing system size (fireball), namely ξ(Pb+Pb) = 6 fm and ξ(p+p) = 2 fm (dashed lines) or ξ(Pb+Pb) = 3 fm and ξ(p+p) = 1 fm (solid lines).

As possible location of the critical point CP_1 (Fig.7 (right)) the μ_B = 360 MeV was taken from lattice QCD calculations [8] and the corresponding T_{chem} = 147 MeV to be on the empirical freeze-out line for the 5 energies of central Pb+Pb collisions. For critical point CP_2 (Fig.7 (left)) the measured chemical freeze-out parameters of p+p reaction at 158 GeV, μ_B = 250 MeV and T_{chem} = 178 MeV, were suggested assuming that this point may be located on the phase transition line.

Fig.7 (right) shows no significant energy dependence of mean p_t and multiplicity fluctuations at SPS energies. Thus the results do not provide evidence for for critical point CP_1 making possible conclusions that either the critical point is not close enough to manifest itself in the data or the correlation length realized in heavy ion collisions is very small.

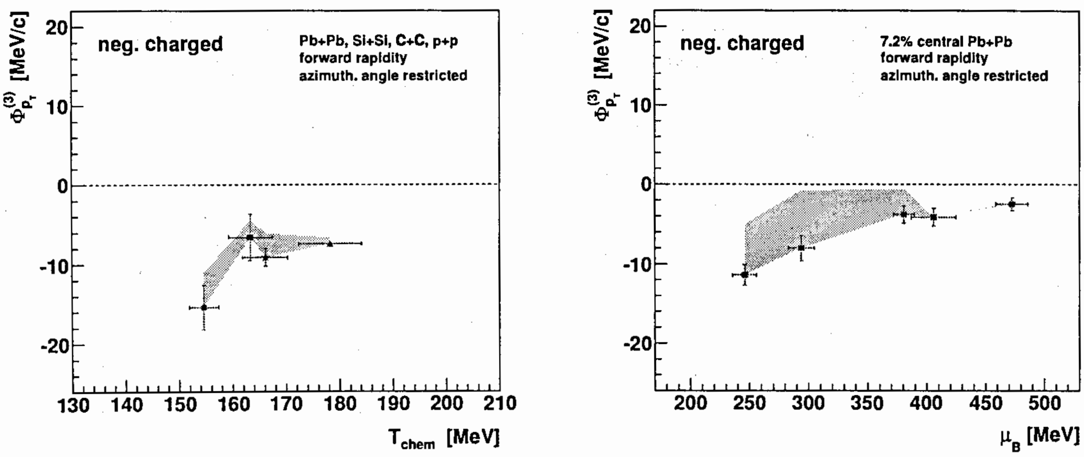

Figure 8: (NA49 very preliminary) Third moment $\Phi_{p_t}^{(3)}$ of average transverse momentum fluctuations versus T (left) and μ_B (right) for negatively charged particles.

The system size dependence of fluctuations presented in Fig.7 (left) exibits a maximum of Φ_{p_t} and ω for intermediate systems C+C and Si+Si interactions at the top SPS energy. The peak is two times higher for all charged than for negatively charged particles as expected for the critical point [12]. Both figures suggest that the NA49 data are consistent with the CP_2 predictions for possible critical point at $\mu_B \approx 250$ MeV and $T_{chem} \approx 165$ MeV.

3.2 Higher moments of transverse momentum fluctuations

Most fluctuation measures discussed to date can be related to a quadratic variances (second moments) of event-by-event observables, such as particle multiplicities, net charge, baryon number, particle ratios, or mean transvere momentum in the event.

For future fluctuation studies, the higher moments of event-by-event distribtions will be of great interest. It was ponted out [41, 42, 43] that the higher moments of fluctuations are much more sensitive to the proximity of the critical point than the commonly employed measures based on the quadratic measures. In this case the amplitude of the critical point peak became proportional to higher powers of the correlation length ξ.

The first attempt of NA49 in studying the higher moment fluctuations was applied to the mean p_t observable using the Φ measure. In general case, the n-th moment is defined as

$$\Phi_{p_t}^{(n)} = \left(\frac{\langle Z_{p_t}^n \rangle}{\langle N \rangle}\right)^{1/n} - \left(\overline{z_{p_t}^n}\right)^{1/n} \tag{3}$$

In present analysis, the third moment $\Phi_{p_t}^{(3)}$ was employed. A very preliminary results on the system size (T) and the energy (μ_B) dependences of the $\Phi_{p_t}^{(3)}$ are presented in Fig.8 (left) and Fig.8 (right), respectively. Some dependence of the $\Phi_{p_t}^{(3)}$ on the mentioned parameters is visible but no evident maximum is observed. For further study of higher moment fluctuations the progress in data analysis and the relevant theoretical predictions are necessary.

3.3 Density fluctuations of low-mass $\pi^+\pi^-$ pairs and protons

At the critical point (CP) local density fluctuations with the power-law singularity are expected both in configuration and momentum space [44] and should appear both for baryonic density and the σ field. It is motivated by the hypothesis that magnitude the net-baryon density and σ field characterise the order parameters for the second order phase transition associated with the QCD critical endpoint.

Significant σ-field fluctuations are expected at the CP (density fluctuations of zero mass σ-particles produced in abundance at the CP) [44]. σ particles at $T < T_c$ may reach the two-pion threshold ($2m_\pi$) and then decay into two pions, therefore density fluctuations of di-pions with $m_{\pi^+\pi^-}$ close to the two pion mass incorporate σ–field fluctuations at the CP.

Critical σ fluctuations are predicted to be observable as an intermittency behaviour of the second order factorial moments [45]. The NA49 experiment searched for an intermittency signal in transverse momentum space of reconstructed di-pions ($\pi^+\pi^-$ pairs) with invariant mass just above $2m_\pi$ [46]. The analysis was performed for p+p, C+C and Si+Si interactions at 158A GeV. First, for each event all possible pairs with $m_{\pi^+\pi^-}$ in a small kinematic window above two-pion threshold were selected. Then, second factorial moments $F_2(M)$ in transverse momentum space were computed for real data and for artificially produced mixed events where only statistical fluctuations are present. The second factorial moment of the di-pion density

$$F_2(M) = \langle \frac{1}{M^2} \sum_{i=1}^{M^2} n_i(n_i - 1) \rangle / \langle \frac{1}{M^2} \sum_{i=1}^{M^2} n_i \rangle^2 \tag{4}$$

was calculated as a function of the number M of subdivisions in each transverse momentum space direction (-1.5 GeV/$c < p_{T,x}, p_{T,y} < 1.5$ GeV/c), where n_i is the number of di-pions in the cell i. The combinatorial background subtracted (by use of mixed events) moments ΔF_2 in transverse momentum space are expected to follow a power-law behavior $\Delta F_2 \sim (M^2)^{\phi_2}$, with $\phi_{2,cr} = 2/3$ for system of a low-mass $\pi^+\pi^-$ pairs freezing out at the QCD critical point [44].

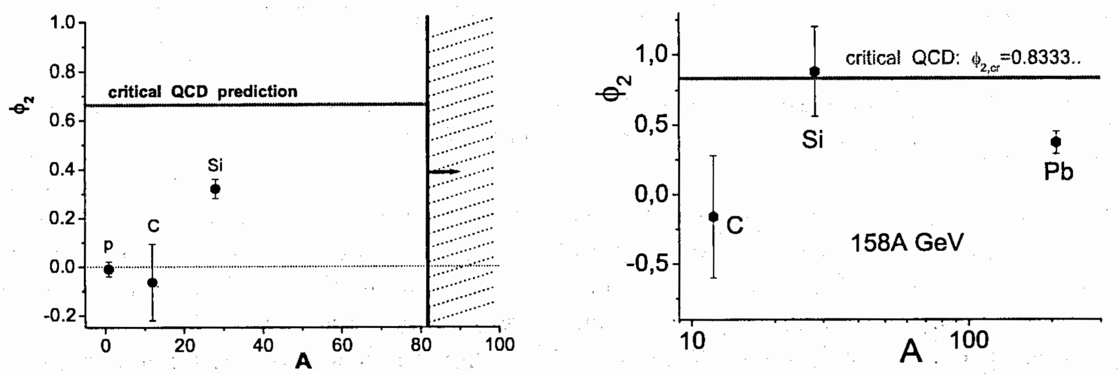

Figure 9: Intermittency signal in p+p and 10% most central C+C and Si+Si interactions at 158A GeV [46] presented in the dependence of intermittency index ϕ_2 on the size A of the colliding nuclei for a systems of low-mass $\pi^+\pi^-$ pairs (left) and net protons (right). The upper horizontal lines indicate the theoretical expected values $\phi_{2,cr} = 2/3$ and $\phi_{2,cr} = 5/6$ for a low-mass $\pi^+\pi^-$ pairs and net protons respectively, freezing out at the QCD critical point.

There is a clear intermittency signal observed in the data although somewhat weaker than in simulation of critical behaviour. Figure 9 (left) shows that ΔF_2 for Si+Si at the top SPS energy measures fluctuations approaching in size the prediction of critical QCD (the remaining departure, $\phi_{2,max} \approx 0.33 \pm 0.04$ instead of 2/3, may be due to freezing out at a distance from the CP). As expected, the analysis of Si+Si events generated via the HIJING model shows no intermittency signal ($\phi_2 \approx 0.02 \pm 0.09$).

From the results of preliminary analysis, a strong intermittency signal is also found in transverse momentum space of protons Fig.9 (right) for Si cluster right compatible with above fluctuation results in the di-pion sector. These findings support further the view that the central Si+Si collision system leads to freeze-out state in the neighbourhood of the QCD critical point.

3.4 Azimuthal angle fluctuations

The main motivation of studying azimuthal event-by-event fluctuations was to search for plasma instabilities [47], critical point and onset of deconfinement, and flow fluctuations [48]. NA49 evaluated the Φ measure of fluctuations (instead of using p_T, as in section 3.1, one uses azimuthal angle ϕ). There are several background effects that can influence the Φ_ϕ measure, among them resonance decays, flow, (di-)jets, momentum conservation, quantum statistics. All of them were studied in [49].

Figure 10 shows the energy dependence of Φ_ϕ for the 7.2% most central Pb+Pb interactions. Color bands represent systematic errors. The values for positive particles are consistent with zero but for negative particles Φ_ϕ is positive. No collision energy dependence of the fluctuations is observed.

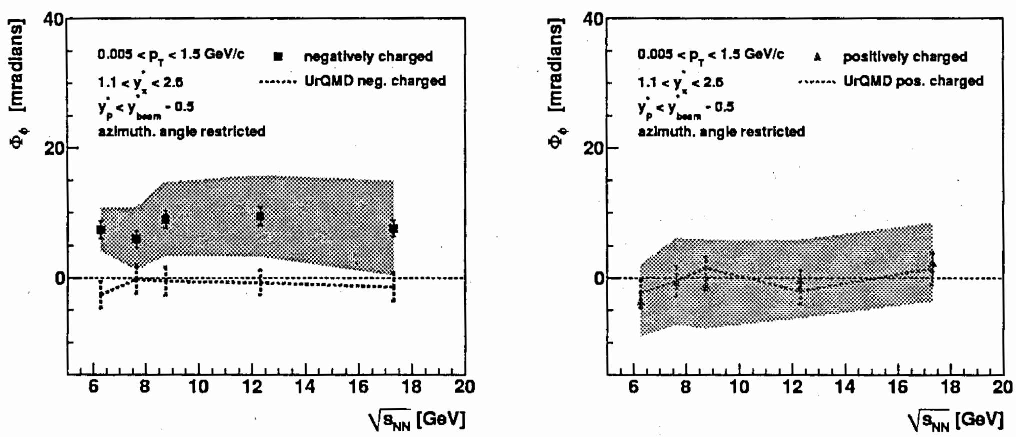

Figure 10: Energy dependence of azimuthal fluctuations. Forward rapidity, limited azimuthal acceptance (as in [50]). The same acceptance for data and UrQMD.

The system size and centrality dependence of Φ_ϕ at the top SPS energy is presented in Fig. 11. For Pb+Pb collisions, the sample of events was split into six centrality classes. Figure 11 shows positive Φ_ϕ values with a maximum for peripheral Pb+Pb interactions. The data are not explained by the UrQMD model. However, the magnitude of Φ_ϕ is reproduced by the effect of directed and elliptic flow [52]. The difference between positive and negative particles is also reproduced and it is caused by a 15% admixture of protons among positive particles (in the MC model calculation [52] v_1 and v_2 values for pions and protons at forward rapidity were taken from [53]).

3.5 Particle ratio fluctuations

In addition to the hadron production properties observed at the phase transition several models suggest the study of hadron ratio fluctuations to gain further insight into the nature of the deconfinement phase transition. Particle ratio fluctuations might also be affected by the critical point.

The measurement of hadron ratio fluctuations by NA49 is expressed in terms of dynamical fluctuations σ_{dyn} which referes to those fluctuations remaining after removing fluctuations

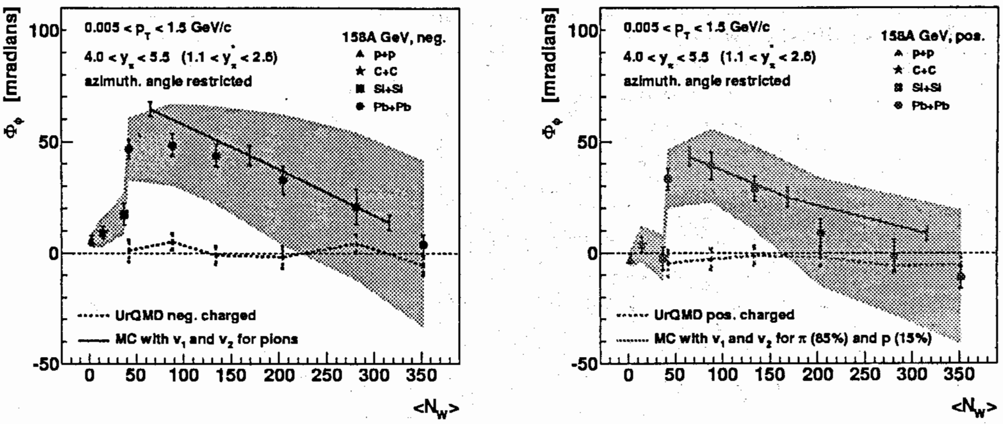

Figure 11: System size dependence of azimuthal fluctuations. Forward rapidity, limited azimuthal acceptance (as in [51]). The same acceptance for data and UrQMD.

from finit number statistics as well as effects from detector resolution and particle identification. The dynamical fluctuation is defined as

$$\sigma_{dyn} = sign(\sigma_{data}^2 - \sigma_{mix}^2)\sqrt{|\ \sigma_{data}^2 - \sigma_{mix}^2\ |}. \tag{5}$$

It measures the difference between widths of the particle ratio distributions for data σ_{data} and for artificially produced mixed events σ_{mix} , where only statistical fluctuations are present (see [54] for details). .

The energy dependence of event-by-event fluctuations of the particle ratios K/π and p/π (for the 3.5% most central Pb+Pb collisions) is shown in Fig. 12. K/π fluctuations show positive values of σ_{dyn}. The steep rise towards low SPS energies is not reproduced by the UrQMD model. The HSD model catches the trend but over-predicts high energy SPS results. The p/π ratio shows negative dynamical fluctuations. This behavior is reproduced by hadronic models and understood in terms of correlations due to nucleon resonance decays.

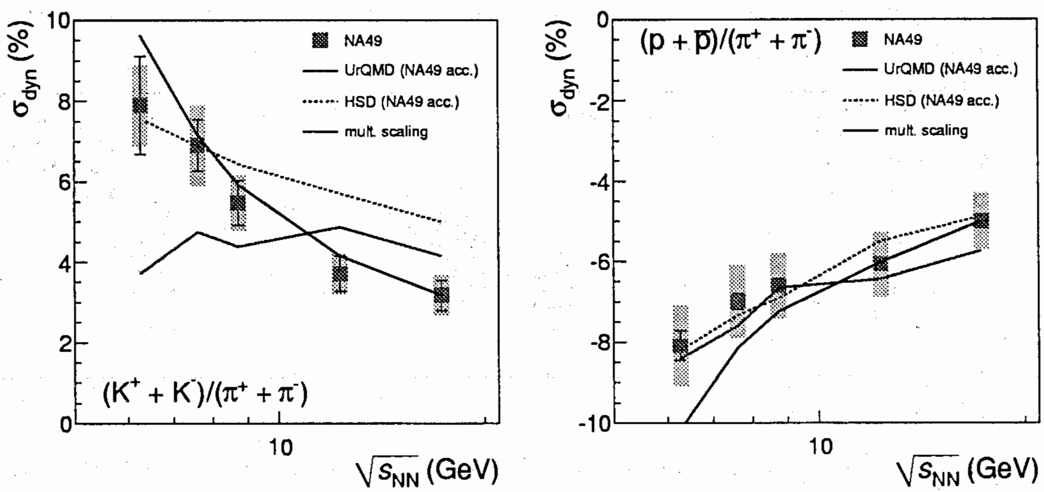

Figure 12: Energy dependence of K/π and p/π fluctuations [54].

An unexpected result was obtained for event-by-event K/p fluctuations (Fig. 13). Dynamical fluctuations change sign close to the onset of deconfinement energy. A jump to positive values at lowest SPS energies is followed by a negative plateau at higher SPS energies. Such structure is not described by hadronic models (UrQMD and HSD). Additionally we show K^+/p fluctuations in which no contributions from resonance production are expected. The relation of this intriguing result to the onset of deconfinement is not known yet.

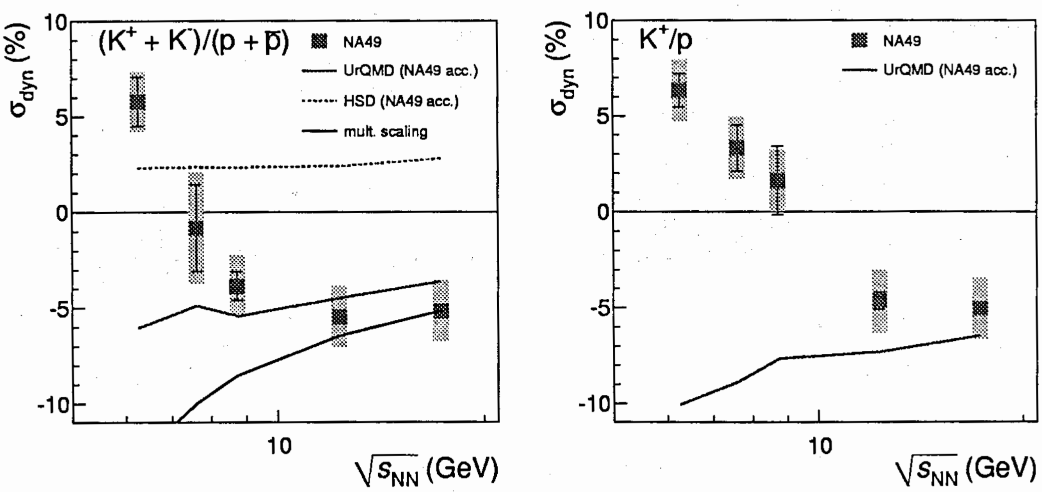

Figure 13: Energy dependence of K/p fluctuations [54].

It has been suggested [55] that σ_{dyn} can be separated into two terms: a correlation strength term and a term purely dependent on multiplicities. In case of unchanged correlations (invariant correlation strength) the general expectation is $\sigma_{dyn} \propto \sqrt{\frac{1}{\langle A \rangle} + \frac{1}{\langle B \rangle}}$, where $A, B = N_K, N_\pi, N_p$, etc. Such scaling is presented in Figs. 12, 13 as black solid lines. One can see that scaling works very well for K/π and p/π fluctuations. The change of sign in K/p fluctuations excludes any simple scaling based on average multiplicities. The above scaling assumed invariant correlation strength, therefore the NA49 results suggest that the underlying correlation between kaons and protons is changing with energy.

The centrality dependence of event-by-event particle ratio fluctuations at 158A GeV ($\sqrt{s_{NN}}$ = 17.3 GeV) is presented in Fig. 14. The absolute values of fluctuations rise towards peripheral collisions, as in UrQMD. The same multiplicity scaling (as in Figs. 12, 13) seems to hold for all three particle ratio fluctuations (black, solid lines in Fig. 14). This is compatible with the hypothesis that at constant energy the underlying correlations are not significantly changing with the system size.

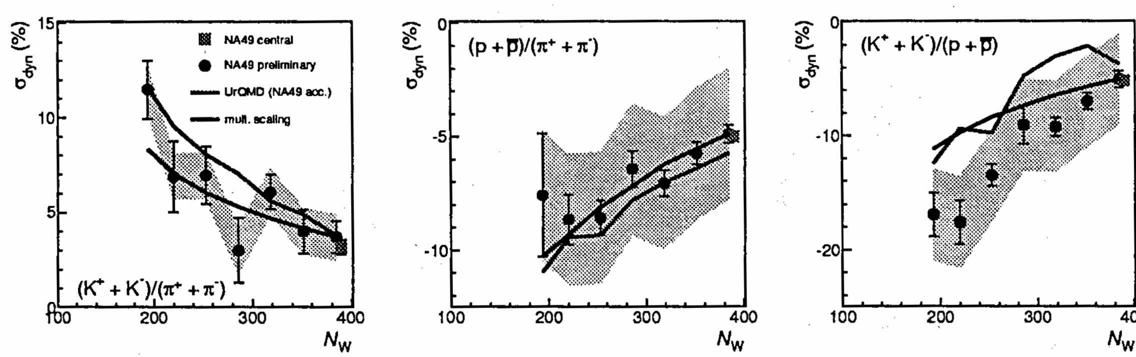

Figure 14: Centrality dependence of particle ratio fluctuations at 158A GeV [54].

4 Research program of NA61/SHINE experiment

The NA61/SHINE experiment at the CERN SPS [56] will continue the program of NA49 with the main goal of searching for the QCD critical point and studying in details the onset of deconfinement by performing a two-dimensional scan (T versus μ_B) of the phase diagram (Fig.1). This will be achieved by varying collision energy (13A - 158A GeV) and size of the

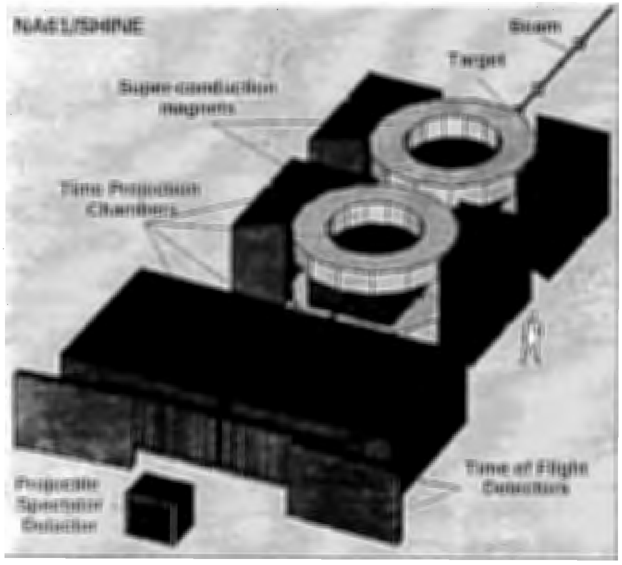

Figure 15: Layout of experiment NA61/SHINE at the CERN SPS.

colliding systems (p+p, p+Pb, B+C, Ar+Ca, Xe+La) in order to cover a broad range of the phase diagram of hadronic matter.

The NA61 experiment (Fig.15) is the successor of NA49. Several upgrades of the detector apparatus inherited from NA49 are complited or in progess.

The first part of the system size and energy scan program, namely p+p collisions at 13, 20, 30, 40, 80 and 158 GeV/c beam energies is being performed [57]. High statistics data on p+p has already been recorded in 2009 and 2010, and will be recorded in 2011. The ion B+C, Ar+Ca and Xe+La runs are foreseen for 2011, 2013 and 2014, respectivelly. They will allow to cover a broad range of parameters T and μ_B of the phase diagram. These parameters vary under changes of the system size and collision energy. The hypothetical positions of the chemical freeze-out points expected for central nucleus-nucleus collisions are shown in Fig.16.

The NA61 program will be complemented by the efforts of other laboratories, BNL RHIC ($5 < \sqrt{s_{NN}} < 39$ GeV), JINR NICA ($3 < \sqrt{s_{NN}} < 9$ GeV), GSI SIS-100(300) ($2.3 < \sqrt{s_{NN}} < 8.5$ GeV).

5 Summary and conclusions

Experiments of NA49 at CERN SPS motivated by predictions of the Statistical Model of the Early Stage indicate that deconfinement starts to occure at the early stage of central Pb+Pb collisions for beam energies above $\sim 30A$ GeV.

The NA49 discovery of the energy threshold for deconfinement is now confirmed. The results from the RHIC Beam Energy Scan agree with NA49 measurements on the onset of deconfinement. LHC data confirm the interpretation of the structures observed at low SPS energies as due to onset of deconfinement.

The NA49 also searched for indications of the predicted QCD critical point where an enhanced event-by-event multiplicity and mean transverse momentum fluctuations are expected. The results from energy scan (variation of baryonic chemical potencial μ_B) in central Pb+Pb collisions show no evidence for the expected critical point location at $\mu_B \approx 360$ MeV and $T_{chem} \approx 150$ MeV, while a visible fluctuations are seen in system size dependence (variation of temperature T_{chem}) for relatively lighter systems produced in $158A$ GeV C+C and Si+Si collisions at $\mu_B \approx 250$ MeV and $T_{chem} \approx 165$ MeV.

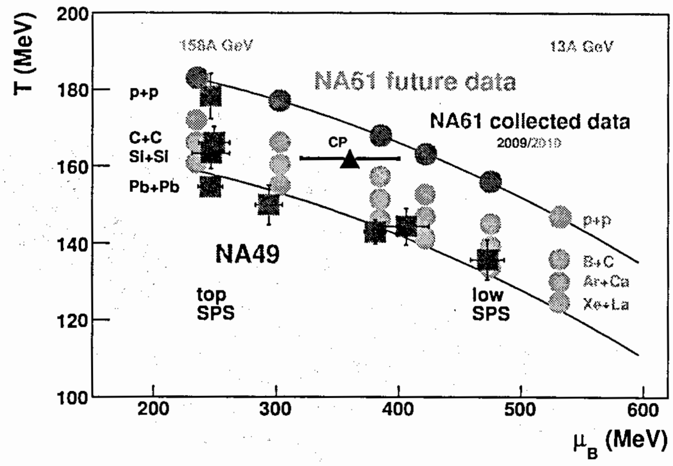

Figure 16: Scan of the phase diagram by varying collision energy (μ_B) and size of colliding nuclei (T). Squares show the freeze-out points covered by NA49, circles indicate the planned measurements of NA61. The estimated location of the critical point is shown be the triangle.

Analysis of density fluctuations of low-mass di-pions (sigma sector) for central Si+Si collisions shows a clear intermittency signal. Compatible fluctuation results is also found from preliminary analysis in transvere momentum of protons. These findings support further the view that the central Si+Si collision system may lead to freeze-out state in the neighbourhood of the QCD critical point.

The azimuthal angle fluctuatuations of charged particles were analyzed using the Φ_ϕ measure. The measurements for central Pb+Pb collisions shows weak energy dependence of Φ_ϕ. However, in the system size dependence the significant rise of the measured fluctuations towards a smaller colliding systems are indicated. This is qualitatively similar to the mean transverse momentum and multiplicity fluctuation results obtained in NA49.

The energy and the system size dependence of K/π and p/π fluctuations can be described in a simple multiplicity scaling model. In contrast, K/p fluctuations show a deviation from this scaling and change sign close to the onset of deconfinement energy; is the underlying correlation physics changing with energy?

For central $A + A$ collisions fluctuations of average p_T, multiplicity, and multiplicity of low mass $\pi^+\pi^-$ pairs and net protons tend to a maximum in Si+Si collisions at 158A GeV. Thus the critical point may be accessible at SPS energies. This result is a strong motivation for future experiments and in fact, the NA49 efforts will be continued by the ion program of the NA61/SHINE experiment .

A further detailed energy and system size scan to investigate the properties of the onset of deconfinement and to establish the existence of the QCD critical point is being performed in the NA61/SHINE experiment at the CERN SPS in order to cover a broad range of the phase diagram of strongly interacting matter.

References

[1] T. Alber *et al.* (NA49 Collaboration), Phys. Rev. Lett. **75** (1995) 3814.

[2] U .W. Heinz and M. Jacob, arXiv:nucl-th/0002042.

[3] M. Gaździcki and M .I .Gorenstein, Acta Phys. Polon. B**30** (1999) 2705.

[4] C. Alt *et al.* (NA49 Collaboration), Phys. Rev. C **77** (2008) 024903.

[5] M. Gaździcki, J.Phys. **G30** (2004) S701.

[6] P. Seyboth, Acta Phys. Polon. B**37** (2006) 3429.

[7] V. Friese (NA49 Collaboration), PoS **CPOD09** (2009) 005.

[8] Z. Fodor and S .Katz, J. High Energy Phys.**0404** (2004) 050.

[9] P. Braun-Munzinger, J. Cleymans, H. Oeschler and K. Redlich, Nucl. Phys. **A697** (2002) 902.

[10] F. Becattini, J. Manninen and M. Gaździcki , Phys. Rev. C **73** (2006) 044905.

[11] F. Becattini, M. Gaździcki, A. Keranen amd R. Stock, Phys. Rev. C **69** (2004) 024905.

[12] M. A. Stepanov, K. Rajagopal and E. V. Shuryak, Phys. Rev. D **60** (1999) 114028.

[13] V. Koch, arXiv:0810.2520 [nucl-th].

[14] S. Afanasiev *et al.* (NA49 Collaboration), Nucl. Instrum. Methods. A **430** (1999) 210.

[15] H. Sorge, H. Stocker and W. Greiner, Nucl. Phys. **A498** (1989) 567.

[16] S. A. Bass *et al.*, Prog. Part. Nucl. Phys. **41** (1998) 225.

[17] E. I. Bratkovskaya *et al.*, Phys. Rev. C **69** (2004) 054907.

[18] M. Gaździcki,M. I. Gorenstein, F. Grassi, Y. Hama, T. Kodama, and O. J. Sokolowski, Braz. J. Phys. **34** (2004) 322.

[19] H. Petersen and M. Bleicher, PoS **CPOD2006** (2006) 025.

[20] S. Akkelin and Y. Sinyukov Phys. Rev. C **73** (2006) 034908.

[21] L. Kumar *et al.* (STAR Collaboration), J. Phys. G **36** (2009) 064066.

[22] G. Wang *et al.* (STAR Collaboration), Nucl. Phys. **A830** (2009) 19c.

[23] D. Cebra *et al.* (STAR Collaboration), arXiv: 0903.4702 [nucl-ex].

[24] J. Schukraft (for ALICE Collab.), *J. Phys.* **G38**, 124003 (2011);
A. Toia (for ALICE Collab.), *J. Phys.* **G38**, 124007 (2011).

[25] L. Kumar (for STAR Collab.), *J. Phys.* **G38**, 124145 (2011);
B. Mohanty (for STAR Collab.), *J. Phys.* **G38**, 124023 (2011).

[26] A. Rustamov, https://indico.cern.ch/conferenceDisplay.py?confId=144745

[27] K. Rajagopal and F. Wilczek, arXiv:hep-ph/0011333.

[28] C. Bernard *et al.*, Phys. Rev. D **75** (2007) 094905.

[29] O. Scavenius *et al.*, Phys. Rev. C **64** (2001) 045202.

[30] P. Gavai and S. Gupta, Phys. Rev. D **78** (2008) 114503.

[31] M. Gaździcki and St. Mrówczyński, Z.Phys. C **54** (1992) 127.

[32] T. Anticic *et al.* (NA49 Collaboration), Phys. Rev. C **70** (2004) 034902.

[33] T. Anticic *et al.* (NA49 Collaboration), Phys. Rev. C **79** (2009) 044904.

[34] C. Alt *et al.* (NA49 Collaboration), Phys. Rev. C **75** (2007).064904.

[35] C. Alt *et al.* (NA49 Collaboration), Phys. Rev. C **78** (2008) 034914.

[36] B. Lungwitz, PhD thesis (2008), http://edms.cern.ch/document/989055/1.

[37] K. Grebieszkow *et al.* (NA49 Collaboration), arXiv:0907.4101 [nucl-ex].

[38] K. Grebieszkow *et al.* (NA49 and NA61 Collaboration), arXiv:0909.0485 [hep-ex].

[39] M. Stepanov, private communications.

[40] Y. Hatta and T. Ikeda, Phys. Rev. D **67** (2003) 014028.

[41] St. Mrówczyński, Phys. Lett. **B465** (1999) 8.

[42] M. A. Stepanov, Phys. Rev. Lett. **102** (2009) 032301.

[43] M. Cheng *et al.*, Phys. Rev. D **79** (2009) 074505.

[44] N. Antoniou *et al.* (NA49 collaboration), Nucl. Phys. **A761** (2005) 149.

[45] A. Bialas and R. Peschanski, Nucl. Phys. **B273** (1986) 703.

[46] T. Anticic *et al.* (NA49 Collaboration), Phys. Rev. C **81** (2010) 064907.

[47] St. Mrówczyński, *Phys. Lett.* **B314**, 118-121 (1993).

[48] St. Mrówczyński and E. V. Shuryak, *Acta Phys. Polon.* **B34**, 4241 (2003).

[49] St. Mrówczyński, *Acta Phys. Polon.* **B31**, 2065 (2000);
T. Cetner, K. Grebieszkow, St. Mrówczyński, *Phys. Rev.* **C83**, 024905 (2011).

[50] T. Anticic et al. (NA49 Collab.), *Phys. Rev.* **C79**, 044904 (2009).

[51] T. Anticic et al. (NA49 Collab.), *Phys. Rev.* **C70**, 034902 (2004).

[52] K. Grebieszkow and St. Mrówczyński, arXiv:1110.4910

[53] C. Alt et al. (NA49 Collab.), *Phys. Rev.* **C68**, 034903 (2003).

[54] T. Schuster (for NA49 Collab.), *J. Phys.* **G38**, 124096 (2011) and ref. therein.

[55] V. Koch and T. Schuster, *Phys. Rev.* **C81**, 034910 (2010).

[56] N. Antoniou *et al.* (NA61 Collaboration), Proposal CERN-SPSC-2006-034/P-330 and addenda.

[57] M. Gaździcki (for NA49 and NA61 Collab.), *J. Phys.* **G38**, 124024 (2011).

NICA COMPLEX AT JINR [1]

A.S. Sorin[1], V.D. Kekelidze, A.D. Kovalenko, R. Lednicky, V.A.Matveev, I.N.Meshkov, G.T.Trubnikov

Joint Institute for Nuclear Research, 141980 Dubna, Russia

Abstract

New scientific program is proposed at Joint Institute for Nuclear Research (JINR) in Dubna aimed at study of hot and dense baryonic matter in the wide energy region from 2 GeV/amu to $\sqrt{s_{NN}}$ = 11 GeV, and investigation of nucleon spin structure with polarized protons and deuterons maximum energy in the c.m. 27 GeV (for protons). To realize this program the development of JINR accelerator facility in high energy physics has started. This facility is based on the existing superconducting synchrotron - Nuclotron. The program foresees both experiments at the beams extracted from the Nuclotron, and construction of ion collider - the Nuclotron-based Ion Collider fAcility (NICA).

1. Introduction

As an introduction it is a pleasure to notice that these year is the 105-th Jubilee year of academician V. I. Veksler who conceived the principle of phase stability in 1944. He was the first director of our Laboratory and was the leader of the Synchrophasotron design and construction. The accelerator was put into operation 55 years ago and at that time it has reached the record energy of 10 GeV for accelerated protons.

Three years ago the 7-years plan of Joint Institute for Nuclear Research (JINR) has been approved for 2010-2016 years. In accordance with this plan the project named "Nuclotron based Ion Collider fAcility" (NICA) aimed to study of hot and dense baryonic matter and spin physics is realizing at JINR as a flagship project in high energy physics (HEP). A study of hot and dense baryonic matter should shed light on: in-medium properties of hadrons and nuclear matter equation of state (EOS); onset of deconfinement (OD) and/or chiral symmetry restoration (CSR); phase transition (PT), mixed phase (Fig.1 *left)* and critical end-point (CEP); possible local parity violation in strong interactions [1-4].

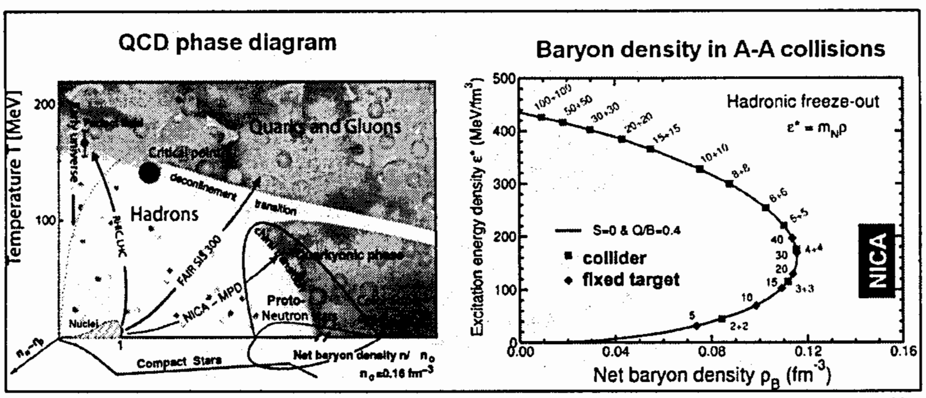

Figure 1. Left: phase diagram for QCD matter (mixed phase is indicated by yellow); right: freezout diagrams for baryonic matter indicating baryon density reachable at different energies in collider and fixed target experiments {CR} (the region covered by the NICA experiments is indicated.

[1] E-mail: sorin@theor.ru

A study of hot and dense baryonic matter should shed light on: in-medium properties of hadrons and nuclear matter equation of state (EOS); onset of deconfinement (OD) and/or chiral symmetry restoration (CSR); phase transition (PT), mixed phase (Fig.1 *left)* and critical end-point (CEP); possible local parity violation in strong interactions [1-4]. It is indicated in series of theoretical works, in particular, in [3] that heavy ion collisions at $\sqrt{s_{NN}} \leq 11$ *GeV* allow to reach the highest possible baryon density in the lab (fig.1 *right).* The high intensity and high polarization (>50%) of colliding beams could provide a unique possibility for spin physics research, which is of crucial importance for the solution of the nucleon spin problem ("spin puzzle") - one of the main tasks of the modern hadron physics.

The project NICA includes:

- an upgrade of the existing superconducting synchrotron Nuclotron to provide variety of ions up to Au with maximum energy of 4.05 *GeV/u;*
- an experiment Baryonic Matter at Nuclotron (BM@N) in the ion beams extracted from the modernized Nuclotron;
- the construction of NICA collider providing collisions of variety of ions up to Au^{79+} at the energy region up to $\sqrt{s_{NN}} \leq 11$ *GeV* with the luminosity $L = 10^{27}$ cm $^{-2}$ s $^{-1}$, and polarized proton and deuteron beams up to the c.m.s. energy of 27 GeV for *pp* collisions with the luminosity higher than $L = 10^{31}$ cm $^{-2}$ s $^{-1}$;
- an experiment with the MultiPurpose Detector (MPD) at the first interaction point (IP) of NICA with a primary goal to study heavy ion collisions;
- an experiment at the second IP of NICA with a primary goal to study spin physics.

2. Accelerator Facility NICA

The Nuclotron - is an existing synchrotron located in the Veksler and Baldin Laboratory of High Energy Physics (VBLHEP) of JINR, which has been put in operation in 1993. It is based on the unique technology of superconducting fast cycling magnets developed at VBLHEP. The upgraded Nuclotron will provide proton, polarized deuteron and multi charged ion beams.

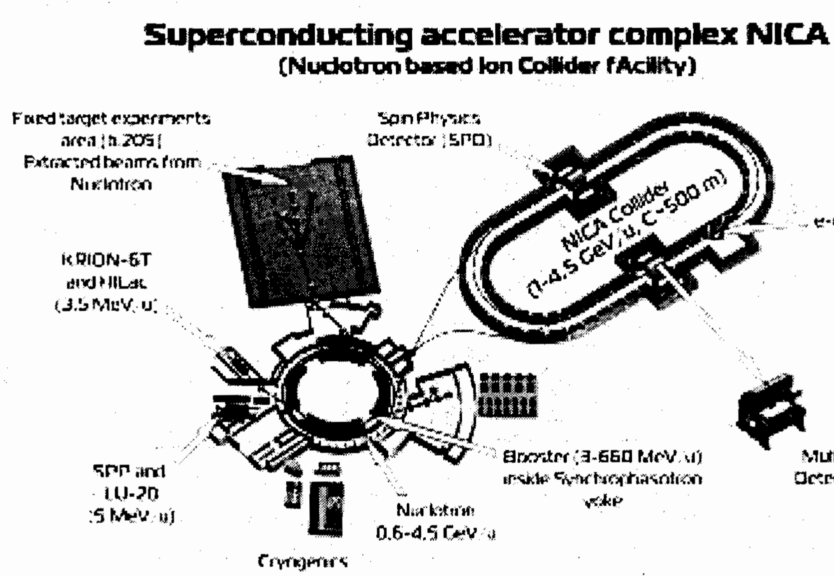

Figure 2. The new accelerator and experimental facility complex NICA at the VBLHEP.

The magnetic field of dipole magnets $B = 1.8\ T$ corresponds to the ion beam energies: 5.2 *GeV/u* for d (A = 2, Z=1); 3.3 *GeV/u* for Xe (A=124, Z=42); and 4.05 *GeV/u* for Au (A=197, Z= 79). The NICA facility (fig.2) includes: an injector complex providing wide spectrum of ions up to the heaviest one Au at energy of 3.5 *MeV/u* with an expected intensity $2\cdot10^9$; a booster accelerating ions up to 660 *MeV/u;* the source of polarized ions (protons and deuterons) SPI with the linac accelerating light ions up to 5 MeV/u; the Nuclotron continuing acceleration up to maximum energy (4.5 *GeV/u)* and two storage rings with two interaction points (IP). The ions are fully stripped before the injection into the Nuclotron. The major parameters of NICA collider are the following: $B\rho_{max}$ = 45 Tm; vacuum in a beam chamber – 10^{-11} Torr; maximum dipole field 2 T; extracted ion kinetic energy range from 1 *GeV/u* to 4.5 *GeV/u* for Au^{79+}; zero beam crossing angle at IP; 9 m space for detector allocations at IP's: maximum luminosity for ion collisions $L = 10^{30}\ cm^{-2}\cdot s^{-1}$. The required Nuclotron upgrade has started in 2008 and will be completed by 2015 including a booster and new linac. The construction of the collider rings and IP's will be started in 2013. The corresponding design project is ready for the Russian State expertise (fig. 3). The overall construction schedule foresees that the collider storage ring and basic infrastructure facility should be available for the first ion collisions already in 2017 [5].

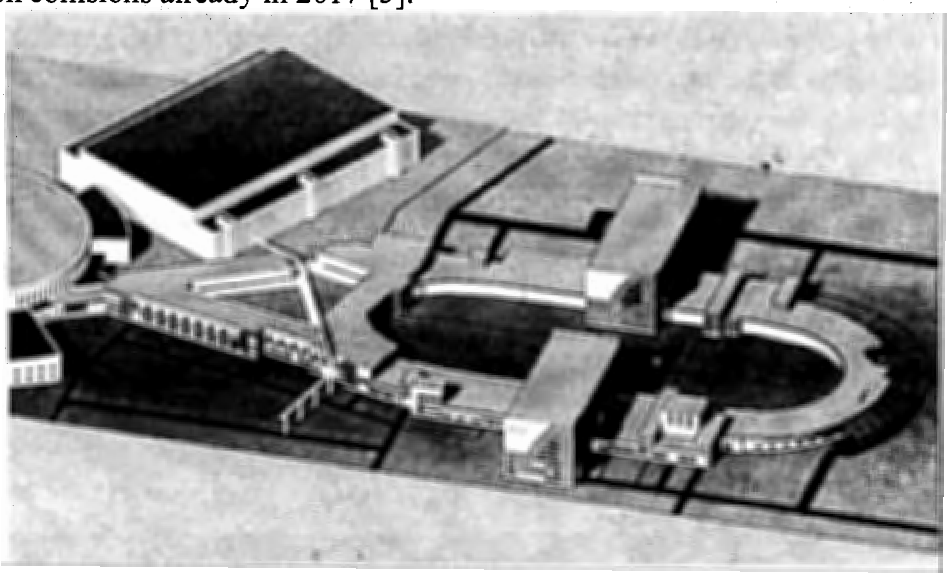

Figure 3. The architecture design of NICA collider and experimental buildings at two IP's.

In the first IP the Multipurpose Detector (MPD) will be installed, while a detector for the second IP is not yet designed. A call for the corresponding proposal is announced.

3. The BM@N Experiment

The energy of the extracted beams provided by upgraded Nuclotron-NICA finally will be reached 6 *GeV/u* for typical values of A/Z = 2. Proton and deuteron beams could reach an intensity of $5\cdot10^{12}$. A typical variety of other possible beams and their intensities provided by Nuclotron-NICA are presented in Table 1.

Table 1: The Nuclotron-NICA beams

beam	^{7}Li	^{12}C	^{40}Ar	^{56}Fe	^{84}Kr	^{124}Xe	^{197}Au
p.p.p	$5\cdot10^{11}$	$2\cdot10^{11}$	$2\cdot10^{11}$	$5\cdot10^{10}$	$1\cdot10^{9}$	$1\cdot10^{9}$	$1\cdot10^{9}$

To realize the first stage of experiments at extracted beams with a fixed target a new set-up – BM@N (Baryonic Matter at Nuclotron) will be constructed using existing wide aperture dipole magnet, tracking chambers, time of flight (TOF) system, hadron calorimeter and fast counter detector providing trigger signal. At the second stage an upgrade is foreseen to accomplish the set-up with a silicon vertex detector (in cooperation with the partners from GSI, Darmstadt), with the electromagnetic calorimeter, and with the neutron detector (optional).

4. The MPD Experiment

The MPD experimental program is aimed to investigate both: the hot and dense baryonic matter, and the nucleon spin structure and polarization phenomena. A list of the first priority physics tasks to be performed in the experiment includes: a) measurement of a large variety of signals at systematically changing conditions of collision (energy, centrality, system size) using as bulk observables the following:
- 4π geometry particle yields (OD, EOS); - multi-strange hyperon yields and spectra (OD, EOS); - electromagnetic probes {CSR, OD); - azimuthal charged-particle correlations (LPV); - event-by-event fluctuation in hadron productions (CEP); - correlations involving π, K, p, Λ (OD); -directed and elliptic flows for identified hadron species (EOS,OD); reference data (i.e. $p+p$) will be taken at the same experimental conditions; b) a study of hyperon polarization and other polarization phenomena; at the second stage after the MPD upgrade it will be possible to study nucleon spin structure via the Drell-Yan (DY) processes.

The MPD is a typical collider detector based on the solenoidal superconducting magnet. It will be installed in the first IP of NICA. The major sub-detectors of the MPD (fig.4) are: solenoidal superconducting magnet with a magnetic field of 0.5 T (~ 5 m in diameter and ~ 8m long); time projection chamber (TPC); inner tracker (IT); time-of-flight (TOF) system;

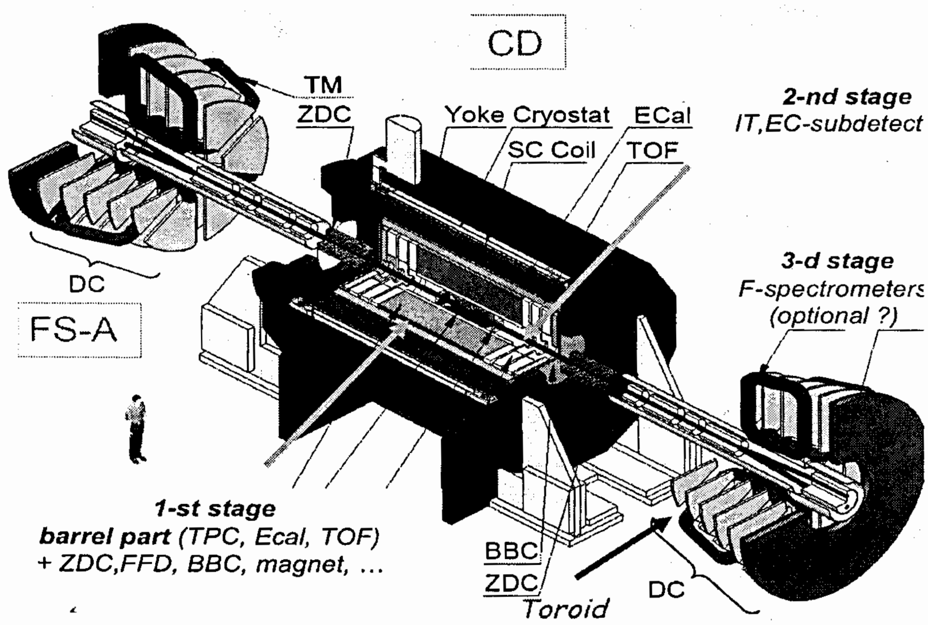

Figure 4. General view of the MPD, and sets of sub-detectors to be put in operation at different stages.

electromagnetic calorimeter (ECal); end cap tracker (ECT); two forward spectrometers based on toroid magnets (optional). There are foreseen three stages of putting MPD into operation. The first stage of operation involves magnet, TPC, TOF, ECal (partially), IT (partially), as well, and should be magnet, TPC, TOF, ECal (partially), IT (partially), as well, and should be ready for the first colliding beams in 2017. At the second stage the end caps of MPD will be fully equipped and some readout system modernized. The third stage related to possible requirement for forward spectrometers and is optional. The MPD experiment should be competitive and at the same time supplementary to ones operated at RHIC [6], and constructed in the framework of FAIR [7] project.

The processes studied with MPD were simulated using the dedicated software framework (MpdRoot). This software is based on the object - oriented framework FairRoot [8] and provides a powerful tool for detector performance studies, development of algorithms for reconstruction and physics analysis of the data. Evaluated rate in Au + Au collisions at $\sqrt{s_{NN}}$ = 7.1 GeV (10% central interactions) taking into account the luminosity of $L = 10^{27}$ cm^{-2} s^{-1} is 7 kHz. The corresponding particle yields are presented in Table 2.

Table 2: The particle yields in Au + Au collision (central) at $\sqrt{s_{NN}}$ = 7.1 GeV.

particle	yield / 4π	yield at y = 0	decay mode	ε,%	yield / 10 w
$\pi^{\pm}$	290	100	-	61	$2.6\cdot10^{11}$
$K^{\pm}$	60	20	-	60	$4.3\cdot10^{10}$
p	140	40	-	60	$1.2\cdot10^{11}$
ρ	30	17	e^+e^-	35	$7.3\cdot10^{5}$
ω	20	10	e^+e^-	35	$7.2\cdot10^{5}$
φ	2.6	1.2	e^+e^-	35	$1.7\cdot10^{5}$
Ω^-	0.14	0.1	ΛK^-	0.7	$2.7\cdot 0^{6}$

More than ten working groups from 12 institutions are intensively working on sub-detector R&D and on prototyping of all detector elements. More detailed information could be found in the conceptual design report [9]. It was shown that MPD is well optimized for study in-medium effects caused by high baryon densities, such as: changing particle properties in hot and dense medium (broadening of spectral functions etc.), event-by-event dynamical fluctuations of strange to non-strange particle ratios and others. These studies could be done with better precision than ones performed at the world current experiments.

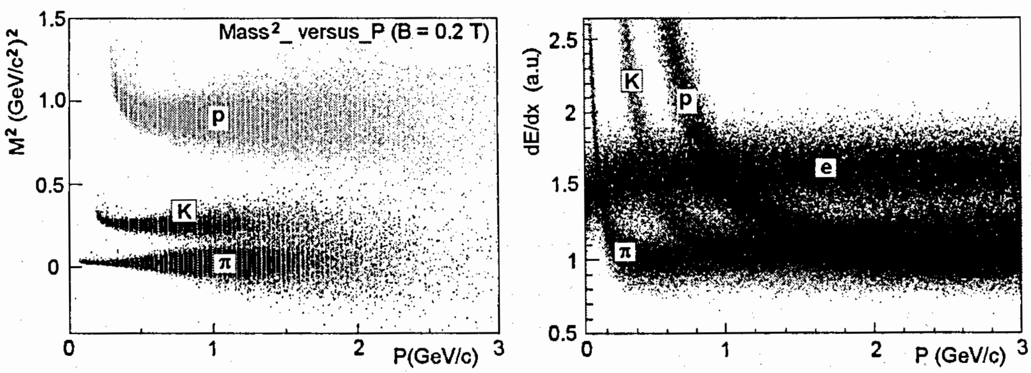

Figure 5. Left: particle ID using TOF system; right: particle ID in the TPC by measuring the losses due to the ionization.

The simulations of MPD capabilities shows that high statistics of studied events could be accumulated (10^9 minimum bias events and 10^8 central events per week), which provide the best precision for femtoscopy study with respect to RP correlation of multistrange particles. In ten weeks of running more than ~ 10^6 of Ω - hyperon decays will be recorded.Charged particles are reliably identified using both techniques: measuring dE/dx of tracks in TPC and by TOF system (see fig. 5).

It was obtained sufficiently high resolution of vertices reconstruction illustrated in fig. 6 *(left)*. The figure *(right)* shows as well an example of $\Omega \rightarrow \Lambda K^-$ decay reconstruction implementing full chain of simulation: central Au+Au collision generation at $\sqrt{s_{NN}}$ = 7.1 GeV; hyperon productions and decays; decay product detection and their reconstruction using necessary MPD sub-detectors.

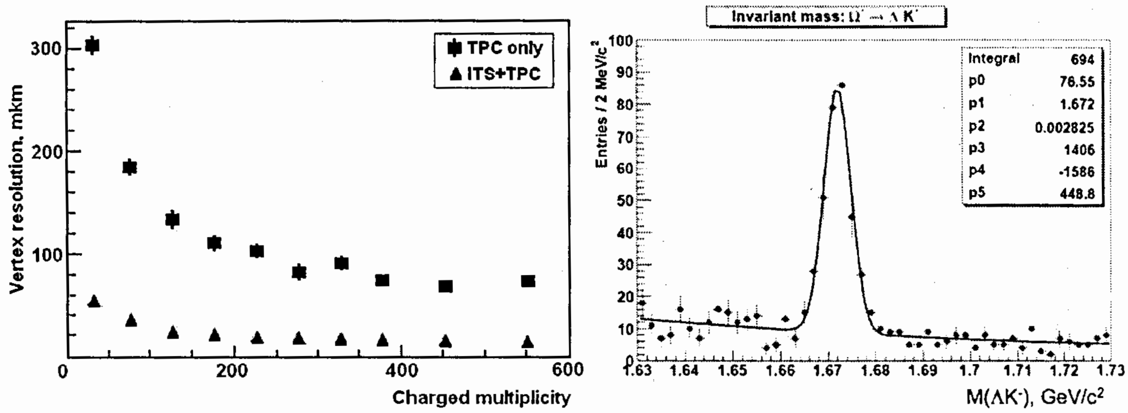

Figure 6. Left: vertex resolutions versus multiplicity for events reconstructed with TPC only (squares), and for events reconstructed using both TPC and IT (triangles). Right: reconstructed invariant mass of Ω decay products (vertex reconstruction with TPC and IT, and particle ID with TPC and RPC).

The MPD performance in general satisfies the required parameters for proposed experimental program. The further optimization of MPD elements design is continued. The corresponding infrastructure is developed as well at the site in the VBLHEP at JINR.

5. Spin physics at NICA

The NICA program foresees that a detector will be designed and installed in the second IP. The physics program of the related experiment should be dedicated, first of all, to the spin physics. There are number of interesting processes which could be studied with this detector and with the fixed target detectors in the beams extracted from the upgraded Nuclotron, namely: DY processes with longitudinally and transversally polarized *p* and *d* beams; extraction of unknown (poor known) parton distribution functions(PDF); PDFs from *J/ψ* production processes; spin effects in various exclusive and inclusive reactions; diffractive processes cross sections; helicity amplitudes and double spin asymmetries (Krisch effect) in elastic reactions; spectroscopy of quarkoniums with any available decay modes. That can be done in the kinematic region not available for other experiments. The creation of motivated collaboration has started. The proposal could be prepared and presented to the JINR scientific committees. The time scale of this experiment will be defined after the consideration of the proposals. Important part of preparation to the NICA spin physics research program is adequate development of the infrastructure including the polarization direction control, polarimetery etc.

6. Conclusion

The accelerator and particle detector complex NICA to be constructed at VBLHEP of JINR, and the related physics program, will provide relevant researches on one hand competitive, and on the other hand complementary to the ones being carried out and developing in other centers: RHIC at BNL, SPS and LHC at CERN, SIS18, SIS100 and SIS300 at GSI. The spin physics at NICA has a good perspective to complement experimental research at CERN SPS. And could have the unique possibilities for the experiments at polarized deuterons.

7. Acknowledgments

The work is supported by the RFBR, # 11- 02 - 01538/12.

References

[1] A.N. Sissakian, A.S. Sorin, M.K. Suleimanov. V.D. Toneev, and G.M. Zinovjev. Part. NucL Lett. 5, 1 (2008).

[2] M.Gazdzicki, M.Gorenstein, and S.Mrowczynski. PL., B585, 115 (2004).
[3] J. Cleymans, and J. Randrup, Phys. Rev. C74 (2006) 04791.
[4] B.Mohanty, J. Phys. G: Nucl.& Part. Phys. 38 (2011) 124023.

[5] A.Sissakian et al. Design and Construction of Nuclotron - based Ion Collider fAcility (NICA). Conceptual Design Report (JINR, Dubna, 2008) http://www.nica.ru
[6] G. S. F. Stephans, J. Phys. G32, S447 (2006), nucl-ex/0607030.
[7] P. Senger. J. Phys. G30, S10S7 (2004).
[8] D.Bertini et al., JoP,Conf.Ser.,119, 032011, (2008). http://cbmroot.gsi.de.

[9] A. Sissakian et. al., Multi Purpose Detector. Conceptual Design Report. v.1.2 (JINR, Dubna, 2010); http://www.nica.ru

VB LHEP accelerator complex development

A. Butenko [1], N. Agapov, A. Alfeev, V. Andreev, V. Batin, D. E. Donets, E. D. Donets, D. Donets, A. Eliseev, A. Galimov, E. Gorbachev, A. Govorov, B. Golovensky, E. Ivanov, V. Karpinsky, V.Kekelidze, H. Khodzhibagiyan, A. Kirichenko, A. Kobets, A. Kovalenko, O. Kozlov, I. Meshkov, V. Mikhailov, V. Monchinsky, K. Levterov, S. Romanov, T. Rukoyatkina, A. Sidorin, N. Shurkhno, I. Slepnev, V. Slepnev, A. Smirnov, A.Sorin, G. Trubnikov, A. Tuzikov, B. Vasilishin, V. Volkov, A. Philippov, O. Brovko

JINR, Dubna, Moscow Region

Abstract

Current development of the VB LHEP accelerator facility is aimed to creation of new modern accelerator-collider facility NICA. The first stage of the NICA creation – upgrade of the existing facility (so called Nuclotron-M project) was fulfilled during 2007 – 2010. After completion of the Nuclotron-M project three runs of the Nuclotron operation were carried out. The machine development shifts were dedicated to the performance increase for current physical program realization and to test equipment and operational modes of the NICA collider.

Introduction

Starting from 2007 the works on development of VB LHEP accelerator complex are carried out at JINR with the aim of creation a modern accelerator-collider facility NICA (Nuclotron-based Ion Collider fAcility) with wide program of fundamental and applied researches [1]. In the field of fundamental researches this program prolongs at qualitatively new level the investigations in relativistic nuclear and spin physics, traditional for LHEP. The new accelerator complex will include existing accelerator facilities as well as new linear accelerator, new synchrotron – booster and two rings of the collider. The facility will have to provide:

- experiments on extracted ion beams (from protons up to gold or uranium nuclei) at the kinetic energy up to 13,8 GeV (for protons), 6 GeV/u (for deuterons) and up to 4,5 GeV/u for heavy nuclei (like Lead, Gold or Uranium);

- experiments on colliding heavy ion beam at kinetic energy in the range from 1 to 4,5 GeV/u at the luminosity of 10^{27} cm^{-2}s^{-1};

- experiments on colliding heavy and light ions with the same energy range and luminosity;

- experiments on colliding polarized beams of light ions at the kinetic energy range from 5 to 12,5 GeV/u for protons, and from 2 to 5,8 GeV/u for deuterons, at the luminosity level not less than 10^{31} cm^{-2}s^{-1}.

For users of the NICA beams the following experimental areas and facilities will be available:

- building #205 for fixed target experiments (presently full-scale reconstruction of the building is being carried out);

- building #1B – here one plans to realize beam slow extraction from the booster for applied researches;

- the collider for heavy and light polarized ions equipped with MPD (MultiPurpose Detector) and SPD (Spin Physics Detector) is aimed for fundamental study of hot and dense state of the nuclear matter;

- the Nuclotron, that will be used as a basic facility for research in the field of accelerator physics and techniques, for development of modern diagnostics and test of prototypes of the collider systems;

- internal target set-up at the Nuclotron.

[1] e-mail: butenko@jinr.ru

“Nuclotron-M” project completed during 2007-2010 considered as a first stage of the NICA construction. The goal of the project was preparation of all the Nuclotron systems for reliable operation as a part of the new accelerator complex. Presently the Nuclotron development is aimed to the performance increase for current physical program realization and for testing equipment and operational modes of the NICA collider.

Results of the Nuclotron upgrade program

Necessity of deep modernization of the VB LHEP accelerator facility explained by two main reasons. From the one hand, Nuclotron main systems were created in the beginning of 1990-th, when the economical situation did not permit to realize the project in the total volume: the modernization of LU-20 accelerator was not completed, booster synchrotron was not constructed, RF acceleration system of the Nuclotron was realized at the level of full-scale prototype for commissioning period, diagnostic of the circulating beam was realized partially only, system for vacuum diagnostics in the beam pipe was absent practically, the power supply and protection systems for main magnetic elements did not satisfy completely to reliability requirements. From the other hand, main technological systems of the Nuclotron worked out their resources for many times, part of them has morally also physically become outdated.

The project working program included the next main tasks:

1. Development of the heavy ion source.
2. Development of the polarized deuteron source.
3. Sufficient improvement of the vacuum conditions in the Nuclotron beam pipe and linear accelerator-injector.
4. Development of the power supply system and energy evacuation system in order to reach magnetic field in dipole magnets of 1.8 T - 2 T.
5. Modernization of the cryogenic system.
6. Upgrade of the Nuclotron RF system, preparation to the adiabatic trapping into acceleration.
7. Development of the slow extraction system.
8. Development of the beam transfer lines and radiation shielding.
9. Beam dynamics investigations, minimizations of the particle losses at all stages of the acceleration.
10. Preparation of the KRION-2 ion source for generation of the ion beam at $A > 100$ and $q/A > 0.33$.
11. Design of new heavy ion linear injector.

Demonstration of acceleration of heavy ions at atomic number larger than 100 (before beginning of the modernization the heaviest ions accelerated at the Nuclotron were the iron ones - $^{28+}Fe^{56}$) with stable and safe operation of the magnetic system at the field of the dipole magnets of 2 T (before the maximum achieved value was 1.2 T) were chosen as indicators of successive completion of the project. 6 runs of the Nuclotron operation at total duration of about 3200 hours were carried out during the “Nuclotron-M” realization course. Commissioning of modernized and newly installed equipment, investigation and optimization of the operational conditions were the first priority tasks.

During the “Nuclotron-M” project development six runs of the Nuclotron operation had been carried out - #37 (November 2007), #38 (June of 2008), #39 (June of 2009), #40 (November 2009), #41 (March 2010) and #42 (December 2010) with total duration of about 3200 hours.

The run (#37) performed after beginning of the project was devoted to the test of the status of the Nuclotron systems and machine development experiments. During this run experimental estimate of average vacuum in the Nuclotron was made based on the studies of $^2H^+$ and deuteron beam circulation at the injection energy (5 MeV/u). It was shown, the beam pipe pressure scaled using equivalent concentration of N_2 molecules at T = 300 K was measured to approximately $2 \cdot 10^{-8}$ Torr, that was not sufficient for heavy ion acceleration. To start modernization of the system for orbit position measurements and the orbit correction the existing beam pick-up stations and correctors were re-tested and calibrated. Preliminary test of new scheme of the lattice magnet supply based on the electrical connection of all magnets in series was performed.

Sufficient part of further runs was devoted to the test of new equipment installed at the Nuclotron accelerator complex (Fig. 1).

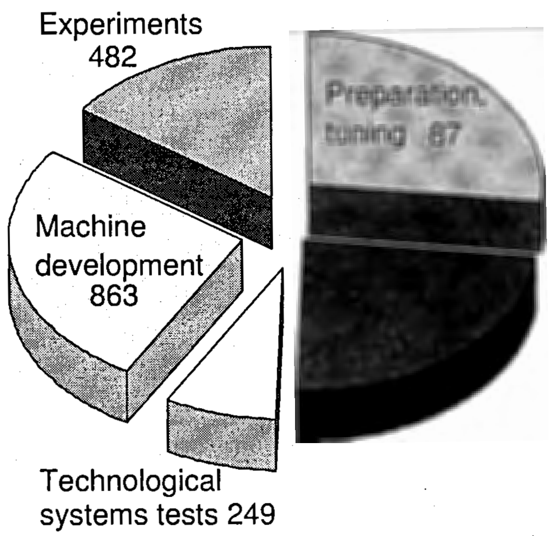

Figure 1: Statistics of the Nuclotron operation in hours.

Within this period two stages of the ring vacuum system upgrade were completed. Deep reconstruction of the cryogenic system was performed. New power supply system for electrostatic septum of the slow extraction system was constructed and tested at the test bench first and after installed at the ring. Partial upgrade of the ring RF system aimed to increase RF voltage and realize the adiabatic particle capture into acceleration was performed. A set of works at LU-20 accelerator was performed to improve the vacuum conditions and to increase the acceleration efficiency. New power supplies for the closed orbit corrector magnets were designed, constructed and put into operation. Electronics for the field cycle control, new power supply and quench protection system for structural magnets and lenses were created and tested at maximum design magnetic field [2].

Upgrade of the Nuclotron ring vacuum system

The Nuclotron vacuum system consists of two sub-systems: insulation vacuum system of the cryostat and high vacuum system for the beam pipe. Insulation vacuum system satisfied to all the requirements of the accelerator operation and its serious upgrade is not necessary. Before beginning of the "Nuclotron-M" project the Nuclotron beam pipe had no effective pumping of gaseous hydrogen and helium.

Upgrade of the vacuum system was performed in two stages:

- reconstruction of a few sections of the ring and installation of new vacuum pumps and diagnostic equipment;
- creation of automatic control system for the vacuum equipment.

The first stage was realized between the runs #37 and #38. Installed vacuum equipment was tested and put into operation during the run #38 and its application was resulted in improvement of the vacuum conditions by about two orders of magnitude.

The automatic control system was put into operation during the runs #40 and #41 that allowed to provide experimental study of evolution of the residual gas pressure and composition during long period of the ring operation [3]. At the moment the vacuum conditions in the beam pipe satisfies to requirements of the NICA project that was additionally demonstrated by successful acceleration of Xe ions.

Heavy ion acceleration

Sufficient improvement of the vacuum conditions, as well as partial modernization of LU-20 linear accelerator and optimization of the ion source KRION-2 made it possible to realize heavy ion acceleration at the Nuclotron facility. During the run #41 the ions of $_{124}Xe^{42+}$ were accelerated up to 1.5 GeV/u. At 1 GeV/u the slow extraction of the accelerated beam was used for a few methodical and physics experiments (Fig. 2) (experiment "Becquerel").

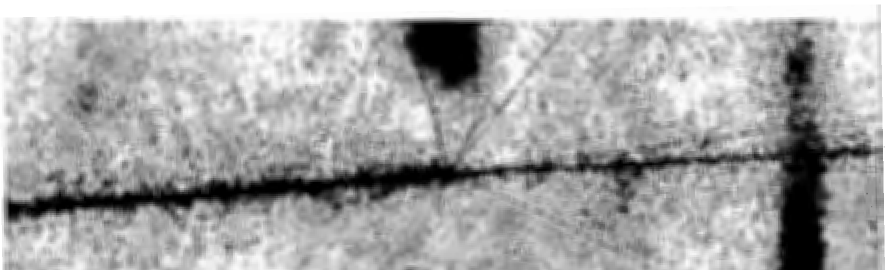

Figure 2: Extracted Xe (1 Gev/u) ion trace on photoemulsion (experiment "Becquerel").

As a part of the NICA injection chain the Nuclotron will be operated for acceleration of fully striped gold ions from 600 MeV/u. One has to mention that injection energy of Xe ions to the Nuclotron was 5 MeV/u. Acceleration of partially stripped heavy ion beam starting from such low energy is demonstrated that the vacuum conditions in the Nuclotron beam pipe is sufficient for the NICA requirements.

Upgrade of the cryogenic system

Starting from August of 2008 the Nuclotron cryogenic system was deeply reconstructed. Almost all the equipment was dismounted, transferred to specialized factories, repaired and transferred back into JINR. From February of 2009 the equipment was tested and step by step put into operation. As a result, presently the cooling capacity of each of the two refrigerators increased from 1.6 kW to 2 kW.

New power supply and energy evacuation systems

Stable and safe operation of the power supply and energy evacuation system was obtained at the magnetic field magnitude of 2 T during the run #42 performed in December 2010. The new power supply and quench protection system, based on the structural magnet connection in series, consists of the following general elements and subsystems [5]:

- New main power supply unit;
- New power supply unit for current adjustment in the quadrupole lenses;

- New 6 kA “warm” cable lines of about 5 km of the length;
- Energy evacuation system consisting of new 6 thyristor energy evacuation keys with dump resistors.

First the main power supply unit and energy evacuation system were tested at equivalent load. At the beginning of the run the main power supply, power supply for current adjustment in the lenses and the energy evacuation system were tested in the cycle at low level of the field. On the basis of obtained results the main power supply unit was adjusted for stable operation at maximum field. Finally the power supply and quench protection system was consequently tested in cycles with the bending field of 1.4, 1.6 and 1.8 T at the plateau. After that during a few hundreds of cycles the magnetic system was successfully operated at 2 T field at the plateau (Fig. 3). The field ramp rate was 0.6 T/s, the duration of the cycle active part was about 7 s. A few tens of the energy evacuation events acquired – in all of them the process was in the nominal regime.

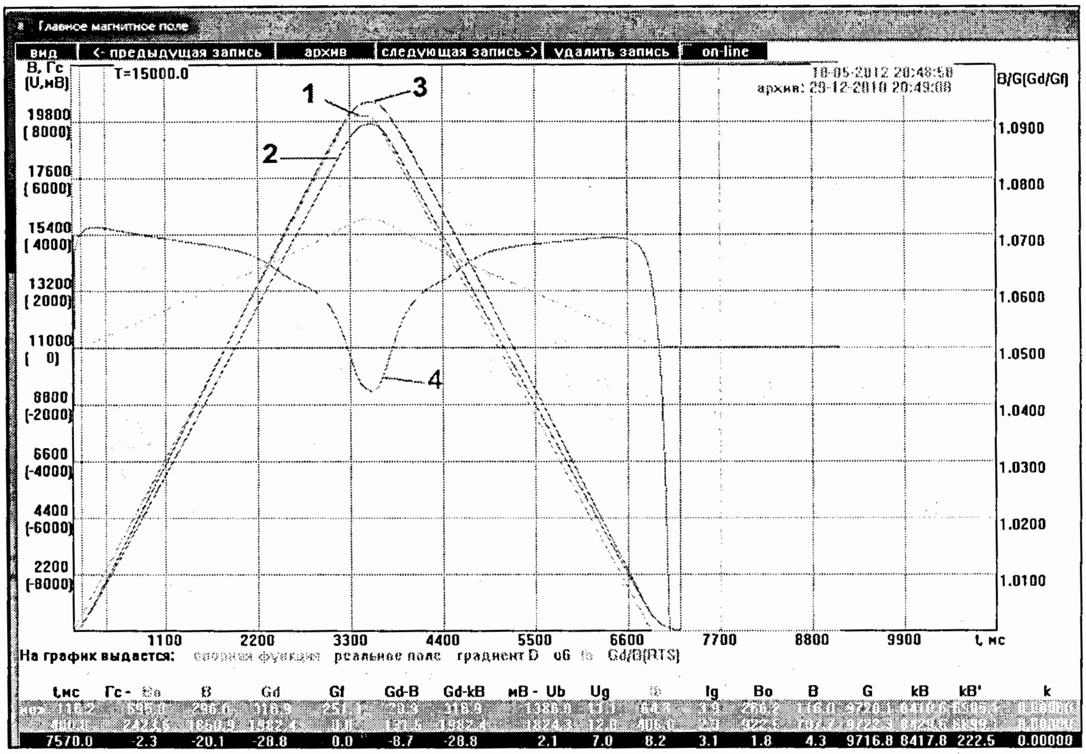

Figure 3: Cycle diagram at dipole magnetic field of 2 T. 1 – basic function, 2 & 3 – field of the magnets and gradient of the lenses correspondingly. December 2010.

In 2010 the Nuclotron-M project was successfully completed. Presently the creation of the NICA general elements is realizing in the frame of three officially approved JINR projects: “Nuclotron-NICA” (accelerator part), MPD (the project oriented to creation of one of the collider detectors) and BM@N (Baryonic Matter at Nuclotron – the new fixed target experiment with heavy ions, the detector is under construction in the building #205 in cooperation with GSI (Germany). The Nuclotron is the key element of all three projects: as the ion source for MPD element testing and for experimental program BM@N realization, as the main synchrotron in the injection chain of the future collider and as the basic facility for testing of new equipment of the booster and collider rings. After completion of the Nuclotron upgrade three runs (#43- #45) at total duration of about 2900 hours were performed. About 1400 hours were spent for physical experiments including the shifts dedicated to machine development.

Machine development

The machine development aimed to increase the Nuclotron ability for the current physical program realization is provided in the following main directions:

- step by step increase the beam energy up to maximum design value (6 GeV/u for deuterons);
- optimization of the beam dynamics in order to minimize the particle losses during acceleration;
- further development of power supply system in order to provide required quality of slow extraction;
- development of the beam diagnostics;
- development of ion sources and fore-injector modernization.

Before modernization the Nuclotron provided the beam energy up to 3 GeV/u maximum (for the ions with A/Z = 2). During the run #44 (December 2012) carbon beam was accelerated up to about 3.5 GeV/u and after slow extraction transported along the transport line to the point of the future location of the BM@N detector. During the same run the slow extraction of deuteron beam-had been realized at 4 GeV/u. In the run #45 (March 2012) the slow extracted 4 GeV/u deuteron beam was routinely used for physical experiments. At the end of the run #45 the possibility of the slow extraction was demonstrated at the deuteron beam energy of 4.5 GeV/u. Further increase of the extracted beam energy is related to development of the slow extraction system (increase of the electrostatic septum voltage and current of the slow extraction quadrupoles) and optimization of operational conditions of the power supply system.

Decrease of the ion losses during acceleration is related with further development of the accelerating RF system, optimization of the closed orbit (including the orbit bump in the slow extraction region), development of the beam diagnostics. Sufficient part of these works was performed during runs #43 – #45.

Fast current transformer (FCT) installed at the Nuclotron before the run #44 was optimized for work in required dynamic range. Now the analogous device is installed in the beam injection line. In future one plans to use such FCTs at the Booster and collider.

New ionization beam profile monitor based on MCP was installed in the «warm» section of the Nuclotron. During run#45 it was optimized for work with heavy ion beams at relatively low intensity.

During the runs #44 and #45 experimental fragment (two octants of the ring) of new system of superconducting element thermometry were tested. Full scale implementation of the new system is scheduled to the end of this year.

In the frame of the Nuclotron upgrade program a new quench detection system was designed. Prototypes of the quench detector were consequently tested during two runs of the accelerator. On the basis of the test results the serial production of the quench detectors was started in 2010. During two runs of the accelerator the fragment of the new quench detection system including 20 quench detectors was operated during more than 1500 hours. Stable and reliable work of all elements was demonstrated. The system performs scheduled self-test diagnostics in real time and controls power elements of energy evacuation. Full-scale implementation of the new quench detection system is scheduled for the Nuclotron run #46 (at the fall of 2012).

The works oriented to creation of new sources of high intensive heavy ions and light polarized nuclei are in the final stage. In 2011 the 6 T solenoid for the heavy ion source (of electron string type – ESIS) was constructed, assembly of the source was completed this year. Experimental investigations of the source parameters have been started. The atomic beam source for the source of polarized particles was assembled and tested at INR (Troitsk), the plasma ionizer and test bench for the final assembly and test of the source is under construction at JINR. Completion of these works is scheduled for 2012.

The LINAC LU-20 fore-injector upgrade is required for operation of the new ion sources. Replacement the electrostatic accelerating tube by RFQ will allow to reduce HV potential of the Ion Source platform from 400-700 kV down to 50-150 kV. The compact isolation transformer (160kV-35kWA) will fine solution as power supply of the ion sources up to 35 kW. The production of RFQ in cooperation with ITEP is in progress, the isolation transformers produced by STL Stewart Transformers Ltd.

Nuclotron as a test facility for NICA

The Nuclotron having the same magnetic rigidity as the future NICA collider and based on the same type of the magnetic system is the best facility for testing of the collider equipment and operational regimes. Simulation of the collider magnetic system operational conditions was performed at the Nuclotron during runs #44 and #45. This presumed test of the Nuclotron magnetic system, power supply and quench protection systems, cycle control and diagnostic equipment in the operational mode with long plateau of the magnetic field. In the run #44 the magnetic field cycle duration was prolonged up to 500 s without beam acceleration, in the run #45 the circulation of accelerated deuteron beam during 1000 s was demonstrated (Fig. 4).

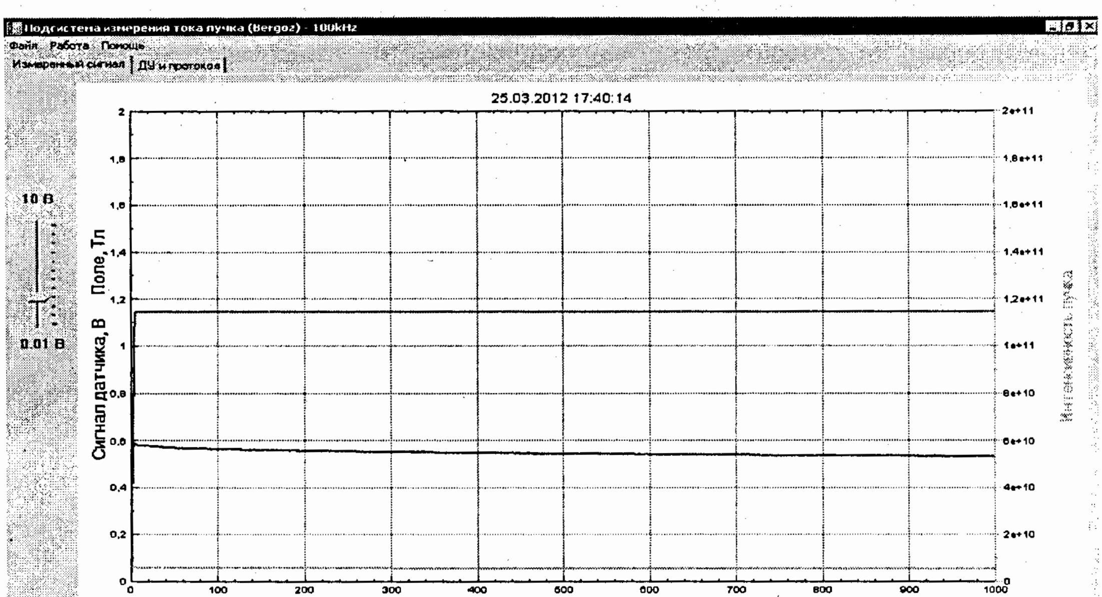

Figure 4: Circulation of the deuteron beam at the field plateau during 1000 s. Dipole field is 1.2 T (upper curve), the beam intensity is $5 \cdot 10^9$ particles (lower curve), middle curve – beam current transformer signal. March 2012.

Application of beam cooling methods (electron and stochastic) in the collider ring has the goals of beam accumulation using cooling + stacking procedure and luminosity preservation during experiments. Experimental test of the stochastic cooling at the Nuclotron is considered as important phase of the collider beam cooling system design. This work is developed in very close collaboration with FZ Juelich (Germany). During 2010-2011 the elements of the stochastic cooling chain for test at the Nuclotron were designed, constructed and after vacuum and cryogenic tests installed at the ring (Fig. 3). Experiments started in December 2011 were continued in 2012. We plan step by step investigate longitudinal and transverse cooling of coasting and bunched beams [6].

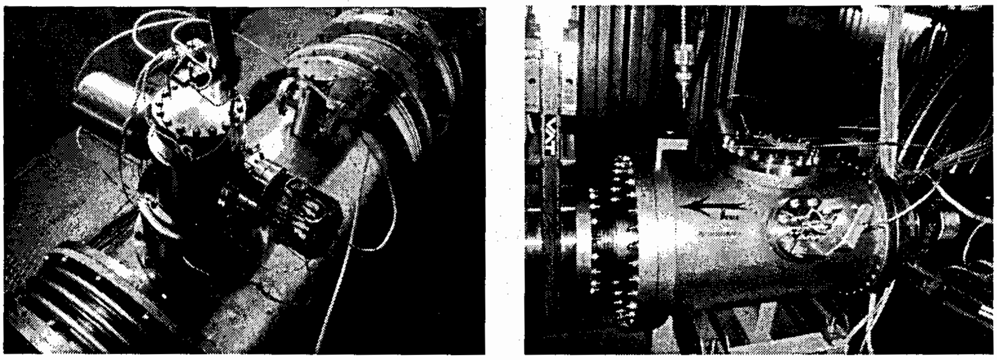

Figure 5: Pick-up (left) and kicker (right) of the Nuclotron stochastic cooling chain.

Conclusions and outlook

The works on design and construction of the new accelerator facilities of the NICA complex are carried out in parallel with development and operation of the Nuclotron. Technical design of the booster is completed: construction of the booster RF accelerating stations is in the final stage at BINP (Novosibirsk), the prototype of the sector dipole magnet was constructed and tested, first measurements of its magnetic field were performed, the prototype of the booster quadrupole lens was constructed and prepared for the test and successfully tested, the power supply, control and diagnostic system, the elements of vacuum system are under development. The design of the collider optic structure is in the final stage. Experts from FNAL and BNL (USA), FZJ and GSI (Germany), CERN, ITEP, BINP actively participate in the design works, the results are analyzed by international machine advisory committee on the regular base. Technical project of the required civil construction works for the collider and beam transport lines location is developed by specialized designer company and prepared for state expertise.

The full-scale Nuclotron–type superconducting model dipole and quadrupole magnets for the NICA booster and collider were manufactured during 2010 – 2012. First dipole and quadrupole magnets for the NICA booster have successfully passed the cryogenic test on the bench. To construct the Booster and collider rings, it is necessary to fabricate more than two and half hundreds of the dipole magnets and lenses during a short period of time. Special area for the magnets assembly and comprehensive tests required for the magnets commissioning are currently being prepared.

References

[1] G. Trubnikov, N. Agapov, V. Alexandrov, et al., Project of the Nuclotron-based ion collider facility (NICA) at JINR, Proceedings of RuPAC-2010, Protvino, Russia

[2] A. Eliseev, N. Agapov, A. Alfeev, et al., Results of the Nuclotron upgrade program, Proceedings of IPAC2011, San Sebastian, Spain.

[3] N.Agapov, A.Alfeev, V.Andreev, et al., Progress in the Nuclotron Development, Proceedings of VIII International Scientific Seminar in Memory of V.P.Sarantsev, Alushta, Ukraine, 2009, Particles and Nuclei, Letters, 2010, V 7, No. 7(163).

[4] N. Agapov, V. Alexandrov, O. Brovko, et al., Status of the Nuclotron. Nuclotron-M project, Proceedings of IPAC'10, Kyoto, Japan.

[5] V.Karpinsky, N.Kondratiev, A.Osipenkov, et al., Upgrade of the Nuclotron Power Supply, Proceedings of VIII International Scientific Seminar in Memory of V.P.Sarantsev, Alushta, Ukraine, 2009, Particles and Nuclei, Letters, 2010, V 7, No. 7(163).d.

[6] I.Meshkov, N.Shurkhno, G.Trubnikov, et al., Stochastic cooling system for Nuclotron, Proceedings of RuPAC-2010, Protvino, Russia.

Научное издание

Relativistic Nuclear Physics: from Hundreds of MeV to TeV
Proceedings of the 11th International Workshop

Релятивистская ядерная физика: от сотен МэВ до ТэВ
Труды 11-го Международного совещания

E1,2-2013-24

Ответственная за подготовку сборника к печати *И. И. Мигулина.*

Сборник отпечатан методом прямого репродуцирования
с оригиналов, предоставленных оргкомитетом.

Подписано в печать 25.04.2013.
Формат 60 × 84/8. Бумага офсетная. Печать офсетная.
Усл. печ. л. 18,72. Уч.-изд. л. 17,19. Тираж 110 экз. Заказ № 57951.

Издательский отдел Объединенного института ядерных исследований
141980, г. Дубна, Московская обл., ул. Жолио-Кюри, 6.
E-mail: publish@jinr.ru
www.jinr.ru/publish/